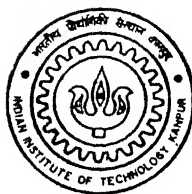


**EVOLUTION AND STABILITY OF TEXTURES DURING
THERMOMECHANICAL PROCESSING OF
Ti-24Al-11Nb ALLOY**

by

SATYAM SUWAS

TH
MME/1998/P
Su 93e



**DEPARTMENT OF MATERIALS AND METALLURGICAL ENGINEERING
INDIAN INSTITUTE OF TECHNOLOGY KANPUR**

JUNE, 1998

Evolution and Stability of Textures During Thermomechanical Processing of Ti-24Al-11Nb Alloy

*A Thesis Submitted in Partial Fulfilment of the Requirements
for the Degree of*

DOCTOR OF PHILOSOPHY

by

Satyam Suwas



to the

Department of Materials and Metallurgical Engineering
Indian Institute of Technology Kanpur, India

June, 1998

15 AUG 1999/MNF
CENTRAL LIBRARY
I.I.T.

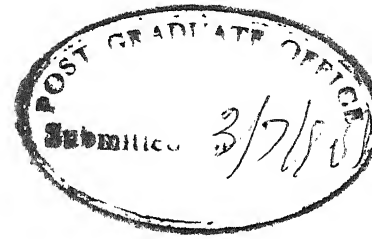
Inv. No. A 128772

TH
Mme/2006/10
SU.93e



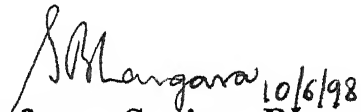
A128772

Certificate



It is certified that the work contained in the thesis entitled **Evolution and Stability of Textures during Thermomechanical Processing of Ti-24Al-11Nb Alloy**, has been carried out by Satyam Suwas (Roll Number : 9410664) under our supervision and that this work has not been submitted elsewhere for a degree.


(Professor Ranjit Kumar Ray)


(Professor Sanjeev Bhargava)

Department of Materials and Metallurgical Engineering

Indian Institute of Technology Kanpur

Kanpur-208016 (INDIA)

To my teachers...

SYNOPSIS

In the pursuit of stronger and lighter aerospace alloys, titanium alloys with high concentrations of aluminium (with concentration exceeding roughly 20 at. %) have been developed. With such high aluminium contents the resulting phases are intermetallic compounds having ordered structures. The system based on the compound Ti_3Al is among the oldest in this series and is also the most comprehensively studied of the titanium aluminides. The need for developing materials with enhanced engine performance through lighter weights and higher operating temperatures spurred research interests on Ti_3Al and its derivatives.

Ti_3Al has a specific modulus and stress rupture resistance comparable to that of the superalloys. However, it suffers from a severe limitation due to complete absence of room temperature plasticity. Attempts have, therefore, been made to identify suitable ternary additives, which could impart the requisite room temperature ductility. Niobium addition has emerged as the most successful means for this purpose. Addition of Nb in Ti_3Al (α_2) stabilise the b.c.c. (β) phase of titanium even at room temperature. Strength, toughness and ductility all increase with Nb addition. The first Ti_3Al based composition which demonstrated satisfactory room temperature ductility has been reported to be Ti-24Al-11Nb (in at %). Since then, a number of studies have been carried out with a view to exploiting the full potential of this material. As the applications of Ti-24Al-11Nb or any other Nb modified Ti_3Al base alloy require the material mostly in sheet form, several attempts have been made for

studying deformation processing of this material. Since, it is not suitable for room temperature rolling, rolling at elevated temperatures with or without a post annealing treatment is usually recommended. Although quite a few papers have been published on the processing of Ti_3Al-Nb alloys and $Ti-24Al-11Nb$ alloy in particular, systematic study of the effects of processing variables has hardly been carried out. In addition, the issue of textures which is likely to be of extreme importance for such h.c.p. structured materials with regard to mechanical properties, has not at all been paid serious attention. It is well known that texture affects most of the properties of materials including tensile properties and fracture, fracture toughness, fatigue and environmentally assisted fracture etc. It has also been established that h.c.p. Ti alloys, composed mainly of basal-textured α grains, exhibit significant improvement in ductility which ultimately decides the sheet formability characteristics of the material. An attempt has therefore been made to explore various possibilities for the production of basal texture in thermomechanically processed $Ti-24Al-11Nb$ alloy sheets. A number of processing routes have been tried and the resulting evolution of textures has been documented and critically examined. Also, a thorough investigation on the stability of basal textures, evolved during thermomechanical processing, has been carried out as functions of both annealing effects and $\alpha_2 \rightarrow \beta \rightarrow \alpha_2$ phase transformation cycle.

The alloy used in the present investigation with the nominal composition $Ti-24Al-11Nb$ (at. %) was cast in the form of a pan cake. This material was suitably cut into small pieces and these were then subjected to hot rolling at four different

temperatures, namely, 1173 K, 1293 K, 1373 K and 1523 K, for three levels of thickness reductions, namely 50%, 70% and 80% at each temperature. All the samples were quenched in water from the rolling temperature. The samples with the highest reduction were also furnace cooled from the respective rolling temperatures. Some pieces of the as-cast material was given a prior heat treatment but for the equilibration of phases and then subjected to rolling at 1173 K by different amounts of reduction followed by water quenching.

Subsequently, the above as-rolled materials were annealed isochronally (for 1 hr) within the temperature range 1123 K-1293 K and (at ~50 K intervals) and also isothermally at 1173 K for time intervals ranging from 1 hr – 12 hrs. In an alternative route of heat treatment, the differently processed as-rolled materials were heat treated at three different temperatures, corresponding to different phase fields, and then finally furnace cooled to room temperature. Extensive microstructural characterisation of the different as-processed samples was carried out using optical and scanning electron microscopy (SEM). Thin foils of selected number of samples, were thoroughly examined under a transmission electron microscope (TEM-JEOL 2000 FX), operated at 160 kV.

X-ray diffraction studies were carried out in the usual manner on samples at different stages of processing, with a view to characterising the phase compositions as well as textural effects. Detailed texture study on most of the as-processed samples was undertaken using both the X-ray pole figure as well as the ODF (Orientation Distribution Function) methods. Each ODF was calculated from the data of 6 pole

figures, namely, $(20\bar{2}0)$, (0002) , $(20\bar{2}1)$, $(20\bar{2}2)$, $(22\bar{4}0)$ and $(20\bar{2}3)$, using the series expansion method upto $l_{\max} = 32$.

The results of the present investigation indicate that the starting material, i.e. the as-cast alloy, which consists of randomly oriented laths of α_2 in β (B2) matrix possess a strong basal texture and that this texture does not change significantly due to prolonged annealing at 1173 K. Strong basal texture is also obtained when the starting material is rolled at 1173 K, both in the water quenched and in furnace cooled conditions. Among these two the former gives rise to the sharpest basal texture. The texture maxima are mainly located along the fibre $[0001] \parallel \text{ND}$ ($\sim 12^\circ$ from the exact location), and a few strong intensity peaks are also observed at $[10\bar{1}0] \parallel \text{RD}$ fibres in these cases.

The material, which was prior heat treated at 1173 K for a long time before rolling at 1173 K upto 80% reduction exhibits an even sharper basal texture as compared to the samples mentioned above. In this case, most of the orientations are concentrated along $[0001] \parallel \text{ND}$ fibre. The degree of deformation during rolling also has a profound effect on the nature and extent of texturing. For example, the material rolled at 80% reduction at 1173 K shows a sharper basal texture than the one rolled to 50% reduction.

The results also clearly show that rolling at temperatures above 1173 K but below the β -transus ($1373 \text{ K} \pm 10 \text{ K}$) is not favourable for obtaining good basal texture. Hot rolling at temperatures above the β -transus followed by water quenching was done in order to have an idea about the hot rolling texture of the β phase. This

information was crucial for understanding the texture formation in α_2 obtained from β by transformation during furnace cooling. Two temperatures were chosen for this purpose, namely, 1373 K which is just near the $\alpha_2+\beta/\beta$ phase boundary, where there is only a feasible chance of β recrystallisation during furnace cooling and the other temperature is 1523 K where the β phase is likely to get an opportunity to recrystallise before transformation. Although the β rolling textures in both the cases are more or less similar, (with $\{011\}\langle uvw \rangle$, $\{112\}\langle uvw \rangle$, $\{113\}\langle uvw \rangle$ and $\{223\}\langle uvw \rangle$ as the main components along with several other weaker components) the resulting transformation textures are significantly different. In the former case, the nature of texture evolved in transformed α_2 (henceforward named as secondary α_2) is completely non basal and in accordance with the Burger's relationships for transformation. In the latter case, furnace cooling gives rise to the basal type of texture. This difference has been attributed to the differences in variant selection during $\beta \rightarrow \alpha_2$ transformation in the above two cases.

After examining the conditions for the development of a satisfactory basal texture, attention was focussed on its stability during further heat treatments, which are usually undertaken for microstructural control. For this purpose, the material obtained by rolling of the prior heat treated alloy, which also exhibited a strong basal texture, has been subjected to isochronal annealing for 1 hr at temperatures 1123 K, 1173 K, 1233 K and 1293 K and then water quenched.

The above temperatures were chosen such that α_2 remained the major phase, thus allowing the effect of heat treatment on the basal texture of α_2 phase to be examined. It was observed that annealing at the lowest temperature, 1123 K, where recrystallisation of the α_2 just begins, the basal texture weakens perceptibly and a number of other non basal orientations develop. However, it more or less, regains its strength on annealing at 1173 K and 1233 K. The basal texture again starts degrading at 1293 K. On the basis of the above results, further isothermal annealing was performed at 1173 K over intervals of time ranging between 15 min – 12 hrs. The isothermally annealed samples also have shown initially a tendency for degradation of basal texture and evolution of non basal components for shorter annealing times and re-intensification of the basal texture after longer annealing times. However, a relatively prolonged annealing for 12 hrs was found to be deleterious for the basal texture. The above observations on textural changes on isochronal as well as isothermal annealing are compatible with the common behaviour of annealing textures of h.c.p. metals and alloys where the rolling textures are retained after recrystallisation. The degradation of rolling texture in the initial stages of annealing has been stipulated to be associated with some changes in the state of order of the α_2 phase. This is in conformity with the annealing behaviour of other aluminide intermetallics, such as Ni_3Al .

Finally, an attempt was also made in this investigation to examine the effect of $\alpha_2 \rightarrow \beta \rightarrow \alpha_2$ transformation cycle on the stability of the basal as well as the non-basal components of texture. For this purpose, samples showing three different types of

textures - basal, weakly basal with non-basal components, and perfectly non-basal texture - were subjected to heat treatments in mostly the α_2 phase field, equiproportional $\alpha_2 + \beta$ phase field and the β phase field followed by furnace cooling.

The texture results indicate that the material which already has a reasonably strong basal texture undergoes degradation on heat treatment in the α_2 phase field for a long time. Heat treatment at the higher temperature of 1293 K degrades it further. After heat treatment above the β -transus, the material undergoes a phase transformation to β followed by a second $\beta \rightarrow \alpha_2$ phase transformation during furnace cooling. This treatment has also been found to be detrimental to the preservation of the basal texture.

Similar heat treatments carried out on the material having a weak near basal texture and other non-basal components have shown results different from that of the material with starting basal texture. Heat treatment of this material 1173 K seems to enhance the intensity of near basal texture. However, heat treating the same material at 1293 K causes a deterioration of the basal texture. Surprisingly, heat treatment at 1373 K caused significant improvement in the basal texture.

Heat treatment of the material was completely non-basal starting texture, followed by furnace cooling does not seem to favour the formation of basal texture irrespective of the heat treatment temperature used. These differences have been attributed to the differences in the nature of stress state of the starting α_2 phase from which β forms, to be re-transformed into secondary α_2 during furnace cooling.

It thus appears that it is essential to have at least some intensity of the basal texture component in the starting material in order that a strong basal texture can be produced upon processing. Rolling at lower temperatures with high amounts of reduction usually favours the development of basal texture which remains reasonably stable even after complete recrystallisation on heat treatment.

Acknowledgements

I express my deep sense of indebtedness to Professor R. K. Ray and Professor S. Bhargava for their excellent teaching as well as careful and encouraging guidance throughout the tenure of the present work. Their able teaching, inspiring guidance and above all intense humane and understanding personalities have left an indelible impression upon me. Never seeking to impose their views upon me, they have consistently treated me with great kindness and evinced a keen interest in my personal welfare.

I also extend my sincere gratitude to Dr. A. K. Singh, Scientist, DMRL, Hyderabad for his constant inspiration, overwhelming co-operation and deep concern for my work as well as my personal welfare. I consider myself fortunate to have academic association with him. His infectious enthusiasm has always been a motivating force for me.

I express my deep sense of gratitude to Dr. D. Banerjee, Director, DMRL, Hyderabad, for providing me the facility for texture measurements at DMRL, as well as for his continuous support, technical as well as moral, throughout my thesis work. In fact, it is more of his concern and support that this work has come to reality.

I gratefully acknowledge Dr. A. K. Gogia and Mr. T. K. Nandy of DMRL for their invaluable suggestions that I received through a number of discussions with them during my stay at DMRL, which enabled me in formulating many an important part of this thesis. I extend my acknowledgement to Dr. P. K. Sagar for benefiting me through his experiences.

My sincere respects go to Dr. V. S. R. Murthy and Dr. S. Sangal for their personal concern for me as well as for providing all kinds of help whenever required. I respectfully acknowledge Prof. B. Deo, Prof. R. K. Dube and Prof. G. S. Upadhyaya for their constant encouragement and concern.

I also gratefully acknowledge the extremely sincere and valuable technical and moral support provided by Mr. V. P. Gupta for most of the tenure of the present work and afterwards as well.

Technical support rendered by Mr. V. Ramakrishna (DMRL), Mr. S. C. Barthwal, Mr. U. S. Singh, Mr. P. K. Pal and Mr. U. S. Lal (all ACMS, IITK) are sincerely acknowledged. . Among the laboratory staff members of MME department, my sincere thanks are due to Mrs. V. Kumar, S.C. Soni, H. C. Srivastava, R. K. Prasad, K. P. Mukherjee, A. K. Awasthi, V. P. Srivastava, P. P. Singh (retd.), A. K. Verma, S. D. Singh, C. L. Sachan, S. B. Shukla, K. S. Bhamra and K. K. Malhotra for their help at many stages of this work. In addition, I must not forget to name Mr. V. V. Rama Rao (Scientist, DMRL), Mr. S. M. Gupta, Mr. M. Yadagiri and Md. Ghose (all DMRL) for their concern and help.

I thankfully acknowledge my senior colleague and friend Dr. B. Bhattacharya for beneficial discussions as well as for providing me a nice company during our stay at IITK. Among my other senior colleagues and fellow researchers, I specially thank Dr. M. N. Mungole, Dr. S. Ghosh Chowdhury and Arvind Agarwal for giving me a nice company in research work. Amongst junior colleagues, Sanjib Rakshit, Piyush Srivastava, Kanchan Kumari, Karadge Mallikarjun, Keshab Patro, Bikash Maji, and Anirban Guha are a few ones, who shared the memories of my pleasant stay at IITK.

One of the most enjoyable company at IIT Kanpur has been of Mr. Joginder Singh. Any word of acknowledgement will be an encomium to his concern he has for me. The most pleasing association that I had at IITK, is of him.

Last but not the least, I am thankful to my friends Neeraj Sachdev, Anirban Guha, Maneesh Srivastava and Pradyot Dutta for their assistance in thesis preparation. In this connection, the painstaking efforts of my friend Mr. Anil Kumar in keeping my computer active is gratefully acknowledged. The efforts of Mr. V. Kumar and Mr. J. K. Mishra at the thesis preparation stage are highly appreciated and acknowledged.

Satyam Suwas

CONTENTS

LIST OF FIGURES	xiv
LIST OF TABLES	xxxi
CHAPTER 1 INTRODUCTION	1
CHAPTER 2 LITERATURE REVIEW	10
2.1 Phases and Crystal Structure	11
2.2 Phase Transformation	15
2.2.1 Transformations during quenching	15
2.2.2 Transformations during continuous cooling	15
2.2.3 Transformations during ageing	17
2.3 Deformation Behaviour	19
2.3.1 Deformation crystallography	19
2.3.2 Deformation processing	24
2.4 Mechanical Behaviour	33
2.4.1 Tensile behaviour	33
2.4.2 Creep and stress rupture behaviour	39
2.4.3 Fracture toughness and fatigue	45
2.4.4 Superplasticity	47
2.5 Texture	49
2.6 Scope of the present investigation	53
CHAPTER 3 EXPERIMENTAL PROCEDURES	54
3.1 Starting Material	54
3.2 Thermomechanical processing	54
3.2.1 Hot rolling	55
3.2.2 Heat Treatments	56
3.3 Characterisation techniques	58
3.3.1 Microstructural characterisation	58
3.3.2 X-ray characterisation	64

	3.3.3	Characterisation of texture	65
	3.3.4	Hardness testing	69
CHAPTER 4		EVOLUTION OF TEXTURE AND MICROSTRUCTURE DURING HOT ROLLING	71
	4.1	Microstructure	72
	4.1.1	Rolling of the as-cast and heat treated material at 1173 K	74
	4.1.2	Rolling of the as-cast material at 1293 K	87
	4.1.3	Rolling of the as-cast material at 1373 K	95
	4.1.4	Rolling of the as-cast material at 1523 K	103
	4.2	X-ray Diffraction Profiles	109
	4.2.1	Starting material	109
	4.2.2	Material rolled at 1173 K and quenched	112
	4.2.3	Material rolled at 1293 K and quenched	115
	4.2.4	Material rolled at 1373 K and quenched	117
	4.2.5	Material rolled at 1523 K and quenched	117
	4.2.6	Material rolled at 1173 K, 1293 K, 1373 K and 1523 K followed by furnace cooling	120
	4.3	Texture Analysis	123
	4.3.1	Texture of material rolled at 1173 K	124
	4.3.1.1	As-cast, rolled and water quenched	124
	4.3.1.2	Heat treated, rolled and water quenched	138
	4.3.1.3	As-cast, rolled and furnace cooled	145
	4.3.2	Texture of material rolled at 1293 K	149
	4.3.2.1	As-cast, rolled and water quenched	149
	4.3.2.2	As-cast, rolled and furnace cooled	151
	4.3.3	Texture of material rolled at 1373 K	156
	4.3.3.1	As-cast, rolled and water quenched	156
	4.3.3.2	As-cast, rolled and furnace cooled	157
	4.3.4	Texture of material rolled at 1523 K	157
	4.3.4.1	As-cast, rolled and water quenched	157
	4.3.4.2	As-cast, rolled and furnace cooled	158
	4.4	Discussion of the Results	165

4.4.1	Evolution of microstructure	167
4.4.1.1	Rolling in $\alpha_2 + \beta$ phase field	169
4.4.1.2	Rolling in the β phase field	180
4.4.2	Evolution of texture	181
4.4.2.1	Texture of the β phase	181
4.4.2.2	Texture of the α_2 phase	188
CHAPTER 5	STABILITY OF BASAL TEXTURE ON ANNEALING	220
5.1	Isochronal Annealing	221
5.1.1	Microstructure	221
5.1.2	X-ray diffraction profiles	225
5.1.3	Textural changes	228
5.2	Isothermal Annealing	238
5.2.1	Microstructure	239
5.2.2	X-ray diffraction profiles	240
5.2.3	Textural changes	248
5.3	Discussion of the Annealing Results	257
CHAPTER 6	EFFECT OF $\alpha_2 \rightarrow \beta \rightarrow \alpha_2$ TRANSFORMATION ON THE STABILITY OF BASAL TEXTURE	266
6.1	Microstructure	268
6.1.1	Heat treatment of 1173 K rolled and furnace cooled materials	268
6.1.2	Heat treatment of 1293 K rolled and furnace cooled materials	273
6.1.3	Heat treatment of 1373 K rolled and furnace cooled materials	273
6.2	X-ray Diffraction Profiles	282
6.3	Texture Results	286
6.4	Discussion of the Results	306
CHAPTER 7	CONCLUSIONS	310
	BIBLIOGRAPHY	313

List of Figures

Fig. 1.1(a) Situation of jet engine materials [1].....	3
Fig. 1.1 (b) Current and future options of jet engine materials (NASA) [1].....	3
Fig. 1.2 Variation of dynamic elastic moduli of α_2 and γ Ti- aluminides and Ti-6242 with temperature [3].....	4
Fig. 2.1 Vertical section of $\text{Ti}_3\text{Al-Nb}$ phase diagram with typical decomposition modes of β superimposed on it. Dashed line indicates the boundary between β and B2, quenching from above which results in B2 ordering[4].....	13
Fig. 2.2 Crystal structures in the $\text{Ti}_3\text{Al-Nb}$ system; (a) the DO_{19} hexagonal superlattice structure α_2 and the B2 structure, (b) Schematics of α_2 and O phase structures showing the important vectors, the unit cell of O phase being presented in such a manner that it corresponds to similar vectors of α_2 phase, and (c) Projected atom positions for the α_2 phase (0001), the O phase (001) and B2 (001) [3,4].....	14
Fig. 2.3 Schematic CCT curves proposed for continuous cooling from β phase field [4].....	18
Fig. 2.4 (a) Hexagonal superlattice structure of Ti_3Al showing slip planes and slip vectors in the structure [3], (b) Variation of CRSS for different slip systems in Ti_3Al as a function of temperature [4] and (c) The three types of Burger's vectors present in the Ti_3Al structure :	

(i) a type, $b=1/6\langle 11\bar{2}0 \rangle$, (ii) c type, $b=[0001]$ and (iii) a+c type, $b=1/6\langle 11\bar{2}6 \rangle$ [60].....	22
Fig. 2.5 True stress-strain curves corrected for deformation heating for cast Ti-24Al-11Nb deformed in compression at constant true strain rates of (a) 10^{-2} s^{-1} , (b) 10^{-1} s^{-1} and (c) 1 s^{-1} [56].....	26
Fig. 2.6 Plot of flow stress (at $\bar{\epsilon} = 0.05$) vs temperature for cast and wrought Ti-24Al-11Nb. Data have been plotted in terms of temperature relative to the β -transus, T_β [56].....	27
Fig. 2.7 Typical true corrected stress-true plastic strain curves of Ti-25Al-11Nb at: (a) 1073 K, (b) 1273 K, (c) 1398 K and (d) 1473 K [57].....	27
Fig. 2.8 Stress-strain curves at three temperatures (a) 1173 K, (b) 1273 K and (c) 1373 K, (d) Process efficiency map for as-cast Ti-24Al-11Nb and (e) Process efficiency map for wrought equiaxed Ti-24Al-11Nb [58].....	30
Fig. 2.9 Typical true corrected stress-true plastic strain curves of Ti-26Al-10Nb-3V-1Mo at (a) 1073 K, (b) 1273 K, (c) 1348 K and (d) 1473 K [59].....	31
Fig. 2.10 (a) Dynamic deformation of Ti-24Al-11Nb at temperatures ranging from 97 K to 973 K (b) Ti-24Al-11Nb compressed to a large strain showing significant change in work hardening rate (c) Quasi-static and dynamic deformation of Ti-24Al-11Nb at room temperature [60].....	32
Fig. 2.11 The variation of (a) yield strength and (b) elongation to failure as a function of α_2 volume fraction [11].....	35
Fig. 2.12 (a) Plot representing the situation with local stress concentrations at grain boundaries and resultant cleavage	

fracture at $\sigma_{c\alpha}$ before macroscopic ductility in single phase α_2 ,	
(b) Critical event for fracture in $\alpha_2+\beta$ (B2) alloys with high α_2	
volume fraction, (c) The critical event for fracture at higher	
volume fractions of B2, (d) The intensification of the <i>in situ</i>	
stress in β (σ_β) by the cracks in α_2 leading to the situation	
shown in figure (d) [4].....	36
Fig. 2.13 (a) Yield strength and (b) ductility of β heat treated Ti-	
25Al-11Nb and Ti-25Al-16Nb as a function of cooling rate	
[4].....	37
Fig. 2.14 Effect of microstructure and heat treatment on the	
strength and ductility of duplex structures [4].....	40
Fig. 2.15 (a) Tensile properties as a function of equiaxed α_2	
volume fraction and ageing temperature in Ti-25Al-11Nb	
and Ti-25Al-16Nb [63], (b) Yield strength as a function of	
solution treatment temperature in Ti-25Al-10Nb-3V-1Mo	
[68].....	40
Fig. 2.16 Steady-state creep rates as a function of stress at 923 K	
for a variety of α_2 based and O based alloys compared with	
a conventional α/β alloy Ti-1100 and density-normalised	
data for INCO 718 [52].....	43
Fig. 2.17 Steady-state creep rate as a function of cooling rate in	
Ti-25Al-11Nb at 923 K (a) in the diffusional creep regime	
and (b) in the dislocation creep regime [77].....	44
Fig. 2.18 Creep curves at 923 K and 275 MPa for equiaxed α_2	
containing 40% primary α_2 and a lath α_2 structure obtained	
by cooling at 0.7°C/s after β solution treatment in Ti-25Al-	
11Nb [4].....	44

List of Figures

Fig. 2.19 (a) Strength - Fracture Toughness, (b) Strength - Elongation, (c) Elongation -Fracture Toughness, and (d) Temperature - Fracture Toughness relationships for different Ti ₃ Al-base alloys [4, 15, 82-84].....	46
Fig. 2.20 {22 $\bar{4}$ 0} pole figures for (a) the hot rolled starting material, heat treated at (b) 1273 K, WQ, (c) 1273 K, WQ/1255 K FC, (d) 1473 K, WQ, (e) 1473 K, WQ/1255 K, FC and (f) 1473 K, FC heat treated conditions [94].....	51
Fig 3.1(a) Flow chart depicting schedule I for thermomechanical processing	59
Fig 3.1(b) Flow chart depicting schedule II for thermomechanical Processing.....	60
Fig 3.2 Flow chart showing the schedule for annealing studies.....	61
Fig. 3.3 Flow chart showing the schedule of heat treatment for phase Transformation.....	62
Fig. 3.5 Schematic representation of three Euler angles ϕ_1 , ϕ , ϕ_2 ; (a) Specimen frame S and crystalline frame C, (b) Transformation of specimen frame into crystalline frame [99].....	67
Fig.3.5c Schematic presentation of <i>Euler Space</i> [100].....	68
Fig. 3.6 Charts of positions of texture components in the Eulerian space for $\phi_2=0^\circ$ and $\phi_2=30^\circ$ sections [106].....	70
Fig. 4.1 (a) Microstructure for the as-cast material.....	73
Fig. 4.1 (b) Microstructure for the heat treated material.....	73
Fig. 4.2 Scanning Electron Micrograph of the materials rolled at 1173 K to (a) 50%, (b) 70% and (c) 80% from the as-cast state (all water quenched).....	77

List of Figures

- Fig. 4.3 Transmission Electron Micrographs from rolling plane section of the 1173 K rolled (water quenched) material upto 50% reduction showing (a) typical cell structure and (b) isolated recovered regions..... 78
- Fig. 4.4 Transmission Electron Micrographs from rolling plane section of the 1173 K rolled (water quenched) material upto 80% reduction showing (a) microbands (b) isolated regions of subgrain formation..... 79
- Fig. 4.5 SEM Micrographs of the as-cast material rolled to 80% reduction at (a) 1173 K, (b) 1293 K, (c) 1373 K and (d) 1523 K (all furnace cooled)..... 80
- Fig. 4.6 TEM Micrographs from the longitudinal section of the specimen rolled at 1173 K (furnace cooled) to 50% reduction, showing (a) highly deformed state and (b) partially recovered regions..... 81
- Fig. 4.7 TEM Micrographs from the longitudinal section of the specimen rolled at 1173 K (furnace cooled) to 70% reduction, showing (a) heavy deformation of α_2 and (b) extensively recovered regions..... 82
- Fig. 4.8 TEM Micrographs from the rolling plane section of the specimen rolled at 1173 K (furnace cooled) to 80% reduction, showing (a) advanced stage of recovery and (b) early stage of recrystallisation..... 83
- Fig. 4.9 SEM Micrographs of specimens heat treated at 1173 K (24 hrs, furnace cooled) and then rolled at 1173 K to (a) 50%, (b) 70% and (c) 80% reduction (all water quenched)..... 84
- Fig. 4.10 TEM Micrograph from the rolling plane section of the material heat treated and 1173 K rolled (water quenched) upto 50% reduction showing the beginning of the cell
-

List of Figures

Formation.....	85
Fig. 4.11 TEM Micrographs from the rolling plane section of the material heat treated and 1173 K rolled (water quenched) upto 80% reduction showing (a) high density of cells and (b) isolated regions of recovery.....	86
Fig. 4.12 SEM Micrographs from the specimens rolled at 1293 K from as-cast state to (a) 50%, (b) 70% and (c) 80% reductions (all water quenched).....	89
Fig. 4.13 TEM Micrographs from rolling plane section of the specimens rolled to 50%reduction at 1293 K (water quenched) showing highly deformed regions	90
Fig. 4.14 TEM Micrographs from rolling plane section of the specimens rolled to 80% reduction at 1293 K (water quenched) showing (a) extensive recovery in α_2 phase and (b) high amounts of deformation in β phase.....	91
Fig. 4.15 TEM Micrographs showing the substructural features of α_2 phase in the material rolled at 1293 K to 80% reduction and furnace cooled showing (a) onset of recovery, (b) an aggregate of small subgrain coalescing to form bigger grains and (c, d) well delineated recrystallised grains.....	92
Fig. 4.16 TEM Micrographs showing the substructural features of the β phase in the material rolled at 1293 K to 80% reduction (furnace cooled) showing (a) signs of recovery in β and (b) nucleation of fine α_2 platelets in recovered β	94
Fig. 4.17 Optical Micrograph of as-cast and 1373 K rolled material with 80% reduction (water quenched).....	96
Fig. 4.18 TEM Micrographs from the rolling plane section of the material rolled at 1373 K (water quenched) to 50%	

List of Figures

reduction showing (a) a highly deformed and dislocated area of β , (b) a few fine α_2 platelets formed during quenching (c) a highly recovered β region and (d) a few larger α_2 platelets in association with deformed β	97
Fig. 4.19 TEM Micrographs from the rolling plane section of the material rolled at 1373 K to 80% (water quenched) reduction showing (a) colonies of fine secondary α_2 platelets in highly recovered β regions and (b) high degree of alignment of secondary α_2 platelets within recovered β	99
Fig. 4.20 TEM Micrograph from the longitudinal section of material rolled at 1373 K to the reduction 50% (furnace cooled) showing fully recrystallised α_2 regions separated by thin β ribbons.....	100
Fig. 4.21 TEM Micrographs from the rolling plane sections of material rolled at 1373 K to 80% reduction (furnace cooled) showing (a) fully recrystallised α_2 and (b) partially recrystallised α_2	101
Fig. 4.22 TEM Micrograph from the rolling plane sections of material rolled at 1373 K to 80% reduction (furnace cooled) showing fine secondary α_2 platelets within recovered β regions.....	102
Fig. 4.23 Optical Microstructure of material rolled at 1523 K from the as-cast condition to the reduction of 80%.....	103
Fig. 4.24 TEM Micrograph from the rolling plane section of 1523	105
Fig. 4.24 TEM Micrograph from the rolling plane section of 1523 K rolled specimen to 50% reduction (water quenched).....	106

List of Figures

Fig. 4.25 TEM Micrographs from the rolling plane sections of the 1523 K rolled specimen to the reduction 80% (water quenched) showing (a) an overall view of the substructure, (b) formation of subgrains and (c, d) intra-subgrain features.....	107
Fig. 4.26 TEM Micrographs of the material rolled at 1523 K to 80% reduction and furnace cooled.....	108
Fig. 4.27 X-ray diffraction patterns for (a) the as-cast material and (b) the heat treated (1173 K, 24 hrs) and furnace cooled Material.....	110
Fig. 4.28 X-ray line profile from a powdered and annealed specimen of Ti-24Al-11Nb alloy (for reference).....	111
Fig. 4.29 X-ray diffraction pattern from samples rolled from the as-cast state by different amounts at 1173 K, (a) 50%, (b) 70% and (c) 80% (all water quenched).....	113
Fig. 4.30 X-ray diffraction pattern from the samples heat treated (1173 K, 24 hrs, FC) and rolled at 1173 K to 50%, 70% and 80% reductions (all water quenched).....	114
Fig. 4.31 X-ray diffraction pattern from samples rolled by different amounts at 1293 K, (a) 50%, (b) 70% and (c) 80% (all water quenched).....	116
Fig. 4.32 X-ray diffraction pattern from samples rolled by different amounts at 1373 K, (a) 50%, (b) 70% and (c) 80% (all water quenched).....	118
Fig. 4.33 X-ray diffraction pattern from samples rolled by different amounts at 1523 K, (a) 50%, (b) 70% and (c) 80% (all water quenched).....	119
Fig. 4.34 X-ray diffraction pattern from samples rolled to different amount of reductions at (a) 1173 K, (b) 1293 K and (c)	

List of Figures

1373 K (all furnace cooled).....	121
Fig. 4.35 X-ray diffraction pattern from the specimens rolled to 80% reduction at 1523 K (furnace cooled).....	122
Fig. 4.36 (a) (0002) _{α2} pole figure for the as-cast material, (b) (200) _β pole figure of the as-cast material and (c) (0002) _{α2} pole figure for the heat treated material.....	125
Fig. 4.37 Complete ODF of the as-cast material.....	126
Fig. 4.38 Complete ODF of the heat treated material.....	127
Fig. 4.39 (200) _β pole figures of materials rolled at (a) 1173 K and (b) 1293 K to 80% reduction (all water quenched).....	128
Fig. 4.40 $\phi_2 = 0^\circ$ and 45° sections of the ODFs from the β -phase of (a) 1173 K, 50%, (b) 1173 K, 80%, (c) 1293 K, 50% and (d) 1293 K, 80%.....	129
Fig. 4.41 $\phi_1 = 0^\circ$ and 90° sections of the ODFs of the as-cast material rolled to 50% and 80% reduction at (a, b) 1173 K and (c, d) 1293 K (all water quenched).....	130
Fig. 4.42 (0002) _{α2} pole figures for the as-cast and 1173 K rolled material subjected to (a) 50%, (b) 70% and (c) 80% reduction (all water quenched).....	133
Fig. 4.43 (a) Complete ODF of the material as-cast and rolled at 1173 K to 50% reduction (water quenched).....	134
Fig. 4.43 (b) Complete ODF of the material as-cast and rolled at 1173 K to 70% reduction (water quenched).....	135
Fig. 4.43 (c) Complete ODF of the as-cast material rolled at 1173 K to 80% reduction (water quenched).....	136
Fig. 4.44 $\phi_2 = 0^\circ$ and 30° sections of the ODFs of as-cast and 1173 K rolled materials for rolling reductions (a) 50%, (b) 70% and (c) 80% (all water quenched).....	137

List of Figures

Fig. 4.45 (0002) _{α2} pole figures of the materials heat treated (1173 K, 24 hrs./ FC) and rolled at 1173 K to reductions (a) 50%, (b) 70% and (c) 80% (all water quenched).....	140
Fig. 4.46 (a) Complete ODF of the material heat treated and rolled at 1173 K to 50% reduction (water quenched).....	141
Fig. 4.46 (b) Complete ODF of the material heat treated and rolled at 1173 K to 70% reduction (all water quenched).....	142
Fig. 4.46 (c) Complete ODF of the material heat treated and rolled at 1173 K to 80% reduction (water quenched).....	143
Fig. 4.47 $\phi_2 = 0^\circ$ and 30° sections of ODFs of the heat treated and 1173 K rolled materials; rolled reductions: (a) 50%, (b) 70% and (c) 80% (all water quenched).....	144
Fig. 4.48 (0002) _{α2} pole figure of the as-cast material rolled to 80% reduction at (a) 1173 K, (b) 1293 K, (c) 1373 K and (d) 1523 K (all water quenched).....	146
Fig. 4.49 Complete ODF of the material as-cast, rolled at 1173 K to 80% reduction and furnace cooled.....	147
Fig. 4.50 $\phi_2 = 0^\circ$ and 30° sections of the ODFs of the as-cast material rolled to 80% reduction at (a) 1173 K, (b) 1293 K, (c) 1373 K and (d) 1523 K (all furnace cooled).....	148
Fig. 4.51 (0002) _{α2} pole figure of the material as-cast, rolled at 1293 K to (a) 50% and (b) 80% reductions and water Quenched.....	152
Fig. 4.52 (a) Complete ODF of the material as-cast, rolled at 1293 K to 50% reduction and water quenched.....	153
Fig. 4.52 (b) Complete ODF of the material as-cast, rolled at 1293 K to 80% reduction and water quenched.....	154

List of Figures

Fig. 4.53 $\phi_2 = 0^\circ$ and 30° sections of ODF for the as-cast material rolled at 1293 K to reductions (a) 50% and (b) 80% (all water quenched).....	155
Fig. 4.54 Complete ODF of the material as-cast, rolled at 1293 K to 80% reduction and furnace cooled.....	159
Fig. 4.55 $(200)_\beta$ pole figure of the as-cast material rolled to 50% and 80% reductions at (a, b) 1373 K and (c, d) 1523 K.....	160
Fig. 4.56 $\phi_2 = 0^\circ$ and 45° sections of the ODFs of the as-cast material rolled to 50% and 80% reductions at (a, b) 1373 K and (c, d) 1523 K (all water quenched).....	161
Fig. 4.57 $\phi_1 = 0^\circ$ and 90° sections of ODF of the material as-cast and rolled at (a, b) 1373 K and (c, d) 1523 K to reductions 50% and 80% each followed by water quenching.....	162
Fig. 4.58 Complete ODF of the material rolled at 1373 K to 80% reduction and furnace cooled.....	163
Fig. 4.59 Complete ODF of the material rolled at 1523 K to 80% reduction and furnace cooled.....	164
Fig. 4.60 Flow behaviour of as-cast Ti-24Al-11Nb alloy within the temperature range 1173 K-1373 K and strain rates 0.1 and 1.0 [58].....	172
Fig. 4.61 Variation of strain rates during successive rolling passes.....	173
Fig. 4.62 Mechanism for conversion of Widmanstätten to equiaxed morphology; (i) platelet α and (ii) grain boundary α [111].....	178
Fig. 4.63 Weiss Mechanism of β penetration for the formation of equiaxed α [112].....	179
Fig. 4.64 Comparison of (0002) pole figures; (a) initial textures, (b) final experimental textures, and (c) simulated	

textures for unalloyed Ti and two Ti alloys.....	203
Fig. 4.65 (0002) α_2 pole figure for a 1153 K rolled material with a standard α_2 (0001) projection having $[10\bar{1}0]$ at the rolling direction superimposed on it [93].....	204
Fig. 4.66 Plot showing the variation of CRSSs for basal slip (0001) $\langle 11\bar{2}0 \rangle$, prismatic slip $\{10\bar{1}0\} \langle 11\bar{2}0 \rangle$ and pyramidal slip $\{11\bar{2}1\} \langle 11\bar{2}6 \rangle$ in Ti_3Al as a function of temperature [38]. Dashed vertical lines represent the rolling temperature used in the present investigation.....	205
Fig. 4.67 Rolling textures of Ti_3Al ; Measured (a), (b),(c) and Simulated (d), (e), (f) [154].....	208
Fig. 4.68 (a) Some important orientations in the section $\phi_2=0^\circ$, (b), (c) and (d) the stable orientation predicted by the activation of basal, prism and pyramidal slip systems respectively [154].....	209
Fig. 4.69 Orientation changes during the simulating calculations in $\phi_2=0^\circ$ section [154].....	210
Fig. 4.70 Stereographic projections showing the Burger's relationship between α_2 and β phases and parallelism of slip vectors and planes. The four possible $\langle 111 \rangle$ slip vectors in β are enclosed in boxes. Dotted lines indicate β zones containing three of the four slip vectors which are parallel to a possible α_2 slip vector [35].....	213
Fig. 4.71 The α/α_2 textures predicted from a few β orientations.....	217
Fig. 5.1 SEM Micrographs of isochronally annealed (1 hr) specimens for the annealing temperatures (a) 1123 K, (b) 1173 K, (c) 1233 K and (d) 1293 K (all water quenched).....	222
Fig. 5.2 TEM Micrograph of material annealed at 1123 K for 1 hr	

List of Figures

showing the onset of recovery process.....	223
Fig. 5.3 TEM Micrograph of material annealed at 1173 K for 1 hr showing the features of (a) recovery process in α_2 and (b) recrystallised α_2 grains.....	224
Fig. 5.4 TEM Micrograph of material annealed at 1233 K for 1 hr.....	226
Fig. 5.5 TEM Micrograph of material annealed at 1293 K for 1 hr.....	226
Fig. 5.6 X-ray diffraction patterns for the isochronally annealed Specimens.....	227
Fig. 5.7 (0002) pole figures for the isochronally annealed specimens; (a) 1123 K, (b) 1173 K, (c) 1233 K and (d) 1293 K.....	230
Fig. 5.8 (20 $\bar{2}$ 0) pole figures for the isochronally annealed specimens; (a) 1123 K, (b) 1173 K, (c) 1233 K and (d) 1293 K.....	231
Fig. 5.9 Complete ODF of the material annealed at 1123 K for 1 hr.....	233
Fig. 5.10 Complete ODF of the material annealed at 1173 K for 1hr.....	234
Fig. 5.11 Complete ODF of the material annealed at 1233 K for 1 hr.....	235
Fig. 5.12 Complete ODF of the material annealed at 1293 K for 1 hr.....	236
Fig. 5.13 $\phi_2 = 0^\circ$ and 30° sections of the ODF for the isochronally annealed materials; (a) 1123 K, (b) 1173 K, (c) 1233 K and (d) 1293 K.....	237
Fig. 5.14 SEM Micrograph of the material annealed at 1173 K for a period of (a) 15 min, (b) 30 min, (c) 2 hrs and (d) 12 hrs.....	241

List of Figures

Fig. 5.15 (a,b)TEM Micrograph of the material annealed at 1173 K for a period 30 min showing an overall view of the microstructure (c,d) showing signs of recovery	242
Fig. 5.16 TEM Micrographs of the specimens annealed at 1173 K for 2 hrs showing (a) partially recovered, (b) fully recovered, (c) partially recrystallised, (d) fully recrystallised and (e) a fish-tail type of structure at the grain Boundary.....	244
Fig. 5.17 X-ray diffraction profiles from the materials isothermally annealed at 1173 K.....	247
Fig. 5.18 $(0002)_{\alpha_2}$ pole figures for the isothermally annealed (1173 K) specimens for (a) 15 min, (b) 30 min, (c) 2 hrs and (d) 12 hrs.....	249
Fig. 5.19 $(20\bar{2}0)_{\alpha_2}$ pole figures for the isothermally annealed (1173 K) specimens for (a) 15 min, (b) 30 min, (c) 2 hrs and (d) 12 hrs.....	250
Fig. 5.20 Complete ODF of the material annealed 1173 K for 15 min.....	252
Fig. 5.21 Complete ODF of the material annealed 1173 K for 30 min.....	253
Fig. 5.22 Complete ODF of the material annealed 1173 K for 2 hrs.....	254
Fig. 5.23 Complete ODF of the material annealed 1173 K for 12 hrs.....	255
Fig. 5.24 $\phi_2=0^\circ$ and $\phi=30^\circ$ sections of the ODFs for the isothermally annealed (1173 K) specimens for (a) 15 min, (b) 30 min, (c) 2 hrs and (d) 12 hrs.....	256

Fig. 6.1 SEM Micrographs of the 1173 K rolled (furnace cooled) material in the (a) as rolled condition, (b) heat treated at 1173 K, (c) heat treated at 1293 K and (d) heat treated at 1373 K (all furnace cooled).....	269
Fig. 6.2 TEM Micrograph of R1173H1173 specimen.....	270
Fig. 6.3 TEM Micrographs of R1173H1373 specimen showing (a) general features, (b) presence of defect - like features inside α_2 grains (c) a film of retained β at the α_2 boundaries, and (d) high dislocation activity at the two sides of the boundary.....	271
Fig. 6.4 SEM Micrographs of the 1293 K rolled (furnace cooled) material in the (a) as rolled condition, (b) heat treated at 1173 K, (c) heat treated at 1293 K and (d) heat treated at 1373 K (all furnace cooled).....	274
Fig. 6.5 SEM Micrographs of the 1373 K rolled (furnace cooled) material in the (a) as rolled condition, (b) heat treated at 1173 K, (c) heat treated at 1293 K and (d) heat treated at 1373 K (all furnace cooled).....	275
Fig. 6.6 TEM Micrograph of R1373H1173 specimen showing (a) general features, (b) dislocations and other defects present inside α_2 grain, (c) a clean α_2 grain surrounded by dislocations and other defects (d) the details of grain boundary feature of the micrograph (a).....	278
Fig. 6.6 (e) TEM Micrographs of the R1373H1173 specimen showing higher magnification views of the grain boundary region (f) the grain boundary region and (g) SAD pattern taken from the area 'X' shown in (e).....	280
Fig. 6.7 TEM Micrograph of the R1373H1373 specimen showing general features.....	281

List of Figures

Fig. 6.8 XRD patterns for the 1173 K rolled (furnace cooled) material in the (a) as rolled condition, (b) heat treated at 1173 K, (c) heat treated at 1293 K and (d) heat treated at 1373 K (all furnace cooled).....	283
Fig. 6.9 XRD patterns for the 1293 K rolled (furnace cooled) material in the (a) as rolled condition, (b) heat treated at 1173 K, (c) heat treated at 1293 K and (d) heat treated at 1373 K (all furnace cooled).....	284
Fig. 6.10 XRD patterns for the 1373 K rolled (furnace cooled) material in the (a) as rolled condition, (b) heat treated at 1173 K, (c) heat treated at 1293 K and (d) heat treated at 1373 K (all furnace cooled).....	285
Fig. 6.11 (0002) pole figure of the 1173 K rolled (furnace cooled) material in the (a) as rolled condition, (b) heat treated at 1173 K, (c) heat treated at 1293 K and (d) heat treated at 1373 K (all furnace cooled).....	287
Fig. 6.12 a Complete ODF of the R1173H1173 material.....	288
Fig. 6.12 b Complete ODF of the R1173H1293 material	289
Fig. 6.12 c Complete ODF of the R1173H1373 material.....	290
Fig. 6.13 $\phi_2 = 0^\circ$ and 30° sections of the ODFs of the 1173 K rolled (furnace cooled) material in the (a) as rolled condition, (b) heat treated at 1173 K, (c) heat treated at 1293 K and (d) heat treated at 1373 K (all furnace cooled).....	291
Fig. 6.14 (0002) pole figure of the 1293 K rolled (furnace cooled) material in the (a) as rolled condition, (b) heat treated at 1173 K, (c) heat treated at 1293 K and (d) heat treated at 1373 K (all furnace cooled).....	293
Fig. 6.15 a Complete ODF of the R1293H1173 material.....	294
Fig. 6.15 b Complete ODF of the R1293H1293 material.....	295

List of Figures

Fig. 6.15 c Complete ODF of the R1293H1373 material.....	296
Fig. 6.16 $\phi_2 = 0^\circ$ and 30° sections of the ODFs of the 1293 K rolled (furnace cooled) material in the (a) as rolled condition, (b) heat treated at 1173 K, (c) heat treated at 1293 K and (d) heat treated at 1373 K (all furnace cooled).....	297
Fig. 6.17 (0002) pole figure of the 1373 K rolled (furnace cooled) material in the (a) as rolled condition, (b) heat treated at 1173 K, (c) heat treated at 1293 K and (d) heat treated at 1373 K (all furnace cooled).....	301
Fig. 6.18 a Complete ODF of the R1373H1173 material.....	302
Fig. 6.18 b Complete ODF of the R1373H1293 material.....	303
Fig. 6.18 c Complete ODF of the R1373H1373 material.....	304
Fig. 6.13 $\phi_2 = 0^\circ$ and 30° sections of the ODFs of the 1373 K rolled (furnace cooled) material in the (a) as rolled condition, (b) heat treated at 1173 K, (c) heat treated at 1293 K and (d) heat treated at 1373 K (all furnace cooled).....	305

List of Tables

Table 1.1 Properties of Titanium Aluminides, Titanium- Base Conventional Alloys and Superalloys [3].....	2
Table 1.2 Properties of some Ti_3Al -Base Alloys [3].....	7
Table 1.3 Microstructural Dependence of Mechanical Properties of some Ti_3Al -Base Alloys [3].....	9
Table 2.1 Alloy designations, compositions and their source references.....	11
Table 3.1 Chemical composition of the alloy.....	54
Table 4.1 Phase fractions after different processing conditions as determined by quantitative Metallography.....	74
Table 4.2 Hardness values for the β -rolled samples.....	105
Table 4.3 The 12 orientation variants according to the Burger's relationship during $\alpha_2 \rightarrow \beta$ transformation [155].....	214
Table 5.1 Relative intensity values of all possible reflections for the Ti_3Al phase obtained from intensity calculation [161].....	259
Table 6.1 Symbols being used in the present chapter for denoting different heat treated materials.....	267

Introduction

Titanium-base alloys have played a key role in the improved performance achieved in gas turbine engines, offering exceptional opportunities for weight reduction, as much as 50% by replacing some of the nickel and iron-base superalloys. However, the temperature capabilities of titanium alloys limit the application of even the most advanced titanium alloy, such as IMI-834 and Ti-1100, to about 873 K (approximately) with regard to both their high temperature strength and oxidation rate. Titanium alloys also suffer from low fracture toughness and low creep strength at higher temperatures. The need for developing new materials that are lighter than superalloys and yet possess roughly the same mechanical properties and oxidation resistance as superalloys is increasing day by day. Figs. 1.1 show the current and future options for the usage of different materials for aerospace applications.

Because of their lower specific weights, remarkably high strength and improved oxidation resistance, intermetallic materials are potential candidates for the substitution of relatively heavier superalloys for both compressor as well as turbine sections of aircraft engines. Due to their excellent strength-to-weight ratio at temperatures well above 973 K, titanium aluminides, specially Ti_3Al and TiAl-base intermetallic alloys have been considered as strong candidates to substitute for conventional materials used in jet engine compressors. The properties of these aluminide alloys are compared with those of conventional titanium alloys and superalloys in Table 1.1.

Table 1.1 Properties of Titanium Aluminides, Titanium-Base Conventional Alloys and Superalloys [3]

Property	Ti-Base Alloy	Ti ₃ Al-Base Alloy	TiAl-Base Alloy	Superalloy
Structure	hcp/bcc	DO ₁₉	L1 ₀	fcc/L1 ₂
Density, g/cm ³	4.5	4.1-4.7	3.7-3.9	8.3
Modulus, GPa	95-115	110-145	160-180	206
Yield Strength, MPa	380-1150	700-900	400-650	--
Tensile Strength, MPa	480-1200	800-1140	450-800	--
Ductility, % at RT	10-25	2-10	1-4	3-5
Ductility, % at HT	12-50	10-20	10-60	10-20
Fracture Toughness, MPa \sqrt{m}	High	13-30	10-20	25
Creep Limit, °C	600	760	1000	1090
Oxidation, °C	600	650	900	1090

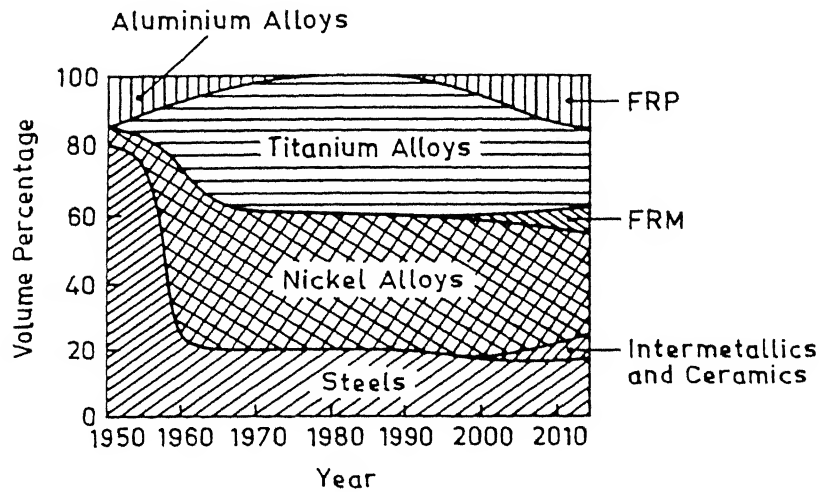


Fig. 1.1(a) Situation of jet engine materials [1]

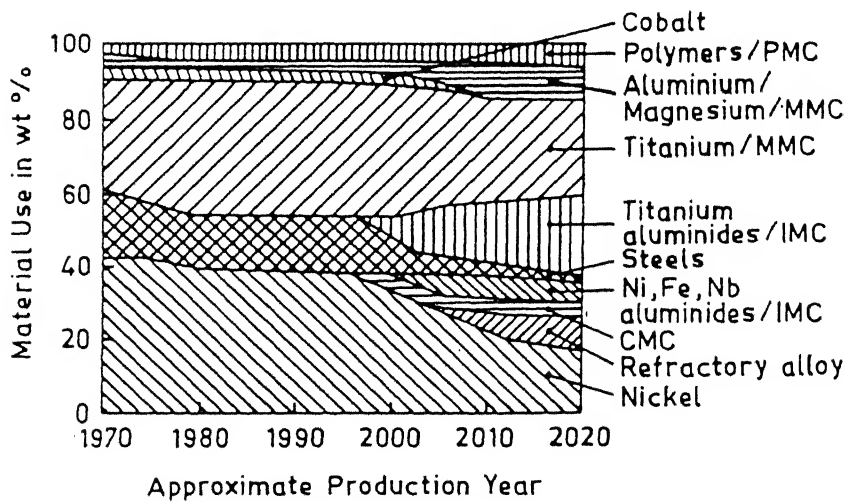


Fig. 1.1 (b) Current and future options of jet engine materials (NASA) [1]

It is to be noted that although the elastic moduli of these compounds are lower than those of superalloys, these values can be retained at a substantial level at high enough temperatures (Fig. 1.2). This can be attributed to the strong A-B bonding in their ordered structures. Similarly, high temperature properties such as strength retention creep/stress rupture life, and high temperature fatigue resistance etc. of these aluminides are far better than those of conventional titanium alloys due mostly to the slow diffusion phenomenon in ordered alloys.

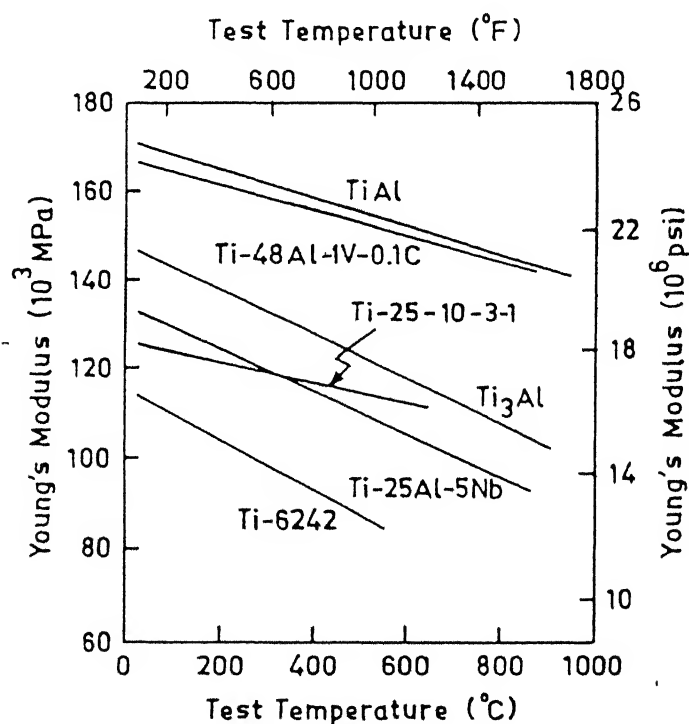


Fig. 1.2 Variation of dynamic elastic moduli of α_2 and γ Ti-aluminides and Ti-6242 with temperature [3]

Titanium aluminides, however, suffer from low ductility at ambient temperature which appears to be the most serious obstacle to the full use of these materials. In addition, the titanium aluminides exhibit a strong TiO_2 - forming tendency rather than formation of the protective Al_2O_3 at high temperatures and therefore their oxidation resistance is not adequate for very high temperature applications. Titanium aluminides also suffer from poor mechanical behaviour in hydrogen environment. This appears to be a key factor while considering the options of using these materials in a hydrogen environment.

In spite of several favourable characteristics, the complete absence of room temperature plasticity in titanium aluminides poses the primary challenge in developing them as structural alloys. A number of studies on alloy development in this regard have resulted in identifying niobium as a primary ternary additive and it has been reported that plasticity at room temperature can be obtained by the addition of > 10 at % Nb which stabilises the high-temperature ductile b.c.c. phase of titanium in the structure. Depending on the Nb content, several modified Ti_3Al -base alloys have been developed which can be classified as follows:

Class I (β -stabiliser $\sim 10 - 12\%$): These alloys consist of two phases : (i) an ordered h.c.p. (DO_{19}) structured phase α_2 and (ii) an ordered or disordered b.c.c. structured phase B2 or β . Usually above 1253 K, the disordered form prevails. However, at room temperature (even after quenching from higher temperature), the b.c.c. phase gets ordered to B2 structure. Compositions Ti-24Al-11Nb and Ti-25Al-8Nb-2Mo-2Ta are prominent examples of this category.

Class II (β -stabiliser $\sim 14 - 17\%$): Alloys with these compositions usually consist of three phases : the ordered h.c.p. phase α_2 , the ordered or disordered b.c.c. phase B2 or β and an orthorhombic structured (Cmcm) phase, known as 'O' phase. Compositions Ti-24Al-(14-15)Nb, Ti-24Al-10Nb-3V-1Mo and Ti-24Al-17 Nb are the typical examples of this class.

Class III (β -stabilizer $\sim 25 - 30\%$): Alloys in this composition range consist of the two phases, the orthorhombic 'O' phase and the b.c.c. β or B2 phase. Prominent alloys of this category are Ti-25Al-27Nb, Ti-22Al-23Nb, Ti-22Al-25Nb etc.

The composition regime between the first and second classes of these alloys has been explored at a fixed Mo equivalent level. Several trends in properties of these alloys are known as a function of composition and are shown in Table 1.2. For example, stress rupture and creep strength are enhanced by increasing Al and Mo contents. However, beyond optimum levels, these elements adversely affect toughness and ductility.

It has been found that apart from modifying phase composition by ternary additions, modification of microstructure has also an important role in affecting the mechanical properties of Ti_3Al -base intermetallics. The sensitivity of mechanical behaviour with respect to the microstructure together with the difficulties in deformation processing poses another challenging task in the area of alloy development.

Table 1.2 Properties of some Ti₃Al-Base Alloys [3]

Alloys	Microstructure	YS (MPa)	UTS (MPa)	Elong. (%)	K _{IC} (MPa \sqrt{m})	Creep Rupture
Ti-25Al	Equiaxed α_2	538	538	0.3	--	--
Ti-24Al-11Nb	Widmanstatten	787	825	0.7	--	44.7
Ti-24Al-14Nb	Widmanstatten	510	--	2.0	20.7	--
Ti-25Al-10Nb-3V-1Mo	Widmanstatten	825	1042	2.2	13.5	>360
Ti-24.5Al-17Nb	Widmanstatten	952	1010	5.8	28.3	62
Ti-25Al-17Nb-1Mo	Fine Widmanstatten	989	1133	3.4	20.9	476

In spite of these drawbacks, a number of components in the compressor and turbine sections of the engine have already been successfully fabricated from titanium aluminides and attempts are underway to improve their low ductility and poor toughness at lower temperature so that their application-base is further extended. Other applications of these alloys in the aerospace industry are typically in the manufacture of honeycomb structures for fuselage panels for advanced aerospace designs, noise damping components in modern jet turbines, turbine nozzle guide veins etc. In addition, Ti₃Al-base alloys also find their applications as laminated composites. Such applications would require titanium aluminide to be processed into thin sheets and foils. However, alloys having low ductility are generally not amenable to cold rolling. It is, therefore, recommended to process them by hot/warm rolling and

annealing route. Further, the phase fractions and other microstructural attributes can be controlled by proper heat treatments. The sheet processing methods are also expected to have pronounced effect on the development of textures in these materials. Since texture is known to affect the mechanical properties very significantly, investigations into these aspects are also of utmost importance. Mechanical processing of materials with h.c.p. structure causes the development of strong texture as well as the refinement in the grain size, and both these changes influence the mechanical properties of the product. The processing parameters that affect the texture development in a rolled material are mainly the temperature of processing and the amount of rolling deformation. Although, the production of Ti_3Al -base alloys ($Ti-24Al-11Nb$, in particular) into sheet form has long been envisaged, very little attention has been given till date to elucidate the evolution of texture in these materials.

The present work was therefore undertaken to carry out a systematic study of the evolution of texture during processes thermomechanical processing of a Nb containing Ti_3Al -base alloy. This has been supplemented by relevant microstructural investigation. The first part of the present study involves the determination, interpretation and evaluation of the microstructural and textural changes that occur during warm/hot rolling as a function of rolling temperature, amount of rolling reduction and post rolling conditions.

Table 1.3 Microstructural Dependence of Mechanical Properties of some Ti₃Al-Base Alloys [3]

Alloys	Micro-structure	YS (MPa)	UTS (MPa)	Elong. (%)	K _{IC} (MPa√m)	Creep Rupture
Ti-24Al-11Nb	W	787	825	0.7		44.7
	FW	761	967	4.8		
Ti-25Al-10Nb-3V-1Mo	W	825	1042	2.2	13.5	>360
	FW	823	950	0.8		
	W+P	759	963	2.6		
	FW+P	942	1097	2.7		
Ti-24.5Al-17Nb	W	952	1010	5.8	28.3	62
	W+P	705	940	10.0		

W = Widmanstatten,
FW = Fine Widmanstatten,
P = Primary

The second part of this study comprises examination of the stability of textures so formed during subsequent heat treatments of the as-rolled alloy. This was considered important since the conventional processing technologies usually require a post rolling heat treatment for proper microstructural control. As the processing temperatures lie very close to the phase boundaries, it is also important to examine the effects of phase transformations on the stability of texture, since any supertransus processing is likely to affect the texture and microstructure of the processed material. The third and last part of the present study, therefore, aims at examining the texture modifications during any such treatments.

Literature Review

Alloys based on titanium aluminium intermetallic compound Ti_3Al , referred as α_2 , have been studied for the last three decades. The development of alloys based on this intermetallic compound has been driven by the need to bridge the gap in the temperature capability between current conventional near α titanium alloys (773 K-873 K) and nickel base superalloys INCO 718 or INCO 713 (923 K-1073 K) [4]. Applications originally intended for this intermetallic class were to be propulsion components, but more recently, it has also been considered for use in hypersonic airframe structural components [5]. Ti_3Al has a specific modulus and stress rupture resistance compared to that of superalloys [6]. However, it does not have any room temperature plasticity, which puts a serious restriction on the engineering applications of this material. In order to explore the merits of such a potential material for applications, several attempts have been made [7, 8, 9]. All these studies revealed that Niobium addition (> 10 at. %) improves the room temperature plasticity by stabilising the high temperature b.c.c. phase of titanium.

The Niobium modified Ti_3Al -base alloys can be classified into three categories:

- (i) alloys having 11-12 at. % β -stabiliser, (ii) alloys having 14-17 at. % β -stabiliser and (iii) alloys having 25-30 at. % β -stabiliser. Different alloys belonging to these three categories are listed in Table 2.1.
-

Table 2.1 Alloy designations, compositions and their source references

Designation	Composition	References
24 - 11	Ti - 24Al - 11Nb	10
25 - 11	Ti - 25Al - 11Nb	11
25 - 16	Ti - 25Al - 16Nb	11
25 - 17	Ti - 25Al - 17Nb	12
27 - 15	Ti - 27Al - 15Nb	11
25 - 24	Ti - 25Al - 24Nb	13, 14
22 - 27	Ti - 22Al - 27Nb	13
27 - 15 - 1	Ti - 27Al - 15Nb - 1Mo	11
8 - 2 - 2	Ti - 25Al - 8Nb - 2Mo - 2Ta	15
10 - 3 - 1	Ti - 25Al - 10Nb - 3V - 1Mo	16, 10
22 - 17 - 1	Ti - 22Al - 17Nb - 1Mo	12
25 - 17 - 1	Ti - 25Al - 17Nb - 1Mo	12

2.1 Phases and Crystal Structure

The Ti-Al-Nb ternary system has been studied by several workers and has been extensively reviewed [17]. Nartova *et al.* [18,19] studied the system $\text{Ti}_3\text{Al-Nb-Ti}$ from 873 K to 1473 K and indicated that a quasibinary system $\text{Ti}_3\text{Al-Nb}$ exists, which was further confirmed by Troitsky [20]. Till this time, the $\text{Ti}_3\text{Al-Nb}$ system was supposed

to be consisting of ordered h.c.p. Ti_3Al phase and disordered b.c.c. β phase of titanium. Banerjee *et al.* [21] reported the existence of a new phase with stoichiometry Ti_2AlNb whose unit cell is orthorhombic structured with the space group Cmcm . The pseudo-binary phase diagram of Ti_3Al -Nb system is also given in Fig. 2.1.

As it can be seen, for the first category of the alloys, there are mainly two phases of interest: the α_2 phase (based on Ti_3Al) and the $\beta(\text{B2})$ phase (disordered or ordered b.c.c.). The second category of alloys consist of three phases: the α_2 phase, $\beta(\text{B2})$ phase and O phase (a distorted form of α_2 based on Ti_2AlNb), depending on the heat treatment. The third class of alloys have the two constituent phases: the O phase and the $\beta(\text{B2})$ phase. The crystal structures of these phases are shown in Fig. 2.2. The α_2 phase has the h.c.p. based DO_{19} (hP8) crystal structure and $\text{P6}_3/\text{mmc}$ symmetry. This structure is characterised by close packed (0001) planes. The Al atoms are bonded with Ti atoms at the nearest neighbour positions. This structure can be described in terms of four interpenetrating primitive sublattices, of which three contain Ti atoms and one contains Al atoms. Niobium atoms substitute the Ti sites in the lattice [22]. The ordered B2 (cP2) phase which is derived from the high temperature b.c.c. (β) phase of titanium has its composition centred around Ti_2AlX , where X is a β stabiliser [23]. In the Ti_2AlNb system, it has been shown that Ti and Al atoms occupy the two separate primitive sublattices constituting the structure while Nb occupies the Al sublattice [24, 25].

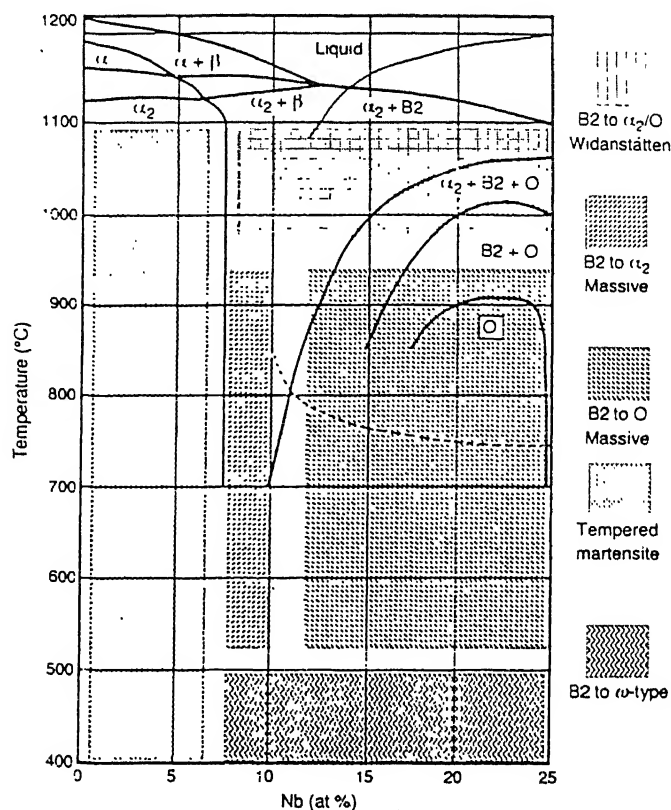


Fig. 2.1 Vertical section of Ti₃Al-Nb phase diagram with typical decomposition modes of β superimposed on it. Dashed line indicates the boundary between β and B2, quenching from above which results in B2 ordering [4]

The third phase belonging to this alloy system, the 'O' phase, which was identified by Banerjee *et al.* [21], possessing a Cmc₂m (oC16) symmetry with an orthorhombic crystal structure, can be viewed as a slightly distorted form of α₂. The 'O' phase is a ternary ordered structure based on the Ti₂AlNb composition in which Nb atoms can be associated with a distinct sublattice-atom in one of the three Ti sublattices of α₂ are replaced by Nb. An alternative site occupation in which Nb atoms occupy Ti sites randomly, as in α₂, has also been observed [26, 27]

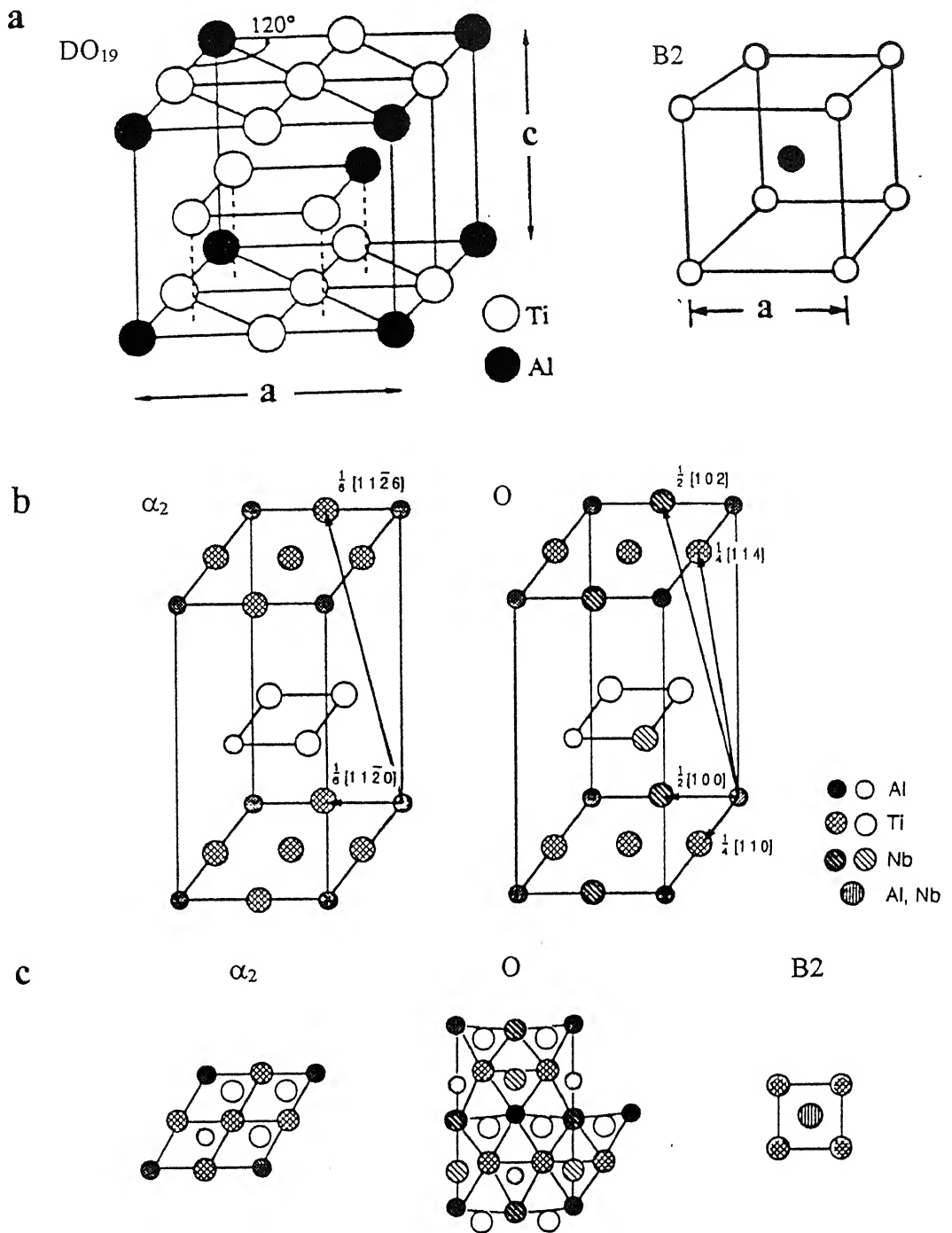


Fig. 2.2

Crystal structures in the Ti₃Al-Nb system; (a) the DO₁₉ hexagonal superlattice structure α_2 and the B2 structure, (b) Schematics of α_2 and O phase structures showing the important vectors, the unit cell of O phase being presented in such a manner that it corresponds to similar vectors of α_2 phase, and (c) Projected atom positions for the α_2 phase (0001), the O phase (001) and B2 (001) [3,4]

2.2 Phase Transformation

The phase transformations studied in the $\text{Ti}_3\text{Al-Nb}$ system can be classified under following subheadings:

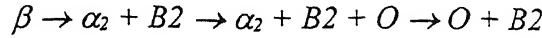
2.2.1 Transformation during quenching

For low Nb containing alloys (< 7.5 at. %), quenching from β phase results in martensitic transformation of β to hexagonal martensite α' as in the case of conventional $(\alpha+\beta)$ titanium alloys. However, ordering of α' to α_2 cannot be suppressed, resulting in the formation of α_2 laths with a fine APB structure. The martensitic transformation is rapidly suppressed beyond 7.5 at. % Nb [28] because of the relative stability of the α phase with respect to α_2 phase. A martensitic transformation from β to α_2/O or B2 to α_2/O is not possible as no atomic site correspondence exists between the parent and product phases. Therefore, at higher Nb contents, the b.c.c. phase can be retained by quenching. However, the b.c.c. phase is difficult to retain in the disordered form and the fine domain of ordered B2 phase are quite commonly observed in the as-quenched β -phase [29]. Another important characteristic of this transformation is the elastic instability resulting from the transformation which do gets reflected in TEM observations.

2.2.2 Transformation during Continuous Cooling

The phase transformation occurring during continuous cooling from the β phase field leads to the formation of laths of α_2 upto the composition $\text{Ti}_3\text{Al-11Nb}$. For

higher Nb contents, say Ti₃Al-16Nb, the sequence of transformation is reported to be as follows [30]:



A schematic continuous cooling transformation (CCT) curve representing such a transformation is given in Fig. 2.3. The precipitation of 'α₂' or 'O' laths from β(B2) takes place according to Burger's relationship as reported by Bendersky *et al.* [31]

$$(0001)_{\alpha_2} \parallel (110)_{\beta},$$

$$[11\bar{2}0]_{\alpha_2} \parallel [1\bar{1}1]_{\beta}$$

and

$$(001)_O \parallel (110)_{\beta}$$

$$[110]_O \parallel [1\bar{1}1]_{\beta}$$

The variation in lath morphology of the α₂ as well as 'O' phase with cooling rate follows the same trend as seen in conventional (α+β) titanium alloys. On increasing the cooling rate, the lath distribution changes from a colony structure to increasingly fine basket-weave structure.

The transformation from the α₂ to the O phase, as seen for a range of compositions on increasing the Nb content from 12 at. %, is reported to follow the relationship [21]:

$$(001)_O \parallel (0001)_{\alpha_2}$$

$$[110]_O \parallel [10\bar{1}0]_{\alpha_2}$$

The microstructural features of the resulting 'O' phase depend on whether α_2 is retained or consumed during transformation. In the former case, the 'O' phase has a lamellar microstructure whereas in the latter case, it is reported to have a mosaic-type of microstructure. With increasing Nb content, the volume fraction of the α_2 phase decreases and it remains only at grain boundary locations for ≤ 25 at. % Nb.

2.2.3 Transformation during Ageing

Several workers have focused their attention to the transformation during ageing of the as-quenched β (B2) form of Ti-Al-Nb alloys. The most comprehensive study of this phenomenon has been due to Strychor *et al.* [28]. Their study revealed that the metastable as-quenched β phase ($< 7.5\%$ Nb) decomposes to ω -related structure when the ageing treatment is performed below 773 K. The above fact has also been verified by Chang and Loretto [29]. At higher temperatures, a composition invariant transformation to ' α_2 ' or 'O' is observed. Two distinct microstructural features have been reported to evolve: (i) a plate like O phase with many substructural features associated with a martensitic transformation and (ii) an equiaxed product which resembles the conventional massive structure. These two decomposition modes can proceed in parallel or sequentially with the equiaxed grains consuming the martensitic type product. Subsequent decomposition of both these phases occur to produce equilibrium phases α_2 and/or β (B2). Above 1273 K, conventional precipitation of Widmanstätten α_2 or O occurs, and a cellular transformation has been observed for Nb content > 25 at. %. The decomposition of

metastable $\beta(B2)$ without long range diffusion has been attributed to the occurrence of a set of displacive or replacive transformations [32].

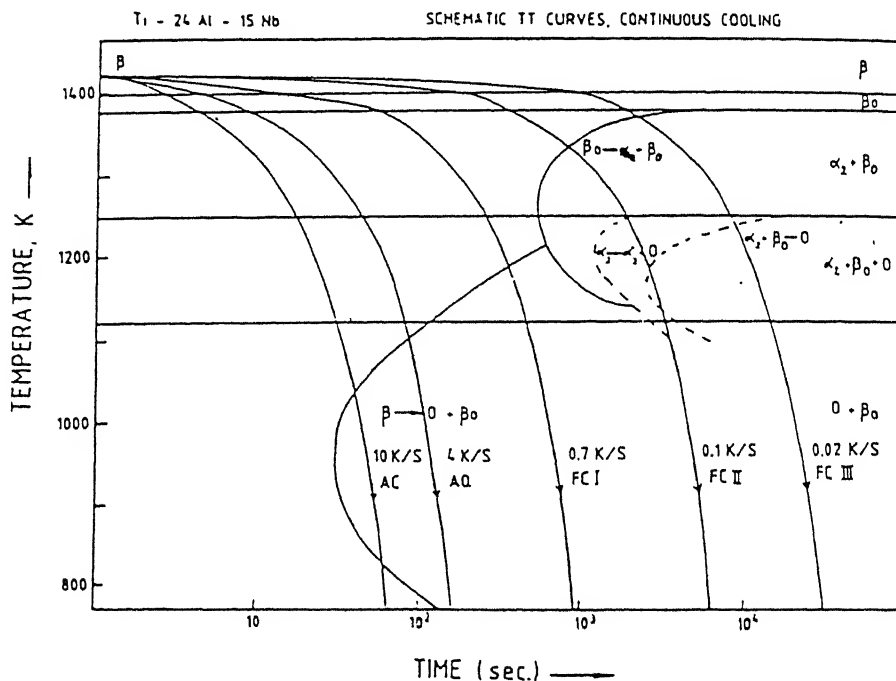
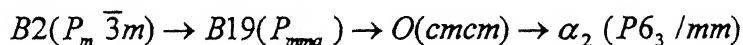


Fig. 2.3 Schematic CCT curves proposed for continuous cooling from β phase field [4]

In a more recent study on the ageing characteristics of a Ti-24Al-11Nb alloy, within the temperature range 723 K-1123 K, Hsuing and Wadley [33] proposed the path of isothermal transformation from the initial B2 to final α_2 structure as follows:



In the same study, they also predicted a 'critical' temperature (about 773 K) above which $B2 \rightarrow B19 \rightarrow O \rightarrow \alpha_2$ transitions take place and below which $O \rightarrow \alpha_2$ reaction becomes very slow. Therefore, the kinetic stability of 'O' phase against its

transformation to α_2 in a β quenched Ti-24Al-11Nb alloy is below (about) 773 K. Earlier the same authors also reported the existence of a tetragonal (T) phase as the intermediate transformation product. However, the existence of the tetragonal phase was further re-examined by Banerjee, and it was found that this was another variant of the O phase only [4]. To distinguish between these two phases, many authors designate them either as O' and O'' or as O₁ and O₂.

2.3 Deformation Behaviour

The deformation behaviour of Ti₃Al-base Ti-Al-Nb alloys has been rigorously studied by several workers. A collective account of these studies covers both the domain of deformation crystallography as well as deformation processing. Both these aspects are reviewed under separate heads.

2.3.1 Deformation Crystallography

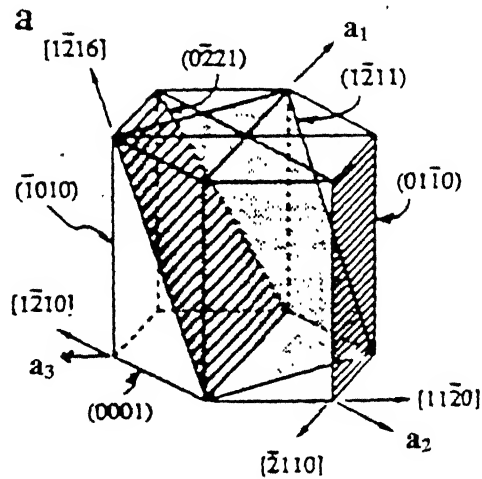
The deformation crystallography of single phase Ti₃Al as well as Nb modified Ti₃Al has been extensively studied by several workers for both its polycrystalline [6, 34-36] and single crystalline [37-39] forms. Attention has been focused in examining the dislocation arrangement generated by tensile deformation in Ti₃Al and in Ti₃Al alloyed with Nb [6]. A collective account of deformation crystallography extracted from the aforesaid studies is presented here.

Based on the shortest lattice translations and the densest slip planes, the possible slip systems in ordered structure of Ti_3Al indicate that three types of dislocations are possible: (1) **a** type, with a Burgers vector of the type $\frac{1}{6} \langle 11\bar{2}0 \rangle$ moving on the basal (0001) plane, the prism $\{10\bar{1}0\}$ plane, or the pyramidal $\{20\bar{2}1\}$ planes: (2) **c** type with a Burgers vector of $[0001]$ on second-order $\{11\bar{2}0\}$ prism planes and (3) **c + a** type with a Burgers vector $\langle 11\bar{2}6 \rangle$ on $\{11\bar{2}1\}$ or $\{20\bar{2}1\}$ pyramidal planes. The **a** type dislocations have been observed in Ti_3Al alloys deformed at room and intermediate temperatures [40], therefore Ti_3Al deforms predominantly by the motion of $\frac{1}{3} \langle 11\bar{2}0 \rangle$ superlattice dislocations on the basal, prism and pyramidal planes. However, operating slip systems involving only **a**-type dislocations do not provide the desired number of slip systems required by the von Mises criterion for polycrystalline ductility without cracking [41]. The present **c**- and **c + a**- type dislocation in Ti_3Al -based alloys deformed at high temperatures have been suggested to be responsible for the increased ductility observed at that time [34, 42-45]. Some **c**- and **c + a**- type dislocations have been reported in Ti_3Al -base alloys deformed at room temperature and at elevated temperatures [35, 46, 47]. However, the density of these $[0001]$ and $\langle 11\bar{2}3 \rangle$ dislocations is very low, especially at temperatures below 873 K [34, 46]. It has also been shown that **c** dislocations are present in undeformed Ti_3Al -base alloys whenever the α_2 phase has been precipitated from the β phase [48] and thus may be a transformation-induced rather than a deformation-induced product. The plot showing the variation of critical resolved shear stress (CRSS) as a function of

temperature is given in Fig. 2.4 along with the Burgers vectors of the dislocations. Observation of differing slip systems in h.c.p. Ti and its DO₁₉ superlattice counterpart Ti₃Al is due to [0001] slip being unusual in simple h.c.p. structures where the smallest unit translation is along the $\langle 11\bar{2}0 \rangle$ direction, but [0001] is the shortest perfect Burgers vector in the DO₁₉ structure. Twinning, a common deformation mode in hexagonal α -Ti, is excluded by the ordered structure of Ti₃Al. Thus, only four independent slip systems exist in polycrystalline Ti₃Al. Nb addition increases the tendency for basal slip and perhaps homogeneous prismatic slip, but does not increase the propensity for 'c' component slip.

Deformation in the B2 phase [35] is extremely inhomogeneous and localised into nonplanar slip bands. The structure in the slip band consists of heavily pinned edge dislocations with $\langle 111 \rangle$ Burgers vectors, which generate screw dislocations on secondary slip planes. The dislocations glide as loosely coupled $\frac{1}{2}a \langle 111 \rangle$ superpartials in Ti-25Al-11Nb, but as closely spaced pairs in Ti-25Al-16Nb, consistent with the higher disordering temperature for the latter. The [100] dislocations have also been observed, but only in the vicinity of α_2 /B2 interfaces in a two-phase structure, where they are presumably generated by incompatibility stresses. The choice of $\langle 111 \rangle$ as the glide vector is consistent with the significantly lower APB energy of this B2 composition relative to that of NiAl [35]. While screw dislocations are generally less mobile in both disordered b.c.c. and B2 phases due to their nonplanar core structure [53], the pinned edge dislocation configurations appear to arise from

dislocation interactions with the defect structure from the $\{110\} \langle 110 \rangle$ elastic instability. Local segments of the slip bands have been identified to be parallel to $\{110\}$ and $\{112\}$ planes. The intense slip localisation is believed to arise from slip plane softening owing to the shearing/dissolution of the ω phase present in the structure (a behaviour also observed in disordered β with ω). As with all inhomogeneously deforming materials, grain size refinement results in refinement and homogenisation of slip [44]. Since the β (B2) phase is metastable with respect to decomposition to α_2 or O, it has not been possible to generate information on its flow stress behaviour as a function of temperature.



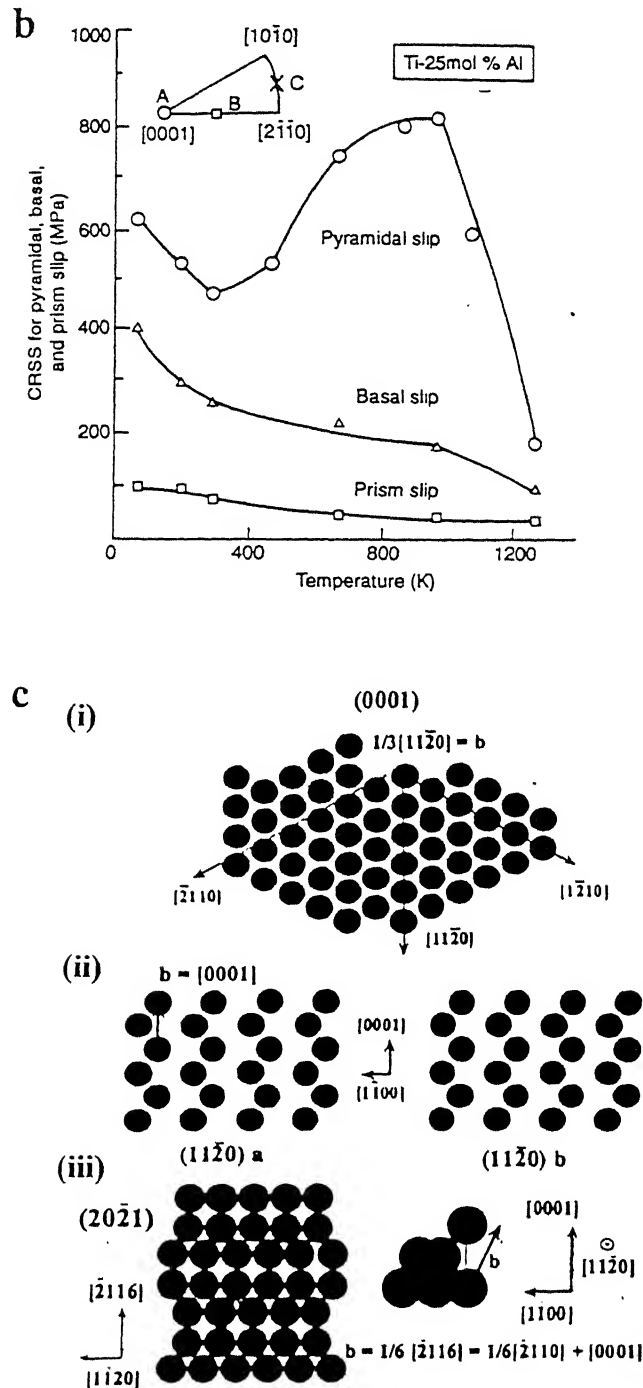


Fig. 2.4

(a) Hexagonal superlattice structure of Ti_3Al showing slip planes and slip vectors in the structure [3], (b) Variation of CRSS for different slip systems in Ti_3Al as a function of temperature [4] and (c) The three types of Burger's vectors present in the Ti_3Al structure : (i) a type, $b = 1/6 \langle 11\bar{2}0 \rangle$, (ii) c type, $b = [0001]$ and (iii) a+c type, $b = 1/6 \langle 11\bar{2}6 \rangle$ [60]

2.3.2 Deformation Processing

Ti₃Al-base alloys modified with Nb are generally processed by hot working. A number of studies have been carried out on hot deformation characteristics of these alloys. One of the preliminary reports in this area in the open literature is due to Witteneauer *et al.* [55]. The work involves hot rolling of Nb modified and (V, Mo) containing Ti₃Al alloy in the temperature range 1213 K-1393 K. The results of Witteneauer *et al.* indicate that the deformation of the super α_2 alloy is not homogeneous in the temperature range 1213 K-1263 K and give rise to pinholes and edge cracks. However, this inhomogeneity does not persist if the material is rolled at 1283 K resulting in a completely recrystallised microstructure.

A more rigorous and systematic study on plastic-flow behaviour and microstructural development in a cast Ti-24Al-11Nb alloy was carried out by Semiatin *et al.* [56], using hot compression testing. The results of this study reveal three elevated temperature deformation zones, namely warm working, hot working in the two phase ($\alpha_2 + \beta$) field and hot working in the single β phase field. When hot working takes place in the first regime, the material exhibits an unrecrystallised microstructure with cavities and wedge cracks. On the other hand, hot working in the ($\alpha_2 + \beta$) phase field results in a fully recrystallised (globularised) structure of primary α_2 phase in a transformed matrix. In contrast, a structure consisting wholly of transformed β is produced if deformation is conducted in the single phase region. The hot working regime extends to as low as ~ 100 K below the β -transus which allows a wide range of

choice for breakdown temperature. Figs. 2.5 (a-c) show the true stress-true strain plots as obtained by Semiatin [56] for different working temperatures and strain rates. The activation energy for hot working of Ti-24Al-11Nb alloy in the two phase field is considerably higher than that of conventional ($\alpha+\beta$) titanium alloy. The value of activation energy has also been found to be considerably higher than the activation energy value characteristic of creep for α_2 titanium aluminides. A comparison of the deformation behaviours of cast and wrought materials indicate that the specific dependence of flow stress upon temperature and strain rate for a wrought alloy of similar composition is the same as the as-cast material, once it is interpreted after correction in β -transus temperature (Fig. 2.6) [56].

A subsequent study by Long and Rack [57] on thermomechanical stability of forged Ti-25Al-11Nb alloy uses dynamic material modelling (DMM) for the analysis of the mechanical behaviour to establish the flow stress-strain rate-temperature-strain criterion. The true stress-true plastic strain behaviour of this alloy at low temperatures and high strain rates is given in Figs. 2.7. The deformation behaviour exhibited by these curves are attributed to continuous strain hardening during deformation. On correlating the unstable and stable flow regimes, as predicted by DMM to the microstructure, it has been revealed that the unstable flow zones are associated with the physical processes like, $O \rightarrow \alpha_2$ transformation, kinking of α_2 lamellae, shear band formation and coarsening of dynamically recrystallised grain structure. The stable flow regimes were associated with dissolution of Widmanstätten α_2 , coarsening of primary α_2 and dynamic spheroidisation of the lamellar α_2 microconstituents.

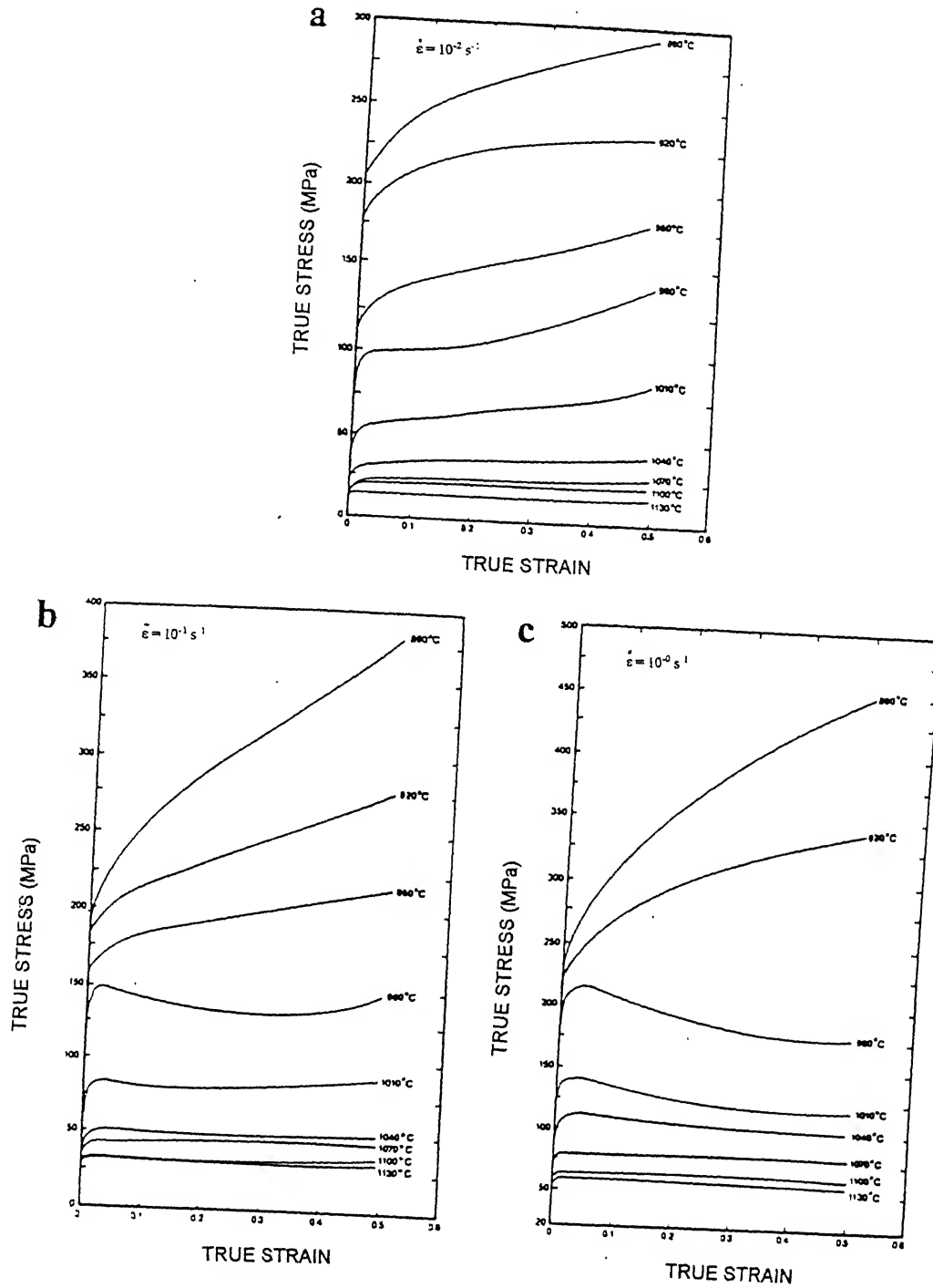


Fig. 2.5 True stress-strain curves corrected for deformation heating for cast Ti-24Al-11Nb deformed in compression at constant true strain rates of (a) 10^{-2} s^{-1} , (b) 10^{-1} s^{-1} and (c) 1 s^{-1} [56].

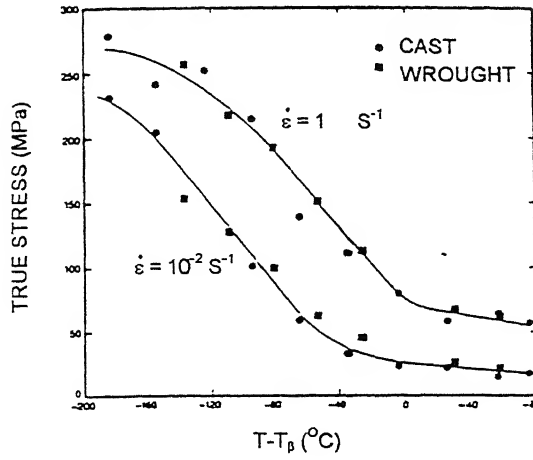


Fig. 2.6 Plot of flow stress (at $\bar{\epsilon} = 0.05$) vs temperature for cast and wrought Ti-24Al-11Nb. Data have been plotted in terms of temperature relative to the β -transus, T_{β} [56].

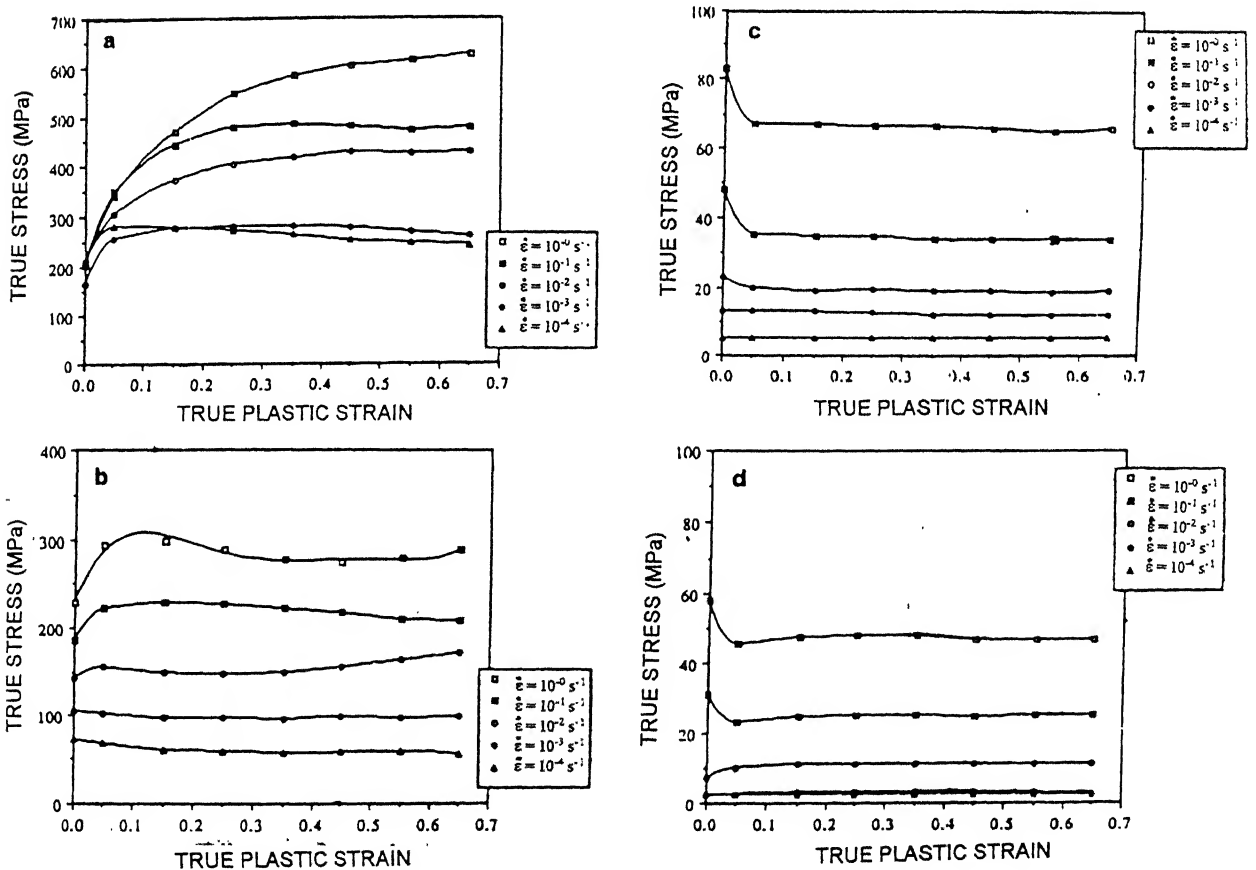


Fig. 2.7 Typical true corrected stress-true plastic strain curves of Ti-25Al-11Nb at: (a) 1073 K, (b) 1273 K, (c) 1398 K and (d) 1473 K [57]

Sagar *et al.* [58] were successful in identifying a domain of dynamic recrystallisation of α_2 in Ti-24Al-11Nb, which is defined by limiting values of strain rate and temperature. Typical stress-strain behaviour for as-cast and mill annealed materials at 1173 K, 1293 K and 1373 K, as obtained by Sagar *et al.*, are shown in Fig. 2.8 (a-c). It can be seen that (i) the flow stress curves corresponding to the air cooled structure lie above those for the mill annealed structure at all temperatures and strain rates, but the stress differential is higher at lower temperatures and higher strain rates, (ii) the flow curves of the air cooled material show flow softening with its onset at higher strains at lower temperatures and higher strain rates, while for the mill annealed material, the flow curves show work hardening followed by a steady state. Consequently, the flow stress of the air cooled structure approaches that of the equiaxed structure with increasing strain, especially at higher temperatures. Fig. 2.8 (d and e) show the processing maps for Ti-24Al-11Nb in as cast as well as wrought conditions. The isocontours plotted on this map represent lines of constant process efficiency of power dissipation through metallurgical processes. A comparison of Figs. 2.8 (d and e) also shows that the dynamic recrystallisation domain for the α_2 phase in wrought Ti-24Al-11Nb alloy with an equiaxed microstructure is shifted to higher strain rates in comparison to cast Ti-24Al-11Nb. The rate controlling mechanism for dynamic recrystallisation is believed to be cross-slip in the α_2 phase. The cast structure is more prone to instability than equiaxed structure and this manifests as shear bands. Another very significant outcome of Sagar's study is regarding β recrystallisation. β recrystallisation has been observed after deformation and subsequent annealing for

different combinations of strain rate and deformation temperature. These combinations of strain rate and deformation temperature are different from those required to recrystallise the α_2 phase.

In another study, Long and Rack employed dynamic material modelling to examine the high strain, elevated temperature behaviour of Ti₃Al-base Ti-26Al-10Nb-3V-1Mo alloy [59]. The stress-strain curves obtained from their study are shown in Fig. 2.9. Their results indicate that kinking of α_2 platelets and shear band formation in the ($\alpha_2+\beta$) phase field leads to unstable type of flow, with flow localisation at the grain boundaries and dynamic grain growth in the β -phase field. The stable flow behaviour, whenever encountered has been interpreted as due to the dynamic spheroidisation of the Widmanstätten α_2 platelets in ($\alpha_2+\beta$) phase field, and due to the dynamic recrystallisation of β phase.

The most recent study on the effect of temperature and strain rate on substructure evolution and mechanical response in Ti-24Al-11Nb alloy is due to Albert and Gray [60]. In their study, deformation behaviour has been examined for compression at both dynamic (10^3s^{-1}) and quasi static strain rates (10^{-1} and 10^{-3}s^{-1}). The results show that the true stress-true strain response of Ti-24Al-11Nb depend on both the applied strain rate and, to a lesser extent, the test temperature (Fig. 2.10 a). The rate of strain hardening increases with increasing strain rate (Fig. 2.10 b). The flow stress of Ti-24Al-11Nb at 3% strain increases with decreasing temperature at both quasi-static and dynamic strain rates (Fig. 2.10 c).

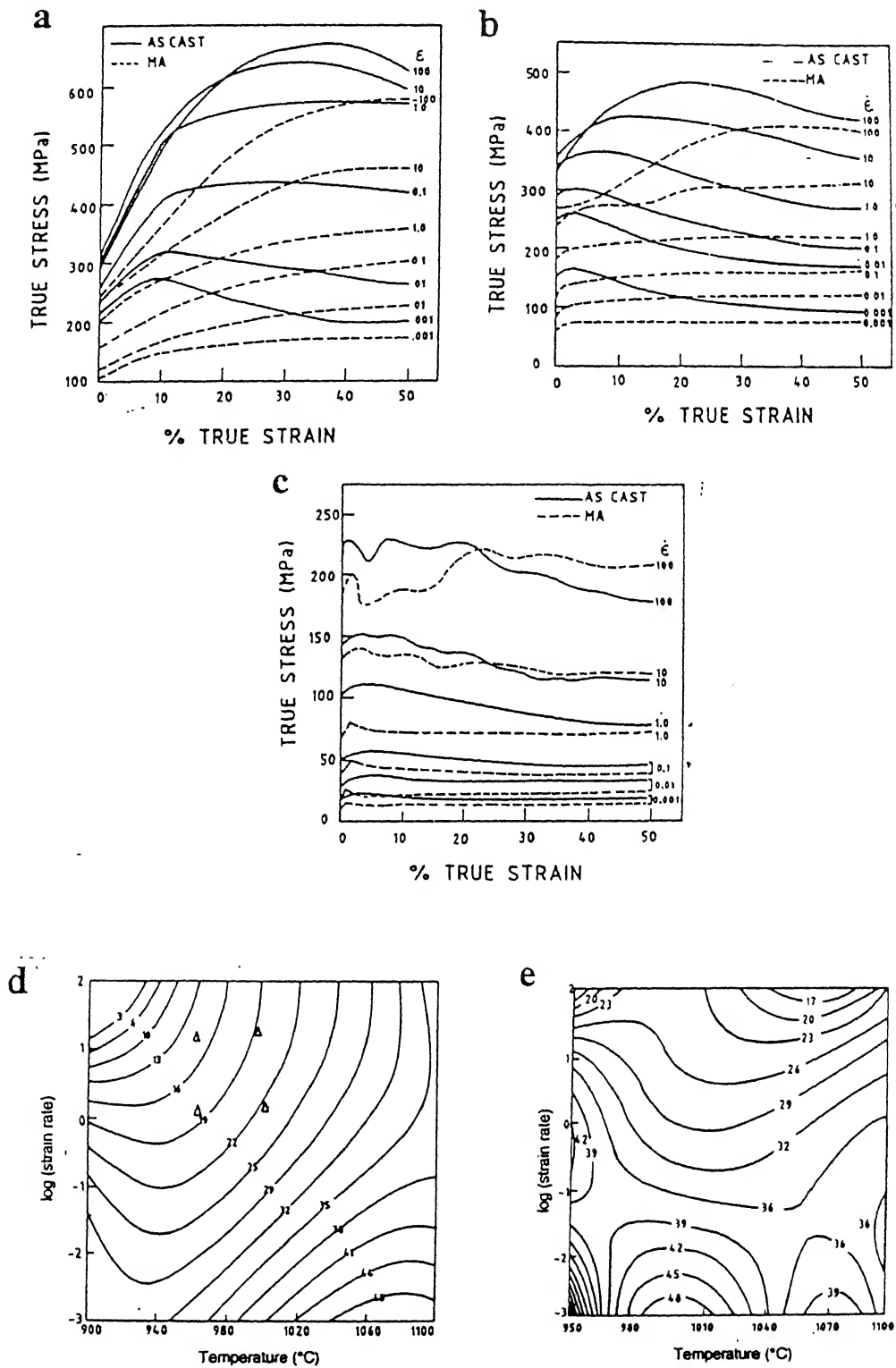


Fig. 2.8 Stress-strain curves at three temperatures (a) 1173 K, (b) 1273 K and (c) 1373 K, (d) Process efficiency map for as-cast Ti-24Al-11Nb and (e) Process efficiency map for wrought equiaxed Ti-24Al-11Nb [58].

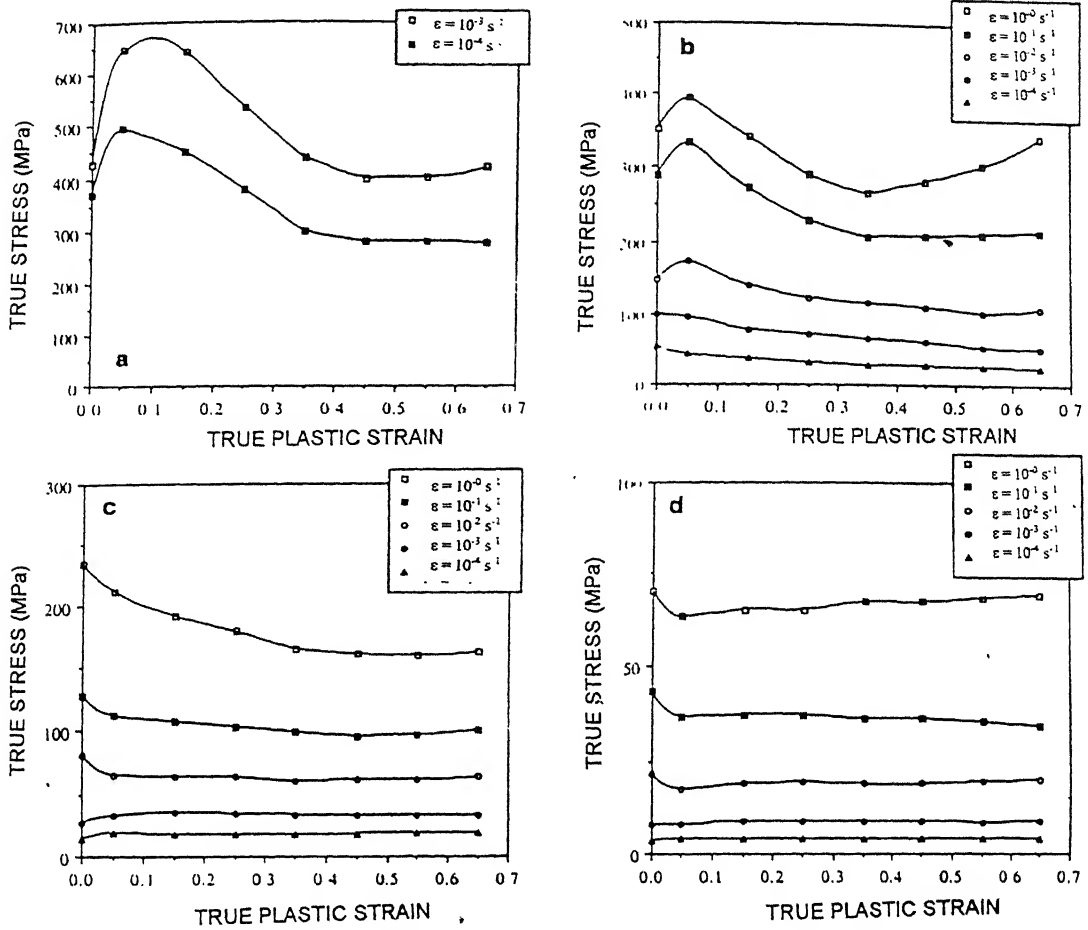


Fig. 2.9 Typical true corrected stress-true plastic strain curves of Ti-26Al-10Nb-3V-1Mo at (a) 1073 K, (b) 1273 K, (c) 1348 K and (d) 1473 K [59].

The high temperature deformation processing of a higher Nb containing Ti_3Al -base alloy Ti-24Al-20Nb has been carried out by Sagar *et al.* [61]. Their study identifies two distinct regions of temperature and strain rate in which efficiency of power dissipation is maximum. The first region, has been reported to be due to dynamic recrystallisation of α_2 phase (1248 K, 0.1 s^{-1}) and the second one has been

identified to correspond to the dynamic recovery of β phase. In addition, two distinct regions of processing instability one at high strain rates and the other at the low strain rates in the lower temperature regions have been identified, within which shear bands are formed. It is to be noted here that although the Ti-24Al-20Nb alloy is a two phase (O+B2) alloy at room temperature, high temperature deformation above 1273 K occurs in a two phase (α_2 +B2) on single phase B2. Niobium, which increases basal slip in Ti_3Al , helps in reducing the temperature and increasing the strain rate required for dynamic recrystallisation of α_2 phase.

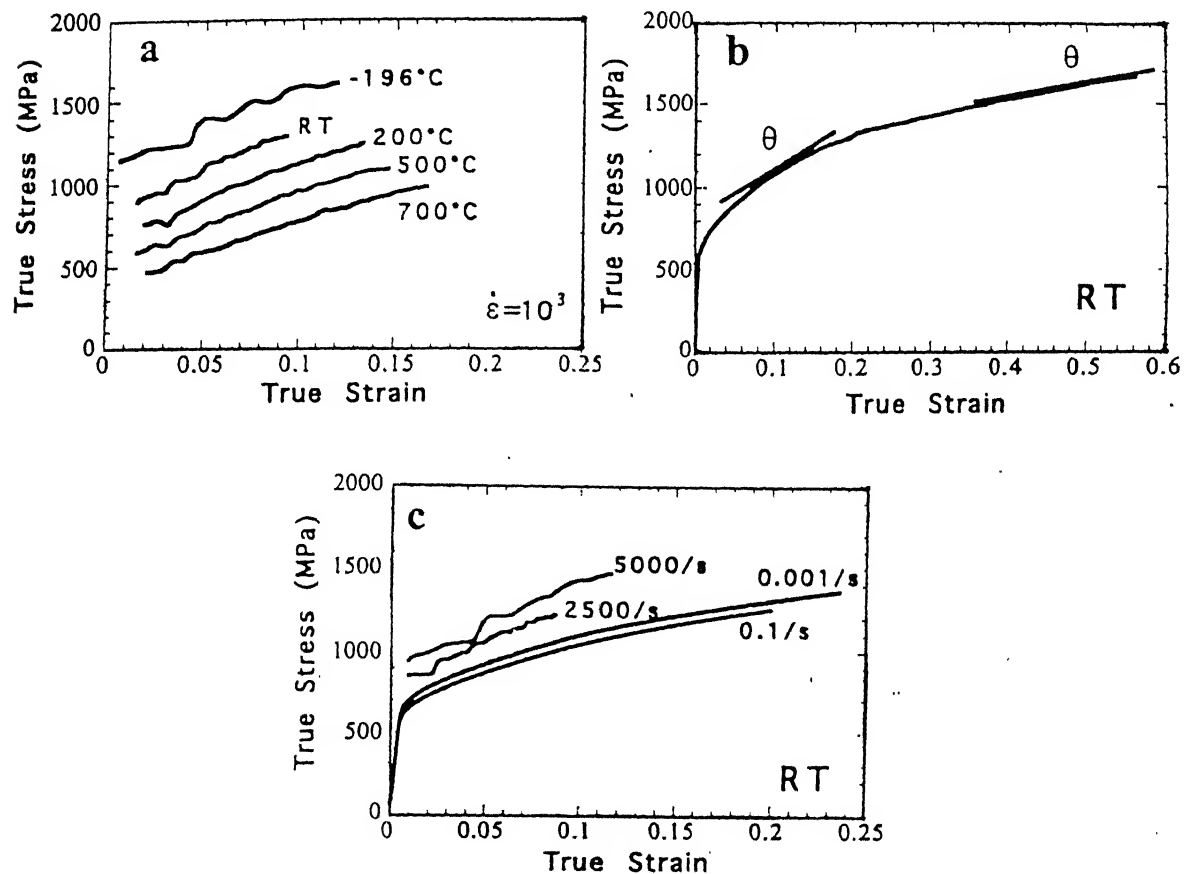


Fig. 2.10 (a) Dynamic deformation of Ti-24Al-11Nb at temperatures ranging from 97 K to 973 K (b) Ti-24Al-11Nb compressed to a large strain showing significant change in work hardening rate (c) Quasi-static and dynamic deformation of Ti-24Al-11Nb at room temperature [60].

2.4 Mechanical Behaviour

2.4.1 Tensile Behaviour

Preliminary studies on alloy development have indicated that Ti_3Al must be alloyed sufficiently to stabilise the $\beta(\text{B2})$ phase in the microstructure to enhance both strength and ductility, and that Nb is the preferred β stabiliser. Even in such a microstructure, however, the α_2 or O phase fractures by cleavage under tensile loading. Factors which strongly influence the ductile-brittle behaviour of metals, such as grain size and the extent of localised stress concentrations at grain boundaries (as influenced by slip modes and slip character), also play a major role in determining the tensile ductility of the materials [62].

Gogia *et al.* [11] have studied the variation of yield strength and ductility with α_2 and B2 contents in a variety of ternary and quaternary alloys. The variation of yield strength and ductility as a function of α_2 volume fraction is shown in Fig. 2.11 (a and b). It has been reported by Gogia *et al.* [11] that the B2 phase is stronger and the rule of mixtures is essentially obeyed for materials with duplex microstructure. The ductility at low B2 volume fractions has been found relatively high (3-8%) in comparison to single phase α_2 . The B2 phase delays cleavage crack nucleation in α_2 to higher strains by its ability to plastically accommodate incompatibility stresses at $\alpha_2/\text{B2}$ interfaces. These distributions of B2, which avoid α_2/α_2 grain boundary contact, have been found more effective in imparting ductility. At higher volume fractions, the B2 phase acts as a barrier to crack extension from α_2 . In that case, the condition for

fracture becomes the local stress at which cleavage cracks in α_2 can propagate into the more ductile B2 phase and therefore the ductility rises steeply in contrast to the low B2 volume fraction case, where the critical event for fracture is the onset of crack nucleation in α_2 . Single phase B2 of large grain size is by itself brittle because of slip inhomogeneity; it fractures by shear decohesion in intense slip bands. Increasing the Al content beyond 25% as well as Mo addition embrittles the B2 phase, rendering it less effective as a ductiliser. The detailed micromechanisms of fracture in Ti_3Al -base alloys is schematically shown in Fig. 4.12 [4].

Microstructural Response of Tensile Behaviour

(a) β Heat Treatment

The solution treatment above the β -transus temperature followed by cooling results in the decomposition of the β (B2) phase producing microstructures composed entirely of Burgers oriented α_2/O laths. Fig. 2.13 shows that the cooling rate after solution treatment strongly affects ductility and strength [9, 44, 63]. While the yield strength increases as the lath size is refined, the ductility goes through a maximum. The colonies of similarly oriented α_2/O variants which form at slow cooling rates are associated with large effective slip lengths since Widmanstätten $\alpha_2/\text{B2}$ interfaces are transparent to slip [35]. Thus, in the context of cleavage, the increasing effective grain size at slower cooling rates results in loss of ductility and strength. At cooling rates that are higher than the optimum, failure is initiated at softer grain boundary nucleated α_2 , which is considerably coarser than the fine intra-granular lath

structure, and the critical cracks thus formed propagate instantaneously to fracture [63, 64]. The optimum lath structure is therefore a fine basket-weave of α_2/O phase without any noticeable grain boundary film or grain boundary initiated colony structure. In addition, the role of alloying elements also influence the intrinsic properties of the α_2/O and B2 phases, as well as the manner in which they affect microstructural parameters such as grain boundary α_2/O and lath distribution [65].

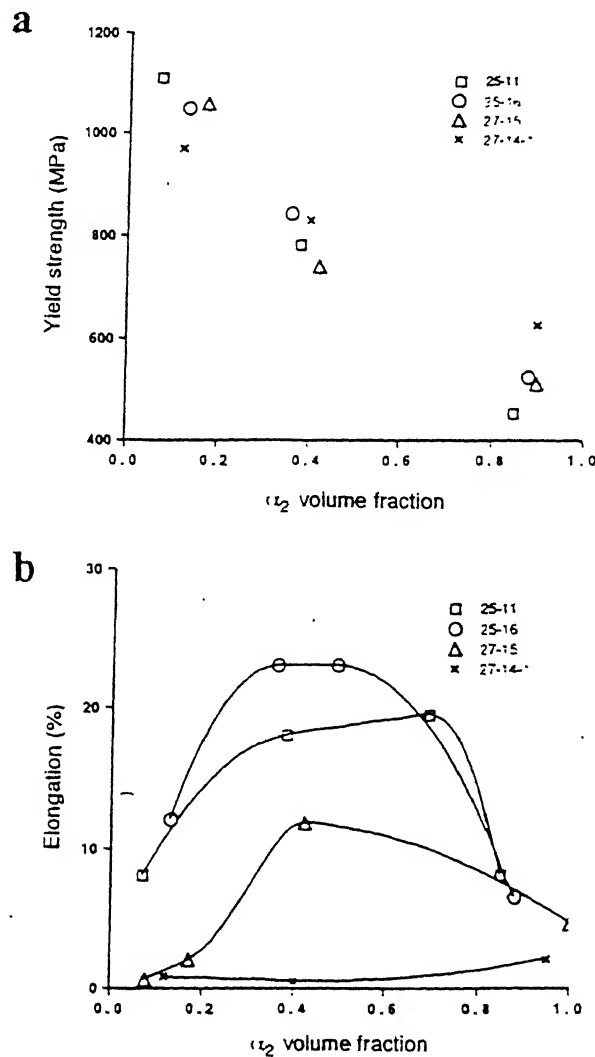


Fig. 2.11 The variation of (a) yield strength and (b) elongation to failure as a function of α_2 volume fraction [11].

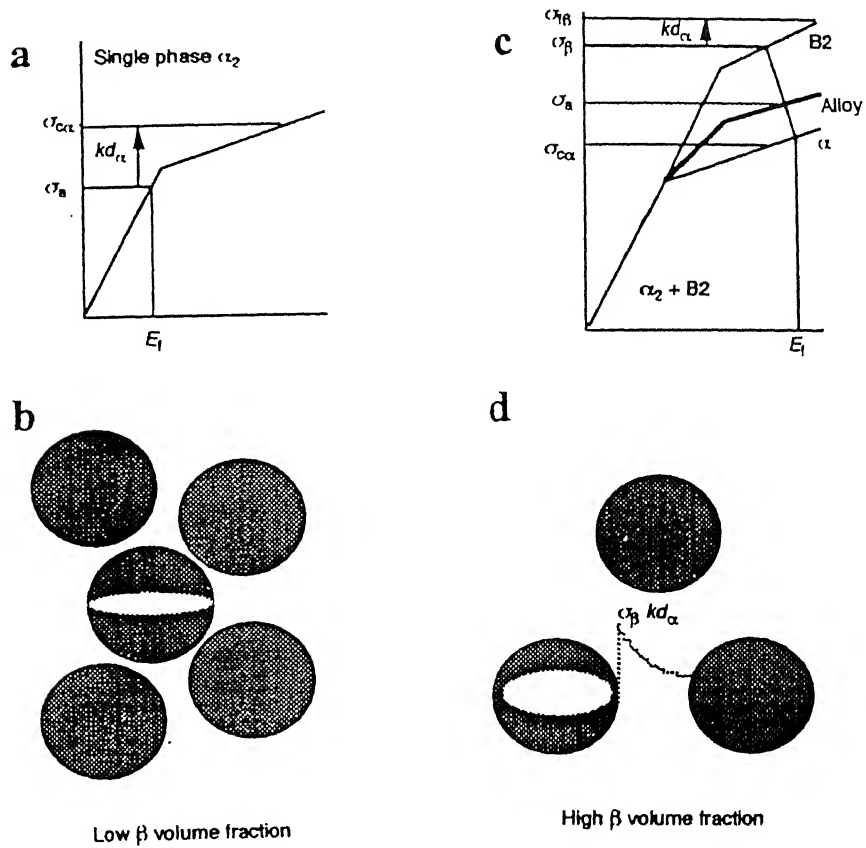


Fig. 2.12 (a) Plot representing the situation with local stress concentrations at grain boundaries and resultant cleavage fracture at σ_{ca} before macroscopic ductility in single phase α_2 , (b) Critical event for fracture in $\alpha_2 + \beta$ (B2) alloys with high α_2 volume fraction, (c) The critical event for fracture at higher volume fractions of B2, (d) The intensification of the *in situ* stress in β (σ_{β}) by the cracks in α_2 leading to the situation shown in figure (d) [4].

The effect of various combinations of solution treatment and ageing temperature on the tensile properties of different alloy compositions [63], is schematically described in Fig. 2.14. Gogia *et al.* [65] also proposed that the strength of primary α (σ_α) is independent of the solution treatment temperature, while σ_β increases with decreasing solution treatment temperature since the amount of retained β increases. If the alloy composition and combination of solution treatment and ageing temperature are such that the secondary α_2/O volume fraction is very high, then σ_β may almost be equal to σ_α . In such a case (Fig. 2.15) the strength may not increase with solution treatment temperature, as shown by a simple application of the rule of mixtures, and may go through a maximum, as experimentally observed in some alloys. However, the studies of Ward *et al.* [67] and Kumpfert *et al.* [68] on a Ti-25Al-10Nb-3Mo-1V alloy, where σ_β is much higher than σ_α , indicate that the overall strength may increase with solution treatment temperature.

The influence of equiaxed microstructures on ductility is not understood very well. Crack initiation in both primary α and transformed β , depending upon heat treatment has been observed [69]. Clearly, the partitioning of stress and strain between these microstructural constituents as well as geometrical parameters such as the size of the primary α_2 and the secondary laths will all influence the macroscopic strain at which cracks initiate in either constituent. The study of Gogia *et al.* [63] on the ternary alloys suggests that the volume fraction and continuity of retained β exert the most important influence, since lower solution treatment temperatures and higher ageing temperatures both increase ductility. Investigations by Kumpfert *et al.* [58, 60]

and Luetjering *et al.* [61] reveal that excellent combinations of strength and ductility in these aluminides can be obtained by thermomechanical processing to refine the overall microstructure and by a judicious combination of solution treatment and ageing.

2.4.2 Creep and Stress Rupture Behaviour

The creep behaviour of Ti_3Al -base alloys are of extreme importance especially for high temperature applications. The steady-state creep behaviour in the temperature range 873 K - 1073 K has been investigated in a variety of alloys following the original work on single phase Ti_3Al by Mendiratta and Lipsitt [62]. Fig. 2.16 illustrates several important aspects of this feature in a number of alloy compositions. The creep strength of single phase 'O' is higher than single phase Ti_3Al , and single phase alloys are, in general, having higher creep strength than their two phase ternary Ti-Al-Nb counterparts. The presence of the β phase, while contributing to strength and ductility, is found to degrade the creep resistance. The steady-state creep rate of the more creep resistant aluminides approaches that of INCO 718 when normalised for density, and is superior to the creep-resistant conventional titanium alloy Ti-1100.

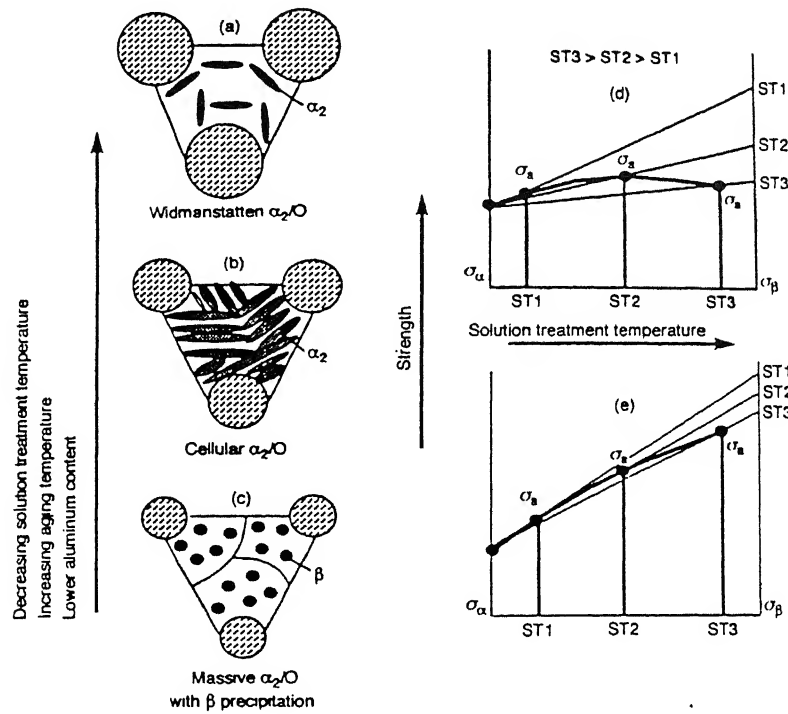


Fig. 2.14 Effect of microstructure and heat treatment on the strength and ductility of duplex structures [4]

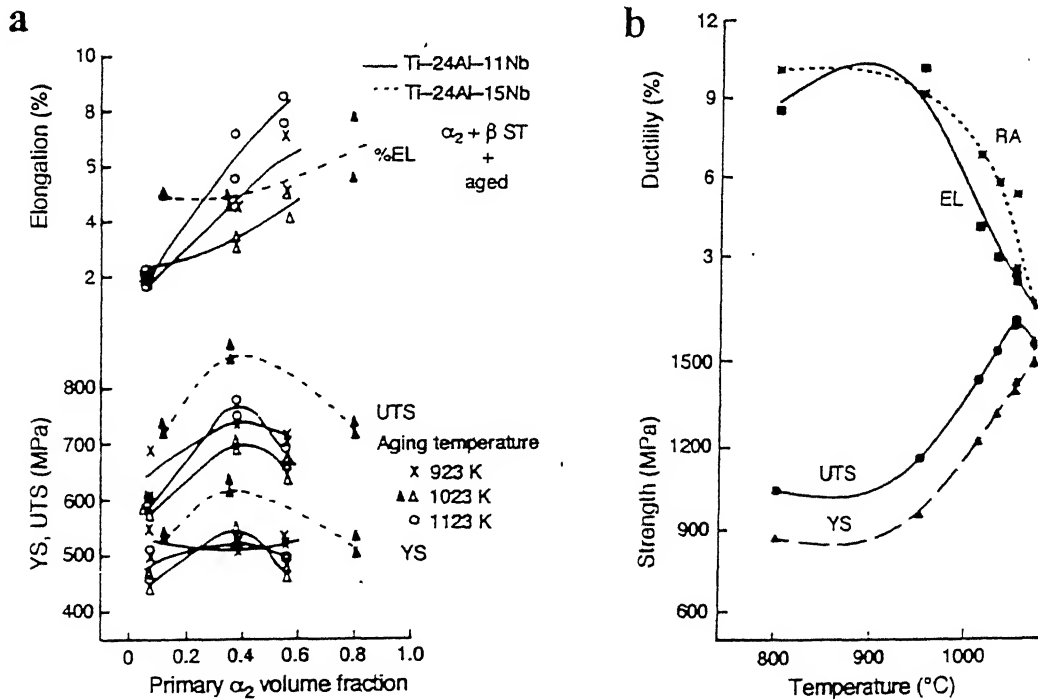


Fig. 2.15 (a) Tensile properties as a function of equiaxed α_2 volume fraction and ageing temperature in Ti-25Al-11Nb and Ti-25Al-16Nb [63], (b) Yield strength as a function of solution treatment temperature in Ti-25Al-10Nb-3V-1Mo [68]

A strong microstructural dependence of creep rate has been established by Mishra and Banerjee [42] and by Cho *et al.*, [63]. It has been reported that the creep resistance decreases with increasing volume fraction of equiaxed α_2 . Two distinct creep processes have been identified [42] : one is associated with diffusional creep with a stress exponent of 1 and activation energy equivalent to that for Coble creep in pure Ti; the other is associated with dislocation creep with stress exponents greater than 4 and activation energy again equivalent to that obtained for climb controlled creep in pure Ti. A variety of stress exponents between 1 and 4 has been reported [63-66], and these exponents are believed to represent the transitions between these basic mechanisms.

It has also been reported by Mishra and Banerjee [67] as well as Cho *et al.*[63] that lath structures show superior creep resistance. A substantial variation in steady-state creep rate with lath size has been demonstrated by these authors, as shown in Fig. 2.17 (a). While an increasing cooling rate refines the lath size, the steady-state creep rate goes through a minimum at an optimum cooling rate. The dependence on lath size is different, depending on the specific operative creep mechanisms. Since sliding of lath α_2/β interfaces has been demonstrated to accompany diffusional creep, a decrease in lath dimension leads to an increase in creep rate in the diffusional creep regime. On the other hand, it has been observed that pile-ups of dislocations at lath α_2/β interfaces occur in dislocation creep. The slight increase in creep rate at faster cooling rates (Fig. 2.17 b) is attributed to the increasing contribution of grain boundary sliding at fine lath

sizes. It has also been reported that the creep resistance of non-optimised lath structure may be poorer than equiaxed structures.

The results of Mishra and Banerjee also indicate that the superiority of lath structures in steady-state creep is carried over to stress rupture as well, although lath structures are generally associated with lower creep ductility. Typical curves for equiaxed α_2 containing 40% primary α_2 and a lath α_2 structure are shown in Figs. 2.18. A common environmental damage mechanism occurs for both lath as well as primary α_2 structure. Intrinsic damage mechanisms are, however, quite different for the different microstructures. For the lath structures, prior β grain boundary wedge cavitation occurs, while for the equiaxed structures, void formation at equiaxed transformed β interfaces is seen. It has been suggested by Ward and Balsone [70] that final fracture occurs as a consequence of tensile overload on the effective area that is undamaged by the annular environmentally affected ring, and therefore rupture resistance is related to the ability of the alloy structure to resist the propagation of the surface cracks in creep.

Although stress rupture and creep resistance, equivalent to those of density normalised INCO 718, can be attained relatively easily in Ti_3Al -base alloys, the design of rotating compressor components in engines is often limited by creep strains of the order of 0.1 or 0.2%. However, the results show that such conditions are typically attained within the primary creep span of these alloys, at specific stress levels comparable to those required to generate 0.1% creep in 100 hours in the INCO 718

alloy. Results of Rowe *et al.* [71] as well as Mishra and Banerjee [67] show that the lath structures show lower primary creep strains than the equiaxed structure. However, Mishra and Banerjee did not propose any quantitative dependence of primary creep strain on lath dimensions as observed in β heat treated structures, either in the diffusional creep or dislocation creep regime.

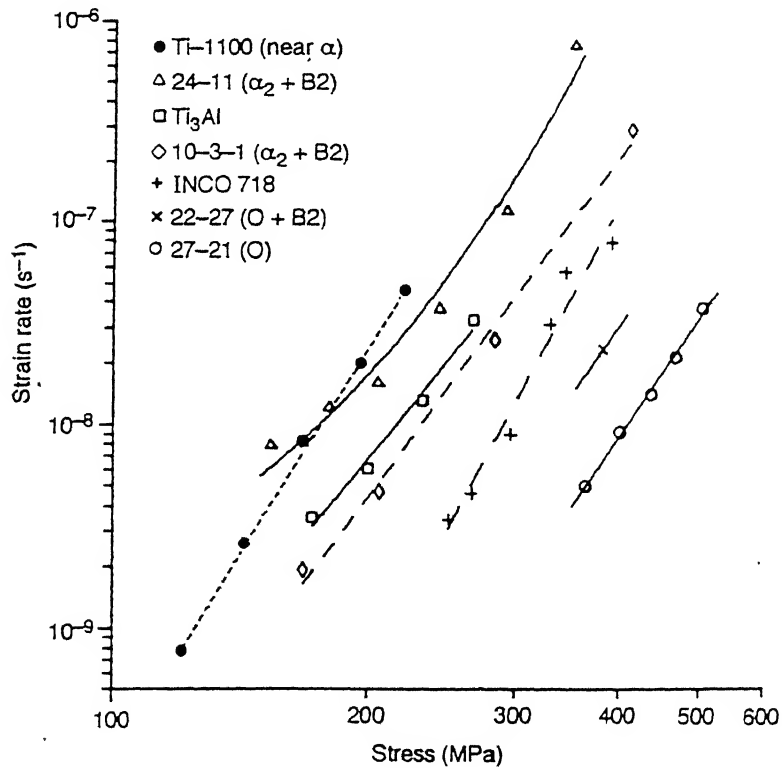


Fig. 2.16 Steady-state creep rates as a function of stress at 923 K for a variety of α_2 based and O based alloys compared with a conventional α/β alloy Ti-1100 and density-normalised data for INCO 718 [52].

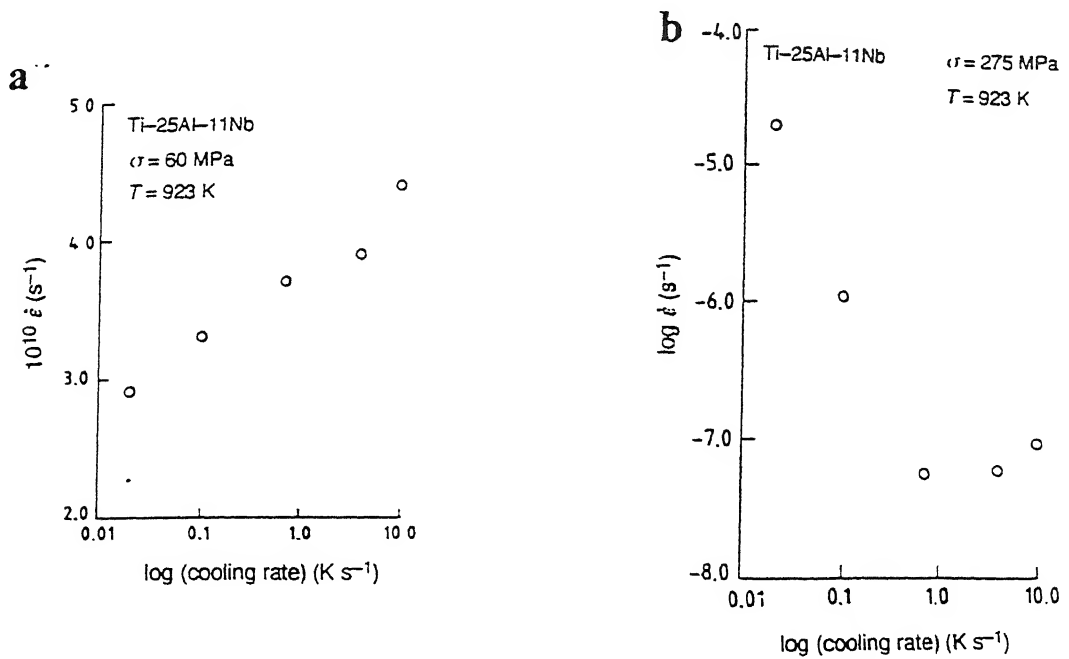


Fig. 2.17 Steady-state creep rate as a function of cooling rate in Ti-25Al-11Nb at 923 K (a) in the diffusional creep regime and (b) in the dislocation creep regime [77]

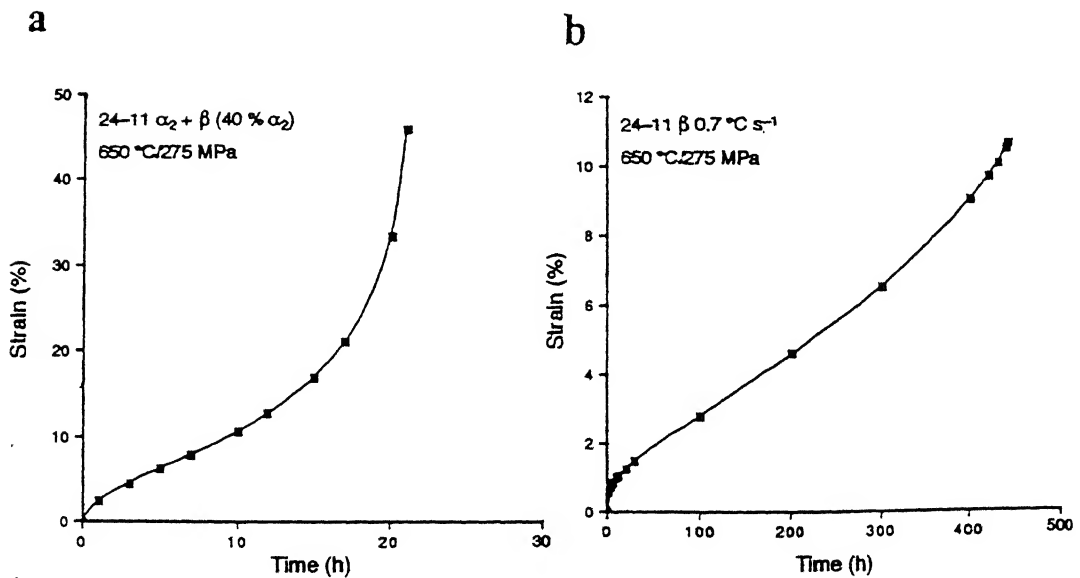


Fig. 2.18 Creep curves at 923 K and 275 MPa for equiaxed α_2 containing 40% primary α_2 and a lath α_2 structure obtained by cooling at 0.7°C/s after β solution treatment in Ti-25Al-11Nb [4]

2.4.3 Fracture Toughness and Fatigue

In a series of papers, Chan [82-84] investigated the role of various micromechanisms imparting toughness. He inferred from his studies that the room temperature fracture toughness of Ti-24Al-11Nb alloy is essentially derived from the role of the β phase in delaying the onset of microcrack nucleation in α_2 through its ability to relax incompatibility stresses at α_2/β interfaces and, in blunting main crack as well as the microcracks. Thus, the β phase appears to play identical roles in imparting tensile ductility and fracture toughness. Also the continuity of the β phase around the grains will play a critical role in imparting resistance against microcrack nucleation, while an increased volume fraction of β phase provides for increased crack blunting capacity.

Since the roles of the β phase in imparting toughness and ductility are identical, there should exist a correlation between tensile ductility and toughness. Fig. 2.19 (a and b), which compare strength-toughness and strength-elongation relationships for different alloy compositions, indicates that such a relationship broadly exists. The same figure also emphasise the relatively superior strength-toughness combinations of the high Nb alloys Ti-25Al-17Nb-1Mo and Ti-22Al-27Nb. It is likely that all three factors influencing toughness may underlie this behaviour: a finer lath size, a greater volume fraction of β phase, and the major constituent phase being the ' β ' phase with its greater number of slip systems in comparison to α_2 . Fig. 2.19 (c) indicates the correlation between toughness and elongation in three different alloy systems. Fig.

2.19 (d) shows that toughness follows the same trend as elongation as a function of temperature and suggests that fracture toughness is also prone to environmental effects. Chan [83] suggested that the increase in toughness with temperature arises from propagation resistance rather than initiation resistance.

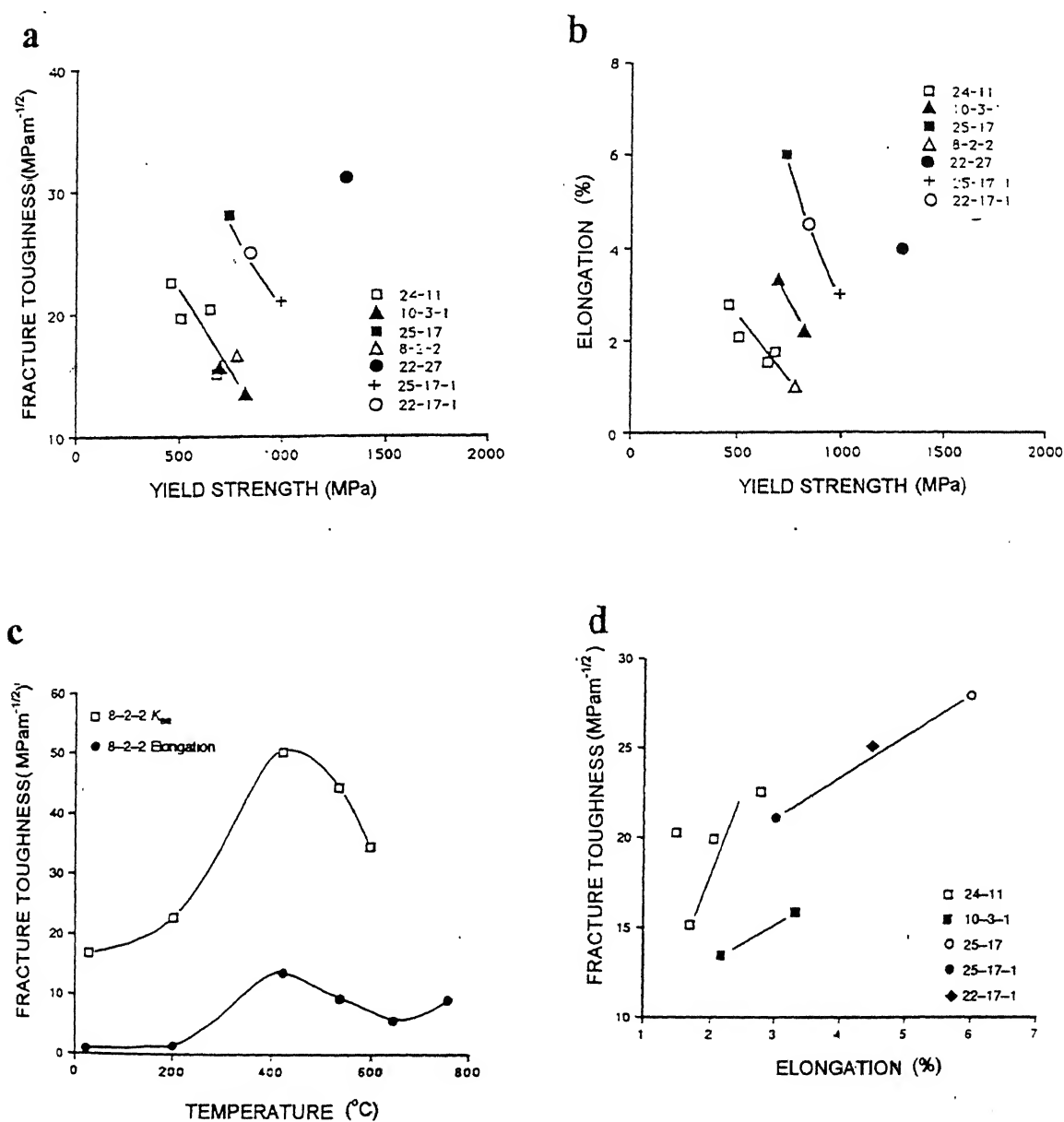


Fig. 2.19 (a) Strength - Fracture Toughness, (b) Strength - Elongation, (c) Elongation - Fracture Toughness, and (d) Temperature - Fracture Toughness relationships for different Ti₃Al-base alloys [4, 15, 82-84]

Fatigue crack growth occurs by nucleation of microcracks within the α_2 phase and their subsequent linkage [85, 86] and it has been suggested that the process of linkage through the β phase retards the macroscopic crack growth rate in β heat treated structures. The trends of reported data, as available for the basket-weave and equiaxed structures (20-30% primary α_2) of Ti-24Al-11Nb and Ti-25Al-1Nb-3Y-1Mo show that threshold for crack growth are different for the two alloys. However, no generalised conclusions on microstructural effects are possible in the absence of quantification of the relevant microstructural parameters.

2.4.4 Superplasticity

The presence of low ductility even at 1173 K has been the main motivation for attention to superplastic forming of Ti₃Al-base materials. Superplastic Ti₃Al has mainly been fabricated either through powder metallurgy route or through casting route followed by hot forging or hot rolling to yield fine grained microstructure. The maximum strain rate sensitivity and tensile elongation observed in these superplastic materials have been obtained within the temperature range 1223-1273 K and at strain rate $1-3 \times 10^{-4} \text{ s}^{-1}$.

Yang *et al.* [87] have studied the superplasticity in super- α_2 alloys and found that the super- α_2 exhibited a maximum elongation of 570% when deformed at 1253 K and a strain rate of $1.5 \times 10^{-4} \text{ s}^{-1}$. The maximum superplastic elongation reported so far are due to Ridley *et al.* [89] and Fu *et al.* [91]. In the study by Fu *et al.* performed on

a sheet material with the thicknesses 1mm and 2mm, a maximum superplastic elongation of 600% and 1500% could be obtained at 1233 K at the strain rates 2×10^{-4} - 5×10^{-4} respectively. Ridley *et al.* [79] studied the superplastic behaviour of super- α_2 in the sheet form (3 mm thick) by conducting constant cross head speed (i.e. decreasing strain rate) tests and achieved an elongation of 1350% at 1233 K and at the initial strain rate $1.7 \times 10^{-3} \text{ s}^{-1}$.

Several studies are aimed at examining the details of superplastic behaviour of α_2 base alloys. Dutta and Banerjee [92] have studied the microstructural dependence of superplasticity and have shown that equiaxed microstructures are amenable to superplastic deformation. The results of Yang *et al.* have revealed that (a) at high temperatures and/or low strain rates, the stress-strain curve showed strain hardening; (b) at low temperatures and/or high strain rates, the stress-strain curve showed strain softening due to dynamic recrystallisation and geometrical necking; (c) the activation energy for superplastic deformation process was calculated to be 308 kJ/mole; (d) transgranular fracture was the predominant mode of failure in the super- α_2 compound and (e) super- α_2 materials did not form cavities during superplastic deformation. Results of Ghosh and Cheng [88] indicate that the regular α_2 compounds work harden continuously and gradually during superplastic deformation which results from gradual grain growth, while the super- α_2 materials undergo continuous softening which might be related to the break down of the elongated structures. In a separate study, Cheng *et al.* [90], have attributed the rate-controlling mechanism to grain boundary sliding. Yang *et al.* [87] have reported the strain-induced morphological change of the α_2 and

β phases during superplastic deformation. Their study reveals that the co-operative grain boundary sliding, i.e. the superplastic deformation, proceeds by means of groups of grains shearing along the grain boundary surfaces. This could explain (a) the formation of irregularities on the sample surface; (b) breaking up of the α_2 phase; and (c) neck formation. In this regard, the results of Fu *et al.* are also very significant which reveals that, during superplastic deformation, the lath like α_2 grains gradually disappear to result in more equiaxed grain structure. Recently, it has been suggested that textures also play a significant role in superplastic behaviour of these alloys [91].

2.5 Texture

The study of texture evolution during processing has received very little attention in spite of the fact that sheet applications of α_2 alloys have been envisaged both in composite and in monolithic form. Out of the existing informations, the most comprehensive one is due to Hon *et al.* [93]. The results of their investigation indicate that the deformation behaviour of α_2 is closely related to the formation of basal texture. Decreasing the rolling temperature and increasing reduction ratios both sharpen (0002)[20 $\bar{2}$ 0] texture. The compressive deformation during rolling tends to cause the (0002) slip plane to become parallel to the rolling plane. Simultaneously, the tension along the rolling direction makes the α_2 grains to slip in the $\langle a \rangle$ direction. Sharp basal textures are associated with low yield strength and ductility as high as 10% even in a Ti-25Al-10Nb alloy with very little or no β phase. This has been attributed to the greater ability of the textured grains to accommodate grain boundary stress

concentration without the operation of five independent slip systems. Another study by Knorr and Stoloff [94] involved the effect of heat treatment on hot cross-rolled sheets of Ti-24Al-11Nb in ($\alpha_2+\beta$) and β phase fields.

It has been reported [94] that heat treatment in ($\alpha_2+\beta$) phase field alters the texture only marginally, that too with respect to intensity and not the main component. The principal texture components of the heat treated material remain the same as in the as-rolled material. Little intensification of texture is however reported for annealing at relatively higher temperatures such as, 1273 K followed by cooling to room temperature.

Knorr and Stoloff [94] reported a more substantial modification of texture is by annealing in the β -phase field followed by cooling to room temperature. The resulting Widmanstätten microstructure has been associated with the sharp texture thus obtained (Fig. 2.20). The sharper component, however, is superimposed on a low intensity, random background texture component which is present in all the ($\alpha_2+\beta$) heat treated equiaxed materials.

Mao *et al.* [95], who examined the textural changes on compression at 1023 K, have shown that $\{0001\} \langle 11\bar{2}0 \rangle$ and $\{11\bar{2}1\} \langle 11\bar{2}6 \rangle$ slip systems are the most active slip systems and these orientations result in a fibre texture with $\{0001\}$ planes located at an angle of about 30° to the compression plane. The optimum ratio of critical resolved shear stresses between the slip systems $\{0001\} \langle 11\bar{2}0 \rangle$ and $\{11\bar{2}1\} \langle 11\bar{2}6 \rangle$, necessary for this kind of a texture, has been estimated to be 1:2. It

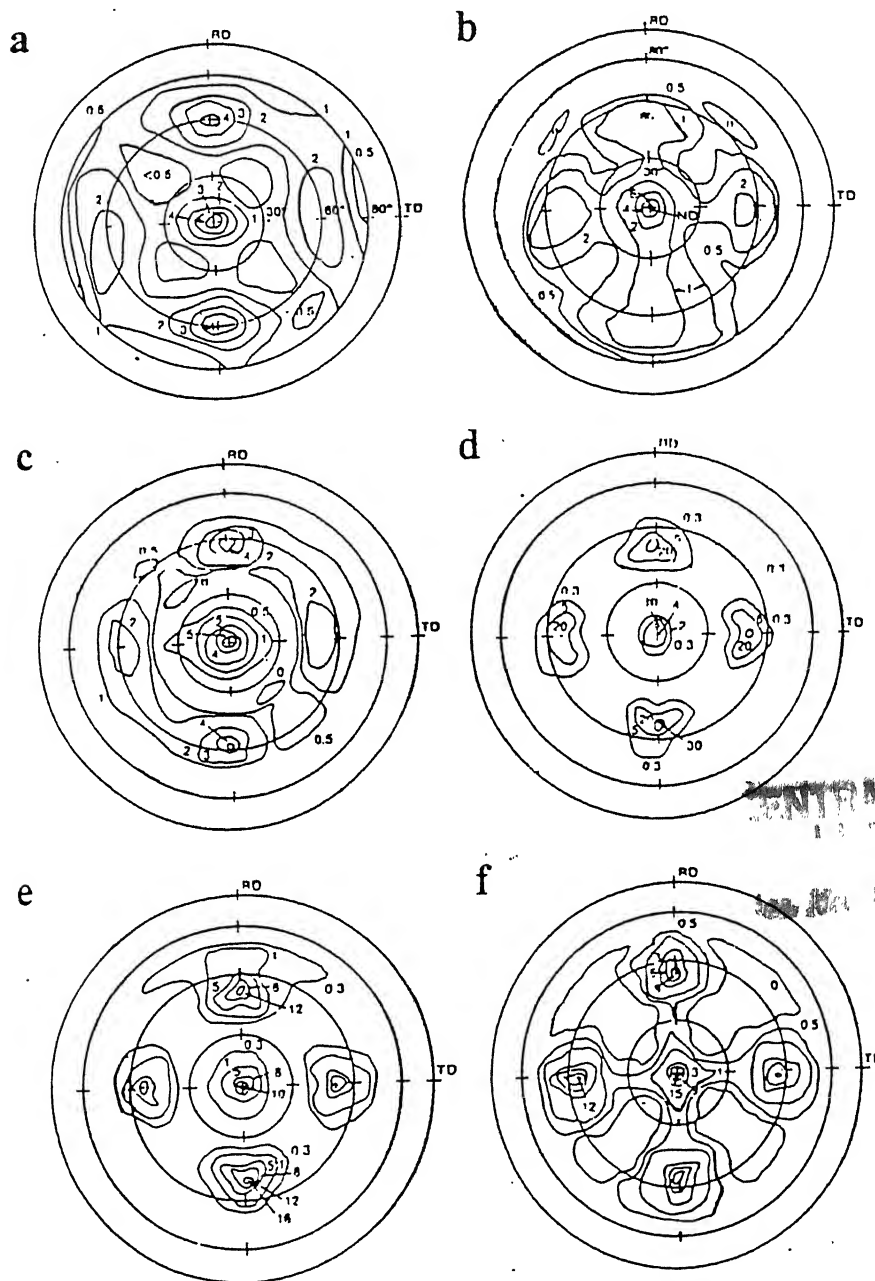


Fig. 2.20 $\{2240\}$ pole figures for (a) the hot rolled starting material, heat treated at (b) 1273 K, WQ, (c) 1273 K, WQ/1255 K FC, (d) 1473 K, WQ, (e) 1473 K, WQ/1255 K, FC and (f) 1473 K, FC heat treated conditions [94]

has also been reported that $\{1\bar{1}00\} \langle 11\bar{2}0 \rangle$ could be activated in very limited orientation space and result in very weak $\{11\bar{2}0\}$ fibre texture. The overall texture are weak and it has been explained to be due to some recovery process.

In addition to the texture of h.c.p. α_2 phase, a couple of studies have also been directed to the texture of (O+B2) structured $\text{Ti}_3\text{Al-Nb}$ alloy. These alloys being more amenable to rolling processes, these could be rolled to foils even by conventional rolling processes. Studies of Rhodes *et al.* [85] on Ti-22Al-23Nb alloy indicate that moderate β phase texture $\{100\} \langle 011 \rangle$ develops during hot rolling which persists during cold rolling. The texture intensities get reduced in the cold rolled foil as compared to the starting texture. This has been explained as due to non dependence of room temperature deformation on the starting texture. However, this study does not reveal any clear information regarding the texture components in the 'O' phase. Another study by Rollett *et al.* [86] on the texture and anisotropy of Ti-22Al-23Nb alloy, shows that the cubic phase ($\beta/\text{B2}$) texture is typical of b.c.c. rolling texture that is dominated by the $\{001\} \langle 110 \rangle$ component.

2.6 Scope of the Present Investigation

Although substantial amount of research work has already been carried out on the development of Ti_3Al -base alloys and also its assessment with regard to the processing and property aspects has thoroughly been done, a systematic study of evolution of textures remains to be carried out. As it has already been stated earlier, the knowledge of textures in these materials is of utmost importance, particularly when the applications of this material are mostly being projected in the sheet form. With this view, the present investigation has been aimed at studying the evolution of textures during various stages of thermomechanical processing of the Ti_3Al -base alloy Ti-24Al-11Nb. Since the basic phenomenon involved in thermomechanical processing are deformation, annealing and phase transformation, a study of their role on textures has been the guideline for defining the domain of present investigation. Further, it has been stated that h.c.p. materials with a good basal texture $(0001)\langle\text{uvw}\rangle$ are likely to possess good forming characteristics, special attention has been focused on examining the possibilities of the development of the basal $(0001)\langle\text{uvw}\rangle$ texture as well as its stability during different stages of processing. The results obtained from various experimental observations have been correlated and discussed.

(Long Correlation?)

Experimental Procedures

3.1 Starting Material

The starting material used in the present investigation was supplied by The Defence Metallurgical Research Laboratory, Hyderabad (INDIA). The as-received material was in the form of a 600 gram pancake made by consumable electrode arc melting. A Ti-Nb master alloy and high purity Al were used for making the alloy. The chemical composition of the as-received pancake is given in Table 3.1.

Table 3.1 Chemical composition of the alloy

Al (at. %)	Nb (at. %)	O	N	H	Ti
24.60	12.39	650 ppm	80 ppm	28 ppm	Balance

The pancake was cut into rectangular pieces of size 30 mm X 20 mm X 10 mm. The surfaces of these pieces were machined to make them perfectly smooth and flat. These were used for subsequent thermomechanical processing.

3.2 Thermomechanical Processing

Elaborate thermomechanical processing was carried out on the experimental alloy in the present investigation. This involved controlled hot rolling along with annealing

treatment in between successive passes. After the finish rolling pass, the samples were either water quenched or furnace cooled to room temperature. A few hot rolled samples were also subjected to further annealing.

3.2.1 Hot Rolling

The coupons for hot rolling were coated with some organic material known as **Delta Glaze** (trade name) for prevention of oxidation during high temperature processing. The coated coupons were soaked at different temperatures in specially designed high temperature furnace kept very close to the rolling mill. A protective atmosphere of argon gas was maintained within the furnace. The furnace had a constant temperature zone of 15 cm in length and was heated by silicon carbide rods. The furnace tube was made up of inconel, and was closed from one end. Argon gas was introduced in the furnace through a 4 mm diameter stainless steel tube passing through the closed end of the furnace chamber.

Hot rolling was carried out in a 2-high laboratory rolling mill having 135 mm diameter rolls. The speed of rotation of the rolls was kept as 55 r.p.m. in all the experiments. The rolls were not pre-heated before carrying out the hot rolling operation. Prior to hot rolling, the samples were placed on a perforated inconel tray, and then pushed carefully into the hot zone of the furnace maintained at the required temperature. After soaking upto 30 minutes at the desired rolling temperature, the samples were taken out and quickly fed to the feeding end of the rolling mill. After each pass the samples were put back into the furnace for 5 minutes so that they re-attain the rolling temperature. The fall

in temperature during the whole process was estimated and found to be negligible. The above sequence of operations were repeated till the samples acquired the final desired thickness. Rolling was kept strictly unidirectional. The amount of reduction per pass varied from 10% (in the initial passes) to 20% (in the final passes). After the finish rolling pass the samples were kept back in the furnace for 5 minutes and then allowed to furnace cool to room temperature. In some cases the samples were water quenched after the finish rolling pass. The details of the thermomechanical processing schedule are shown in Fig. 3.1.

Nearly $1/8$ th of the thickness of the hot rolled samples was removed from both the surfaces by grinding and then it was subjected to pickling in 10% HNO_3 + 5% HF solution for nearly 4 hrs at 323 K. The pickled strips were cleaned by belt grinding and emery polishing before further investigation.

3.2.2 Heat Treatments

As mentioned earlier, a few of the hot rolled strips were annealed at desired temperatures for different periods of time. These heat treatments were carried out in the same furnace described above. After the required temperature was attained, the specimens were inserted into the constant temperature zone of the furnace and the open end of the furnace was closed with an O-ring fitting. The heat treatments were done under a continuous flow of argon atmosphere. The heat treatments followed in the present investigation can be classified into two categories:

(i) Heat treatments to study the effect of annealing on textures and microstructures

Isochronal Annealing

Initially the as-cast and heat treated material (24 hrs at 1173 K, followed by furnace cooling) which was rolled at 1173 K to 80% thickness reduction and then quenched, was subjected to heat treatment for 1 hr duration at temperatures ranging from 1073 K to 1293 K at about 50 K intervals. After completion of the treatments, the samples were water quenched again. X-ray diffraction (XRD), texture and microstructural characterisations were carried out on these specimens in order to have an overall idea of the effect of annealing on the stability of textures and microstructures of the hot rolled samples.

Isothermal Annealing

After determining the response of the samples to different annealing temperatures, the material was subjected to isothermal anneal at 1173 K for time durations ranging from 15 minutes to 12 hours. The starting materials in the present case were the same as the ones used for the isochronal anneal, that is, the as-cast and heat treated material which was rolled at 1173 K to 80% thickness reduction followed by water quenching. As in the previous case, the specimens were water quenched again after the heat treatments.

(ii) Heat treatments to study the effect of $\alpha_2 \rightarrow \beta \rightarrow \alpha_2$ phase transformation on textures and microstructures

The materials furnace cooled to room temperature from the as rolled conditions (only 80 % rolled sample) were treated as the starting material for this study. All the three

different types of microstructures, namely, Widmanstätten, equiaxed and heavily deformed, as obtained after rolling at 1373 K, 1293 K and 1173 K respectively, were subjected to heat treatments at 1373 K, 1293 K and 1173 K in order to examine the structural and microstructural stabilities for given periods of time. After the completion of the desired heat treatment, the furnace was switched off but the argon flow was continued till the temperature was brought down to room temperature.

The overall processing schedules as described above are shown schematically in Figs. 3.1 (a, b), Fig. 3.2 and Fig. 3.3.

3.3 Characterisation Techniques

The characterisation techniques used in the present investigation include microstructural characterisation, structural characterisation, characterisation of texture and mechanical testing. The experimental techniques employed for these characterisations are described in the subsequent sections.

3.3.1 Microstructural Characterisation

Optical Microscopy

The samples for optical microscopy were cold mounted and polished on emery papers (0 to 4 grades) followed by wet polishing with alumina powders of sizes 1 μm , 0.3 μm and 0.05 μm respectively. The polished samples were etched with Kroll's etchant (2% HF + 3% HNO₃ + 95% H₂O). Microstructural observations were carried out on the longitudinal section of the specimens using a LEITZ Metallux optical microscope.

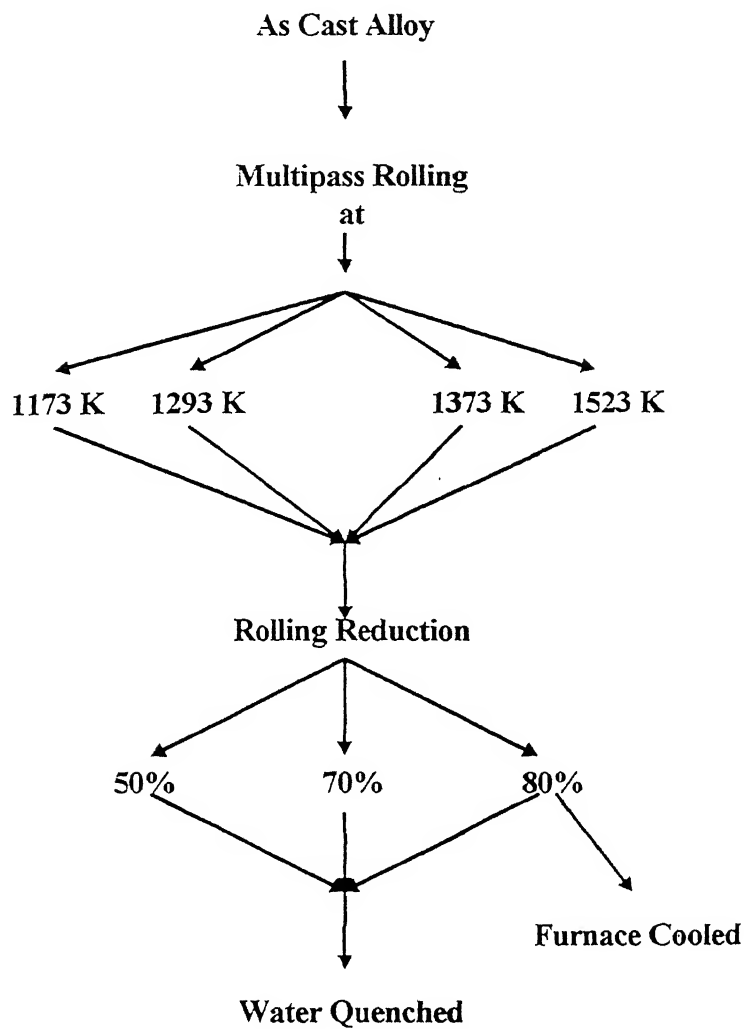


Fig 3.1(a) Flow chart depicting schedule I for thermomechanical processing

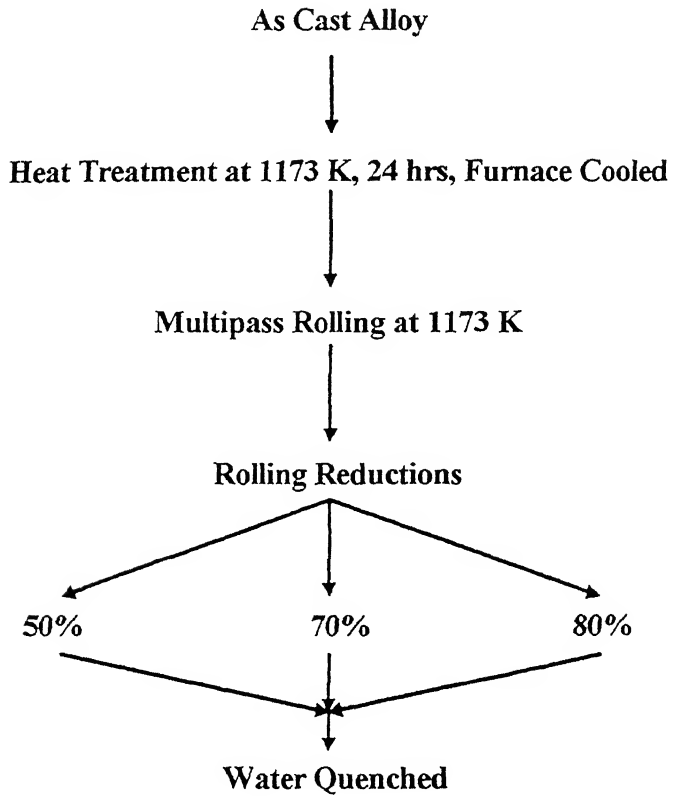


Fig 3.1(b) Flow chart depicting schedule II for thermomechanical processing

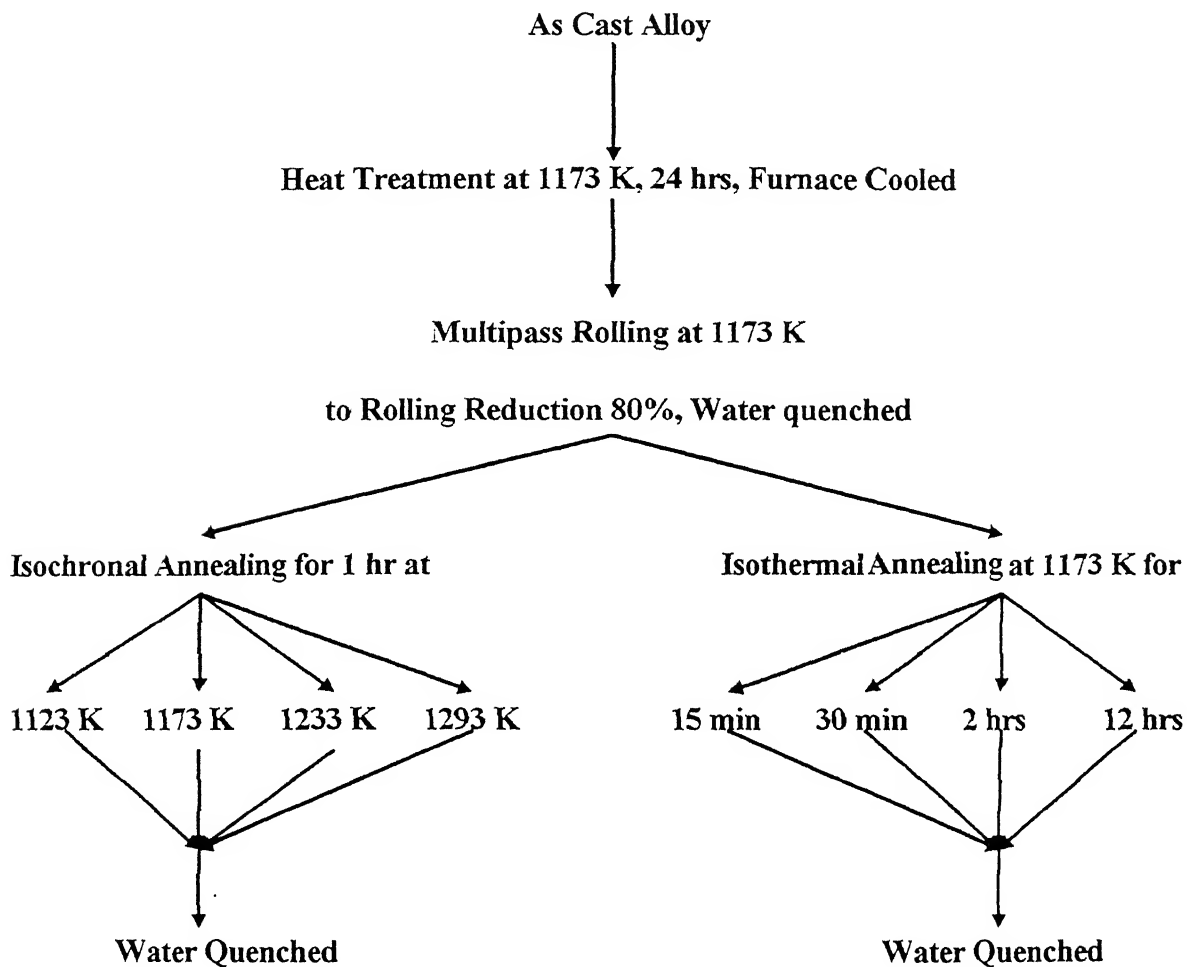


Fig 3.2 Flow chart showing the schedule for annealing studies

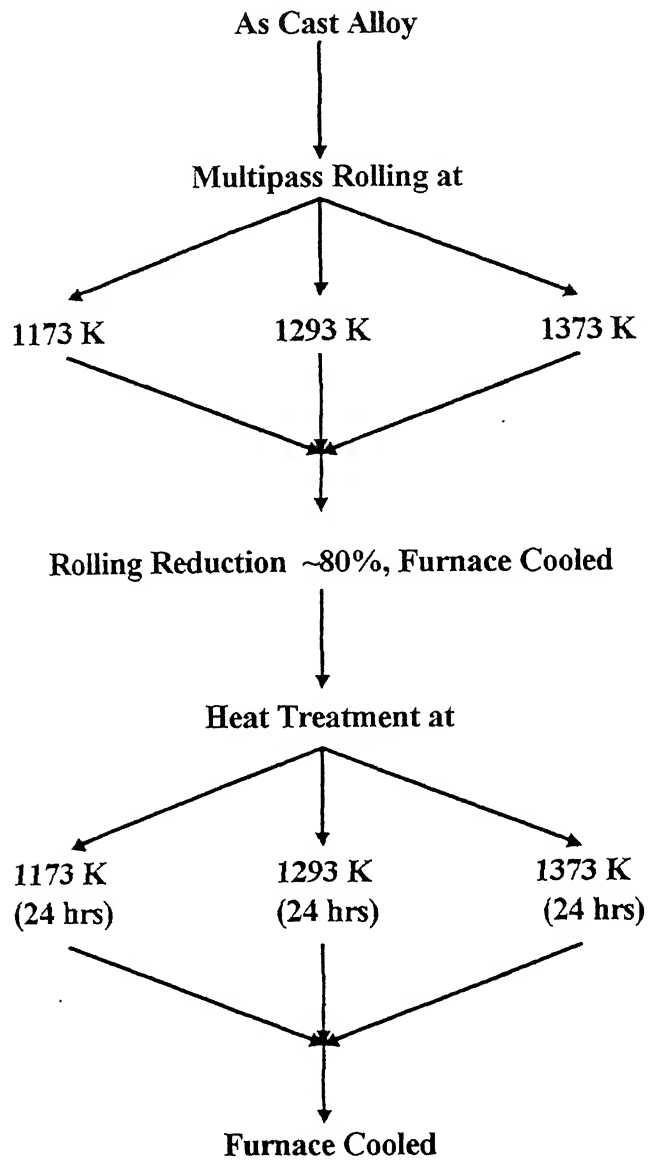


Fig 3.3 Flow chart showing the schedule of heat treatment for phase transformation

Quantitative metallography was carried out using *swift counting method*. For each of the samples measurements were done from nine microstructures.

Scanning Electron Microscopy

Most of the microstructural characterisation in the present investigation was carried out using a Scanning Electron Microscope (JEOL-JSM 840 A). For this purpose, the samples were first polished and then electropolished in the usual manner. The electrolyte consisted of a 6% perchloric acid solution in methanol. The solution was kept at a temperature 223 K. Etchant was carefully avoided to prevent the formation of any artifact, if any. The polished samples were seen under the SEM operated at 25 kV using mainly the back scattered electron (BSE) mode.

Transmission Electron Microscopy

In order to examine the finer microstructural features, selected number of specimens were subjected to transmission electron microscopy. For this purpose, thin foils were prepared from the rolling plane as well as the longitudinal sections of the specimens. Foil preparation involved mechanical thinning to a thickness of $\sim 10\ \mu\text{m}$, punching of 3 mm discs and finally electrolytic jet polishing leading to sufficient transparent area in the discs. Jet polishing was carried out in a FISHIONE Twin Jet Polisher using the electrolyte consisting of 30 ml perchloric acid, 175 ml n-butanol and 300 ml methanol maintained at a temperature of 248 K. The foils were examined under a JEM 2000FXII JEOL Transmission Microscope operated at an accelerating voltage of 160 kV. A few of the

thin foils were also examined under a PHILIPS EM300 Transmission Electron Microscope operated at 300 kV.

3.3.2 X-Ray Characterisation

All the as-processed samples, including the starting material, were subjected to extensive x-ray examination using normal Bragg Scan. XRD profiles were recorded from polished surfaces of the specimens using a SEIFERT ISO-DEBYEFLEX 2002 X-ray Diffractometer operated at 30 kV with CuK_α radiation. A few samples were subjected to continuous rapid scanning within the range (2θ) of 20° - 100° , while others were subjected to slow scanning near and at the peak positions. The measurement parameters are as follows :

Rapid Scanning	Voltage	30 kV
	Current	20 mA
	Scanning Speed	$3^\circ / \text{min}$ (in 2θ)
	Chart Speed	3 cm / min
	Time Constant	10 sec
	Counts per minute	5 K

Slow Scanning	Voltage	30 kV
	Current	20 mA
	Scanning Speed	$0.3^\circ / \text{min}$ (in 2θ)
	Chart Speed	0.6 cm / min
	Time Constant	10 sec
	Counts per minute	5 K

In order to have consistency, all the experiments were performed using a fixed beam dimension. To avoid the instrumental error, the diffractometer was initially calibrated with a standard silicon single crystal specimen.

3.3.3 Characterisation of Texture

For a cubic material, the crystallographic texture of a rolled polycrystalline sheet is usually represented as $\{hkl\} \langle uvw \rangle$, where $\{hkl\}$ set of planes of the crystals are parallel to the rolling plane and $\langle uvw \rangle$ set of directions are along the rolling direction. The texture of a particular specimen may also consist of a number of components. Texture data from a specimen are generally represented with the help of pole figures [98]. A pole figure actually contains all the information regarding the texture components of a particular material. However, the information given by pole figures is qualitative or at best semi quantitative in nature. A much more comprehensive and quantitative description of texture can be given with the aid of *Orientation Distribution Function* (ODF) technique.

An ODF actually describes the frequency of occurrence of orientations in the three dimensional (*Euler*) orientation space. The *Euler space* can be defined by three *Euler angles* ϕ_1 , ϕ and ϕ_2 . These angles constitute a set of three consecutive rotations which transform the sample frame S to crystallite frame C, as shown in the Fig. 3.4 [99]. From the figure, it is readily understood that a particular texture component $\{hkl\} \langle uvw \rangle$ can be completely represented by a point (ϕ_1, ϕ, ϕ_2) in the *Euler space*. Quite naturally, each component of texture has a distinct position in the orientation space. As a result, a

quantitative analysis of texture is possible, with a much better resolution. Fig. 3.5 shows the schematic diagram of the *Euler space* [100]. Mathematical methods are available for calculating ODF from several experimentally determined pole figures. The most widely accepted methods are those proposed independently by Bunge [101] and Roe [102], who used generalised spherical harmonic functions to represent the orientation distributions. A thorough mathematical treatment of the ODF can be found in the texts by Bunge [103, 104]. The *Bunge notation* [101] is the more common and this has been used throughout in the present investigation unless otherwise stated. For the cubic crystal symmetry, the orientation space is defined by three orthogonal axes ϕ_1 , ϕ and ϕ_2 , each ranging from 0° to 90° . This total volume is divided into three basic ranges in which each orientation appears only once. The value of the orientation density at each point is the intensity of that orientation in multiples of the random.

The maxima of the pole density variations can be described as single peaks or fibres [105]. In case of peak type texture, the maxima can be described by assuming a crystallographic plane (hkl) perpendicular to the normal direction ND and a crystallographic zone axis [uvw] parallel to the rolling direction RD. The fibre types are defined by an orientation rotated around a given axis with the intensity along the fibre being constant.

Texture in a rolled polycrystalline hexagonal material is represented as $\{hkil\}\langle uvw \rangle$, where $\{hkil\}$ is the crystallographic plane of the grains which lie parallel to the rolling plane, and $\langle uvw \rangle$ the direction that lies parallel to the rolling direction. The orientation space for an h.c.p. material extends over $\phi_1 = 0^\circ$ to 90° , $\phi = 0^\circ$ to 90° and $\phi_2 =$

0° to 60° . Although in the present work, the orientation distribution functions have been plotted for all the ϕ_2 sections at 6° intervals, however, the analysis has been carried out mainly using the $\phi_2 = 0^\circ$ and 30° sections as most of the important orientations appear in these two sections. Contrary to the cubic case, the representation of the hexagonal texture components depends upon the c/a ratio of the material. The major orientations appearing in the above two ϕ_2 sections, as calculated for titanium ($c/a=1.601$), are shown in Fig. 3.6.

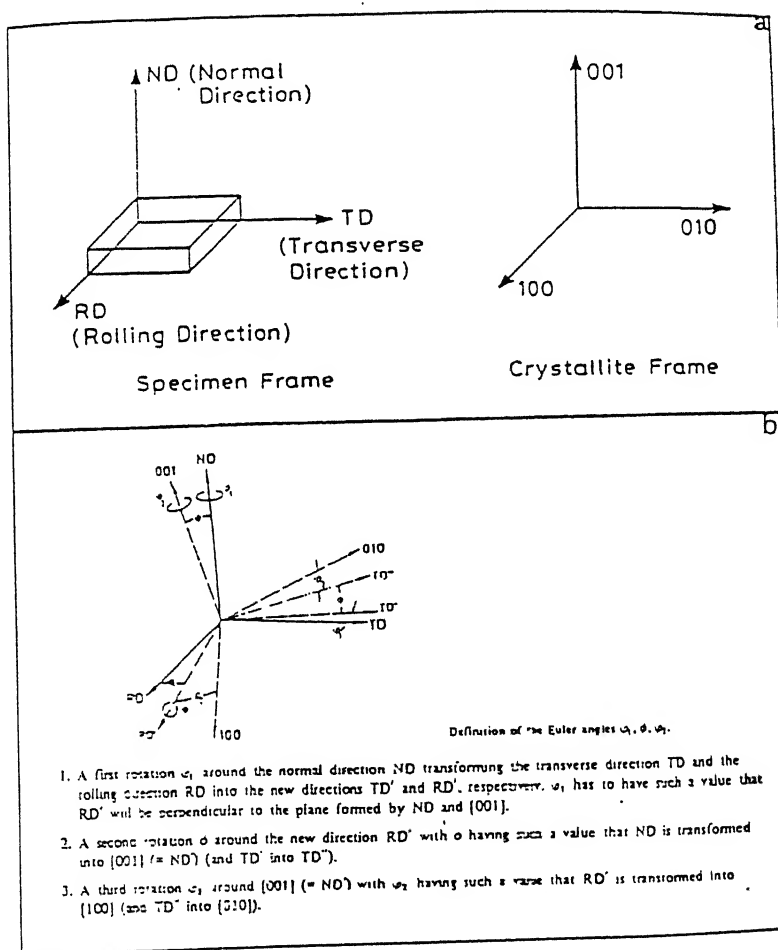


Fig. 3.5

Schematic representation of three Euler angles ϕ_1 , ϕ , ϕ_2 ; (a) Specimen frame S and crystalline frame C, (b) Transformation of specimen frame into crystalline frame [99]

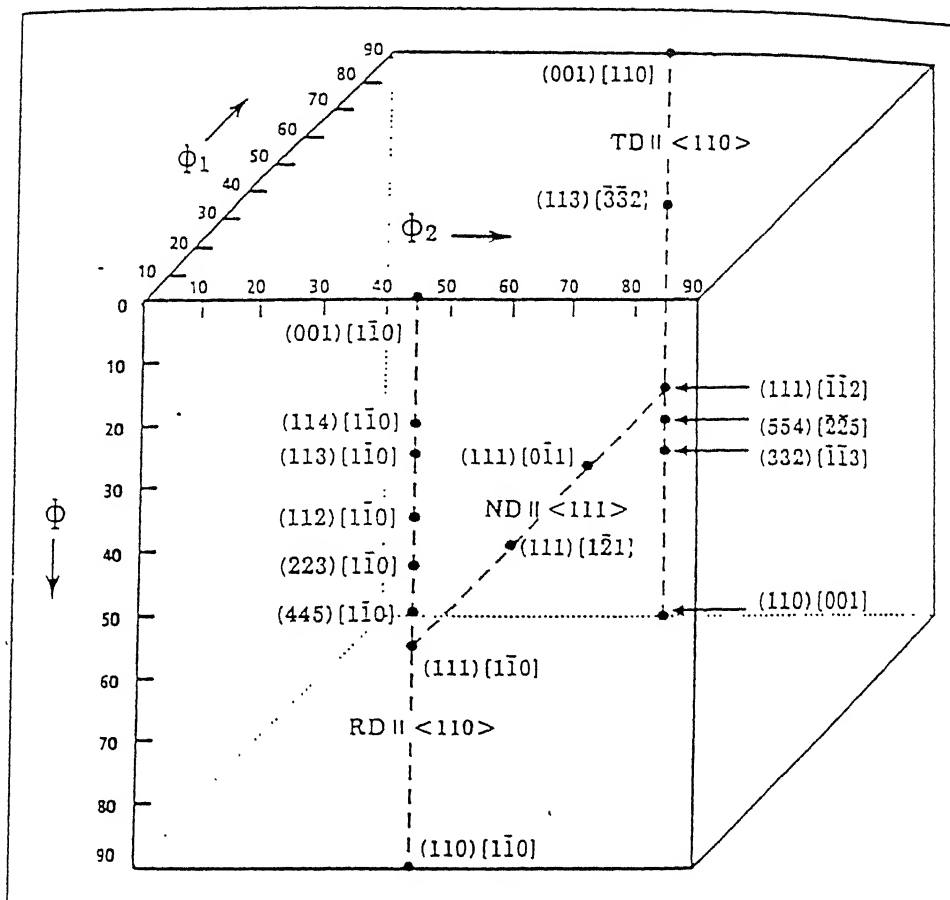


Fig.3.5 Schematic presentation of *Euler Space* [100]

In order to calculate the ODFs of the hexagonal α_2 phase, data obtained from the measurement of six pole figures, namely, $(20\bar{2}0)$, (0002) , $(20\bar{2}1)$, $(20\bar{2}2)$, $(22\bar{4}0)$, $(20\bar{2}3)$ were employed. Out of these, the pole figure (0002) was computed from the data obtained from the other five measured pole figures. This was done to avoid the possibility of error in measurement, which is likely to be caused by the overlap of the (110) peak of the β phase with the (0002) peak of α_2 . The series expansion was carried out upto l_{\max}

=30. The ODFs from the b.c.c. β phase were plotted from the data of four pole figures, namely (200), (211), (220) and (222). In this case the ODFs were computed upto $l_{\max}=22$.

In all the ODF computations, positivity corrections were employed. All the measured pole figures were recorded from the mid-thickness section parallel to the rolling plane of all the specimens. A SEIMENS CRYSTALLOFLEX D-5000 texture goniometer with Mo k_{α} radiation was used for this purpose.

3.3.4 Hardness Testing

Vickers' Hardness measurement was carried out on the longitudinal sections of a few of the as-rolled specimens using a SHIMADZU Hardness Tester. The dimensions of the indentations were measured with the help of microscope attached to it. Minimum 10 indentations were taken from each sample for calculating the average value in terms of Vickers' Hardness Number (VHN).

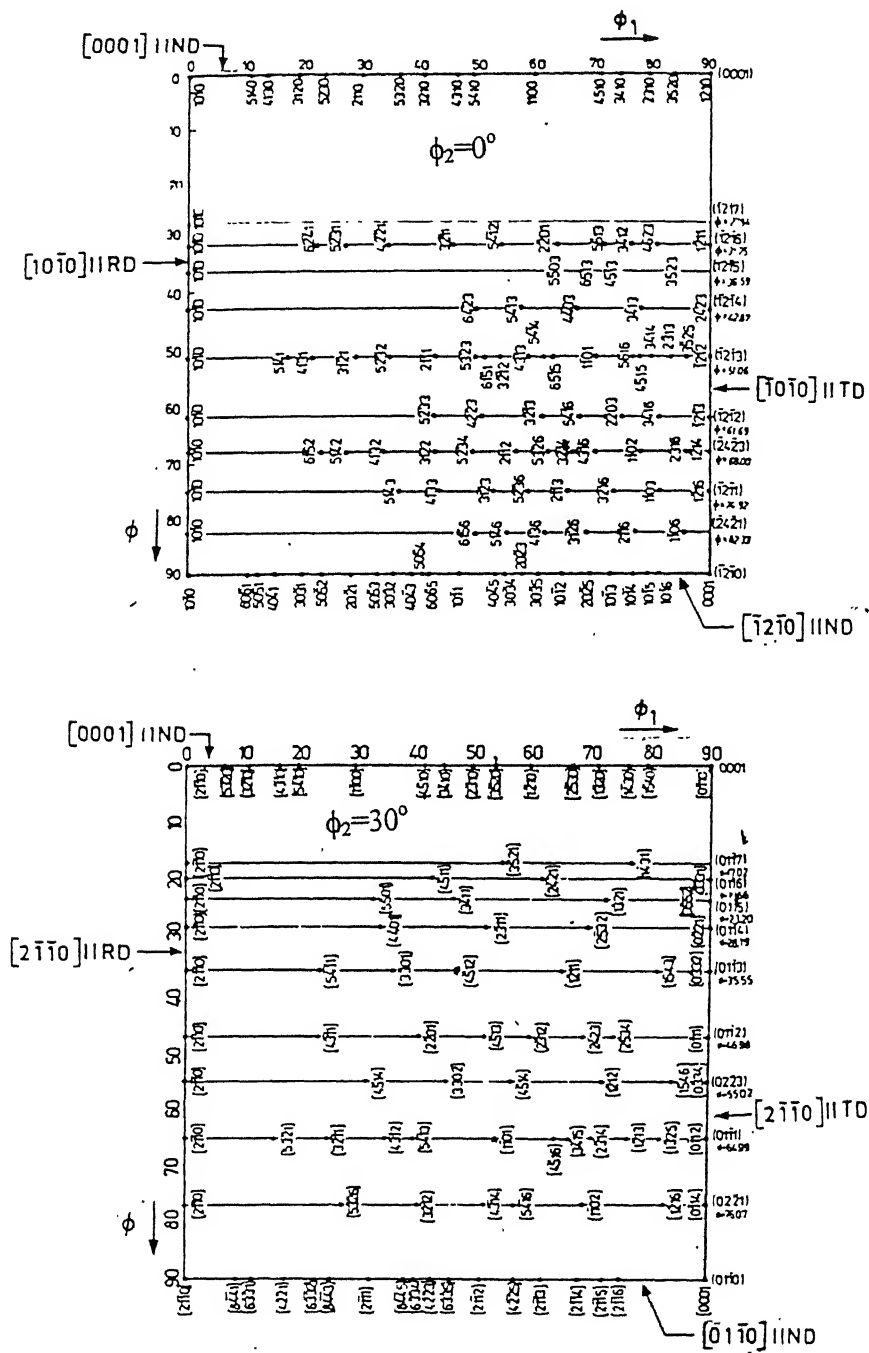


Fig. 3.6

Charts of positions of texture components in the Eulerian space for $\phi_2=0^\circ$ and $\phi_2=30^\circ$ sections [106]

Evolution of Texture and Microstructure during Hot Rolling

As discussed in chapter 1, Ti-24Al-11Nb intermetallic alloy generally consists of two phases namely, α_2 and β or B2. For reference, the $\text{Ti}_3\text{Al-Nb}$ pseudo binary phase diagram [4] is shown in Fig. 2.2. It is clear from this diagram that in the $\text{Ti}_3\text{Al-Nb}$ alloy, the volume fraction of α_2 decreases with increasing temperature and above the β -transus temperature, the α_2 phase gets fully transformed into β . The volume fraction of α_2 and β phases are expected to be roughly equal at ~ 1293 K. Below this temperature the volume fraction of α_2 increases and as indicated by the steep slope of the α_2 solvus line in the $\text{Ti}_3\text{Al-Nb}$ phase diagram, it gets stabilised at the maximum value of $\sim 85\%$ at 1173 K. Hot rolling of the alloy at different temperatures below the β -transus temperature, therefore, involves the deformation processing of different mixtures of α_2 and β phases. The plastic properties as well as the recrystallisation behaviour of the α_2 and β phases are reported to be different at different temperatures and strains [4]. Due to all these aforesaid reasons, the hot deformation behaviour of $\text{Ti}_3\text{Al-Nb}$ alloy is expected to vary with temperature in the $(\alpha_2+\beta)$ phase field in a complex manner.

Thermomechanical processing of the alloy is, therefore, expected to produce a variety of microstructures and textures, depending on the temperature of processing and the amount of deformation as well as the cooling rate from the deformation

temperature. The results of the present investigation on the evolution of texture and microstructure during hot rolling of the experimental $\text{Ti}_3\text{Al-Nb}$ alloy are described in the following sections.

4.1 Microstructure

The microstructure of the as-cast material, shown in Fig. 4.1 (a), consists of coarse $\beta(\text{B2})$ grains. The internal structure of $\beta(\text{B2})$ grains consists of Widmanstätten and coarse α_2 . A quantitative determination of volume fractions of the constituting phases reveals that the α_2 and $\beta(\text{B2})$ phases occupy nearly 70% and 30% respectively in the microstructure.

Since the as-cast structure of the alloy comprised of non-equilibrium volume fractions of the two phases, the cast alloy was given a heat treatment at 1173 K for 24 hours followed by furnace cooling. The microstructure of the heat treated material is shown in Fig. 4.1 (b). The phase fractions determined for this material showed the near attainment of equilibrium volume fractions, namely, ~85% of α_2 and ~15% of the β phase, within the limits of accuracy of the quantitative metallographic method employed (Table 4.1).

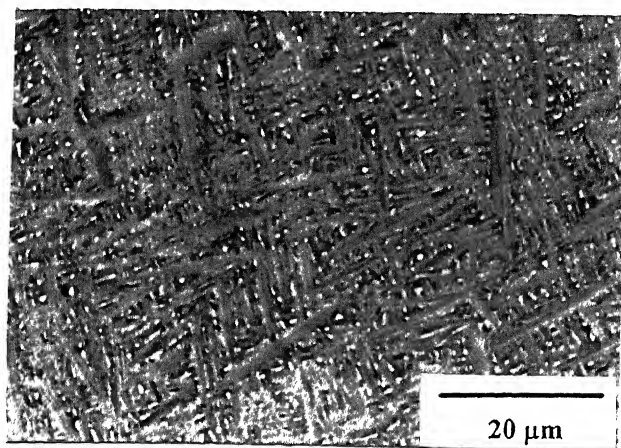


Fig. 4.1 (a) Microstructure for the as-cast material

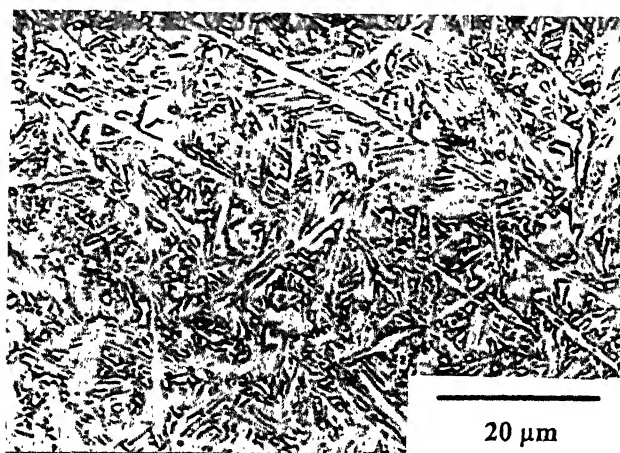


Fig. 4.1 (b) Microstructure for the heat treated material

Table 4.1 Phase fractions after different processing conditions as determined by quantitative metallography

Sample	Vol. Fraction (%) α_2	Vol. Fraction (%) β
As-cast	69.9	30.1
Heat Treated (HT)	84.6	15.4
Rolled at 1173 K (50 %), WQ	71.8	28.2
Rolled at 1173 K (70 %), WQ	69.0	31.0
Rolled at 1173 K (80 %), WQ	72.9	27.1
Rolled at 1293 K (50 %), WQ	53.8	46.2
Rolled at 1293 K (70 %), WQ	54.7	45.3
Rolled at 1293 K (80 %), WQ	46.6	53.4
HT and Rolled at 1173 K (50%), WQ	82.0	18.0
HT and Rolled at 1173 K (70%), WQ	81.8	18.2
HT and Rolled at 1173 K (80%), WQ	80.3	19.7

4.1.1 Rolling of the as-cast and heat treated material at 1173K

Hot rolling of the as-cast material at 1173 K produces significant microstructural changes as a function of the amount of deformation imparted (Figs. 4.2 a-c). It is apparent from these microstructures that a rolling reduction of 50% leads to the rotation of α_2 platelets in order to bring them along the rolling direction. Further

reductions cause fragmentation of these platelets and the distribution of α_2 phase becomes bimodal. An overall reduction of 70%-80% produces a drastic refinement of the microstructure resulting in submicron grain size. In addition, deformation bands, which are characteristic of heavy deformation, also appear in the microstructure. The TEM micrographs of the 50% deformed material (Fig. 4.3 a) shows a typical cell-structure. Sometimes, small areas showing signs of recovery are also seen (Fig. 4.3 b). The TEM micrograph from the rolling plane section of 80% rolled specimen sometimes reveals the presence of microbands (Fig. 4.4 a). At some places subgrain formation processes are also noticed indicating the onset of recovery processes (Fig. 4.4 b). In all the above cases, the samples were water quenched to room temperature after hot rolling.

When the specimens are furnace cooled to room temperature after hot rolling, the volume fraction of α_2 phase increases and more or less gets stabilised to the equilibrium volume fraction at that temperature. However, the signs of deformation are still very much present (Fig. 4.5 a). The TEM micrographs from the samples hot rolled 50% at 1173 K, followed by furnace cooling show features corresponding to both highly deformed (Fig. 4.6 a), as well as and partially recovered (Fig. 4.6 b) regions. The TEM micrographs from the 70% rolled and furnace cooled sample also show signs of heavy deformation in the α_2 phase (Fig. 4.7 a), and extensive recovery at places (Fig. 4.7 b). The TEM micrographs for both these above cases are taken from the longitudinal sections of the rolled sheets. The relevant TEM micrographs from the rolling plane section of the 80% rolled sample (Fig. 4.8 a and b) exhibit

features characteristic of an advanced stage of recovery as well as the very early stage of recrystallisation. From the above it is quite apparent that furnace cooling leads to much more extensive static recovery followed by recrystallisation, as compared to water quenching.

A prior heat treatment at 1173 K for 24 hrs followed by furnace cooling results in the maximisation of the α_2 phase, as predicted by the phase diagram. Fig. 4.9 (a to c) show the microstructures of the heat treated material after rolling at 1173 K by 50%, 70% and 80% reductions respectively followed by water quenching. The volume fraction of the α_2 phase has been estimated to be ~85% in the heat treated material which is much higher than the volume fraction of α_2 (~70%) in the as-cast material. As revealed from the microstructures, increasing rolling reduction of this material from 50% to 80% leads to a gradual refinement of the microstructural features. The TEM micrograph (Fig. 4.10) of the 50% rolled material shows the beginning of cell formation. A high density of cells is observed after 80% deformation (Fig. 4.11 a). At this stage, some isolated regions also show the signs of recovery (Fig. 4.11 b).

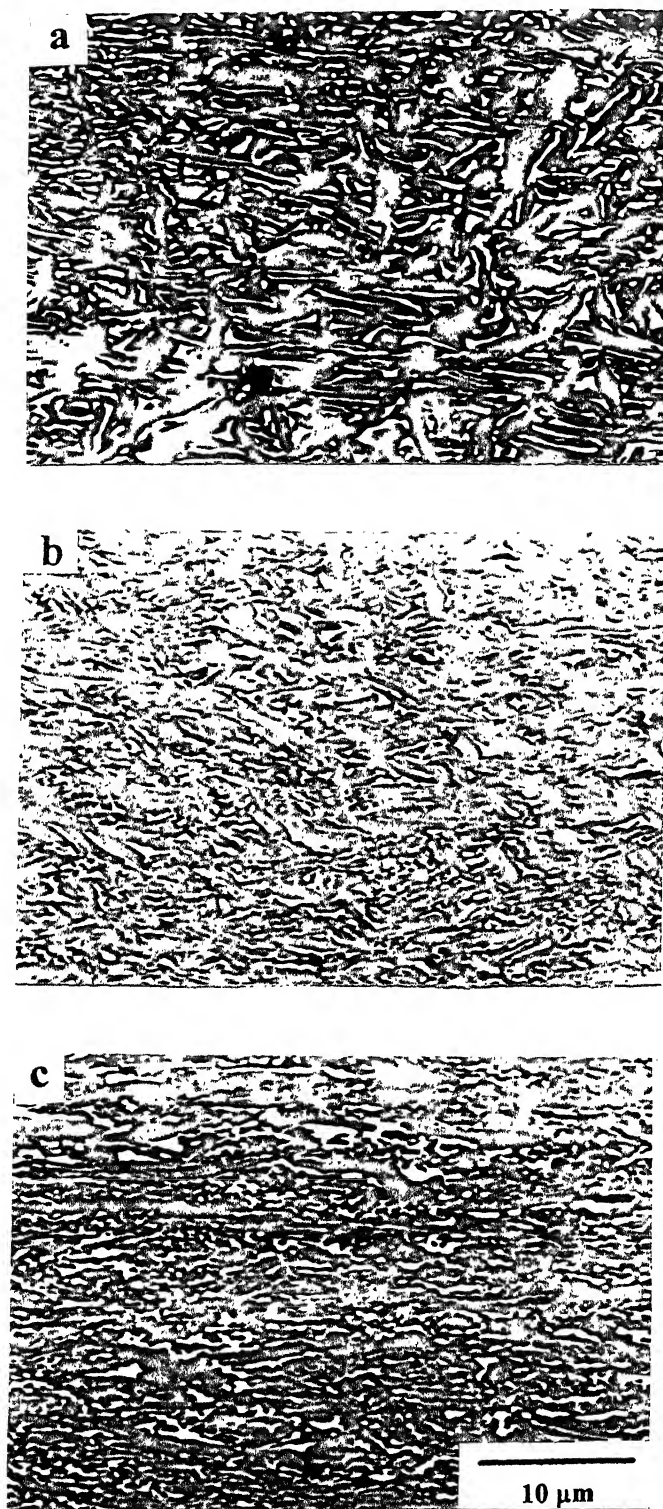


Fig. 4.2 Scanning Electron Micrograph of the materials rolled at 1173 K to (a) 50%, (b) 70% and (c) 80% from the as-cast state (all water quenched)

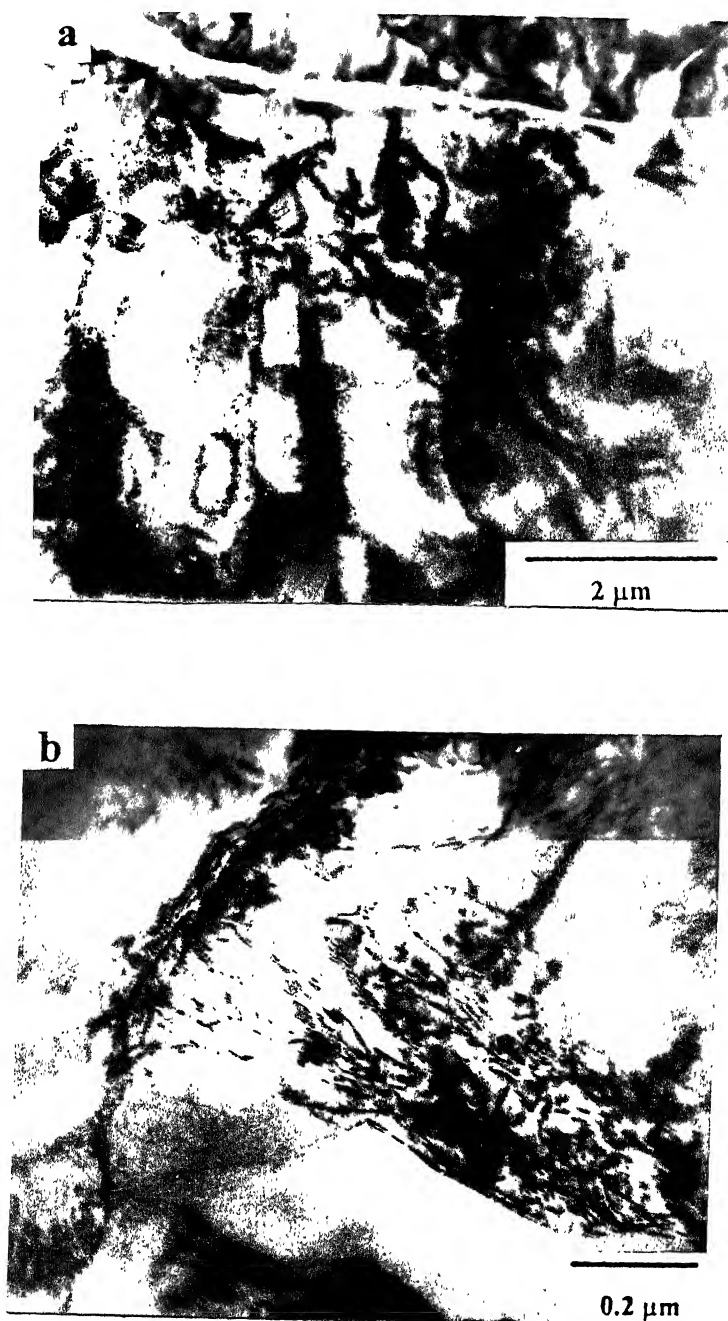


Fig. 4.3 Transmission Electron Micrographs from rolling plane section of the 1173 K rolled (water quenched) material upto 50% reduction showing (a) typical cell structure and (b) isolated recovered regions

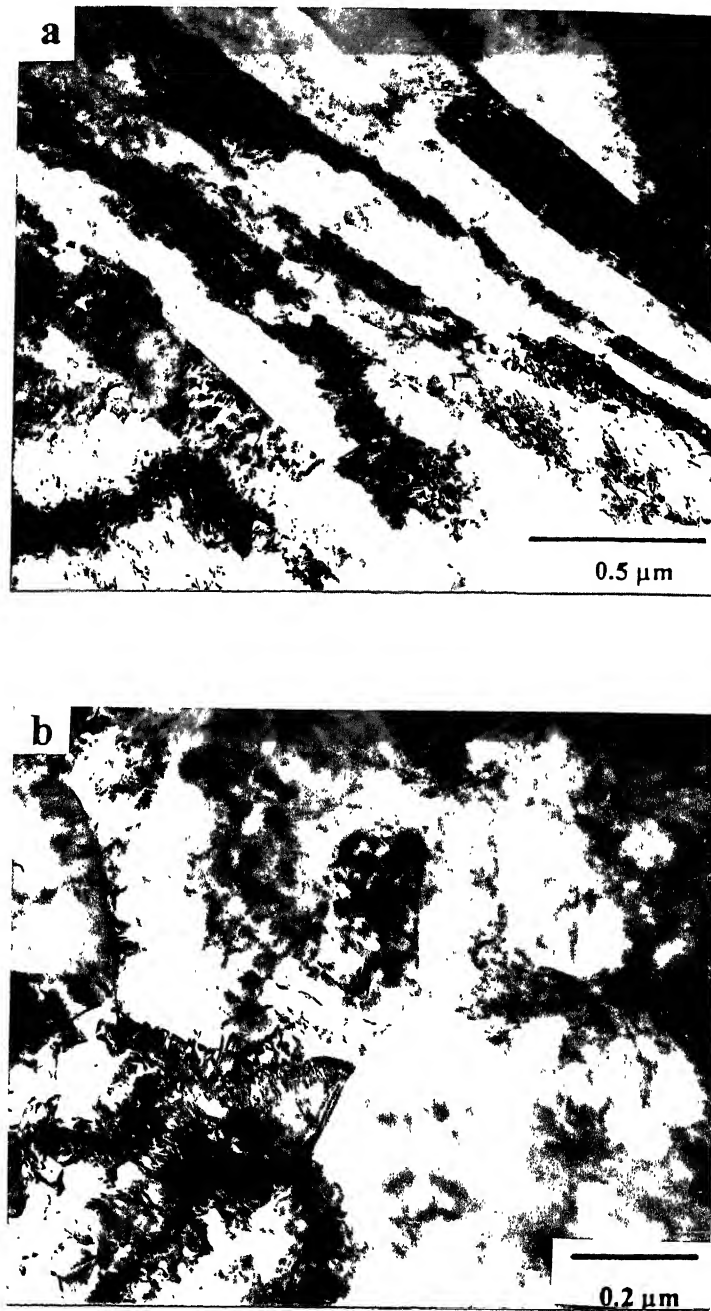


Fig. 4.4 Transmission Electron Micrographs from rolling plane section of the 1173 K rolled (water quenched) material upto 80% reduction showing (a) microbands (b) isolated regions of subgrain formation

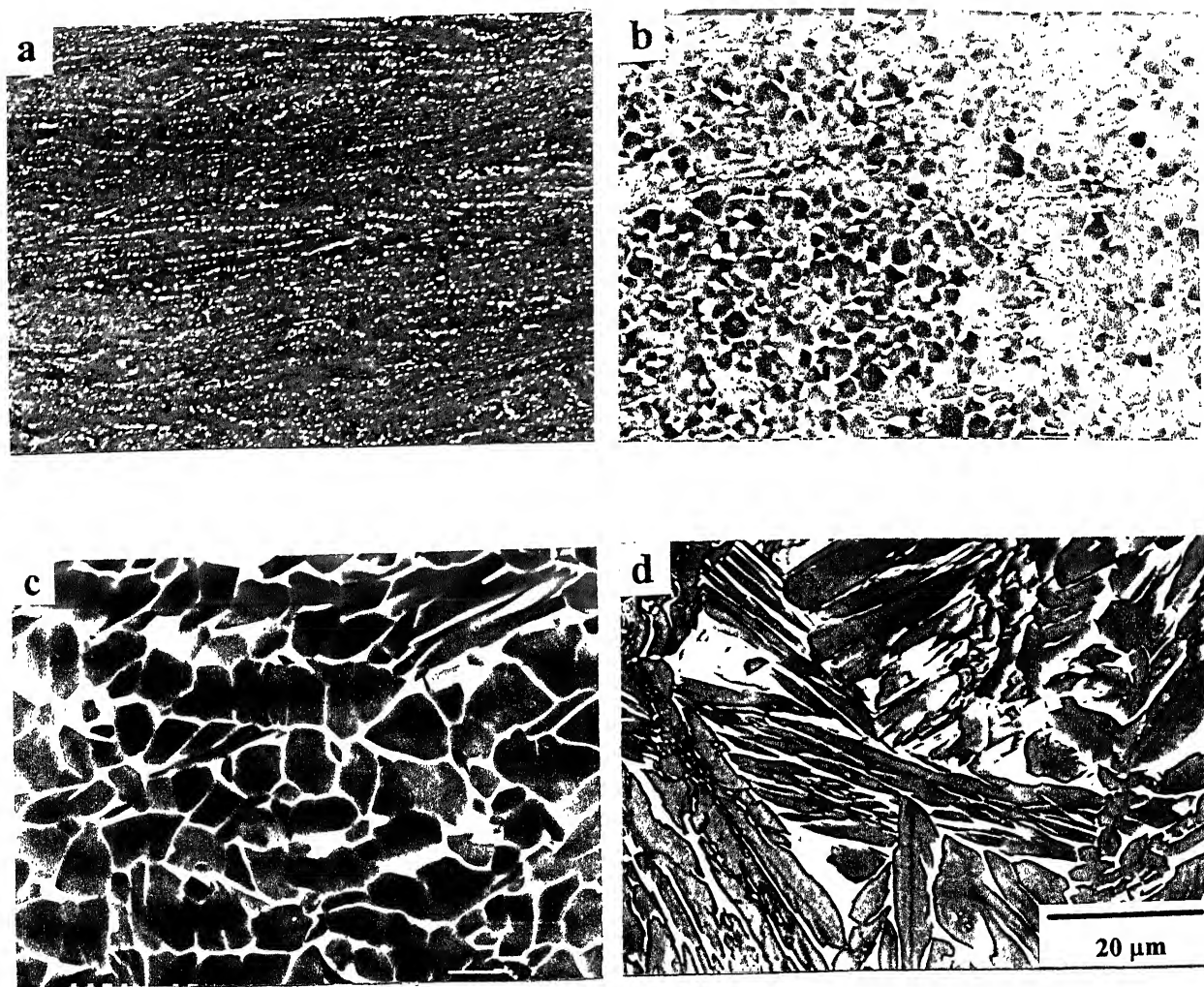


Fig. 4.5 SEM Micrographs of the as-cast material rolled to 80% reduction at (a) 1173 K, (b) 1293 K, (c) 1373 K and (d) 1523 K (all furnace cooled)

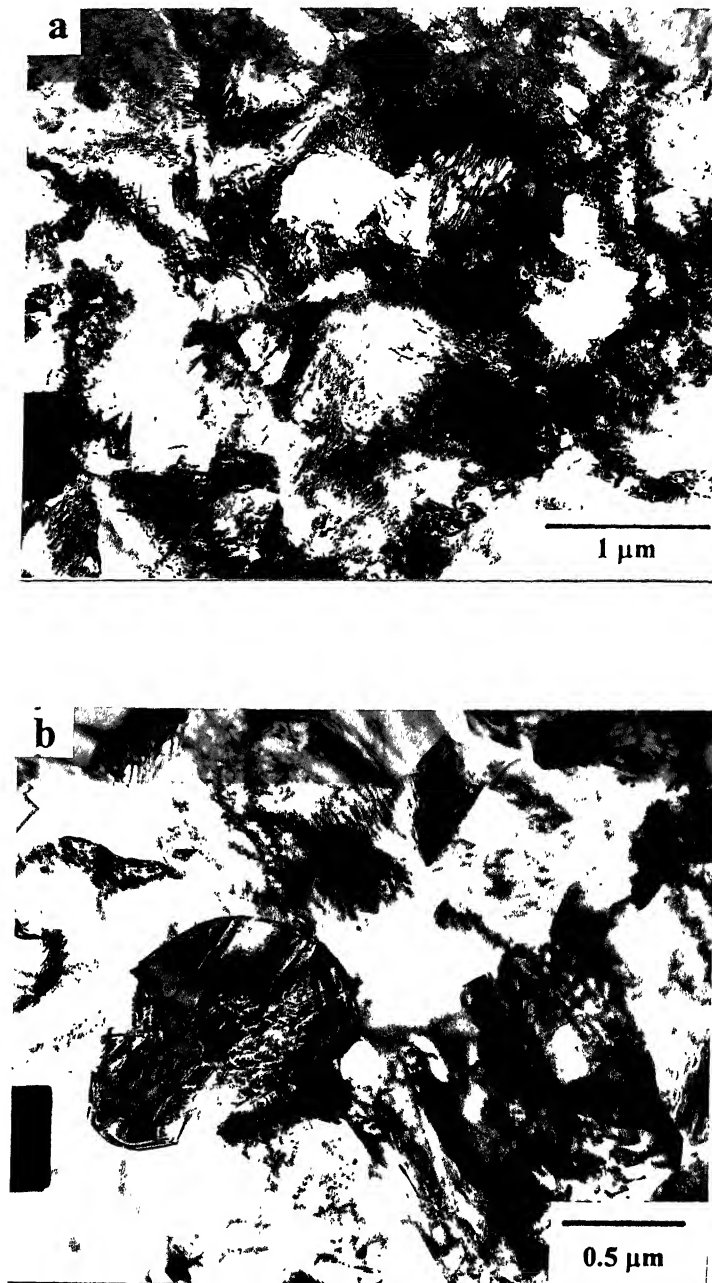


Fig. 4.6 TEM Micrographs from the longitudinal section of the specimen rolled at 1173 K (furnace cooled) to 50% reduction, showing (a) highly deformed state and (b) partially recovered regions

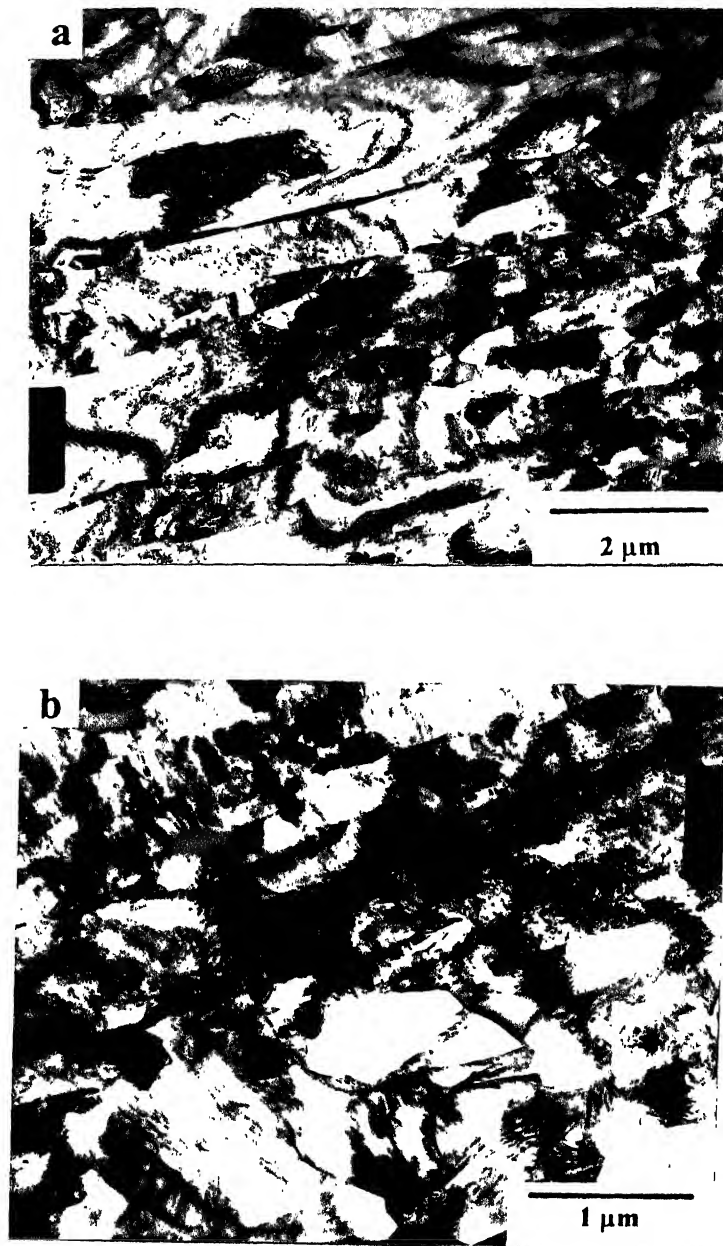


Fig. 4.7 TEM Micrographs from the longitudinal section of the specimen rolled at 1173 K (furnace cooled) to 70% reduction, showing (a) heavy deformation of α_2 and (b) extensively recovered regions

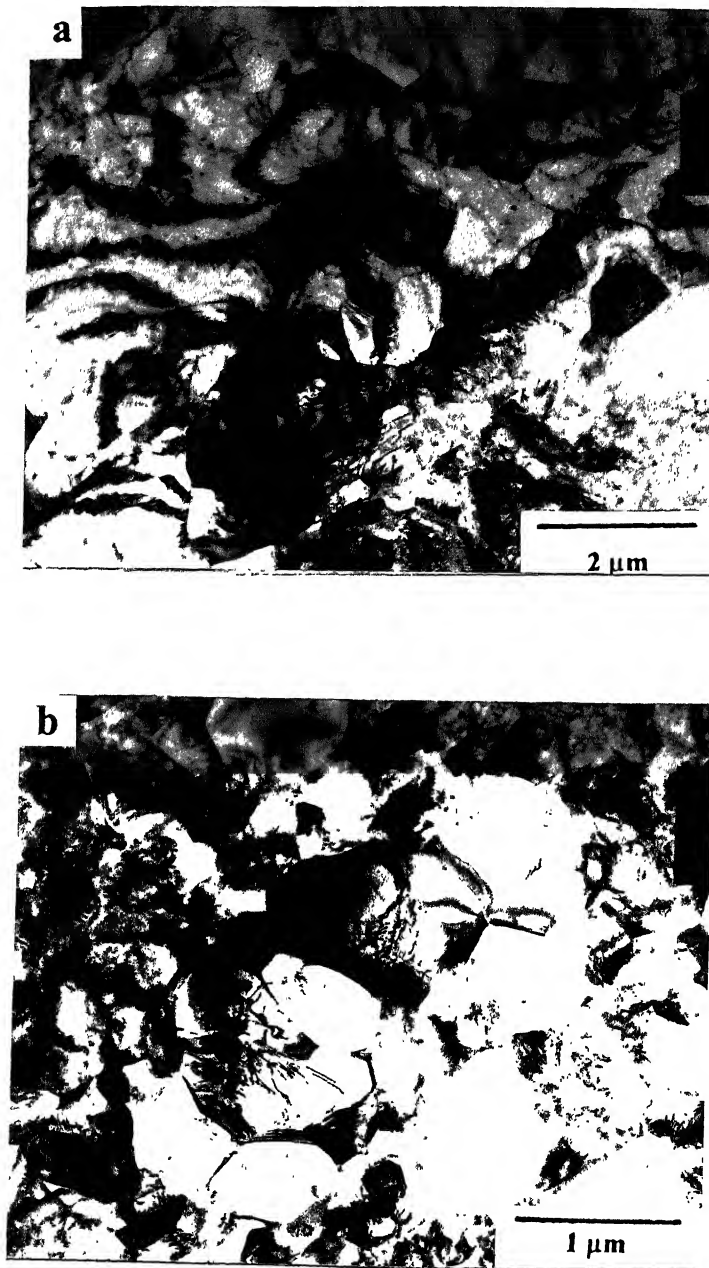


Fig. 4.8 TEM Micrographs from the rolling plane section of the specimen rolled at 1173 K (furnace cooled) to 80% reduction, showing (a) advanced stage of recovery and (b) early stage of recrystallisation

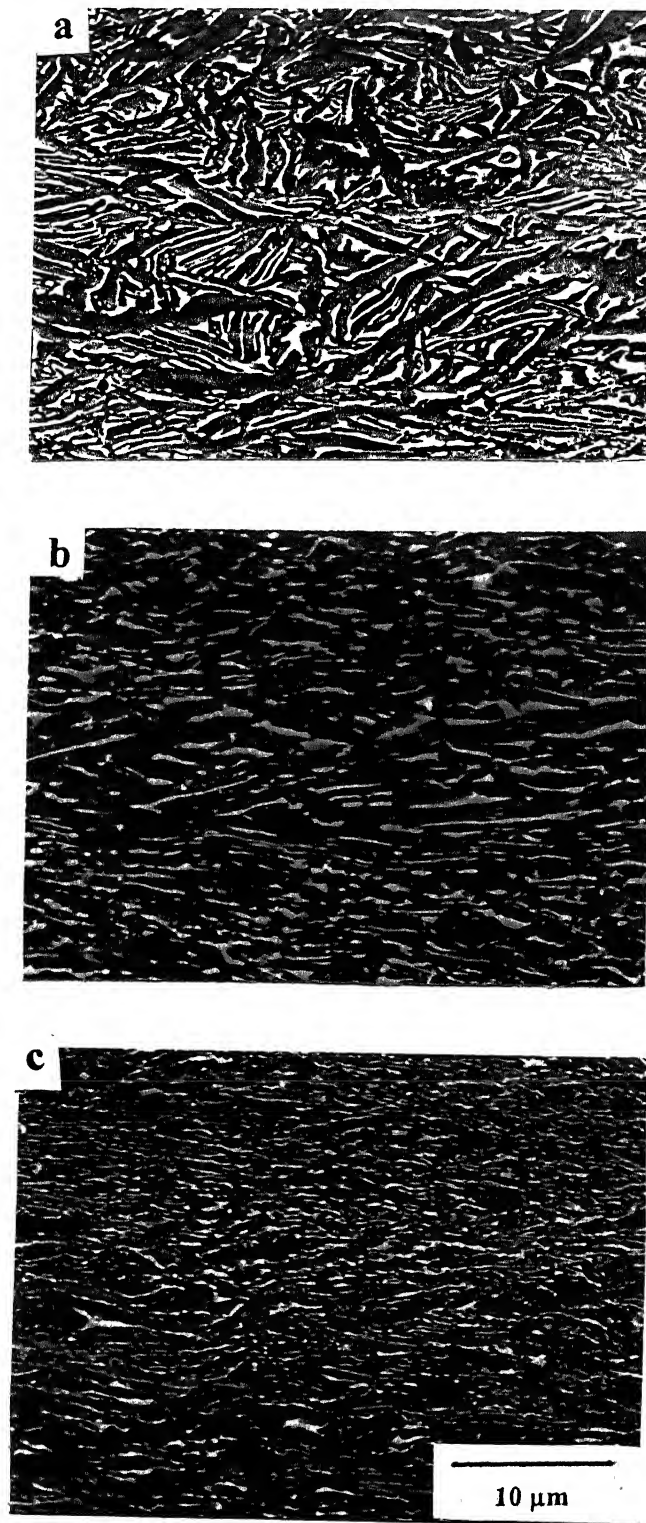


Fig. 4.9 SEM Micrographs of specimens heat treated at 1173 K (24 hrs, furnace cooled) and then rolled at 1173 K to (a) 50%, (b) 70% and (c) 80% reduction (all water quenched)

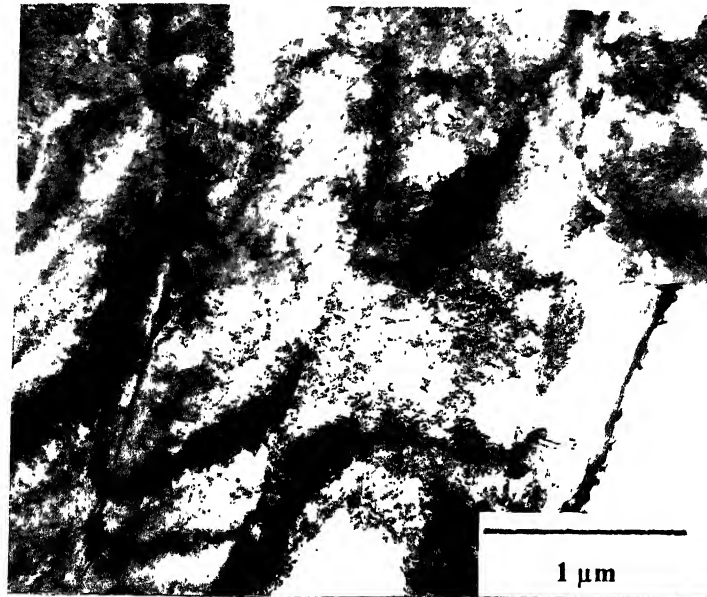


Fig. 4.10 TEM Micrograph from the rolling plane section of the material heat treated and 1173 K rolled (water quenched) upto 50% reduction showing the beginning of the cell formation

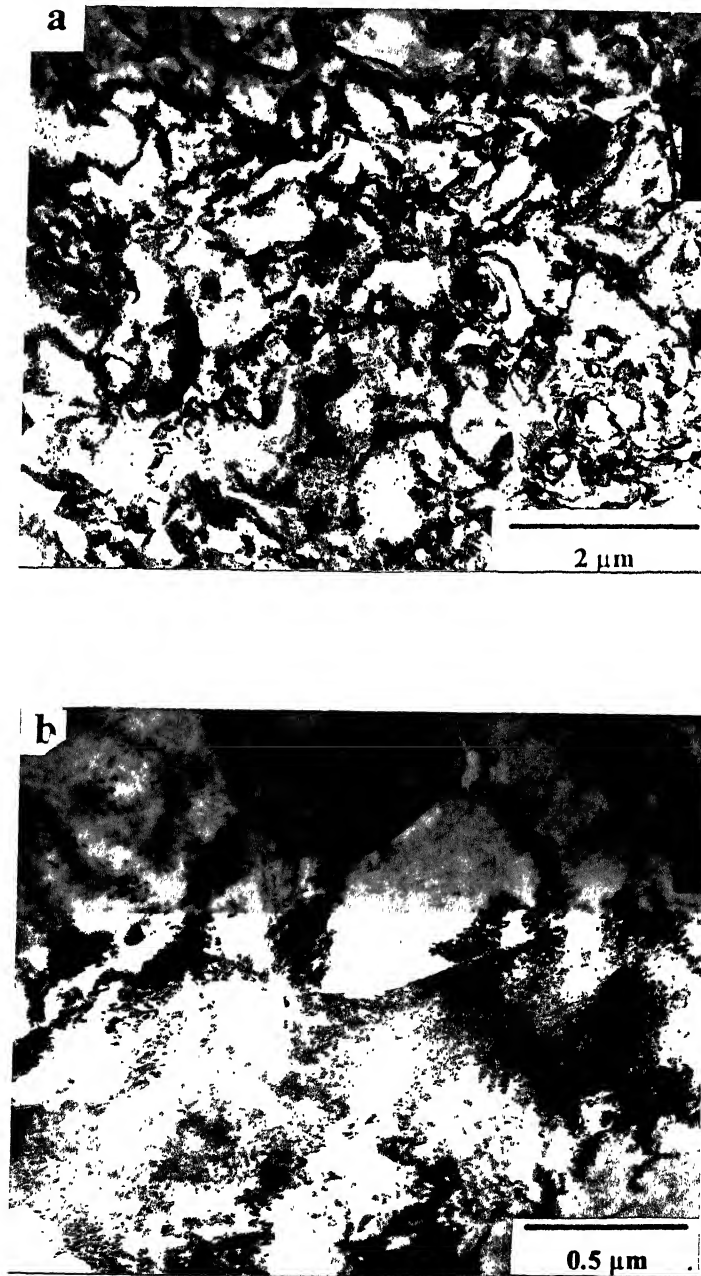


Fig. 4.11 TEM Micrographs from the rolling plane section of the material heat treated and 1173 K rolled (water quenched) upto 80% reduction showing (a) high density of cells and (b) isolated regions of recovery

4.1.2 Rolling of the as-cast material at 1293 K

Figs. 4.12 (a to c) show the scanning electron micrographs taken from samples rolled at 1293 K by 50%, 70% and 80% rolling reductions. At lower degree of deformation, say 50%, the α_2 platelets rotate to some extent towards the rolling direction. With the increase in the amount of deformation, the grain morphology as well as the volume fraction of the constituting phases undergo a gradual change. The α_2 grains are found to have a tendency to acquire an equiaxed morphology; the process however, remains incomplete. The volume fraction of β phase increases with deformation as a result of the availability of larger α_2/β grain boundary region available for the nucleation of β . After 80% rolling reduction, the volume fraction of β phase further increases and attains more or less the equilibrium volume fraction predicted by the phase diagram for this temperature. Another noticeable observation at this stage is the presence of long stringers of the α_2 phase. Presumably, after 80% deformation, some of the α_2 phase undergoes recrystallisation. The general structural features from a highly deformed region of the sample rolled 50% at 1293 K are shown in Fig. 4.13 (a and b). The selected area diffraction (SAD) pattern corresponding to the area in Fig. 4.13 (b) indicates a zone of the α_2 phase. The extent of recovery of the α_2 phase is more prominent in the TEM micrograph of the 80% rolled material (Fig. 4.14 a). While the α_2 undergoes extensive recovery, the β phase exhibits signs of heavy deformation (Fig. 4.14 b).

The microstructure of the specimen furnace cooled from this condition (80% rolling deformation at 1293 K) shows a completely equiaxed kind of morphology for α_2 with β phase present at the triple point of the grains (Fig. 4.5 b). The α_2 phase appears to be in a very advanced stage of recovery and there are signs of recrystallisation of α_2 at many places. This is possibly due to the sample remaining at temperatures above 1173 K for substantially longer periods of time during the process of slow cooling. A series of TEM micrographs taken from thin foils of this specimen (Figs. 4.15 a-d) depict the microstructural features of α_2 at this stage. Fig. 4.15 (a) indicates the onset of recovery, while Fig. 4.15 (b) shows an aggregate of small subgrains coalescing to form a bigger grain that has developed a sharp boundary with the adjacent cold worked and recovered regions. Figs. 4.15 (c and d) show well delineated recrystallised grains. The β phase at this stage, shows the signs of recovery (Fig. 4.16 a). At the same time, some secondary α_2 platelets also appear within the recovering β (Fig. 4.16 b).

The volume fractions of the α_2 and β phases in the as-processed materials after water quenching, as measured by quantitative metallographic method, are already presented in Table 4.1.

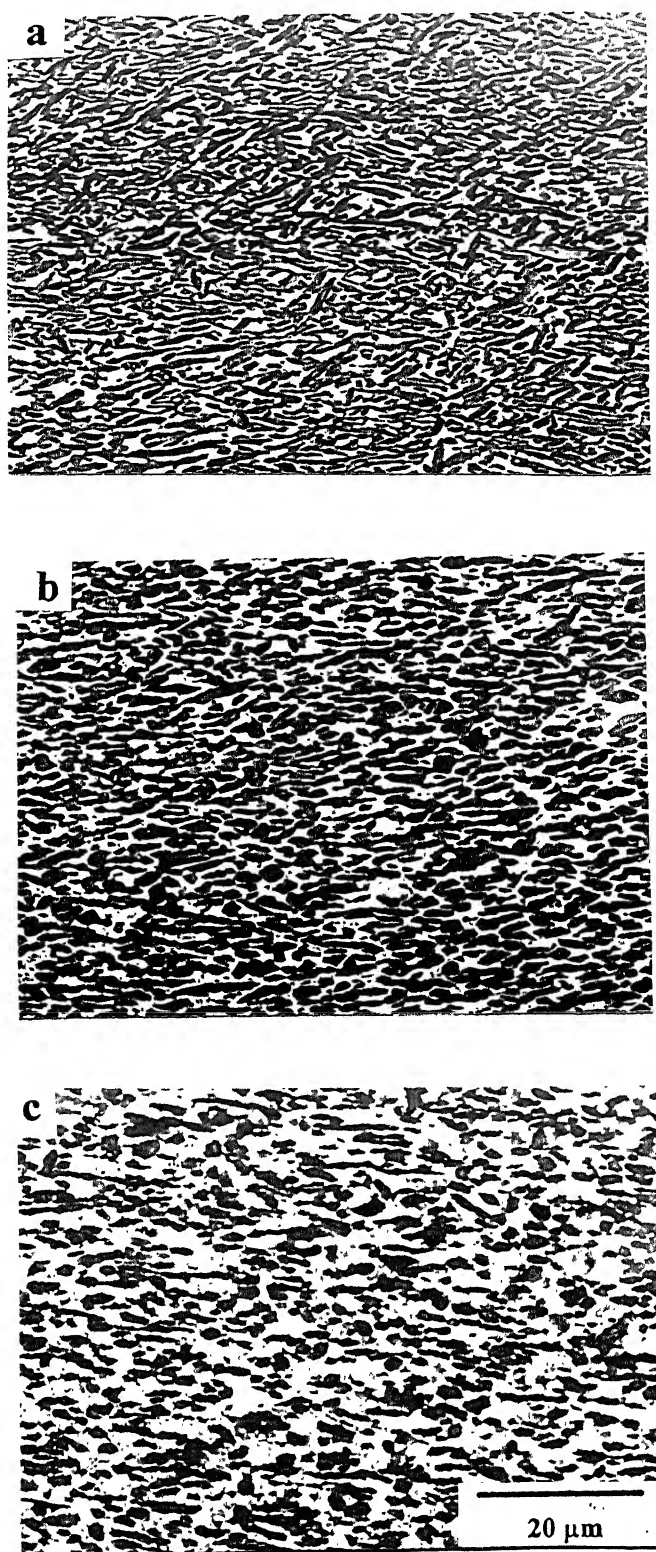


Fig. 4.12 SEM Micrographs from the specimens rolled at 1293 K from as-cast state to (a) 50%, (b) 70% and (c) 80% reductions (all water quenched)

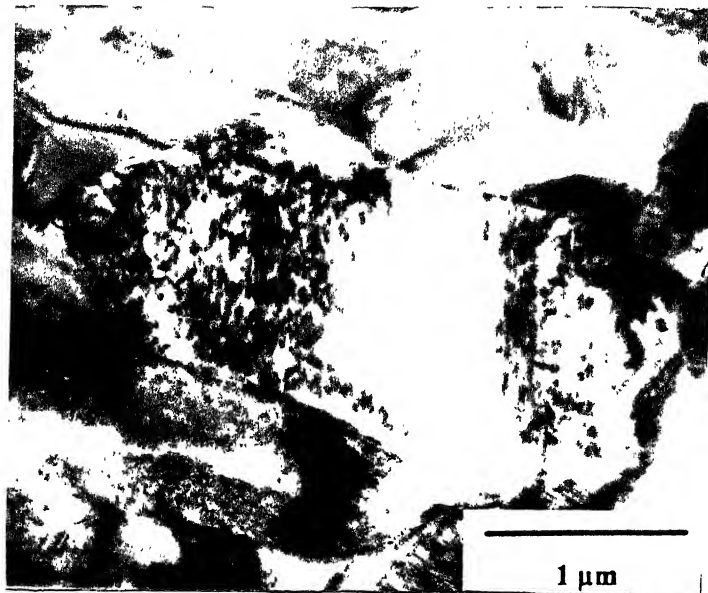


Fig. 4.13 TEM Micrographs from rolling plane section of the specimens rolled to 50% reduction at 1293 K (water quenched) showing highly deformed regions

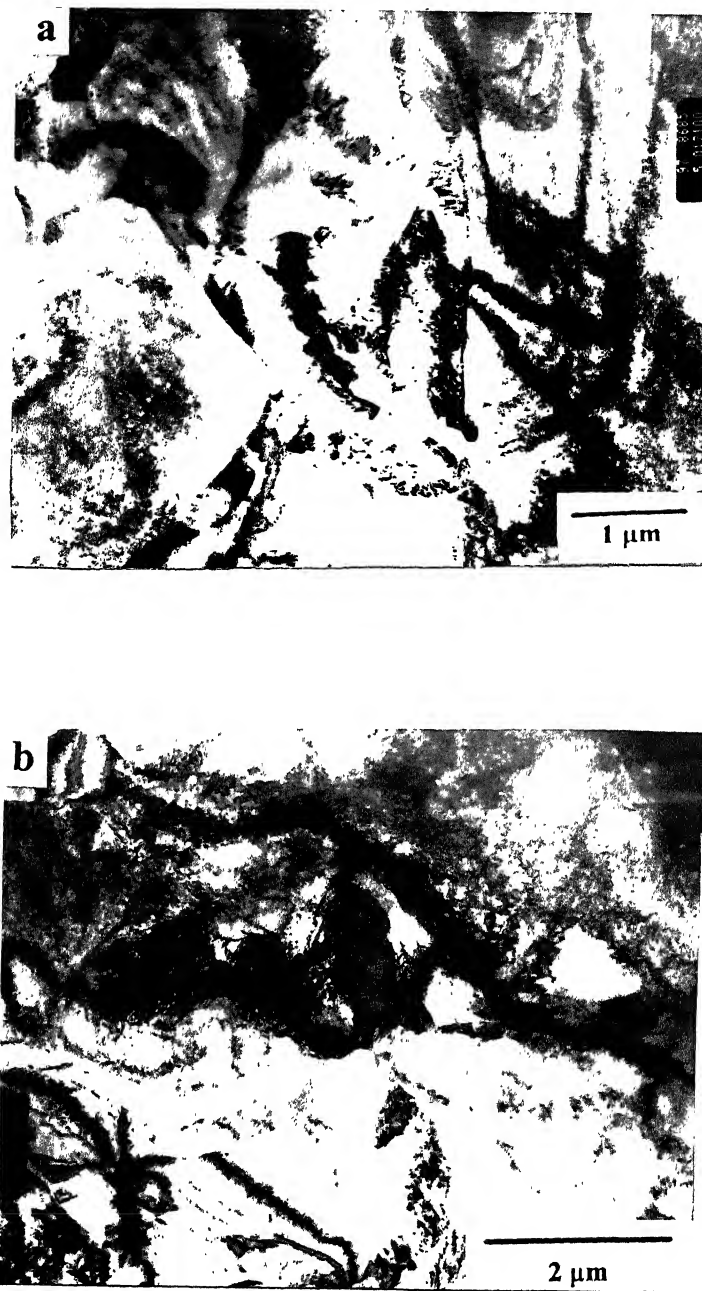
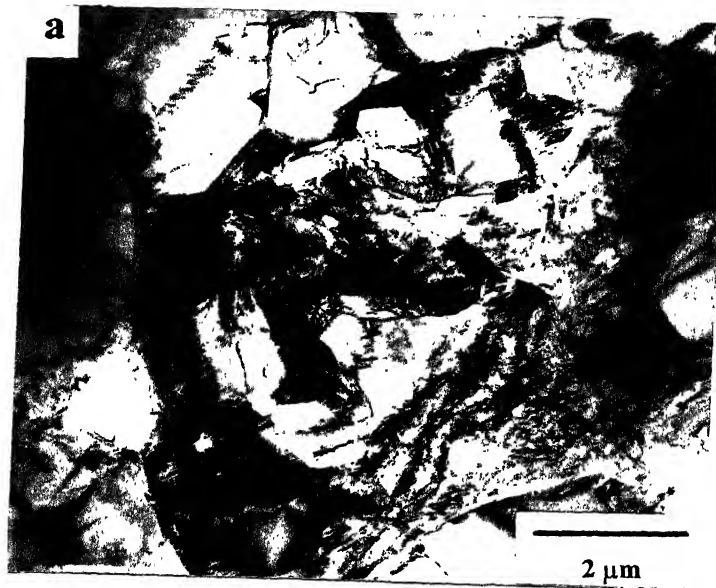


Fig. 4.14 TEM Micrographs from rolling plane section of the specimens rolled to 80% reduction at 1293 K (water quenched) showing (a) extensive recovery in α_2 phase and (b) high amounts of deformation in β phase



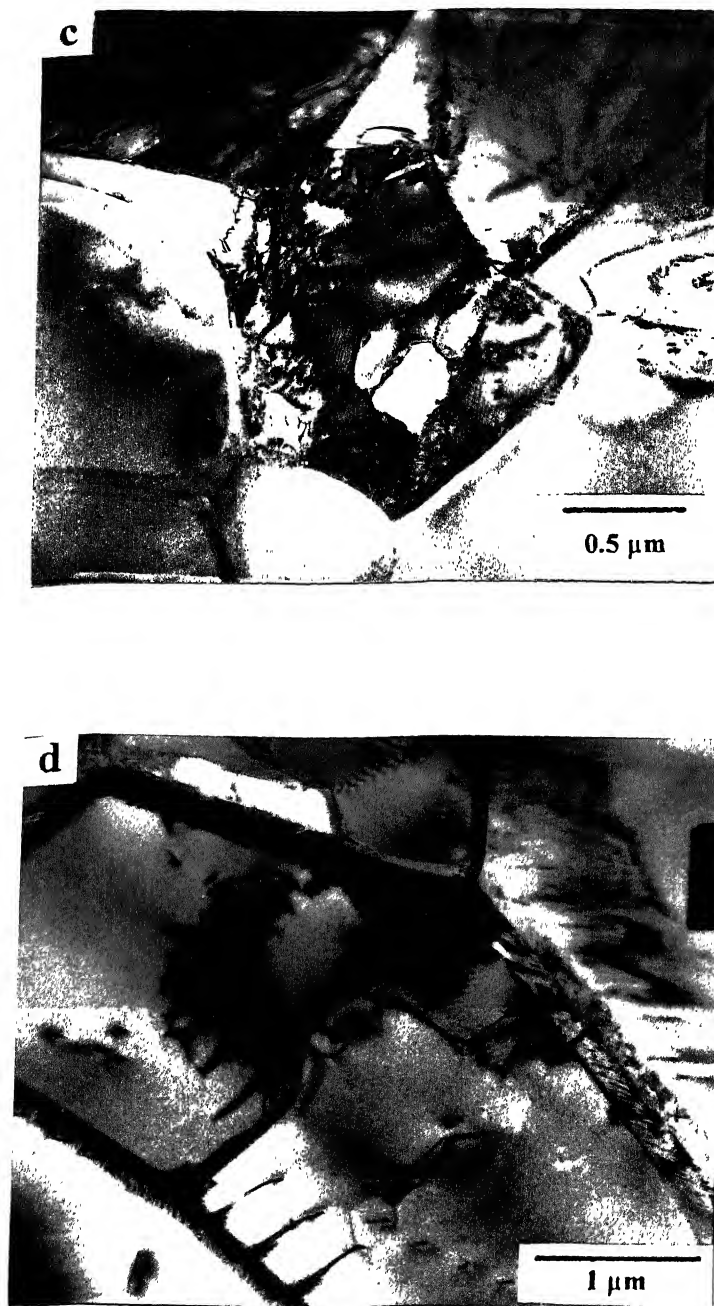


Fig. 4.15 TEM Micrographs showing the substructural features of α_2 phase in the material rolled at 1293 K to 80% reduction and furnace cooled showing (a) onset of recovery, (b) an aggregate of small subgrain coalescing to form bigger grains and (c, d) well delineated recrystallised grains

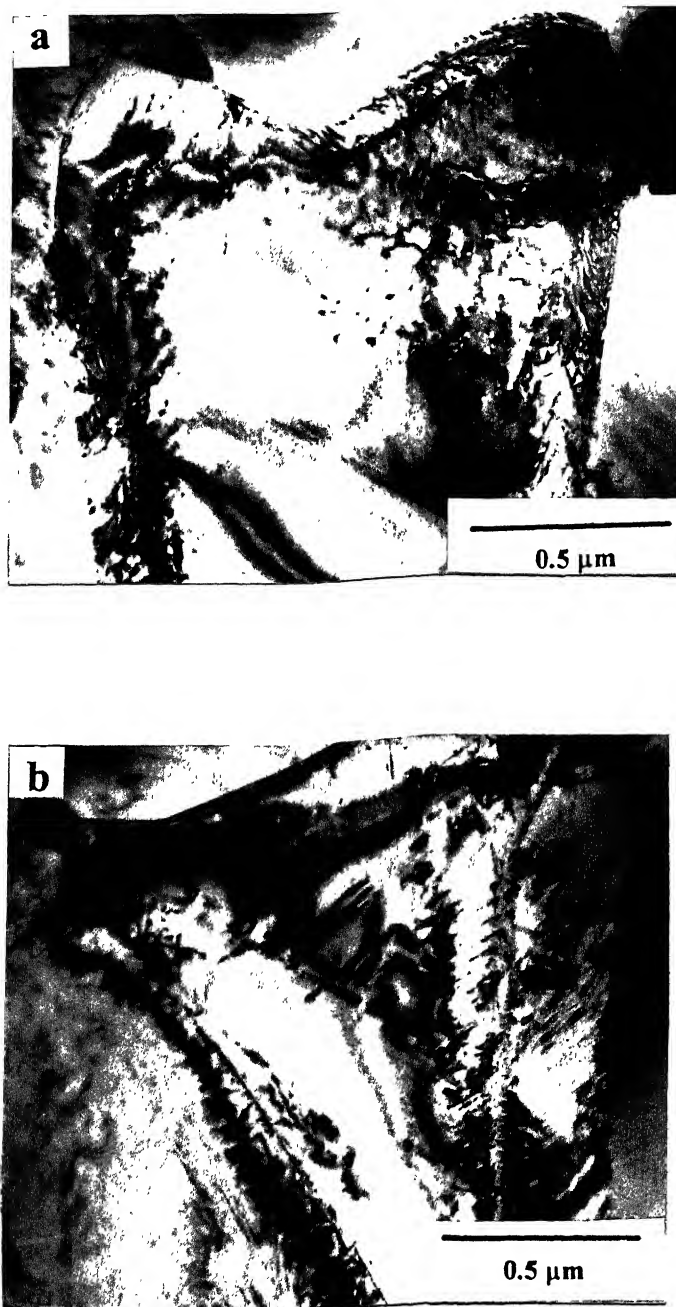


Fig. 4.16 TEM Micrographs showing the substructural features of the β phase in the material rolled at 1293 K to 80% reduction (furnace cooled) showing (a) signs of recovery in β and (b) nucleation of fine α_2 platelets in recovered β

4.1.3 Rolling of the as-cast material at 1373 K

At this temperature, the material consists mainly of the β phase. The transus lies very close to the working temperature ($1373\text{ K} \pm 10\text{ K}$). The optical microstructure of the 80 % deformed samples, after water quenching from the hot rolling temperature of 1373 K, is shown in Fig. 4.17. Clear-cut β grains with features similar to deformation bands inside the grains are observed. The fine lines seen in the optical micrograph is unlikely to represent the α_2 phase, which are much finer as will be evident from the TEM micrographs. Figs. 4.18 (a to d) show typical TEM microstructures from the 50% deformed sample. A highly deformed and dislocated area from the β phase can be seen in Figs. 4.18(a and b). There are also a few α_2 platelets formed during quenching. Fig. 4.18(c) shows a highly recovered β region. In some areas larger primary α_2 platelets can also be seen in association with deformed β (Fig. 4.18 d). The TEM micrographs of the 80% rolled sample typically show colonies of fine secondary α_2 platelets in highly recovered β regions (Figs. 4.19 a and b).

The SEM microstructure for the 1373 K rolled (80%) and furnace cooled material as given in Fig. 4.5(c) clearly shows reasonably large transformed secondary α_2 grains with some β at the grain boundaries. Some β is also seen to penetrate inside the α_2 platelets leading to partially globularised features of the transformed α_2 . Fig. 4.20 shows a TEM micrograph from the longitudinal section of a sample rolled 50 % at 1373 K and then furnace cooled. Fully recrystallised α_2 regions separated by thin ribbons of β can be seen in the micrograph. The TEM micrographs of the sample hot

rolled 80% at 1373 K, followed by furnace cooling show fully recrystallised (Fig. 4.21 a), and partially recrystallised as well as highly recovered α_2 regions (Fig. 4.21 b). At the same time, precipitation of fine secondary α_2 platelets within recovered β regions can also be seen (Fig. 4.22).

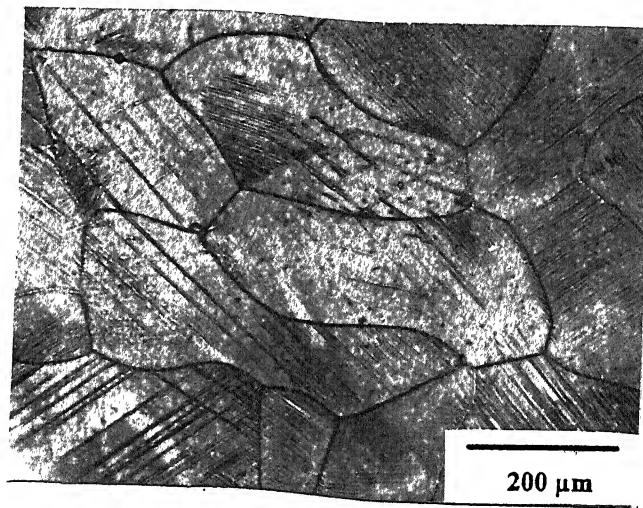
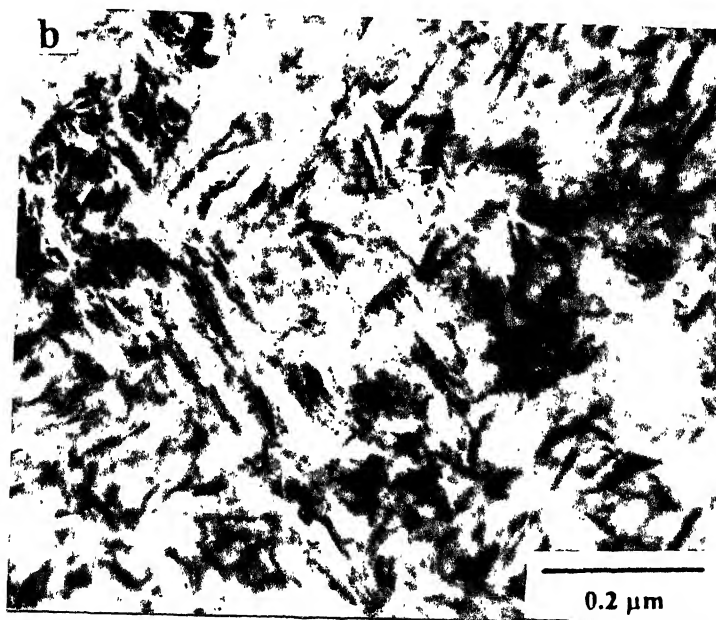
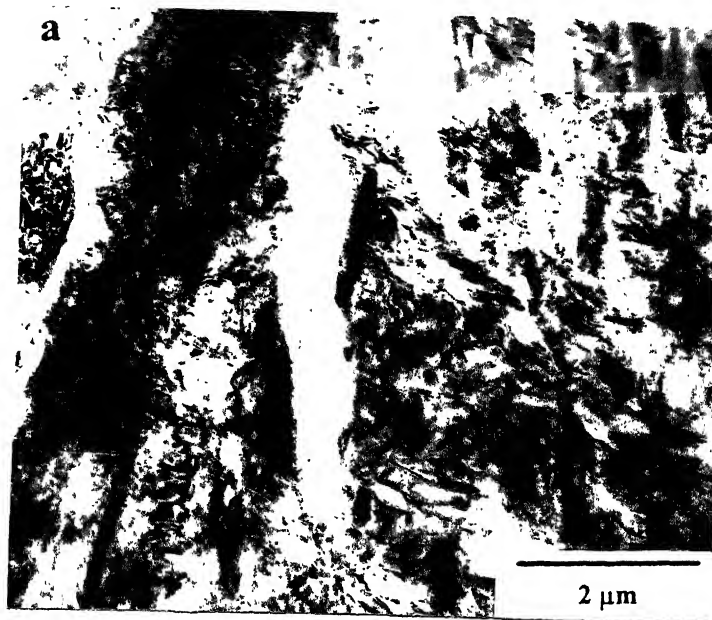


Fig. 4.17 Optical Micrograph of as-cast and 1373 K rolled material with 80% reduction (water quenched)



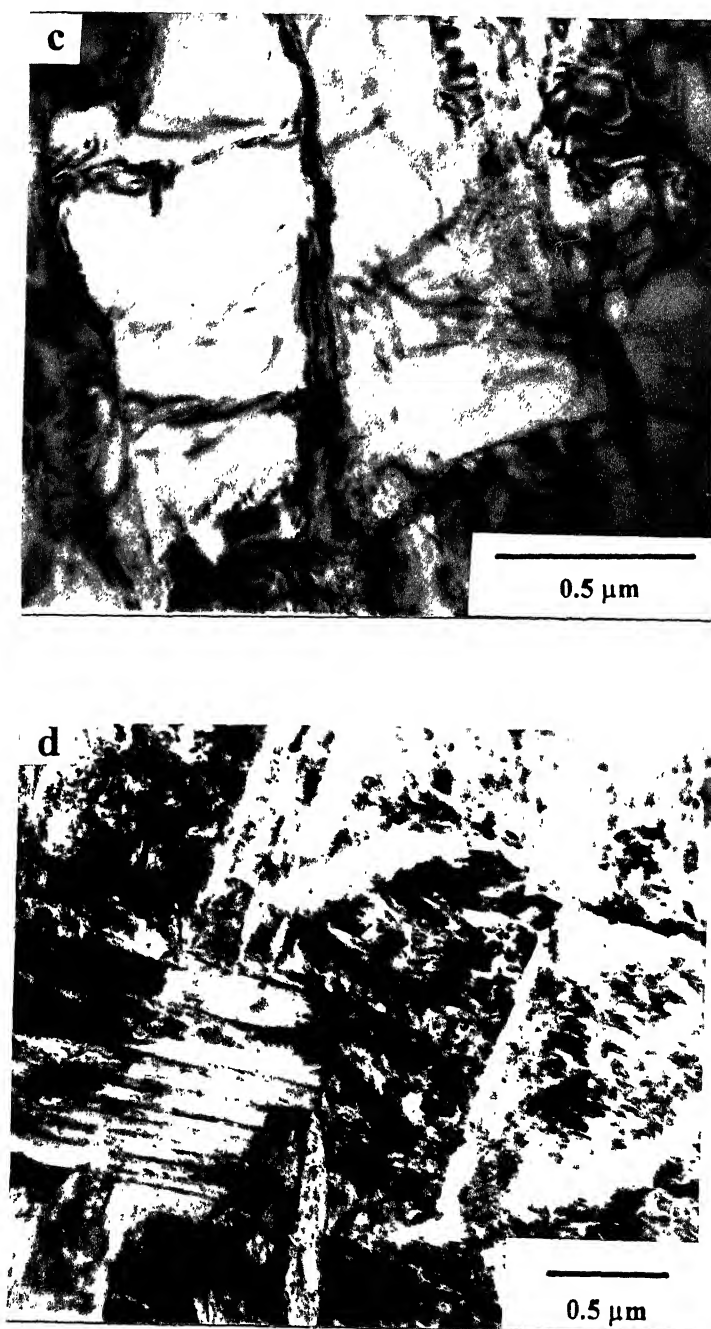


Fig. 4.18 TEM Micrographs from the rolling plane section of the material rolled at 1373 K (water quenched) to 50% reduction showing (a) a highly deformed and dislocated area of β , (b) a few fine α_2 platelets formed during quenching (c) a highly recovered β region and (d) a few larger α_2 platelets in association with deformed β

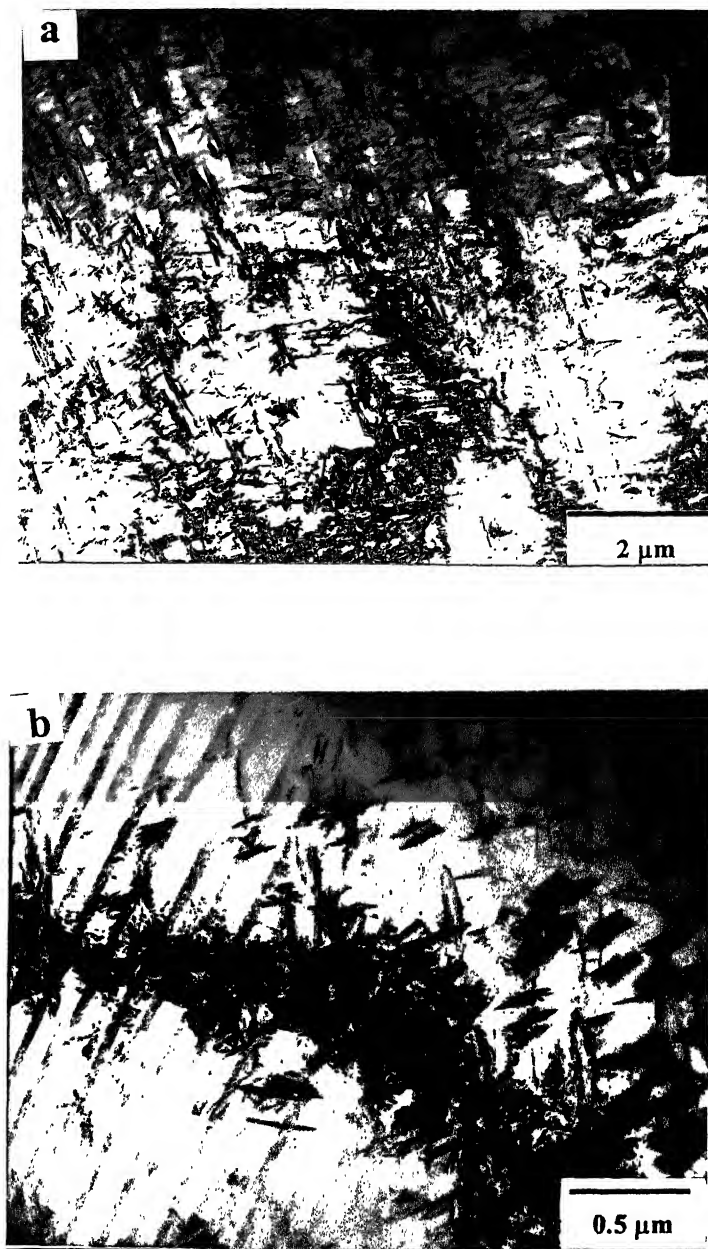


Fig. 4.19 TEM Micrographs from the rolling plane section of the material rolled at 1373 K to 80% (water quenched) reduction showing (a) colonies of fine secondary α_2 platelets in highly recovered β regions and (b) high degree of alignment of secondary α_2 platelets within recovered β

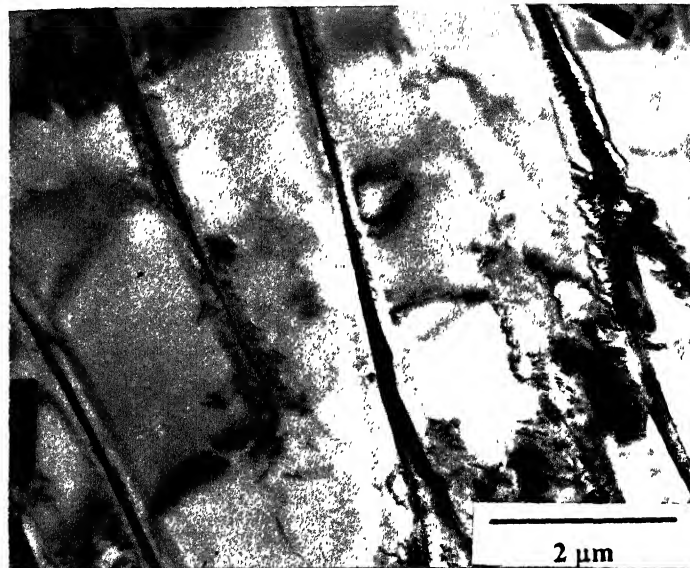


Fig. 4.20 TEM Micrograph from the longitudinal section of material rolled at 1373 K to the reduction 50% (furnace cooled) showing fully recrystallised α_2 regions separated by thin β ribbons

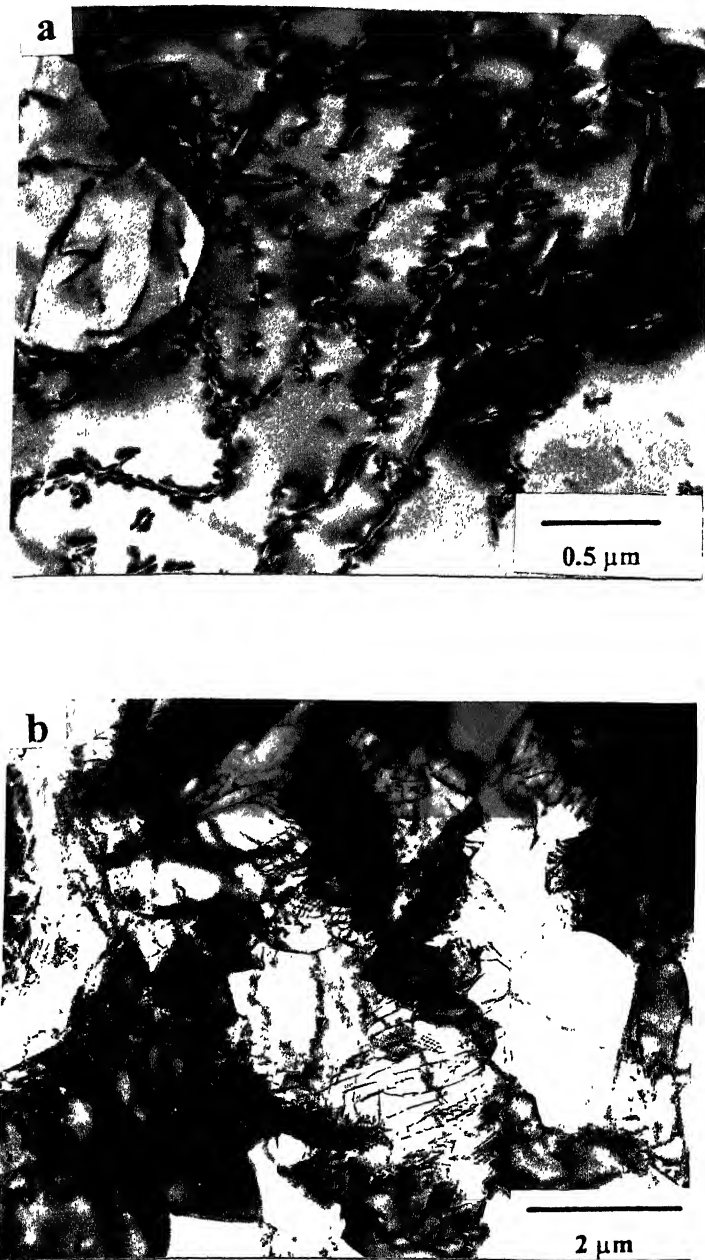


Fig. 4.21 TEM Micrographs from the rolling plane sections of material rolled at 1373 K to 80% reduction (furnace cooled) showing (a) fully recrystallised α_2 and (b) partially recrystallised α_2

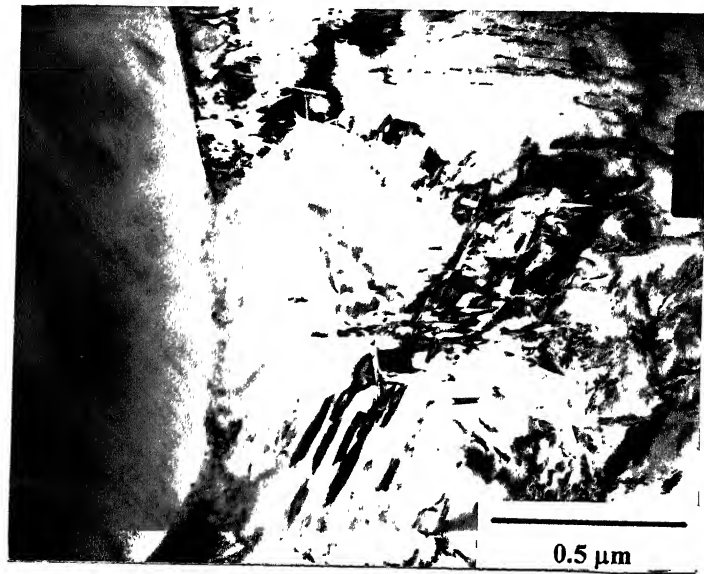


Fig. 4.22 TEM Micrograph from the rolling plane sections of material rolled at 1373 K to 80% reduction (furnace cooled) showing fine secondary α_2 platelets within recovered β regions

4.1.4 Rolling of the as-cast material at 1523 K

The temperature of 1523 K is nearly 150 K above the β -transus; therefore the material at this temperature is likely to consist of the β phase only. The optical microstructure of the material rolled at 1523 K to 80% reductions, followed by water quenching is shown in Figs. 4.23. Evidently, the β grains coarsen during soaking prior to rolling as well as during intermediate annealing treatment between the successive rolling passes. Fig. 4.24 represents the microstructural features of the 50% rolled specimen as seen under TEM. It can be seen that the deformation is localised into slip bands within the rather clean β matrix.

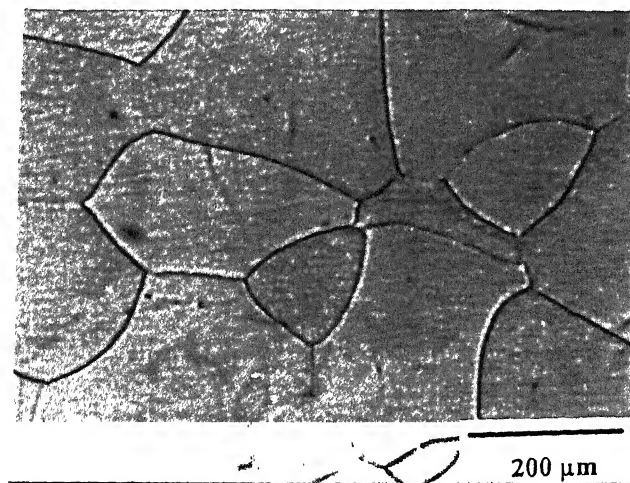


Fig. 4.23 Optical Microstructure of material rolled at 1523 K from the as-cast condition to the reduction of 80%

A series of TEM micrographs taken from the rolling plane section of the 80% deformed material are shown in Figs. 4.25 (a to d). These microstructures illustrate the effects of various kinds of static/dynamic phenomena that might be occurring inside the material during processing. Fig.4.25 (a) represents an overall view, while Fig.4.25 (b) shows the formation of subgrains inside the material. Figs. 4.25 (c and d) exhibit some of the intra-subgrain features.

The material furnace cooled from 1523 K after the finish rolling pass shows a true Widmanstätten microstructure. Fig. 4.5 (d) shows the SEM view of the 80% rolled material followed by furnace cooling. Randomly oriented laths of α_2 phase in β can be very clearly seen in the microstructure. A typical TEM micrograph of the material at this stage (Fig. 4.26 a) clearly shows the secondary α_2 grains separated from one another by thin ribbons of β . A higher magnification micrograph taken from an α_2 grain (Fig. 4.26 b) shows the substructure within.

The Vickers' Hardness Test results for β processed materials are given in Table 4.2. These results seem to be in conformity with the microstructural states of the materials for both the respective processing conditions.

Table 4.2 Hardness values for the β -rolled samples

Sample		Hardness (VHN)
R 1373 K	50%	444
	70%	432
	80%	331
R 1523 K	50%	341
	70%	336
	80%	336

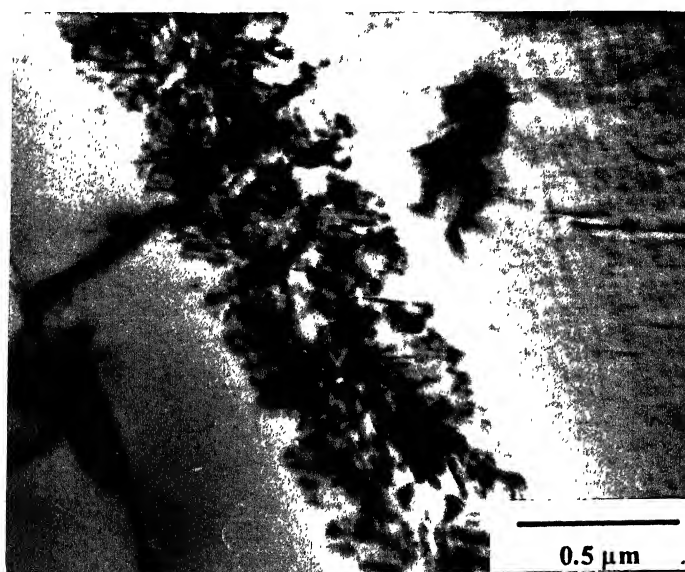
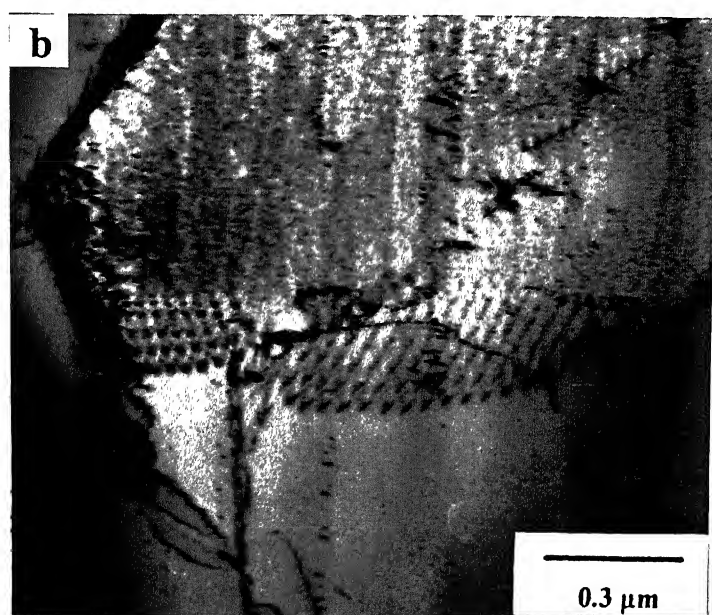
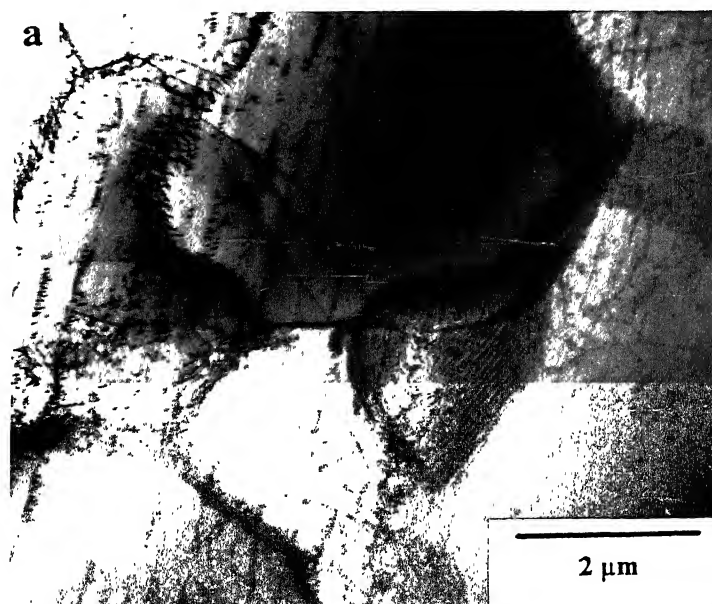


Fig. 4.24 TEM Micrograph from the rolling plane section of 1523 K rolled specimen to 50% reduction (water quenched)



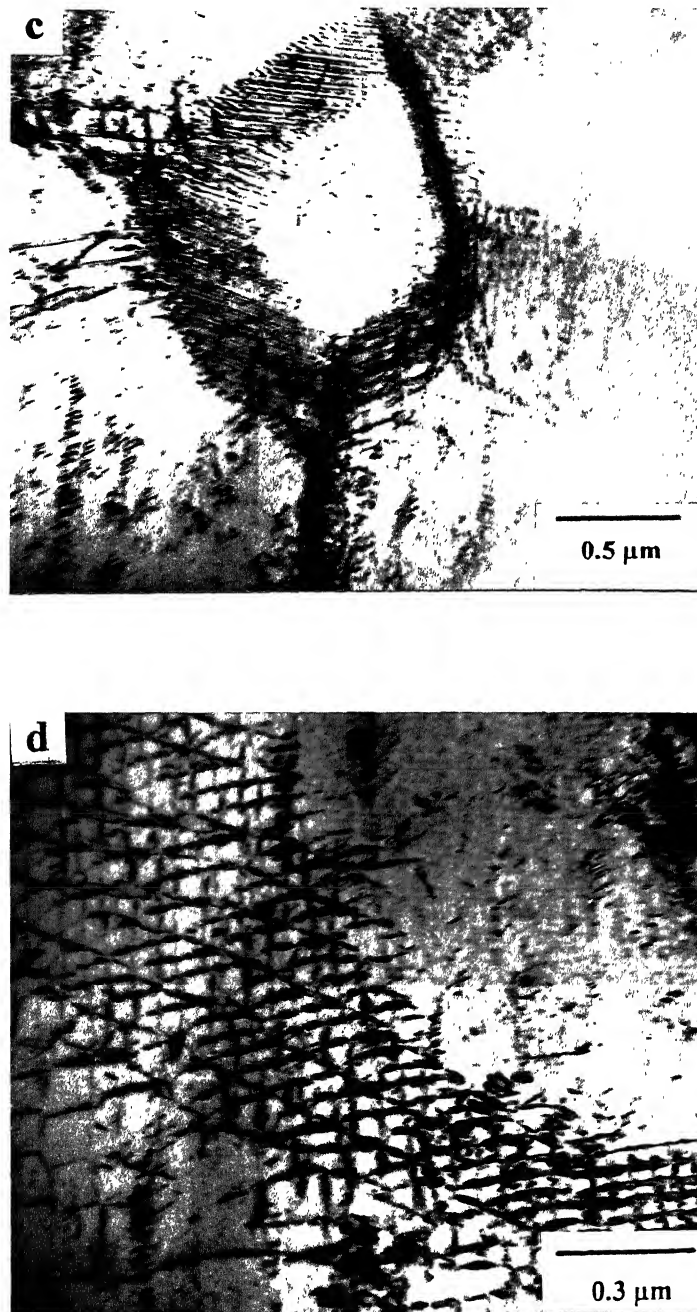


Fig. 4.25 TEM Micrographs from the rolling plane sections of the 1523 K rolled specimen to the reduction 80% (water quenched) showing (a) an overall view of the substructure, (b) formation of subgrains and (c, d) intra-subgrain features

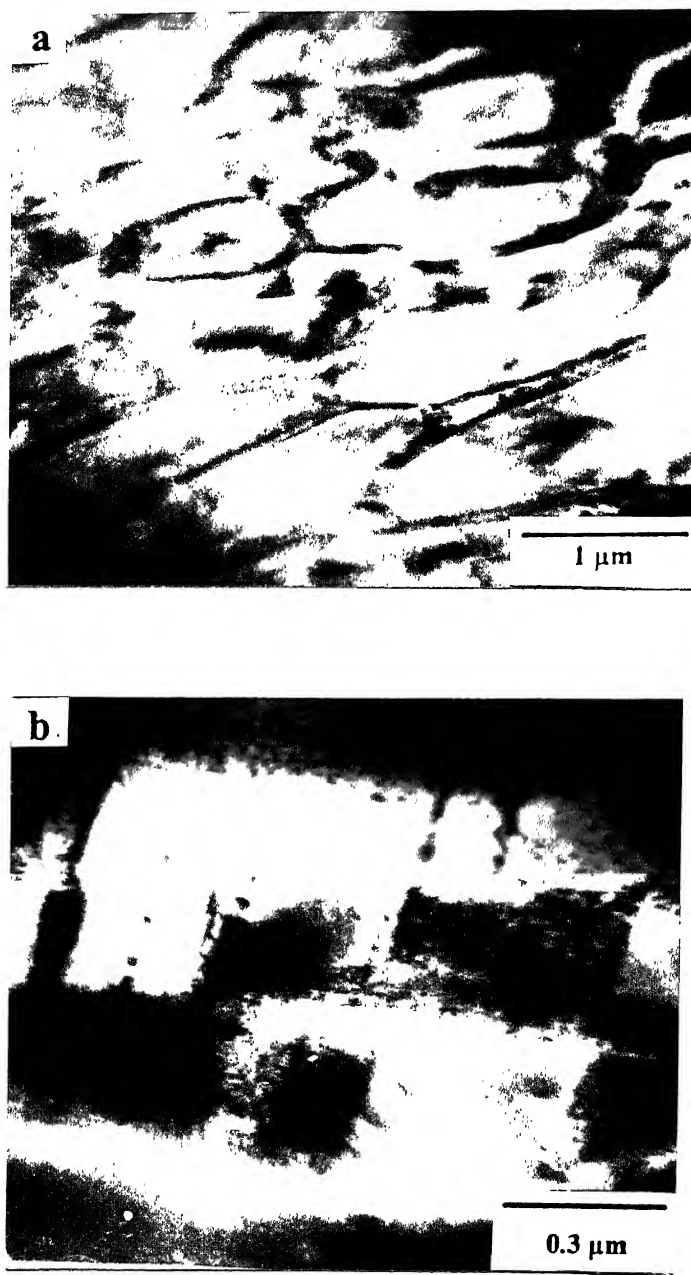


Fig. 4.26 TEM Micrographs of the material rolled at 1523 K to 80% reduction and furnace cooled

4.2 X-ray Diffraction Profiles

4.2.1 Starting Material

The X-ray diffraction pattern from the as-cast alloy is shown in Fig. 4.27(a). In addition to the peaks due to diffraction from the h.c.p. α_2 phase, a few peaks corresponding to the b.c.c. β phase can also be identified in the pattern. For the reference, the X-ray diffraction pattern from a powdered and annealed specimen is also shown in Fig. 4.28. A comparison of the intensities of the lines from α_2 in the as-cast material corresponding with the intensities reported for the random powder sample reveals that the as-cast material has a strong (0002) basal texture. This is evidently produced during the process of solidification from the alloy melt. The X-ray line profiles from the β phase indicate a reasonably intense (110) line, which is also the strongest amongst all the reflections for this phase. This is quite usual for materials having a b.c.c. crystal structure.

The X-ray diffraction profile of the heat treated and furnace cooled sample shows (Fig. 4.27 b) that the lines of β are less intense here than in case of the as-cast material. Evidently, heat treatment has led to a decrease in the β volume fraction. The heat treated sample also shows a significant decrement in the intensity of the (0002) line of the α_2 phase in comparison with that in the as-cast sample, while the $(20\bar{2}1)$ α_2 peak appears to be of nearly the same intensity in both. Thus, heat treatment followed by furnace cooling is found to weaken the basal texture.

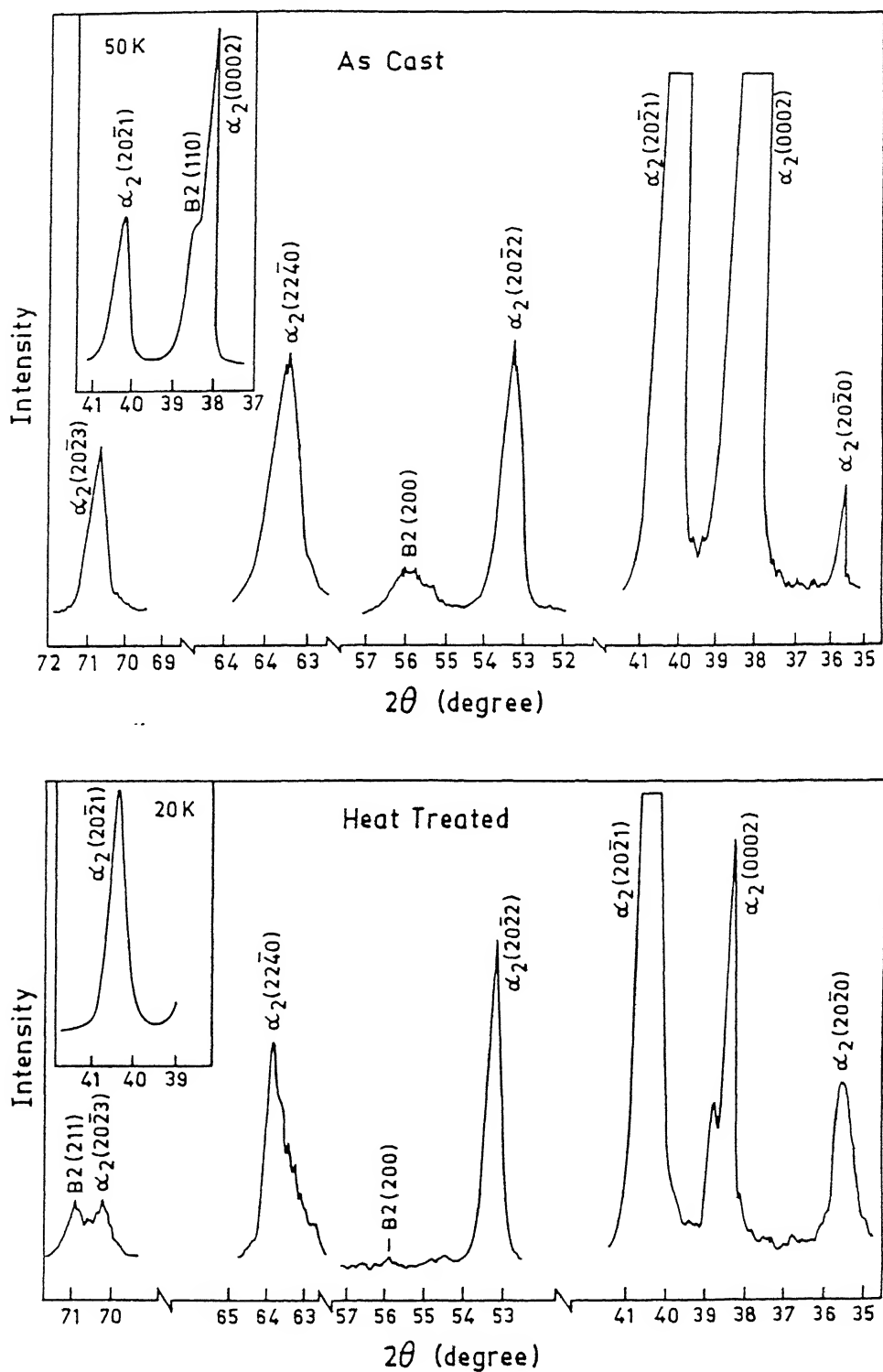


Fig. 4.27 X-ray diffraction patterns for (a) the as-cast material and (b) the heat treated (1173 K, 24 hrs) and furnace cooled material

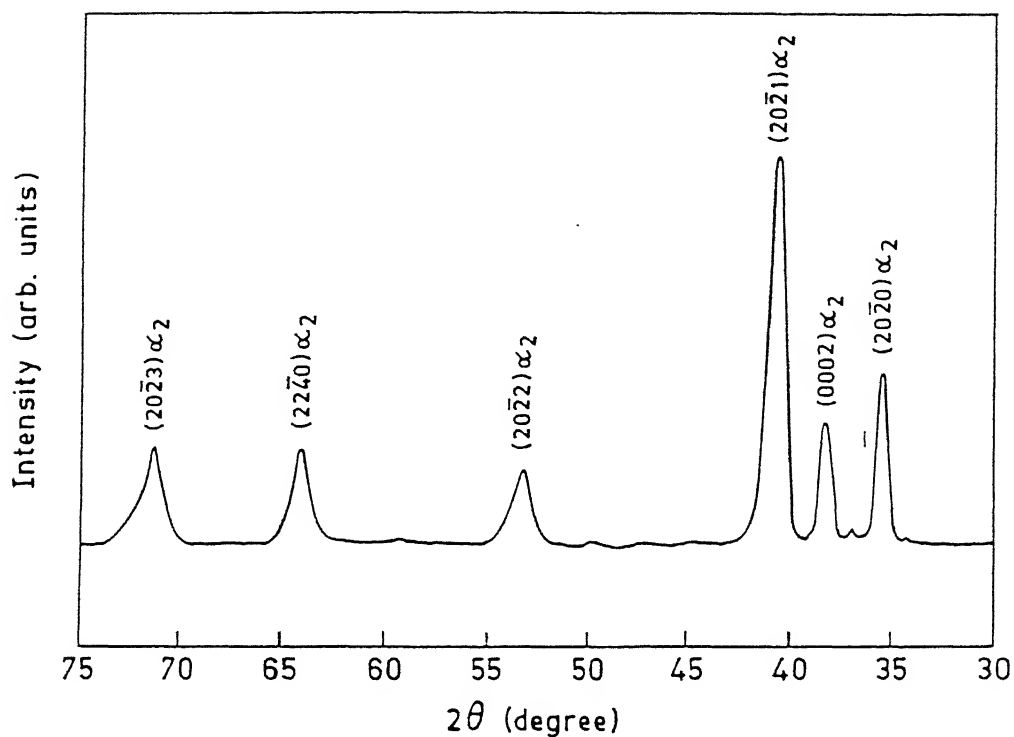


Fig. 4.28 X-ray line profile from a powdered and annealed specimen of Ti-24Al-11Nb alloy (for reference)

4.2.2 Material rolled at 1173 K and quenched

The X-ray diffraction patterns from samples rolled by different amounts at 1173 K are presented in Fig. 4.29. Clearly, the intensity of the basal (0002) reflection gradually increases with the amount of rolling reduction. Heavy deformation by 80% is found to reduce the intensity drastically for the $(20\bar{2}1)$ peak, which is the strongest line in case of the random powder sample (Fig. 4.28). In addition to the (0002), the $(22\bar{4}0)$ and the $(22\bar{4}2)$ peaks also become quite intense after 80% rolling deformation, as compared to the same lines in the random sample. On the other hand, the lines $(20\bar{2}1)$, $(20\bar{2}2)$ and $(20\bar{2}3)$ intensify after 70% deformation and then weaken after further deformation upto 80%. The XRD line profiles for the β phase show that the (110) is no longer the strongest peak. In fact, its intensity appears to diminish with increasing amounts of rolling reduction. By contrast, the (200) and (211) lines of β phase show steady increase in intensity.

The XRD patterns from the material which are prior heat treated before rolling, followed by water quenching, are shown in Fig. 4.30. A comparison between the patterns in Fig. 4.30 with those in Fig. 4.29 shows a more or less similar trend. As before, the (0002) α_2 peak sharpens on increasing the amount of rolling reduction, while the other peaks $(20\bar{2}0)$, $(20\bar{2}1)$, $(20\bar{2}2)$, $(22\bar{4}0)$, $(20\bar{2}3)$ and $(22\bar{4}2)$ weaken perceptibly. Although the amount of B2 phase here is rather small (~15 %), the (110) and (200) B2 peaks duly appear in the XRD pattern and their intensities diminish as the amount of reduction increases.

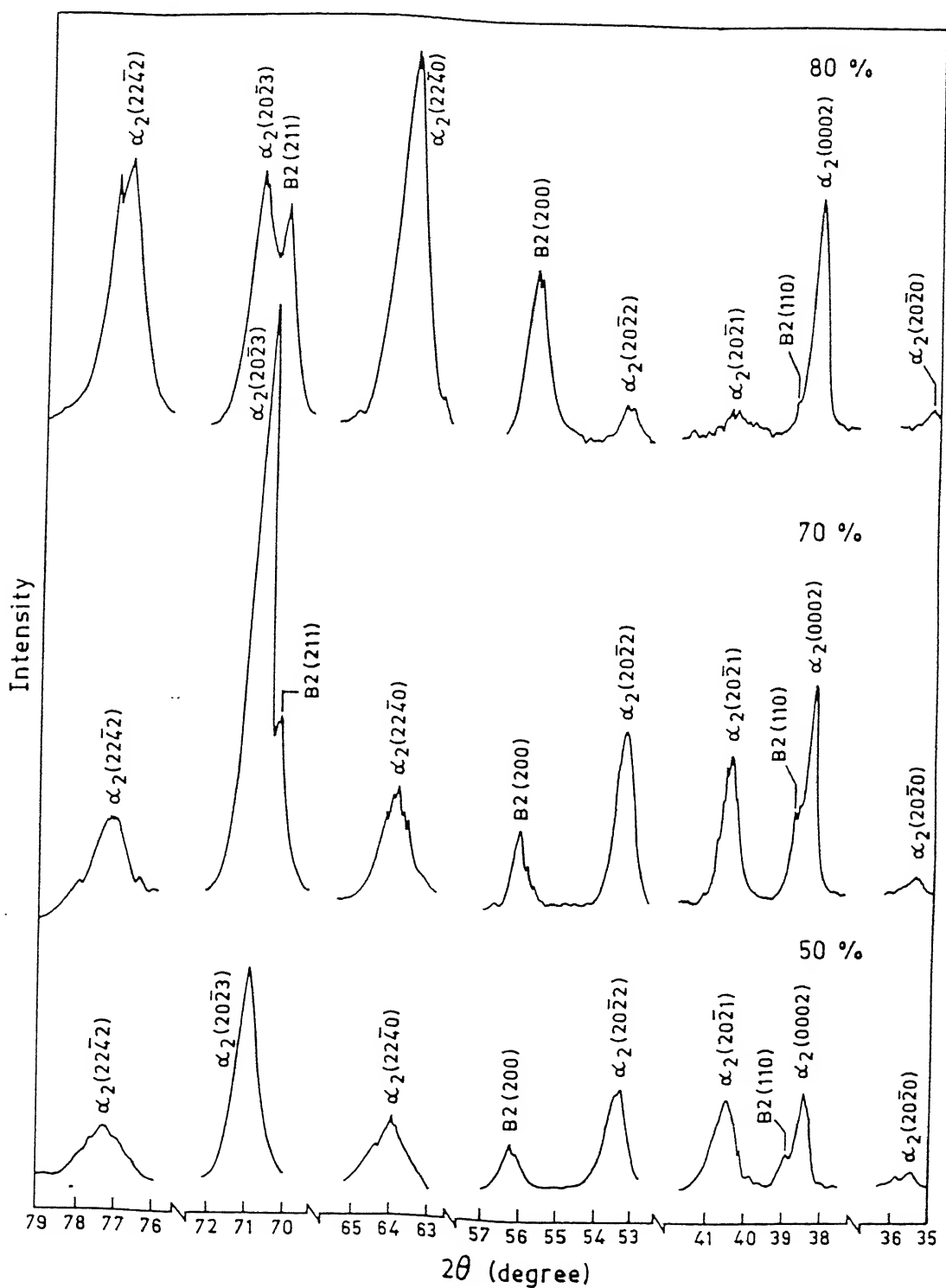


Fig. 4.29 X-ray diffraction pattern from samples rolled from the as-cast state by different amounts at 1173 K, (a) 50%, (b) 70% and (c) 80% (all water quenched)

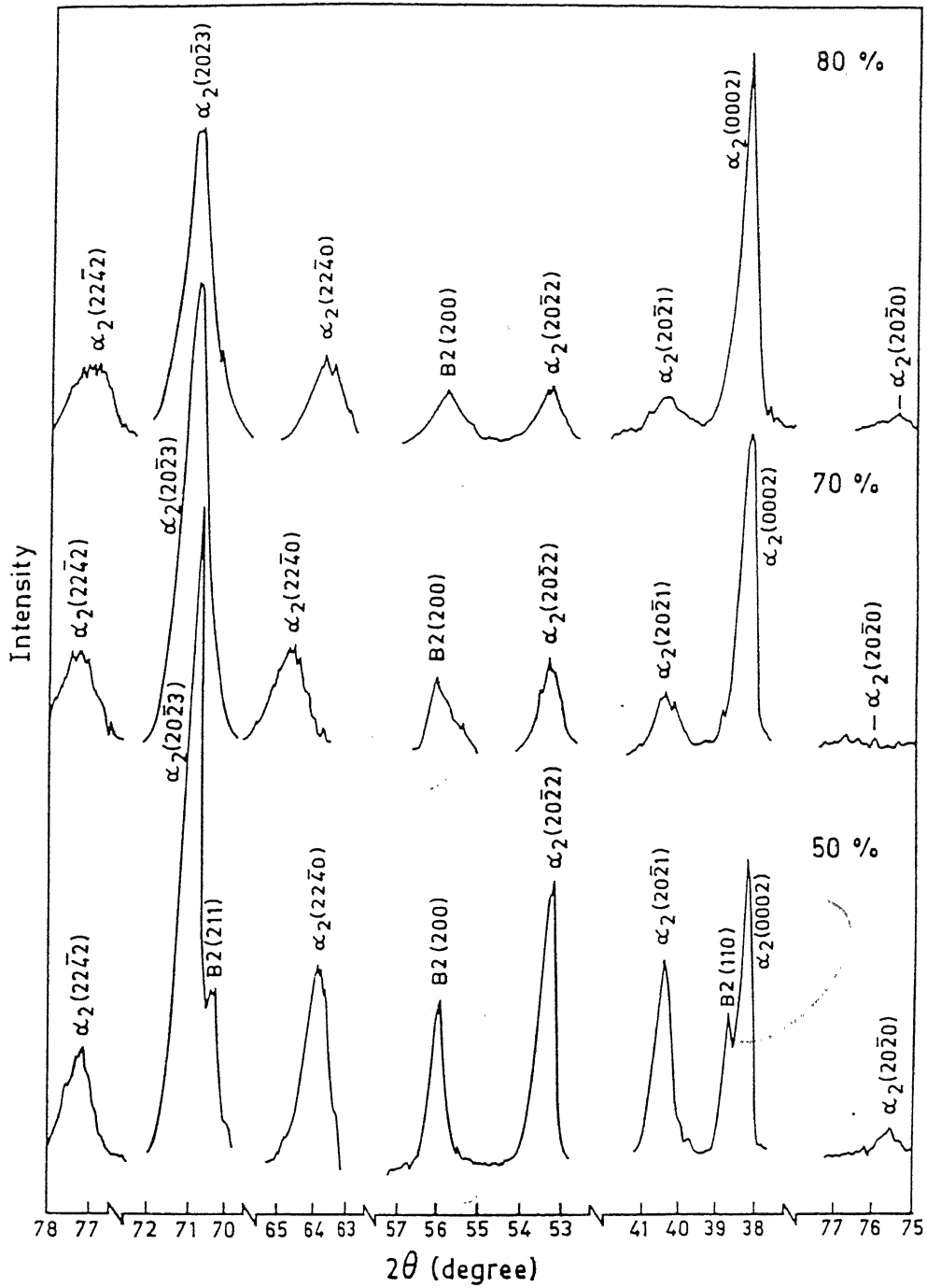


Fig. 4.30 X-ray diffraction pattern from the samples heat treated (1173 K, 24 hrs, FC) and rolled at 1173 K to 50%, 70% and 80% reductions (all water quenched)

4.2.3 Material rolled at 1293 K and quenched

The XRD pattern from the α_2 phase shows a discontinuous behaviour in the intensities of the lines with increase in rolling reduction (Fig. 4.31). For example, the (0002) and (20 $\bar{2}$ 1) peaks sharpen considerably after 70% rolling reduction, from the corresponding value after 50% deformation, and then show a drastic decrease after 80% reduction. The intensity of the (20 $\bar{2}$ 2) peak does not seem to change much with rolling. On the other hand, (22 $\bar{4}$ 0) and (20 $\bar{2}$ 3) peaks show a slight decrease in intensity after 70% rolling which is followed by substantial increase after 80% deformation.

So far as XRD profiles from the β phase are concerned, the behaviour of the (110) line appears to be opposite to those of (200) and (211). While the former peak sharpens after 70% rolling and then weakens drastically after 80% rolling reduction, the latter ones become very low in intensity after 70% rolling and then sharpen considerably after 80% rolling deformation.

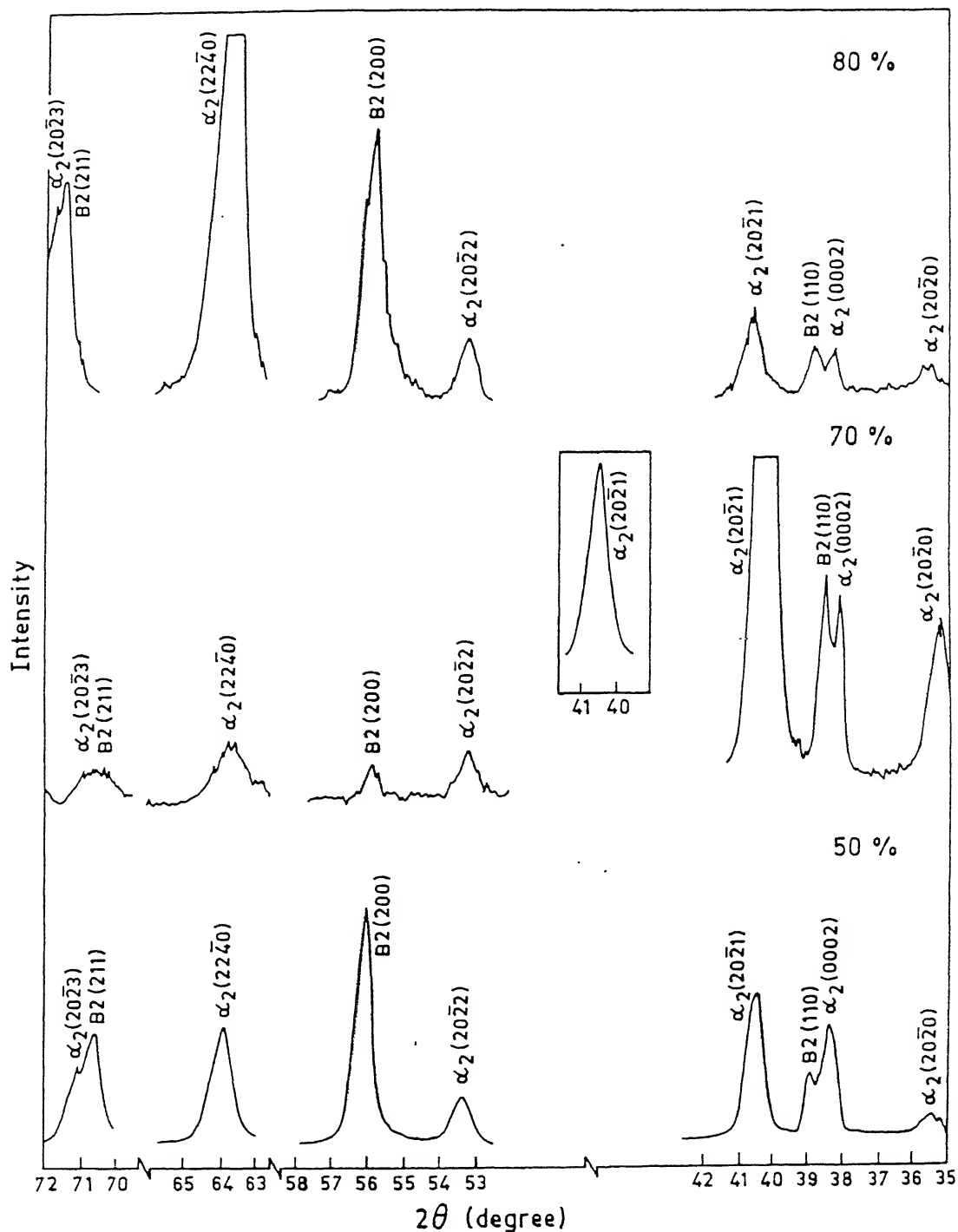


Fig. 4.31 X-ray diffraction pattern from samples rolled by different amounts at 1293 K, (a) 50%, (b) 70% and (c) 80% (all water quenched)

4.2.4 Material rolled at 1373 K and quenched

The XRD patterns of the as rolled samples in this condition (Fig. 4.32) show that the intensities of all the α_2 peaks are drastically low indicating a small α_2 volume fraction. There is no perceptible change in line intensities of this phase with rolling reduction also. The sharp lines at this stage all appear to belong to the β phase. The 50% deformed material shows hardly any peak for (110) and a moderately intense (200), while the (211) line is intensely strong. With increase in rolling reduction, the intensity of the (110) peak increases continuously and attains a rather high value after 80% deformation. The (200) and (211) lines, on the other hand, show first a decrement in intensity after 70% rolling, followed by substantial sharpening after 80% reduction. Evidently, the β phase is textured during the rolling deformation.

4.2.5 Material rolled at 1523 K and quenched

The XRD patterns of the sample at this stage show practically the lines due to the β phase only (Fig. 4.33). While the (110) peak is very weak, the (211) is moderately strong and the (200) the strongest in the 50% rolled material. The (110) peak continuously sharpens and attains a substantially high intensity after 70% and 80% rolling. The same is true for the (211) peak. On the other hand the intensity of the (200) peak does not seem to change much with increasing rolling reduction.

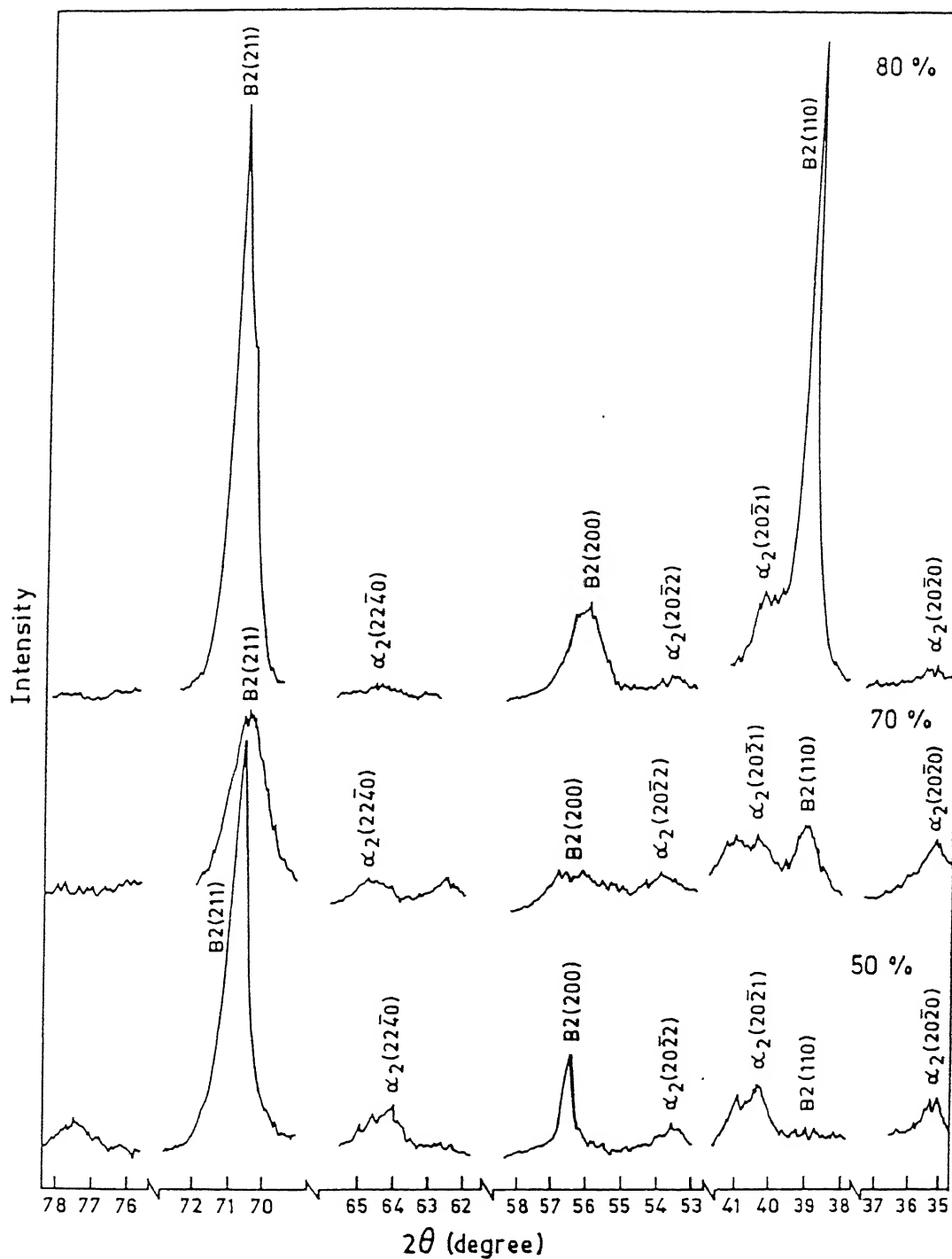


Fig. 4.32 X-ray diffraction pattern from samples rolled by different amounts at 1373 K, (a) 50%, (b) 70% and (c) 80% (all water quenched)

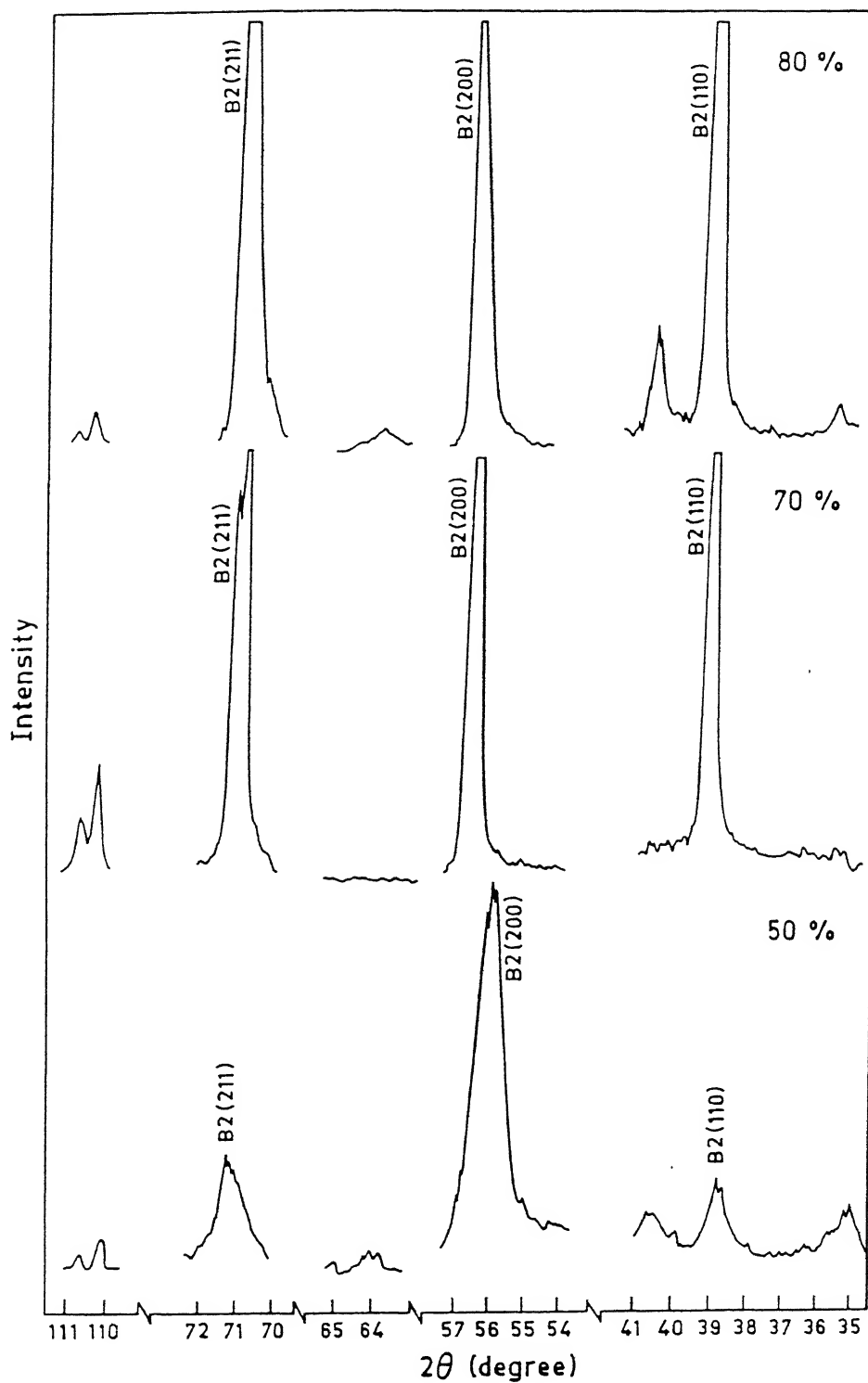


Fig. 4.33 X-ray diffraction pattern from samples rolled by different amounts at 1523 K, (a) 50%, (b) 70% and (c) 80% (all water quenched)

4.2.6 Materials rolled at 1173 K, 1293 K, 1373 K and 1523 K followed by furnace cooling

XRD patterns for the specimens rolled at 1173 K, 1293 K and 1373 K followed by furnace cooling from these temperatures after the finish rolling pass are displayed in Fig. 4.34 (a-c). A very systematic trend can be noticed in the variations of peak intensities both with respect to rolling temperature as well as amounts of deformation at each of these temperatures. In the specimens rolled at 1173 K and furnace cooled, a gradual increment in the intensity of (0002) α_2 reflection can be seen from 50% to 80%, while the other peaks, say, (20 $\bar{2}$ 0), (20 $\bar{2}$ 1), (20 $\bar{2}$ 2) and (22 $\bar{4}$ 0) gradually weaken. On the other hand, in the 1373 K rolled materials, the (20 $\bar{2}$ 0), (20 $\bar{2}$ 1) and (20 $\bar{2}$ 2) peaks get sharpened, while the (0002) and (22 $\bar{4}$ 0) reflections weaken. An intermediate trend is seen in the case of 1293 K rolled material, where the (20 $\bar{2}$ 0), (0002) and (20 $\bar{2}$ 1) peak intensities get enhanced on increasing the amount of rolling deformation and the intensity of the (22 $\bar{4}$ 0) peak decreases. The XRD pattern recorded from the specimen rolled at 1523 K to 80% reduction followed by furnace cooling is separately shown in Fig. 4.35.

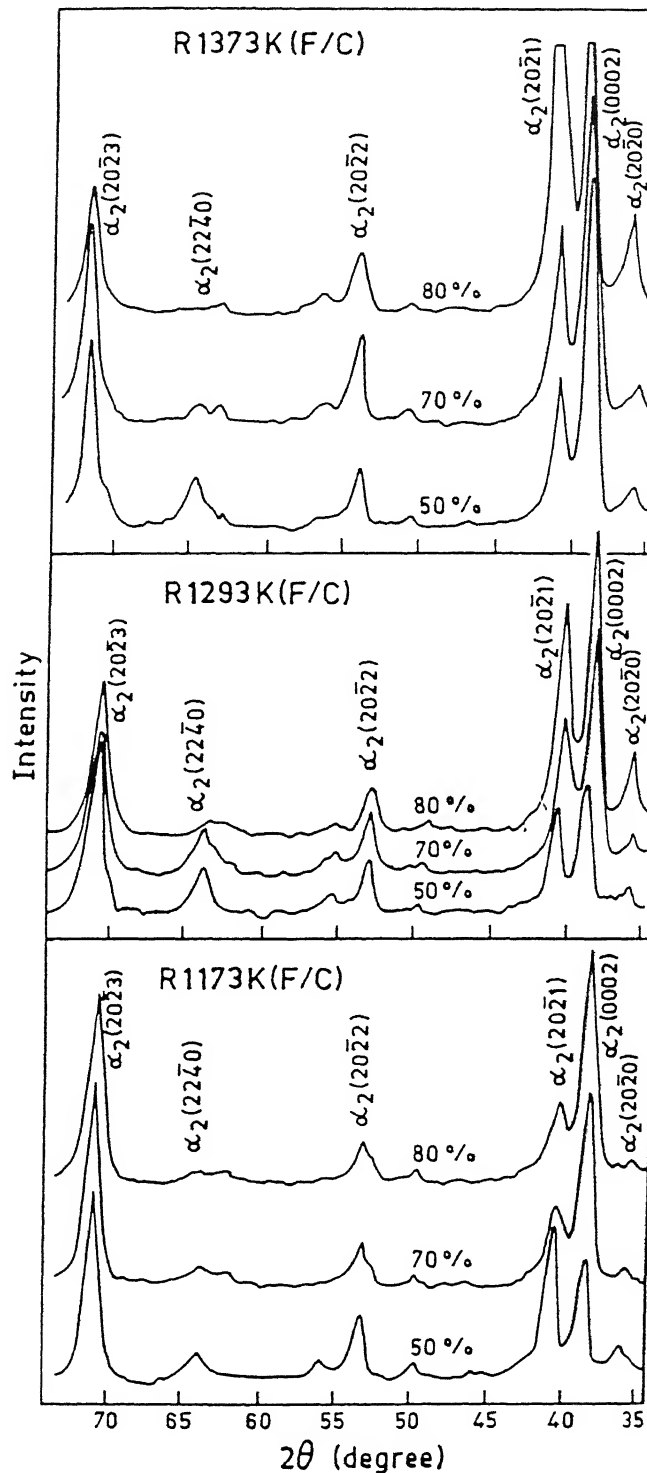


Fig. 4.34 X-ray diffraction pattern from samples rolled to different amount of reductions at (a) 1173 K, (b) 1293 K and (c) 1373 K (all furnace cooled)

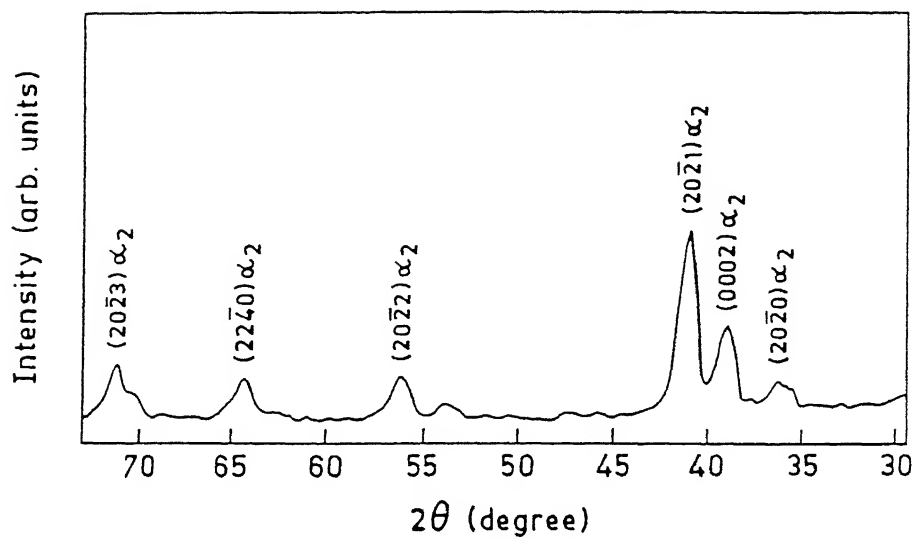


Fig. 4.35 X-ray diffraction pattern from the specimens rolled to 80% reduction at 1523 K (furnace cooled)

4.3 Texture Analysis

As mentioned earlier (Section 4.2), the X-ray diffraction pattern of the as-cast material shows the presence of both the h.c.p. α_2 and the b.c.c. β phase. While β has been found to be only weakly textured, if at all, the α_2 has a reasonably strong (0002) basal texture. The (0002) pole figure recorded from the specimen surface, which is normal to the direction of heat extraction during solidification from the melt, is shown in Fig. 4.36 (a). The basal poles here exhibit $\{0002\}\langle uvw \rangle$ type of texture, where $\langle uvw \rangle$ is the longitudinal direction of the specimen. The orientation distribution function plot for this material is given in Fig. 4.37. The analysis of $\phi_2 = 0^\circ$ and 30° sections, in which most of the important orientations of the h.c.p. texture appear, clearly shows the presence of strong (0001)[10 $\bar{1}$ 0] and (0001)[2 $\bar{1}$ $\bar{1}$ 0] maxima of the basal texture. A number of non-basal orientations, namely, ($\bar{1}$ 2 $\bar{1}$ 8)[4 $\bar{8}$ 43], ($\bar{1}$ 2 $\bar{1}$ 6)[1 $\bar{2}$ 11] and ($\bar{2}$ 4 $\bar{2}$ 1)[4 $\bar{1}$ $\bar{3}$ 6] are also found to be substantially strong.

As has already been stated, the as-cast material contains substantial amount of the β phase which is slightly higher than the equilibrium volume fraction at the room temperature. The (200) XRD peak of the β phase is the only strong peak which does not have an overlap with any of the α_2 peaks. It was therefore decided to determine the texture of the β phase by recording the (200) pole figure of it. The same is shown in Fig. 4.36 (b). The strongest fibre, as evident from this pole figure, is $\{113\}\langle uvw \rangle$ with $\langle uvw \rangle$ along the direction parallel to the longitudinal direction.

Heat treatment (24 hrs at 1173 K) of the as-cast material followed by furnace cooling has been found to weaken the texture only slightly, as revealed from the relevant (0002) pole figure (Fig. 4.36 c). The ODF of this specimen, given in Fig. 4.38, shows that the main orientations in this case are the $(0001)\parallel ND$ fibre with the maxima located at $\sim 6^\circ$ along ϕ from the ideal $(0001)[3\bar{1}\bar{2}0]$, plus $(0001)[1\bar{1}00]$ and $(0001)[1\bar{2}10]$ components. In addition to these, a few other orientations like $(12\bar{1}5)[5\bar{5}03]$ and $(2\bar{4}\bar{2}1)[41\bar{3}6]$ also appear to be quite strong in the ODF of the heat treated material.

4.3.1 Texture of material rolled at 1173 K

4.3.1.1 As-cast, rolled and water quenched

β -Phase

The (200) pole figures of this material, for both the reduction levels 50% and 80%, show a number of fibres, the strongest among these is $\{113\}\langle uvw \rangle$. There are a few other relatively weak fibres also. The pole figure for the 80% rolled material is shown in Fig. 4.39 (a). The $\phi_2 = 0^\circ$ and 45° sections of the ODF are shown in Figs. 4.40 (a and b). The presence of host of fibres is also clear from the $\phi_2 = 0^\circ$ and 45° sections of the ODF. The prominent fibres are $\{113\}\langle uvw \rangle$, $\{223\}\langle uvw \rangle$, $\{332\}\langle uvw \rangle$, $\{221\}\langle uvw \rangle$, $\{013\}\langle uvw \rangle$, $\{021\}\langle uvw \rangle$ and $\{023\}\langle uvw \rangle$. A number of peak orientations could also be located in the $\phi_1 = 0^\circ$ and 90° sections (Fig. 4.41 a). These are $\{112\}\langle 110 \rangle$, $\{112\}\langle 111 \rangle$, $\{012\}\langle 100 \rangle$, $\{013\}\langle 031 \rangle$ and $\{110\}\langle 011 \rangle$.

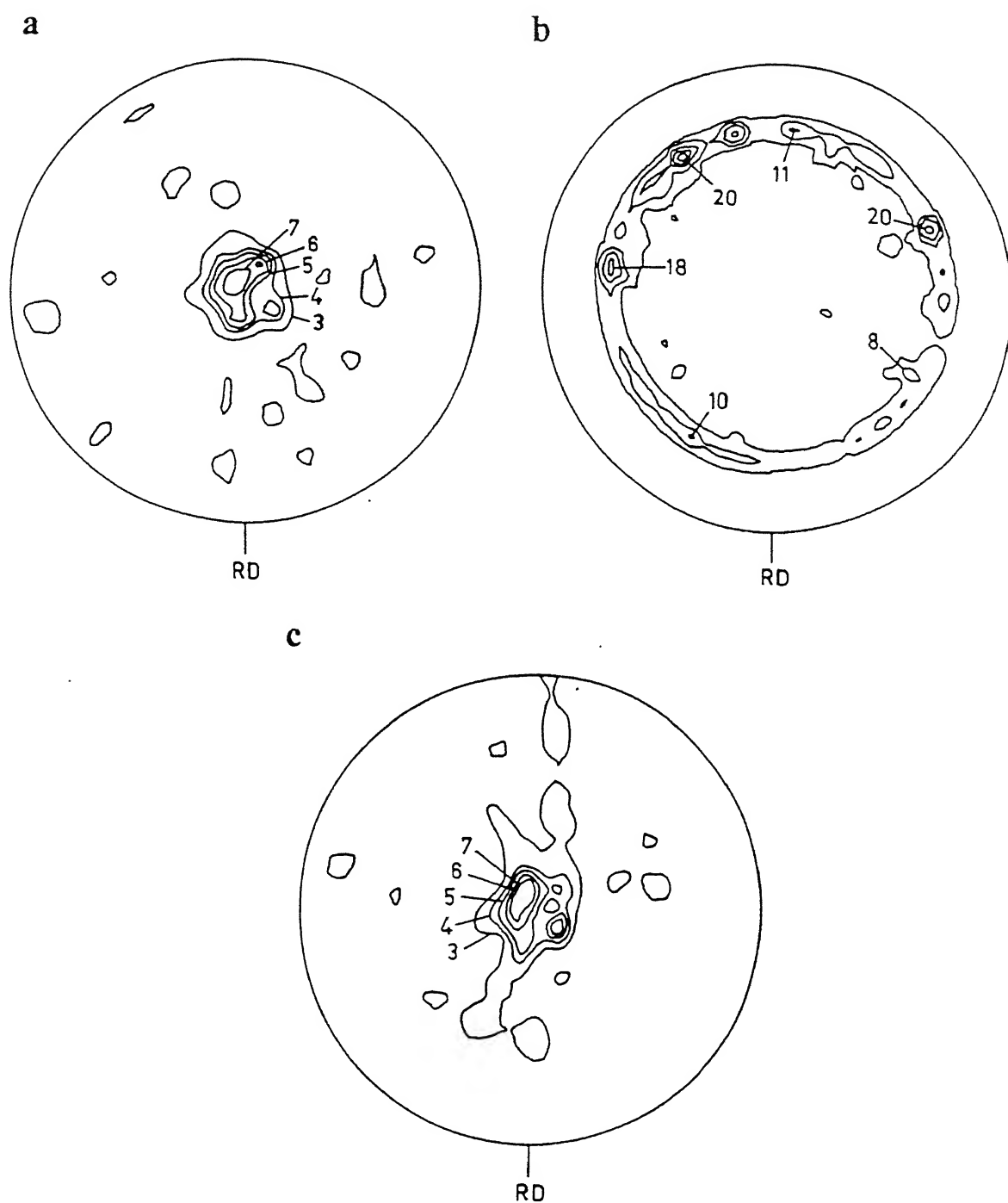


Fig. 4.36 (a) $(0002)_{\alpha_2}$ pole figure for the as-cast material, (b) $(200)_{\beta}$ pole figure of the as-cast material and (c) $(0002)_{\alpha_2}$ pole figure for the heat treated material

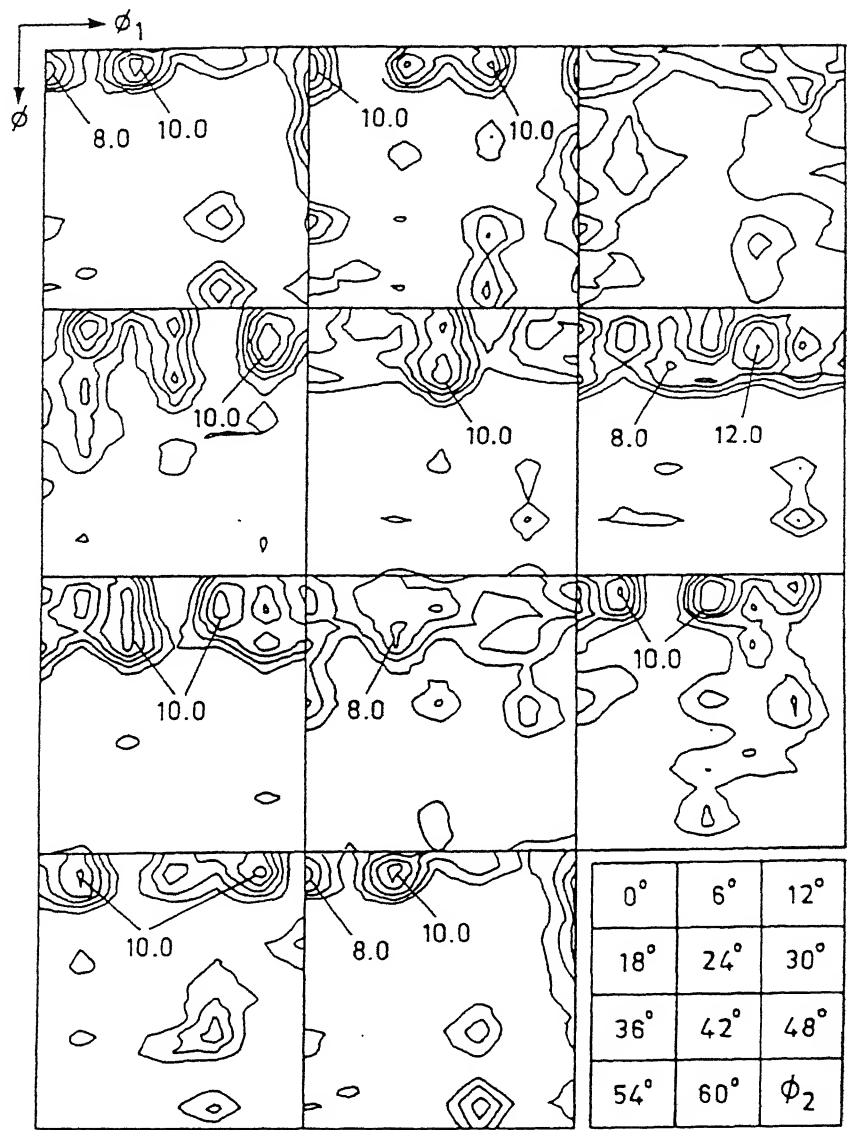


Fig. 4.37 Complete ODF of the as-cast material

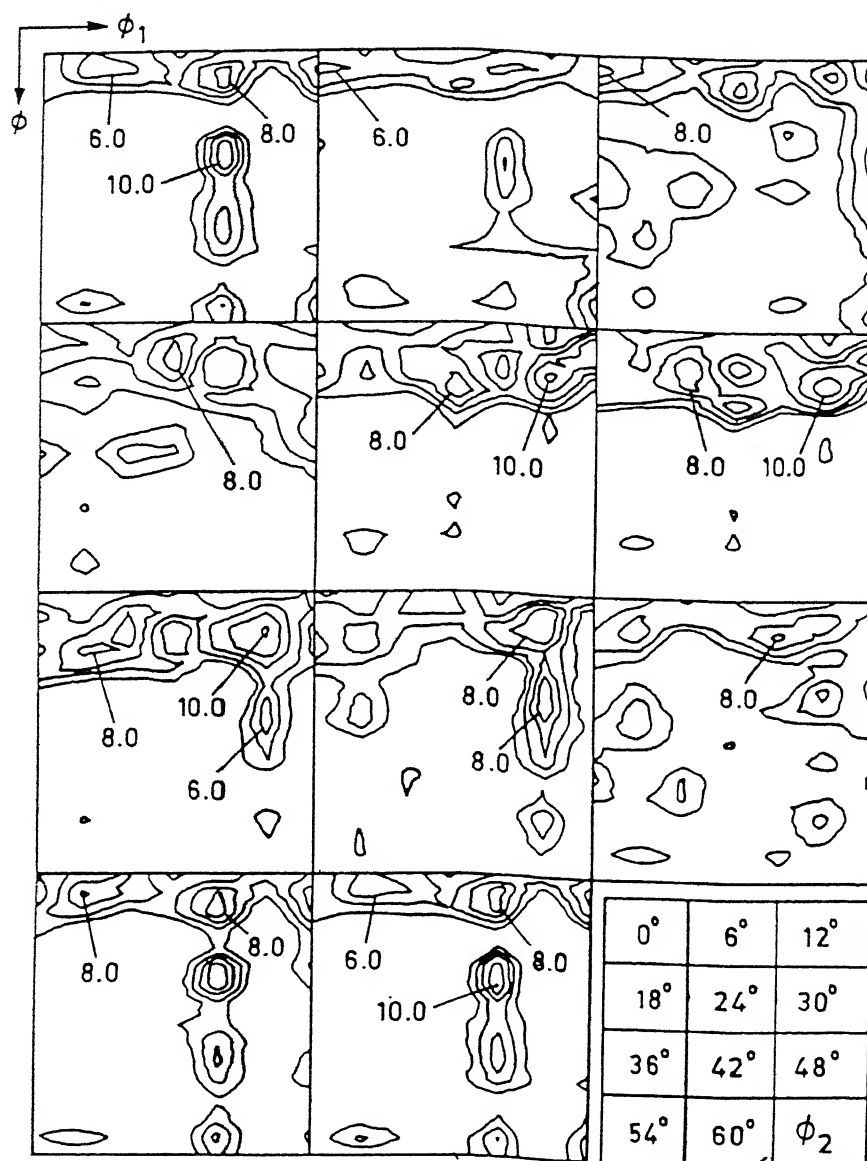


Fig. 4.38 Complete ODF of the heat treated material

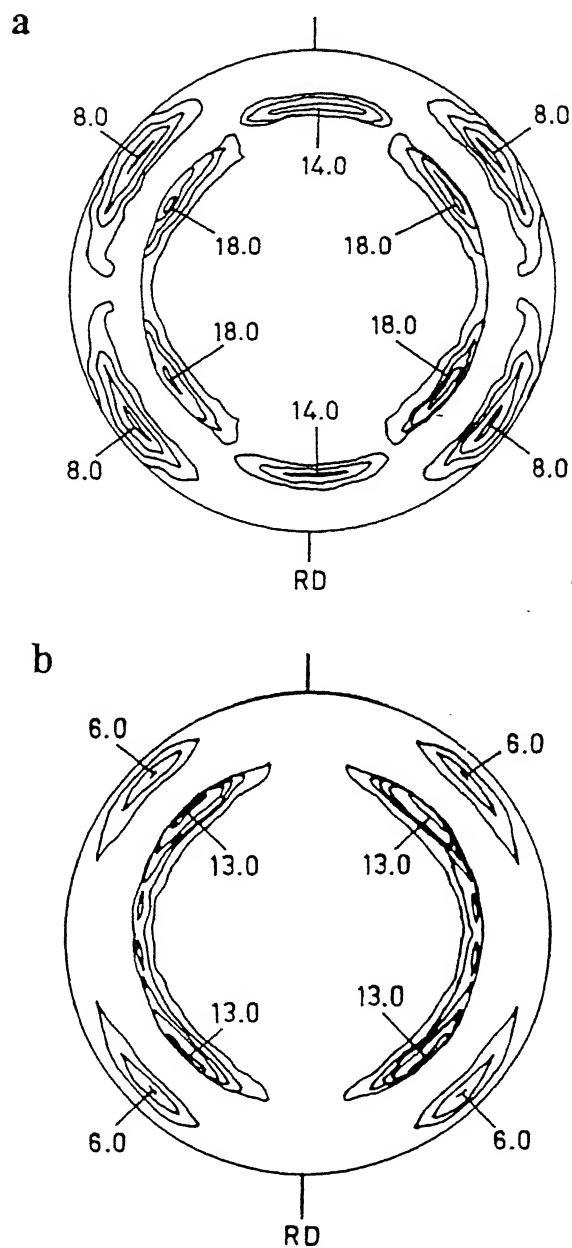


Fig. 4.39 $(200)_\beta$ pole figures of materials rolled at (a) 1173 K and (b) 1293 K to 80% reduction (all water quenched)

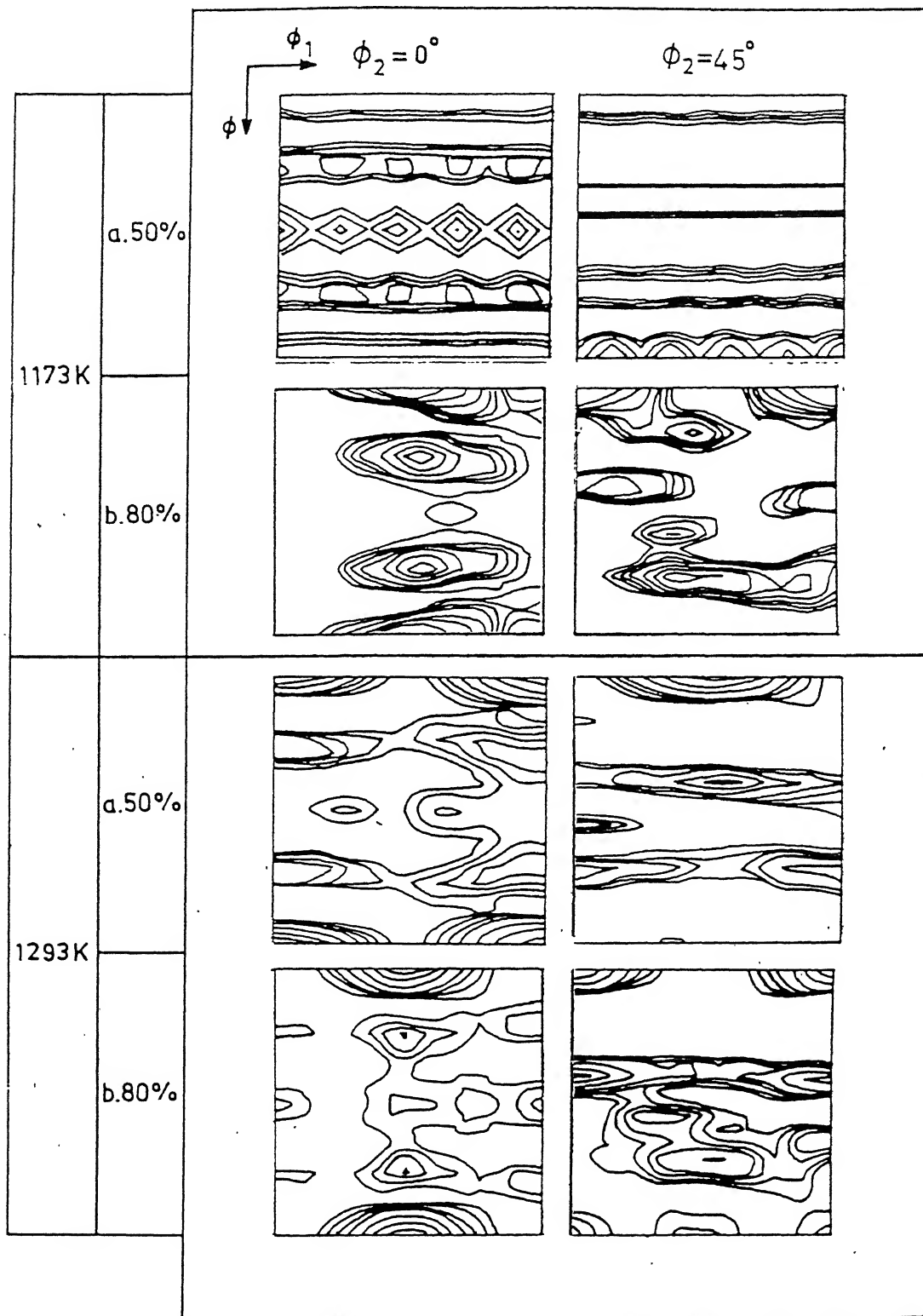


Fig. 4.40 $\phi_2 = 0^\circ$ and 45° sections of the ODFs from the β -phase of (a) 1173 K, 50%, (b) 1173 K, 80%, (c) 1293 K, 50% and (d) 1293 K, 80%

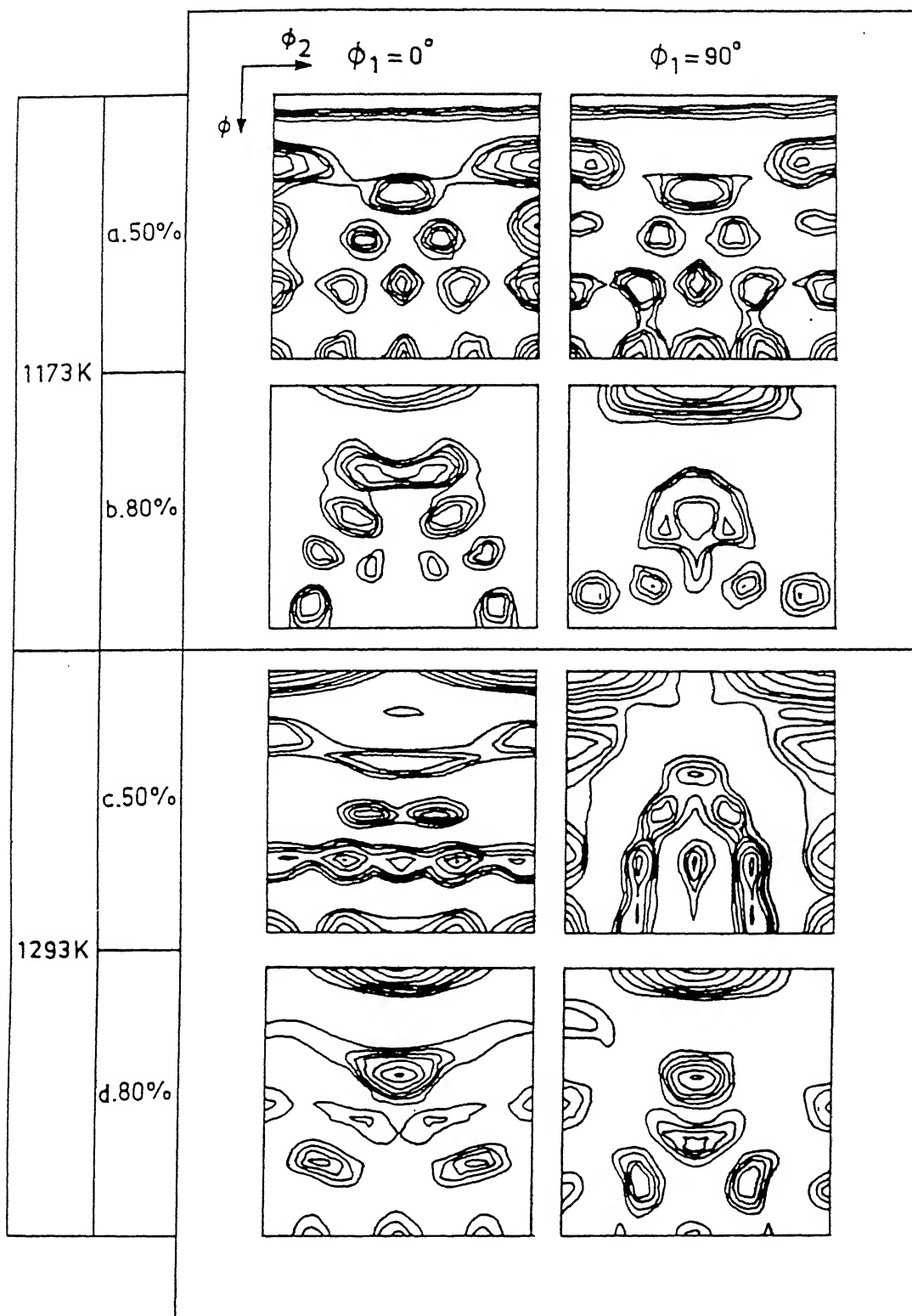


Fig. 4.41 $\phi_1 = 0^\circ$ and 90° sections of the ODFs of the as-cast material rolled to 50% and 80% reduction at (a, b) 1173 K and (c, d) 1293 K (all water quenched)

α_2 - Phase

The (0002) pole figure for the α_2 phase in the 50% rolled material shows a reasonably strong ($\sim 6 \times$ Random) near basal component of texture (Fig. 4.42 a). The pole density at the centre of the pole figure shows splitting along both RD and TD - the splitting along TD being most prominent. After 70% rolling the near basal component maintains its strength and shows splitting along TD only (Fig. 4.42 b). The basal component becomes more perfect after 80% rolling, although there is a slight tendency towards splitting along RD (Fig. 4.42 c). In all the above cases, a host of other weak components of texture is also seen.

In order to have a clearer idea of the different texture components, the orientation distribution function ODF plots of the 50%, 70% and 80% rolled specimens are presented in Figs. 4.43 (a to c). However, as the major orientations appear in the $\phi_2 = 0^\circ$ and 30° sections of the ODF, these have been separately displayed in Figs. 4.44 (a), (b) and (c). In all three of them, the orientations are found to be grouped near the $[0001] \parallel$ ND direction, indicating that some kind of a fibre is present along that direction. The intensity maxima, however, are shifted away from this exact location by different amounts in all the above plots. The $\phi_2 = 0^\circ$ section of the ODF for the 50% rolled material shows that the most intense peaks are present at $\phi \sim 6^\circ$ away from the ideal $(0001)[4\bar{1}\bar{3}0]$ and $(0001)[1\bar{2}10]$ locations. The $\phi_2 = 30^\circ$ section gives orientation maxima at near $(0001)[4\bar{3}\bar{1}0]$, at $\phi \sim 6^\circ$ from $(0001)[3\bar{4}10] \sim [1\bar{2}10]$ and also at locations in the neighbourhood of $(0001)[4\bar{4}01]$ and at

(0001)[$2\bar{5}32$] locations. The pole densities have been marked on the appropriate ϕ_2 sections.

The $\phi_2 = 0^\circ$ and 30° sections of the ODF for the 70% rolled material do not show any remarkable change from the corresponding sections for the 50% rolled material, except some little change in the locations of some of the maxima. The overall sharpness of the texture here does not seem to change significantly from that of the 50% rolled material.

Distinct changes in texture appear after the material is rolled by 80% reduction in thickness. Here, in addition, to having a fibre along [0001] || ND at $\phi = 6^\circ$ position, texture intensities are present along $[10\bar{1}0]$ || RD ($\phi_2 = 0^\circ$ section) and also to some extent along $[2\bar{1}\bar{1}0]$ || RD ($\phi_2 = 30^\circ$ section). The intensities along these lines show distinct peaks at the following locations : at $\sim 6^\circ$ along ϕ from ideal (0001)[$10\bar{1}0$], (0001)[$3\bar{4}10$], ($\bar{1}2\bar{1}0$)[$10\bar{1}0$], ($\bar{1}2\bar{1}2$)[$10\bar{1}0$] and ($\bar{2}4\bar{2}1$)[$10\bar{1}0$] (in the $\phi_2 = 0^\circ$ section) and at $\phi = 6^\circ$ from ideal (0001)[$4\bar{3}\bar{1}0$] as well as at ($01\bar{1}0$)[$2\bar{1}\bar{1}0$] and ($01\bar{1}4$)[$0\bar{2}21$] locations (in the $\phi_2 = 30^\circ$ section). There is a perceptible increase in the overall intensity of the texture after 80% rolling.

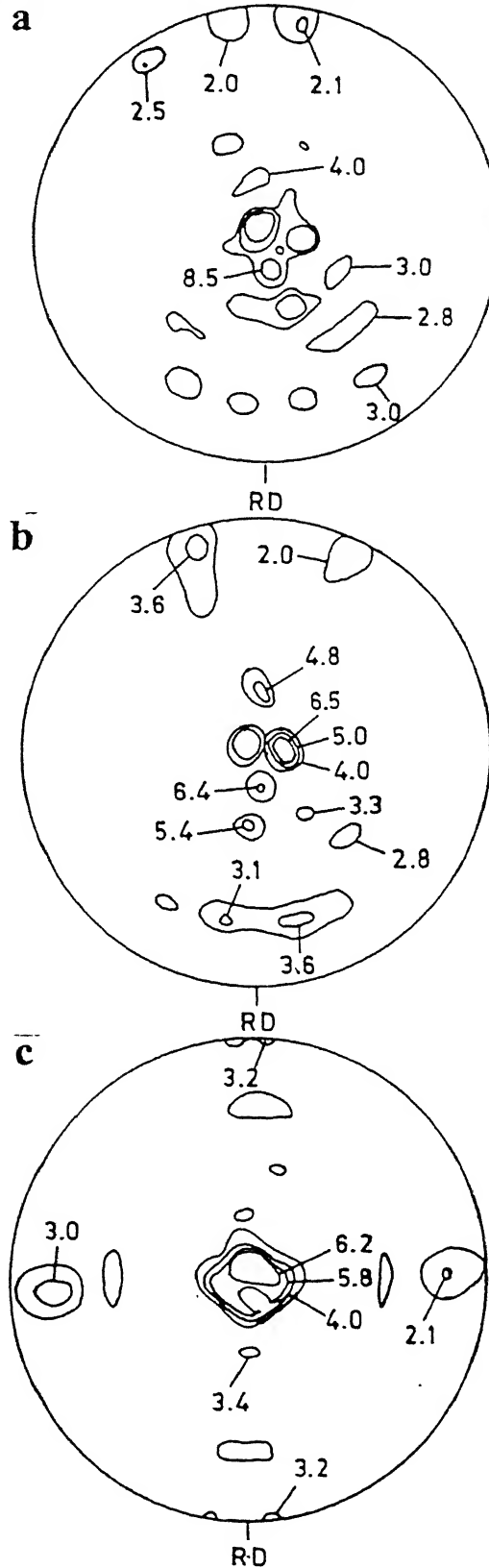


Fig. 4.42 $(0002)_{\alpha_2}$ pole figures for the as-cast and 1173 K rolled material subjected to (a) 50%, (b) 70% and (c) 80% reduction (all water quenched)

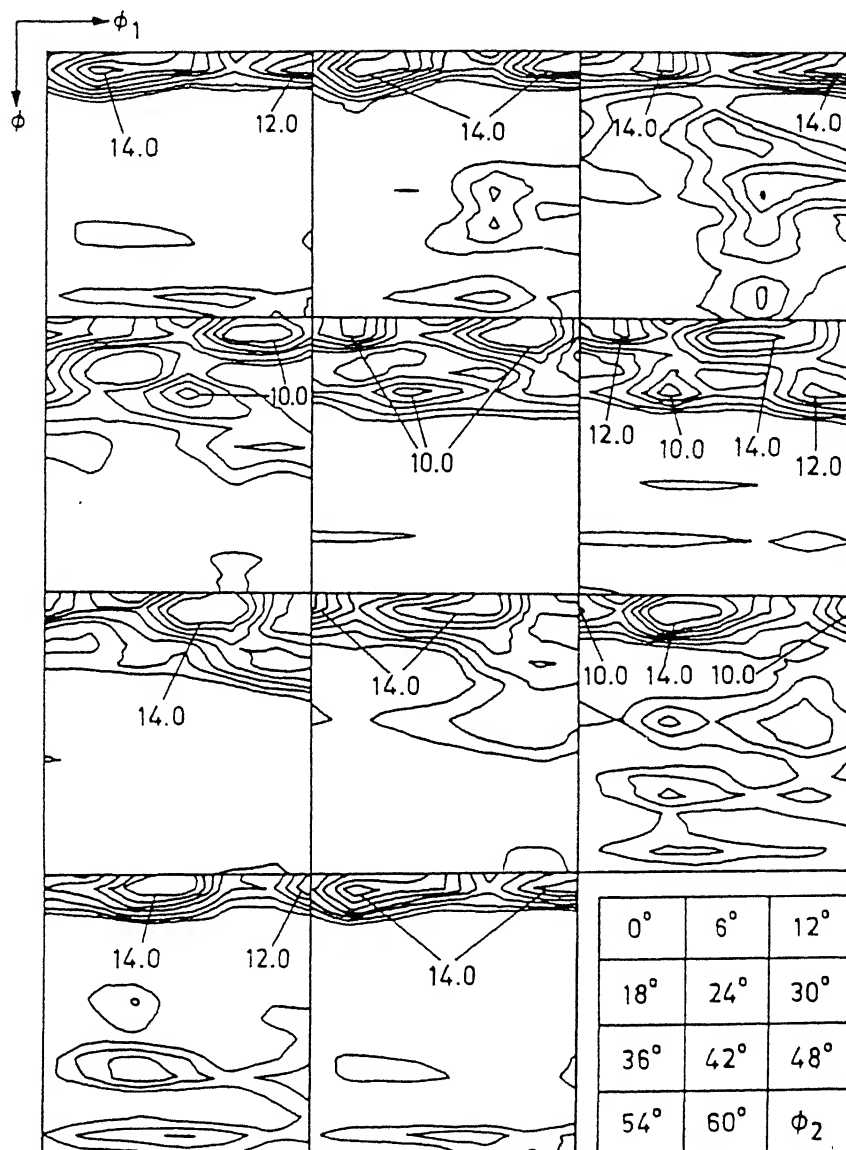


Fig. 4.43 (a) Complete ODF of the material as-cast and rolled at 1173 K to 50% reduction (water quenched)

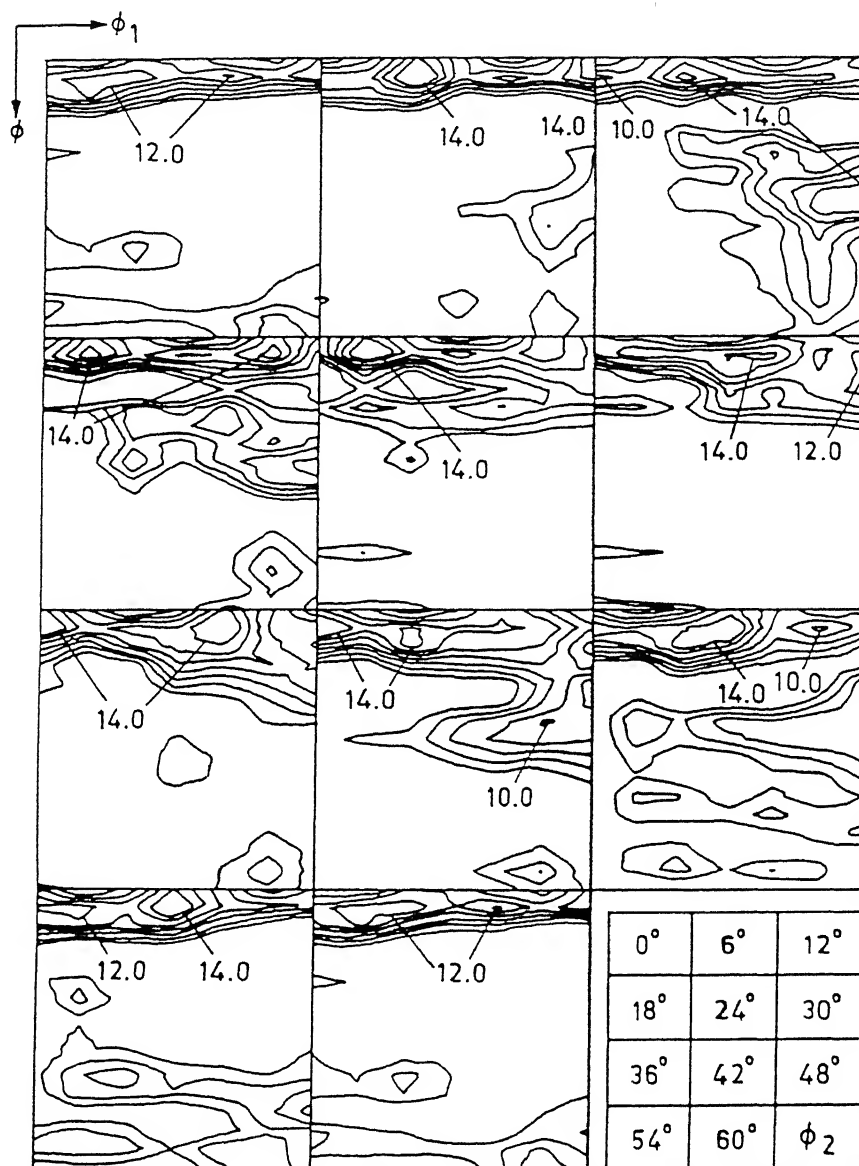


Fig. 4.43 (b) Complete ODF of the material as-cast and rolled at 1173 K to 70% reduction (water quenched)

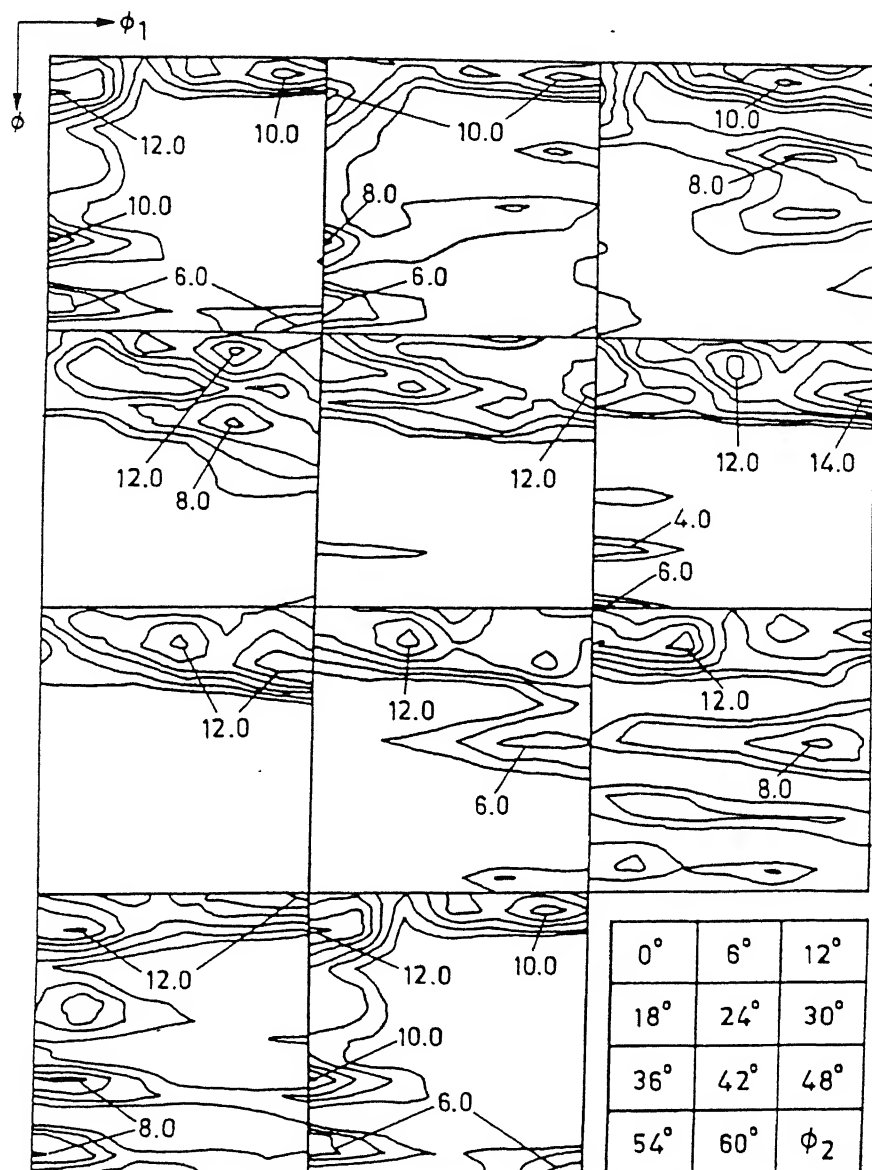


Fig. 4.43 (c) Complete ODF of the as-cast material rolled at 1173 K to 80% reduction (water quenched)

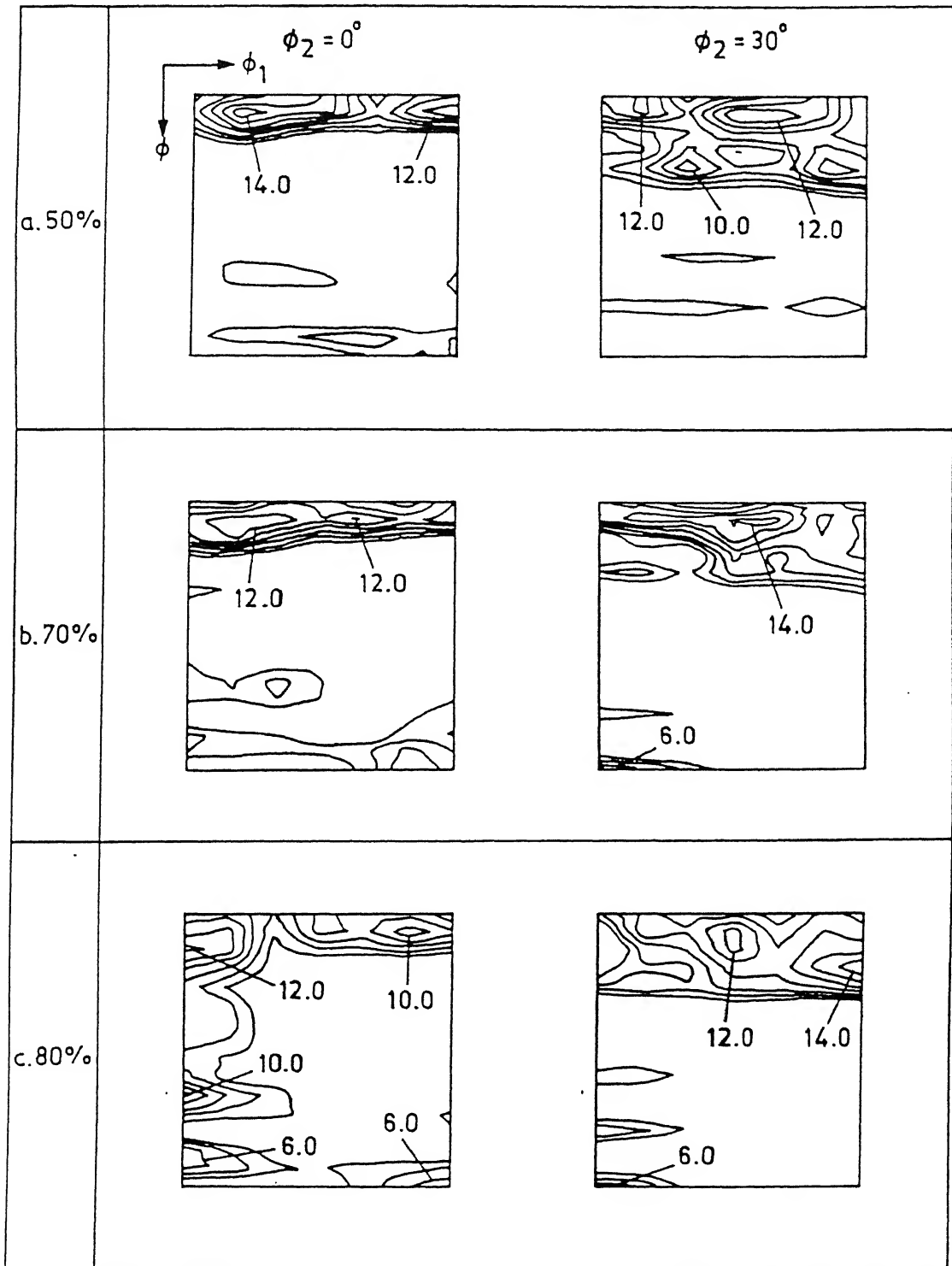


Fig. 4.44 $\phi_2 = 0^\circ$ and 30° sections of the ODFs of as-cast and 1173 K rolled materials for rolling reductions (a) 50%, (b) 70% and (c) 80% (all water quenched)

4.3.1.2 Heat treated, rolled and water quenched

α_2 - Phase

As mentioned in section 4.2, the XRD patterns for the α_2 phase in this material clearly show that the intensity of the (0002) basal peak increases continuously with increase in the rolling reduction. This is also corroborated by the pole figure data of the material. Figs. 4.45 (a), (b) and (c) show the (0002) pole figures of the heat treated material rolled 50%, 70% and 80% respectively. All the three pole figures show reasonably perfect basal texture, the degree of perfection increasing with the amount of rolling reduction. In all of them, in addition to the basal component, some other weak components can also be seen.

The ODF plots for these specimens are presented in Figs. 4.46 (a to c). For a comparison and for the sake of indexing the individual components, the $\phi_2 = 0^\circ$ and 30° sections of the ODFs for the three rolled materials are separately shown in Figs. 4.47 (a to c). The overall texture intensity appears to be quite comparable in case of the 70% and the 80% rolled materials, and this is perceptibly higher than in case of the 50% rolled sample. All these ODF sections clearly indicate the presence of a fibre tube along $(0001)\parallel ND$, the width of the tube is less in the $\phi_2 = 0^\circ$ section than in the $\phi_2 = 30^\circ$ section. The maxima of the fibre tubes, in each case, appear to lie not along the exact $(0001)\parallel ND$ fibre direction, but somewhat away from it.

For the 50% rolled material, in the $\phi_2 = 0^\circ$ section, the texture peaks appear at $\phi \sim 12^\circ$ away from $(0001)[10\bar{1}0]$, at $\phi \sim 6^\circ$ away from the $(0001)[4\bar{3}\bar{1}0]$ and also at

$\phi \sim 6^\circ$ away from the $(0001)[1\bar{2}10]$. In the $\phi_2 = 30^\circ$ section, the most intense peaks are $(01\bar{1}5)[3\bar{4}11]$ and $(01\bar{1}5)[0\bar{5}52]$.

For the 70% rolled material, in the $\phi_2 = 0^\circ$ section, the orientation maxima appear at $\phi \sim 12^\circ$ away from $(0001)[10\bar{1}0]$, at $\phi \sim 6^\circ$ away from $(0001)[2\bar{1}\bar{1}0]$ and at $(0001)[1\bar{2}10]$ locations. In the $\phi_2 = 30^\circ$ section, the most intense peaks are at $(01\bar{1}5)[5\bar{5}01]$ and $(01\bar{1}5)[0\bar{5}52]$ positions.

For the 80% rolled material, in the $\phi_2 = 0^\circ$ section, the maxima appear at $\phi \sim 12^\circ$ away from $(0001)[10\bar{1}0]$ and at $\phi_2 = 6^\circ$ away from $(0001)[1\bar{2}10]$. In the $\phi_2 = 30^\circ$ section, the most intense peaks are the ones near $(01\bar{1}5)[2\bar{1}\bar{1}0]$ and $(01\bar{1}5)[2\bar{1}\bar{1}0]$ locations. The distinguishing feature of the ODF sections in this case, as compared to the previous ones, is the presence of a more or less continuous fibre with substantial intensity all along $(0001)\parallel ND$ at $\phi = 6^\circ$ instead of having too many isolated peaks. In addition, most of the orientations get concentrated near to the aforementioned fibre unlike the previous case where several other orientations are also present in the ODF sections.

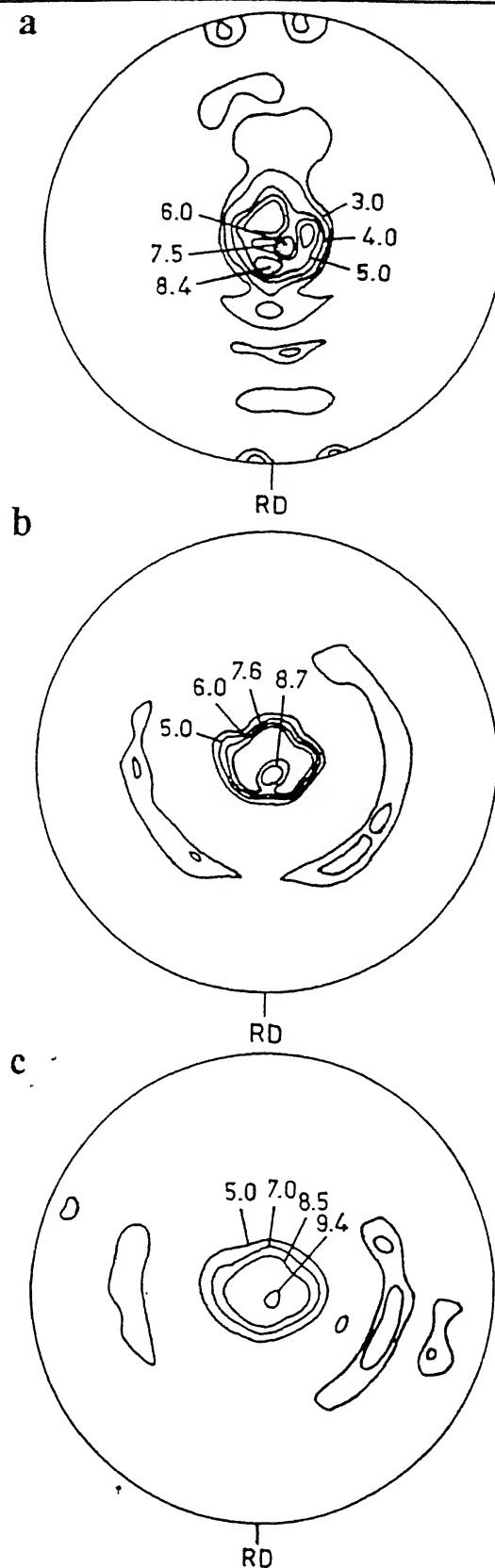


Fig. 4.45 (0002) α_2 pole figures of the materials heat treated (1173 K, 24 hrs./ FC) and rolled at 1173 K to reductions (a) 50%, (b) 70% and (c) 80% (all water quenched)

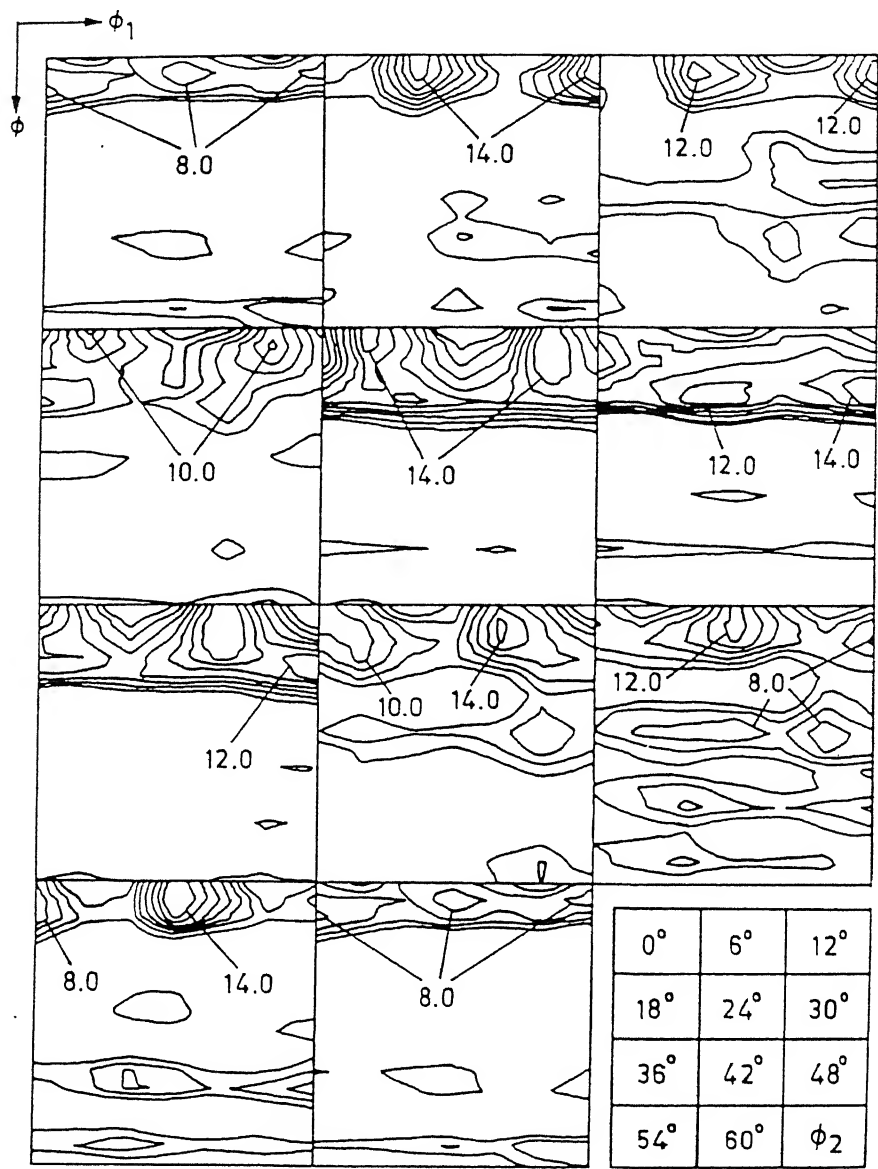


Fig. 4.46 (a) Complete ODF of the material heat treated and rolled at 1173 K to 50% reduction (water quenched)

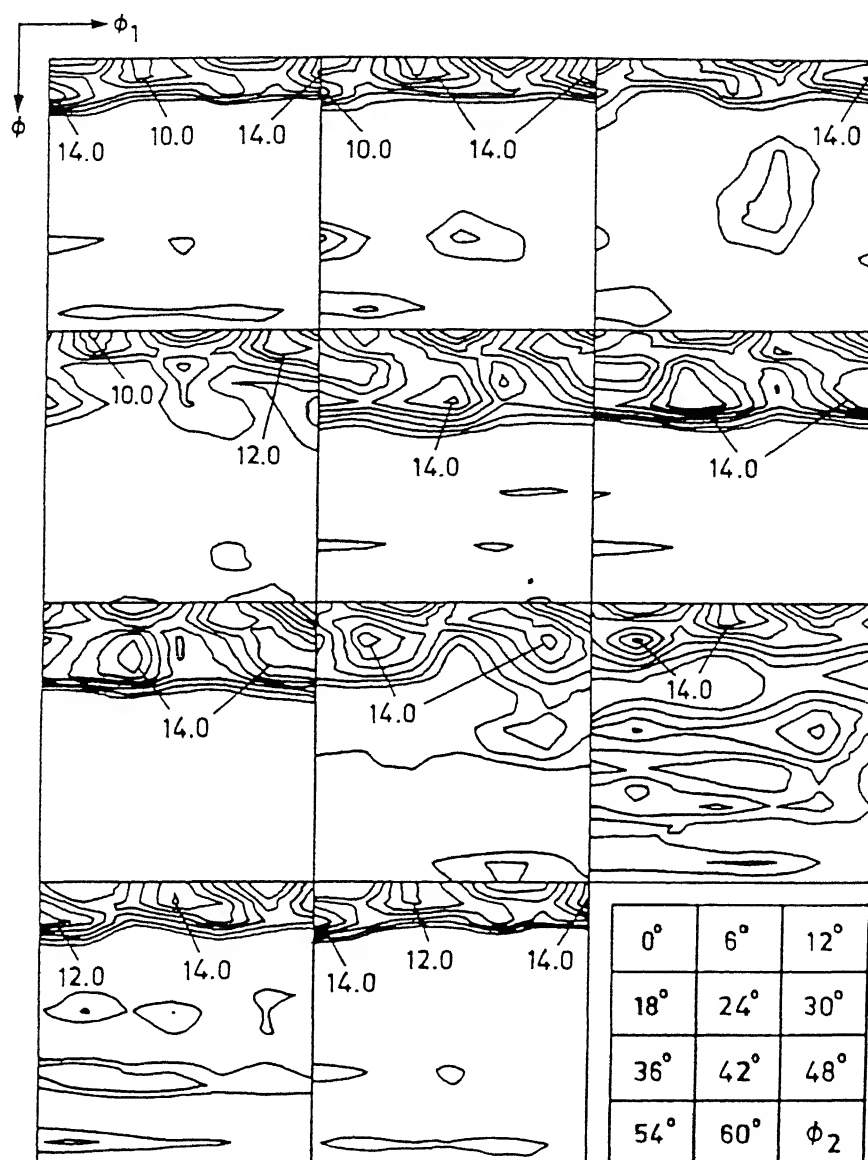


Fig. 4.46 (b) Complete ODF of the material heat treated and rolled at 1173 K to 70% reduction (all water quenched)

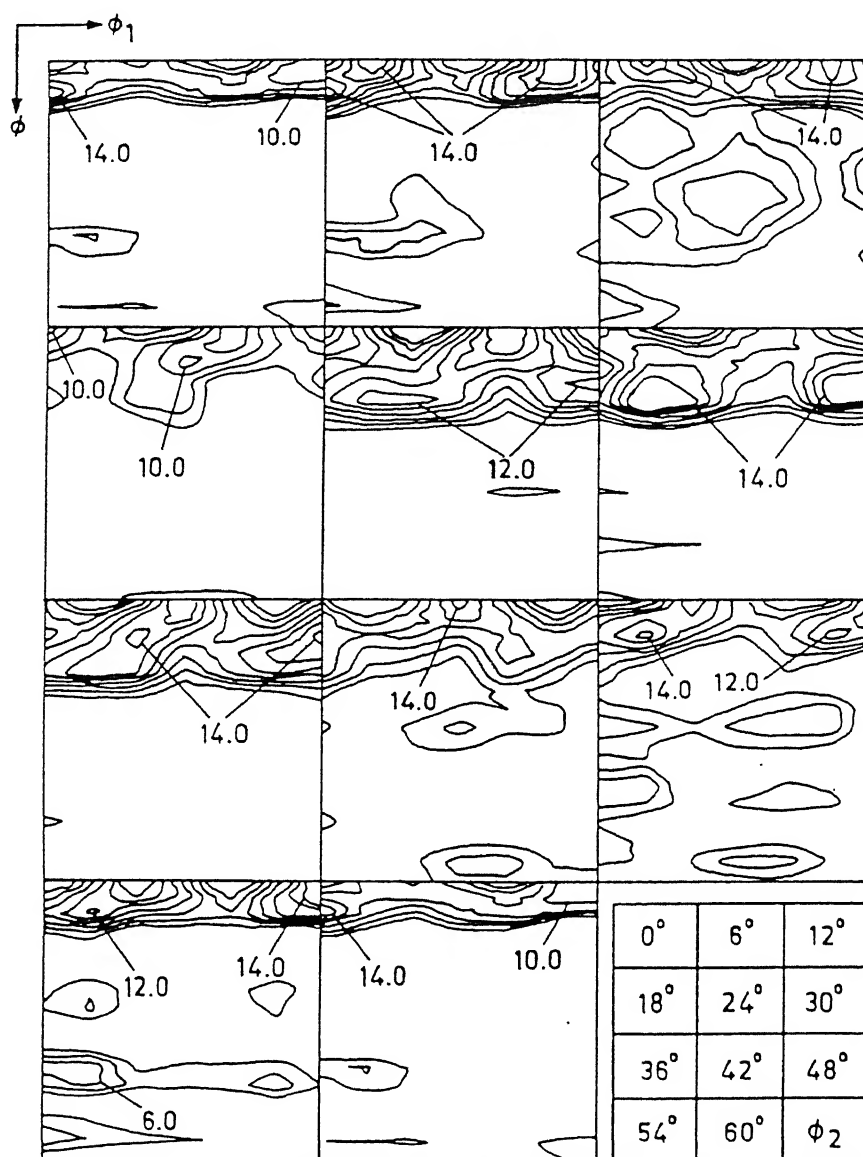


Fig. 4.46 (c) Complete ODF of the material heat treated and rolled at 1173 K to 80% reduction (water quenched)

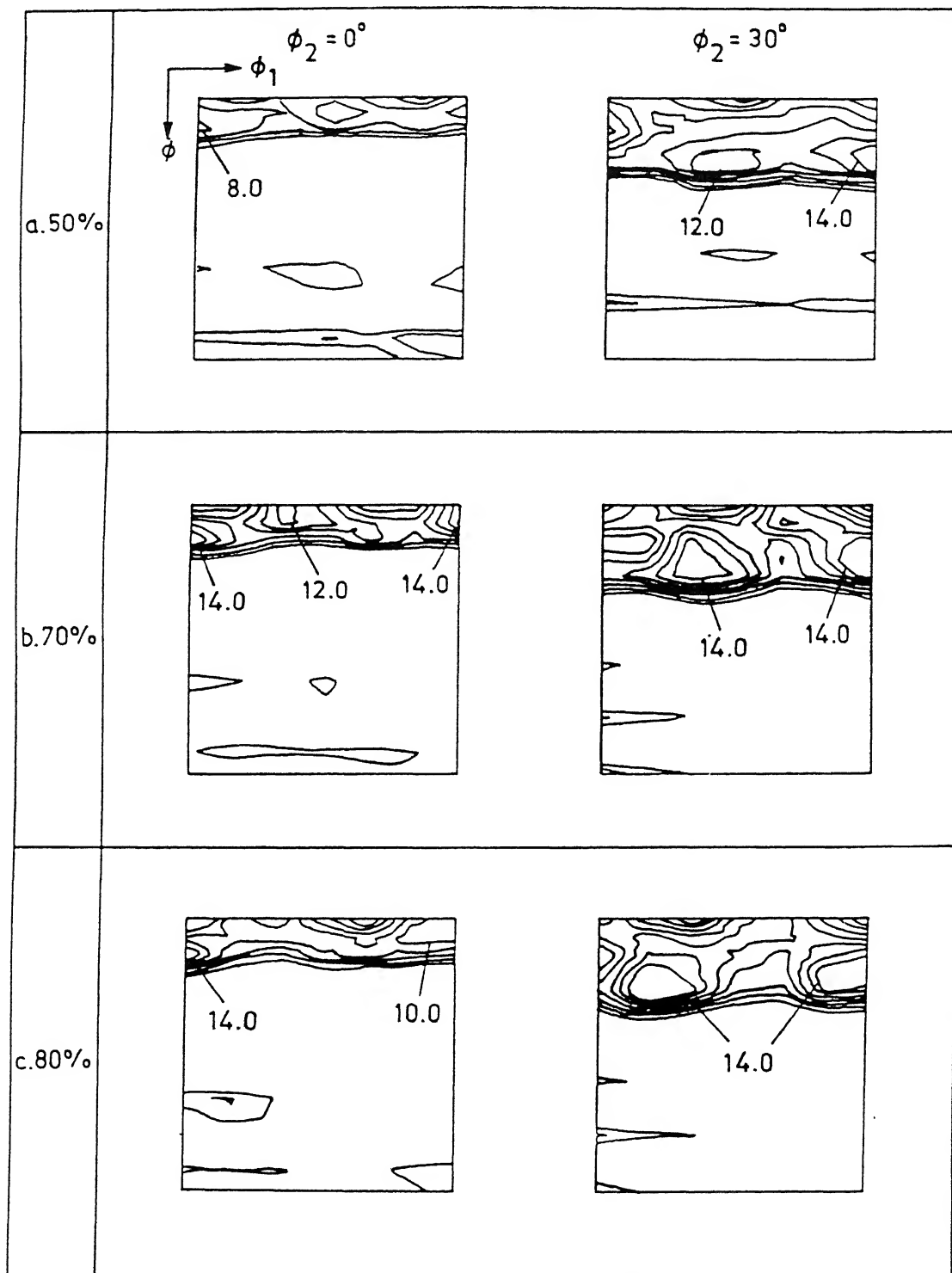


Fig. 4.47 $\phi_2 = 0^\circ$ and 30° sections of ODFs of the heat treated and 1173 K rolled materials; rolled reductions: (a) 50%, (b) 70% and (c) 80% (all water quenched)

4.3.1.3 As-cast, rolled and furnace cooled

α_2 - Phase

The (0002) pole figure of this material (Fig. 4.48 a) shows a reasonably sharp and perfect basal texture [$f(g) = 5.0$]. In addition, there are high pole densities at many places along the periphery of the pole figure. These texture components may be indexed as $\{1230\}\langle uvw \rangle$, $\{1120\}\langle uvw \rangle$, $\{1010\}\langle uvw \rangle$ where $\{1230\}$, $\{1120\}$ and $\{1010\}$ planes belong to the zone for which $[0002]$ is the zone axis.

The ODF plot for this specimen is given in Fig. 4.49 and the $\phi_2 = 0^\circ$ and 30° sections are separately given in Fig. 4.50 (a). The $\phi_2 = 0^\circ$ section of the ODF shows a fibre along the $(0001)\parallel ND$ having a maxima at $(0001)[4\bar{3}\bar{1}0]$. In addition, two other texture components can be seen at $(\bar{1}2\bar{1}0)[10\bar{1}0]$ and $(\bar{1}2\bar{1}3)[2\bar{1}\bar{1}1]$ or $(\bar{1}2\bar{1}3)[5\bar{3}23]$ locations.

The $\phi_2 = 30^\circ$ section shows the presence of weak texture components such as $(0001)[4\bar{3}\bar{1}0]$ and $(0001)[1\bar{4}30]$ along the $(0001)\parallel ND$ fibre. Presence of a fibre running along ϕ_1 with maxima at $(01\bar{1}6)[4\bar{5}11]$ is also discernible. In addition, there is another fibre along ϕ_1 in the neighbourhood of $(01\bar{1}1)\langle uvw \rangle$ which also has a couple of orientation maxima lying on it. Furthermore, there are two other components also present such as $(01\bar{1}0)[4\bar{2}2\bar{1}]$ and $(01\bar{1}0)[2\bar{1}\bar{1}6]$.

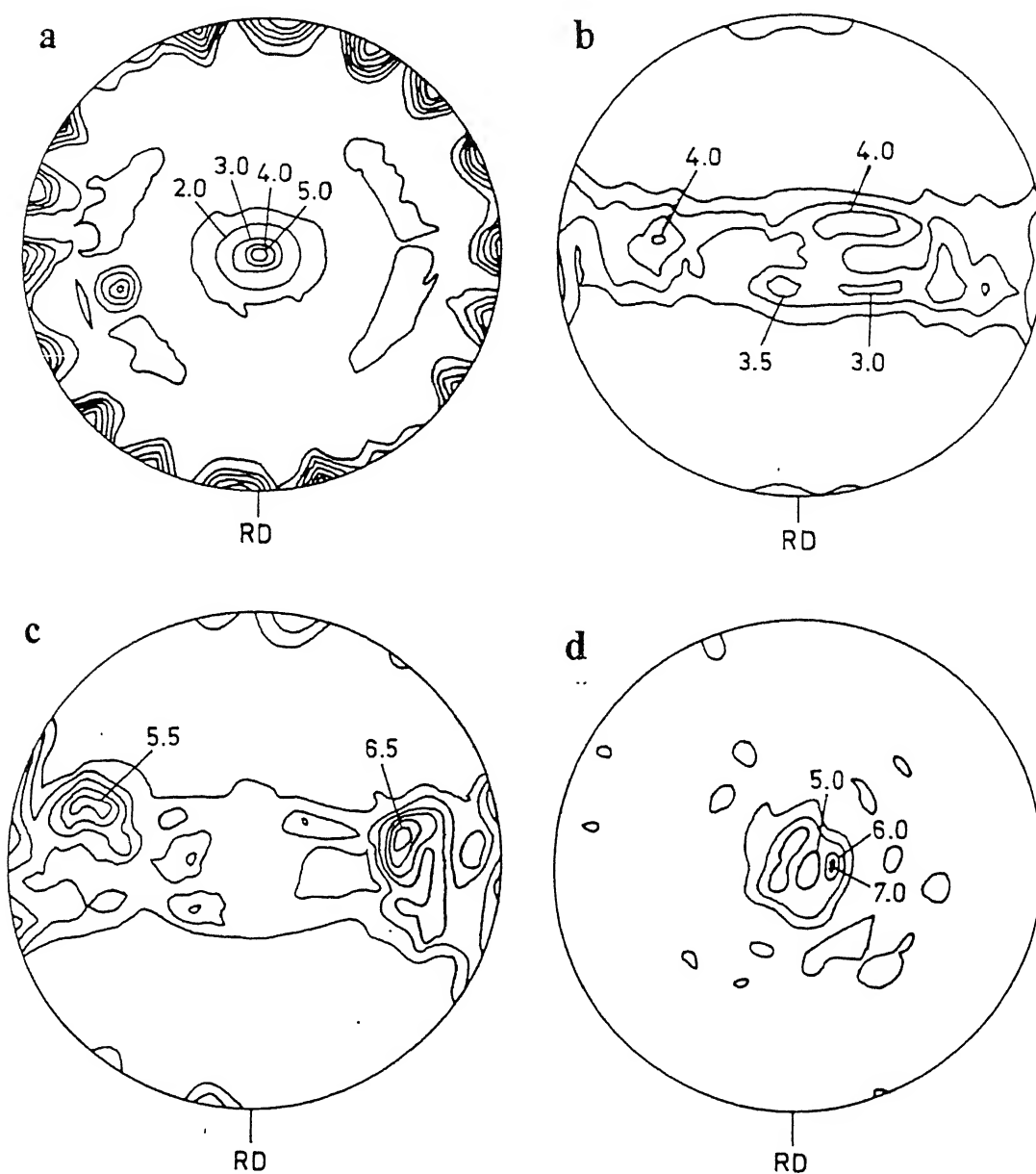


Fig. 4.48 $(0002)_{\alpha}$ pole figure of the as-cast material rolled to 80% reduction at (a) 1173 K, (b) 1293 K, (c) 1373 K and (d) 1523 K (furnace cooled)

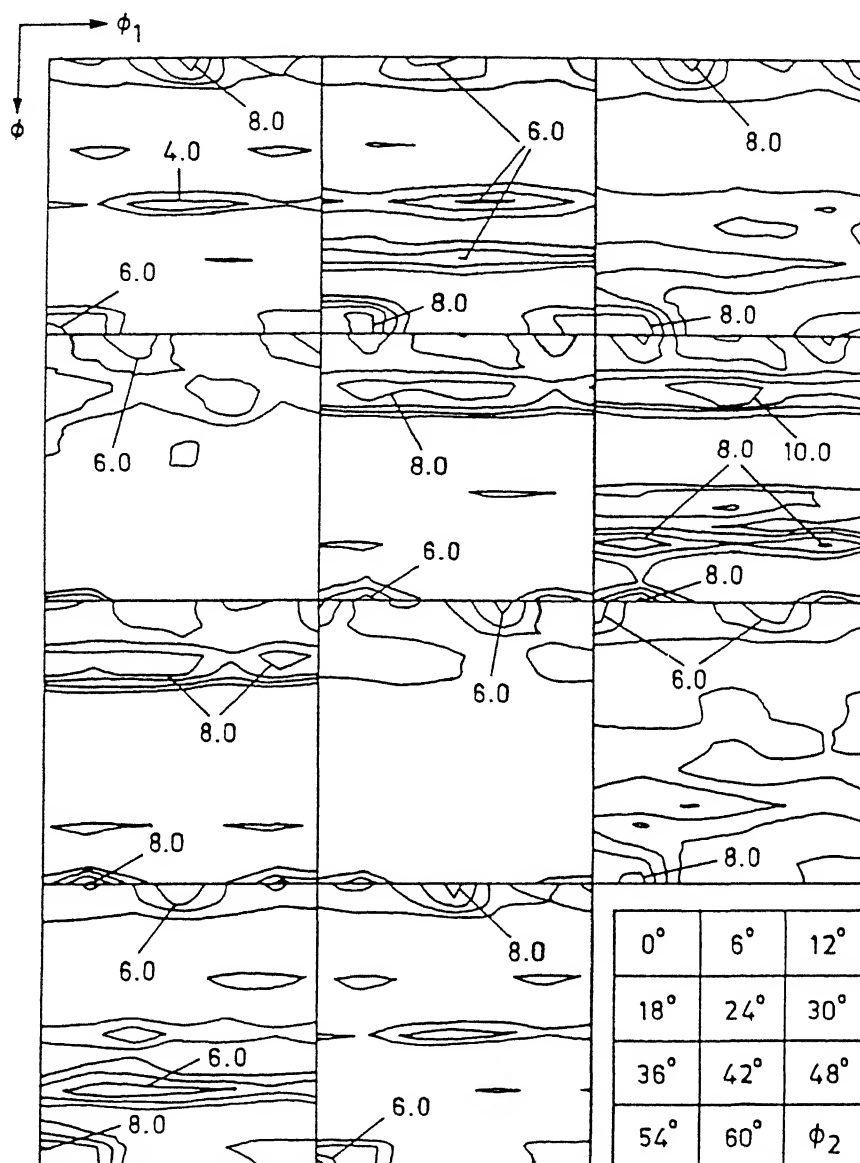


Fig. 4.49 Complete ODF of the material as-cast, rolled at 1173 K to 80% reduction and furnace cooled

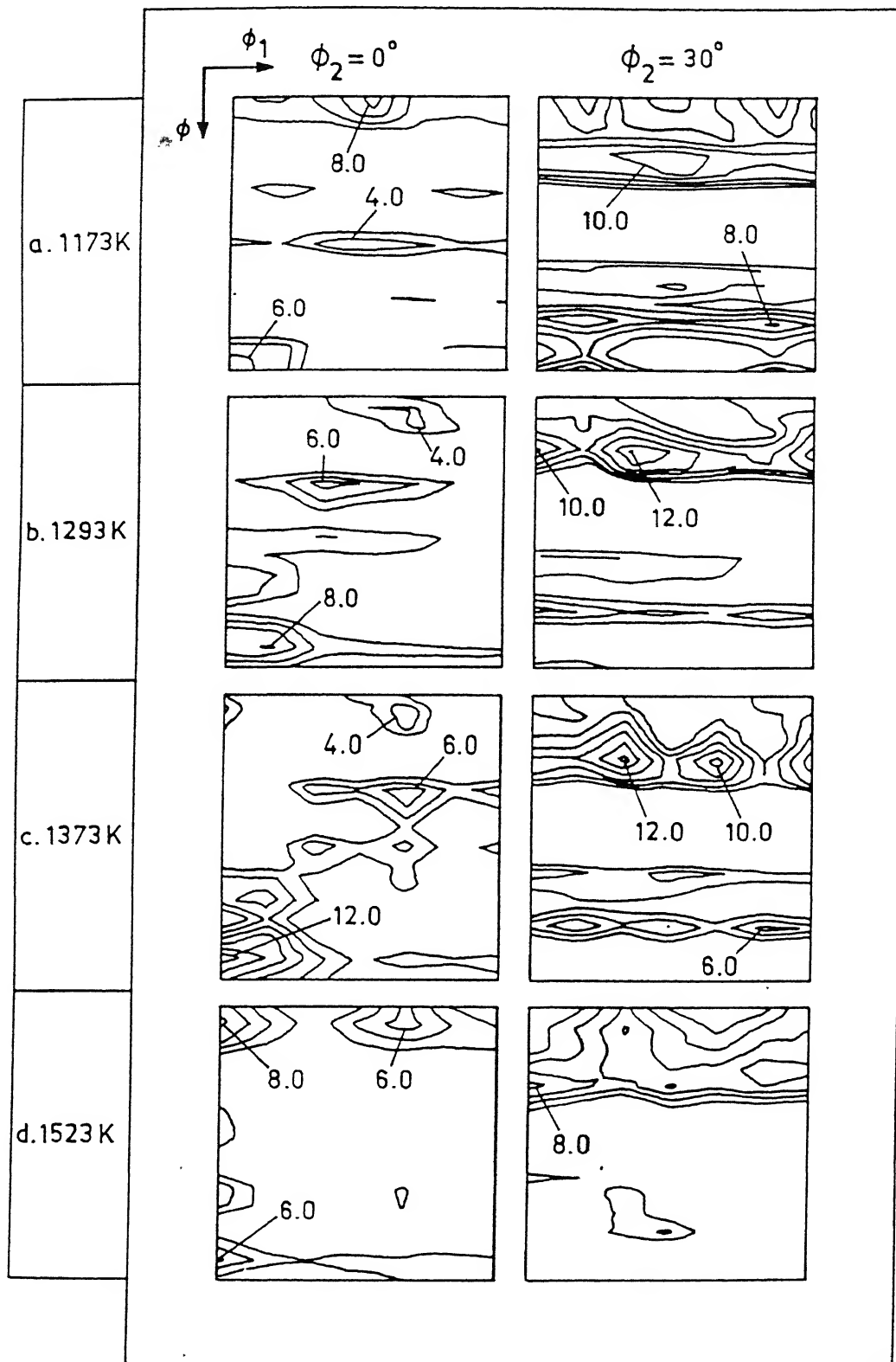


Fig. 4.50 $\phi_2 = 0^\circ$ and 30° sections of the ODFs of the as-cast material rolled to 80% reduction at (a) 1173 K, (b) 1293 K, (c) 1373 K and (d) 1523 K (all furnace cooled)

α_2 - Phase

The (0002) pole figure for the α_2 phase in the 50% rolled material shows a basal component of texture plus few other components (Fig. 4.51 a). The intensity level for the basal orientation appears to be 6xRandom. At the higher degree of deformation (80%), the basal component shows a tendency of splitting (Fig. 4.51 b), although the intensity remains as high as in the 50% rolled case. Some extra orientations do appear in this case also but with lesser intensity (4xRandom).

The orientation distribution function plots for the materials rolled 50 % and 80 % at 1293 K and water quenched are shown in Figs. 4.52 (a and b). The $\phi_2 = 0^\circ$ and 30° sections of the ODFs are shown separately in Figs. 4.53 (a and b). The 50% rolled material shows a relatively weak h.c.p. texture with (0001)[01 $\bar{1}$ 0], (0001)[1 $\bar{1}$ 00], an orientation nearly 12° off from (0001)[2 $\bar{1}$ $\bar{1}$ 0] and ($\bar{1}$ 2 $\bar{1}$ 0)[0001] as the major components. Other relatively weak orientations are identified as ($\bar{1}$ 2 $\bar{1}$ 4)[4 $\bar{4}$ 03] and ($\bar{2}$ 4 $\bar{2}$ 3)[1 $\bar{2}$ 14]. For the 80% rolled material, a strong basal texture with the components (0001)[4 $\bar{1}$ $\bar{3}$ 0], (0001)[5 $\bar{4}$ $\bar{1}$ 0], (0001)[3 $\bar{4}$ 10], ($\bar{2}$ 4 $\bar{2}$ 1)[10 $\bar{1}$ 0] and ($\bar{2}$ 4 $\bar{2}$ 3)[10 $\bar{1}$ 0] are observed in the $\phi_2 = 0^\circ$ and (01 $\bar{1}$ 7)[1 $\bar{4}$ 31], (01 $\bar{1}$ 5)[2 $\bar{1}$ $\bar{1}$ 0], (0001)[4 $\bar{3}$ 10] and (0001)[3 $\bar{4}$ 10] in the $\phi_2 = 30^\circ$ sections of the ODF.

4.3.2.2. As-cast, rolled and furnace cooled

α_2 - Phase

The (0002) pole figure for the material furnace cooled from 1293 K after the finish rolling pass is shown in Fig. 4.48 (b). It shows the presence of a weak texture of mixed character, that is, the basal poles show a tendency of splitting along both RD as well as TD. The corresponding ODF is presented in Fig. 4.54. The $\phi_2 = 0^\circ$ and 30° sections of the ODF for the furnace cooled material (Fig. 4.50 b) do not show the presence of strong (0001) $\langle uvw \rangle$ orientations unlike in the previous case of the 1173 K rolled and furnace cooled material. Only a weak basal component (0001)[1 $\bar{1}$ 00] is seen in the $\phi_2 = 0^\circ$ section of the ODF. The main orientations, in the $\phi_2 = 0^\circ$ section are (10 $\bar{1}$ 7)[uvw], ($\bar{2}$ 4 $\bar{1}$ 0)[10 $\bar{1}$ 0], ($\bar{1}$ 2 $\bar{1}$ 2)[10 $\bar{1}$ 0] and (01 $\bar{1}$ 7)[uvw] with one of the maxima at (01 $\bar{1}$ 7)[2 $\bar{1}$ $\bar{1}$ 0] and the orientation (02 $\bar{2}$ 1)[1 $\bar{1}$ 02] in the $\phi_2 = 30^\circ$ section.

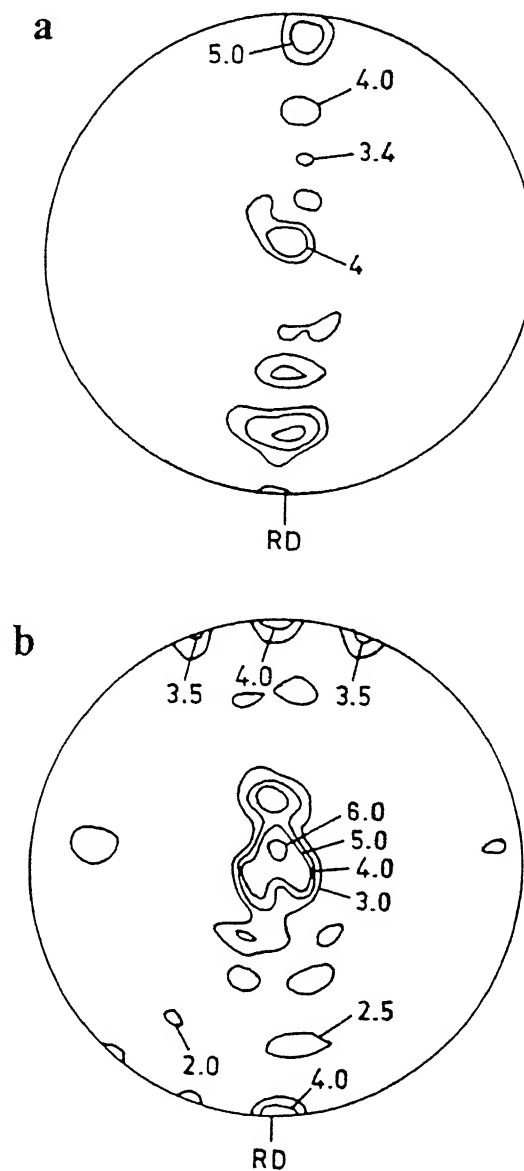


Fig. 4.51 $(0002)_{\alpha_2}$ pole figure of the material as-cast, rolled at 1293 K to (a) 50% and (b) 80% reductions and water quenched

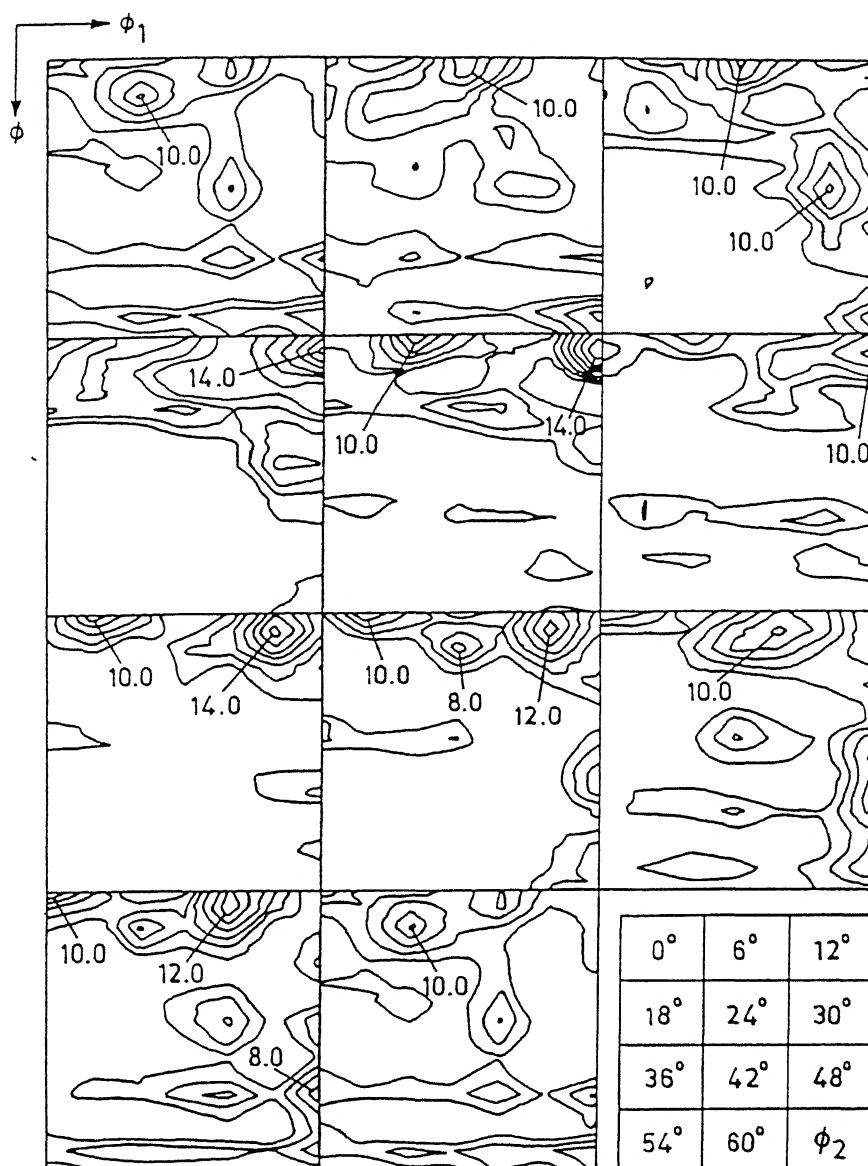


Fig. 4.52 (a) Complete ODF of the material as-cast, rolled at 1293 K to 50% reduction and water quenched

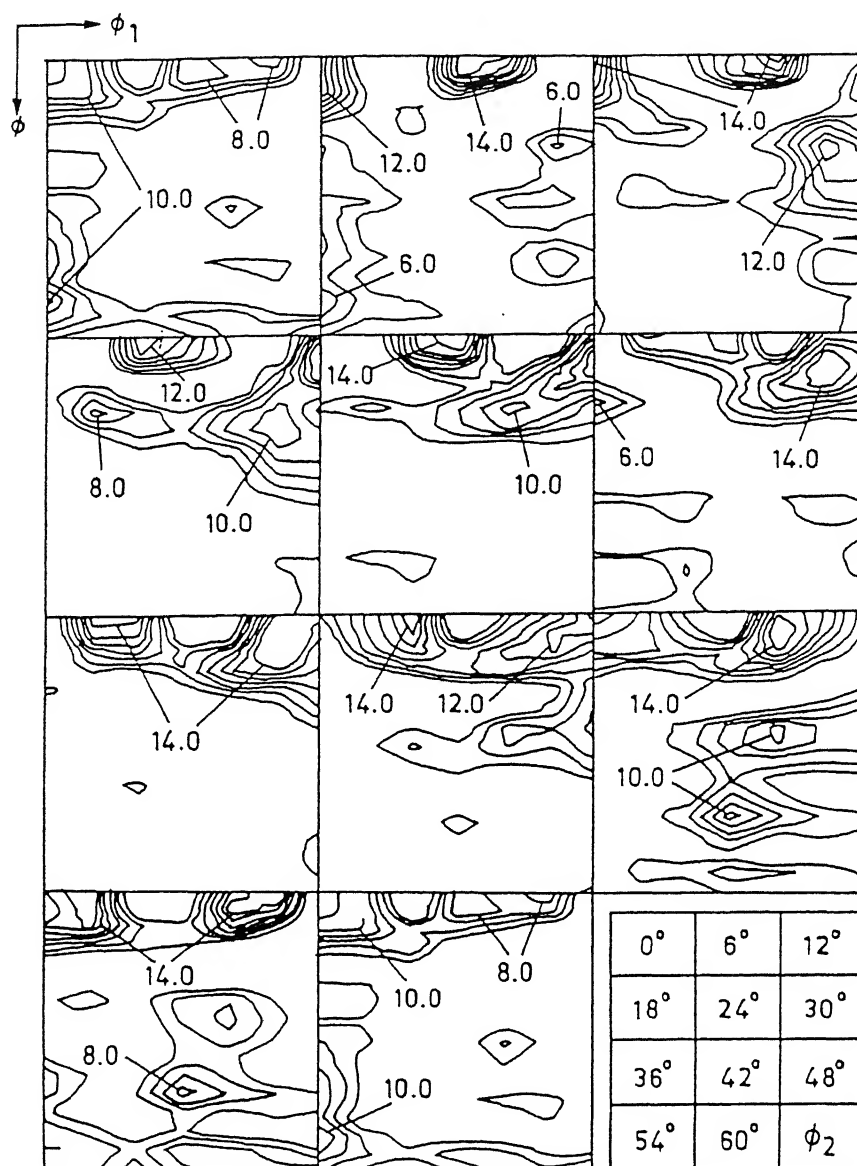


Fig. 4.52 (b) Complete ODF of the material as-cast, rolled at 1293 K to 80% reduction and water quenched

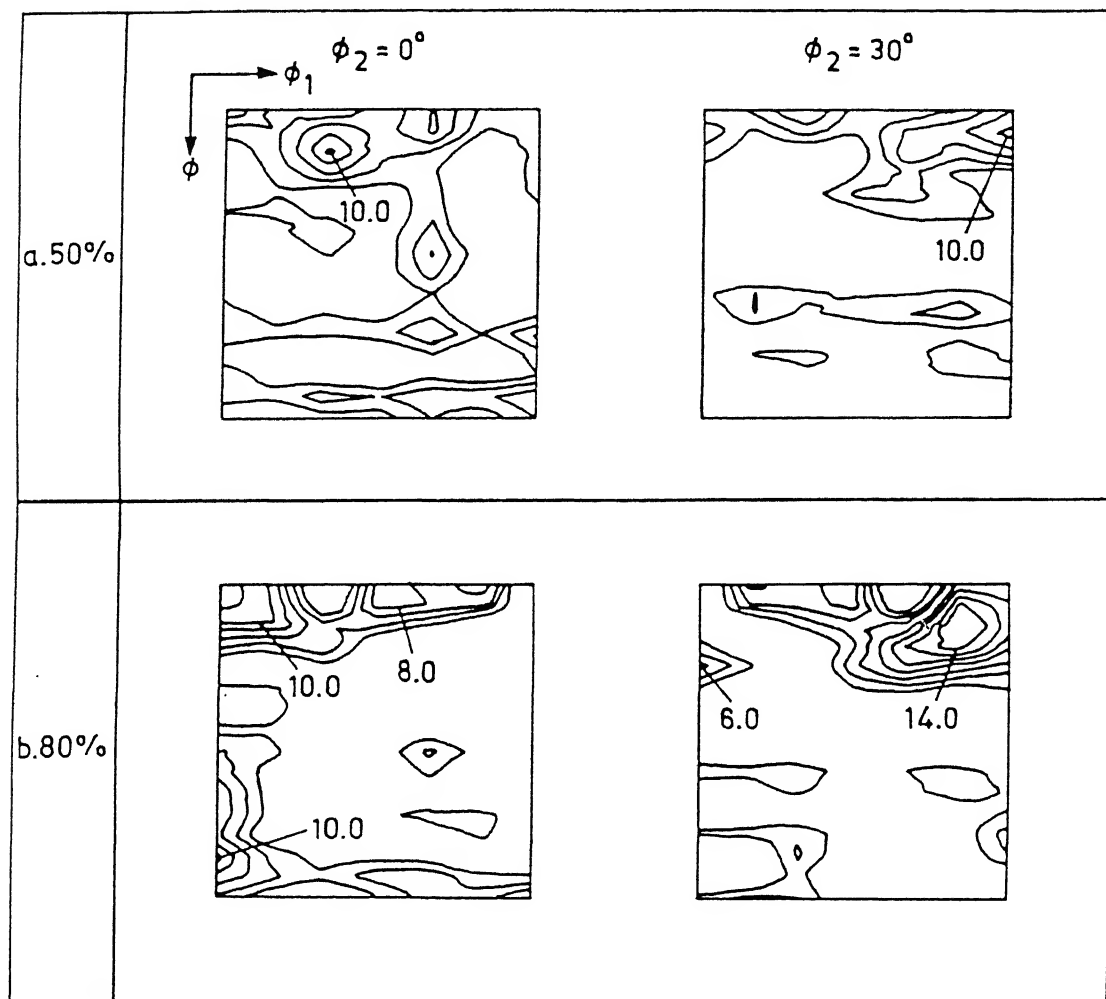


Fig. 4.53 $\phi_2 = 0^\circ$ and 30° sections of ODF for the as-cast material rolled at 1293 K to reductions (a) 50% and (b) 80% (all water quenched)

4.3.3 Texture of material rolled at 1373 K

4.3.3.1 As-cast, rolled and water quenched

β - phase

The material, at 1373 K, mainly consists of the b.c.c. β phase. The (200) pole figures for the 1373 K rolled material are displayed in Figs. 4.55 (a and b). Parts of $\{210\}\langle uvw \rangle$ and $\{113\}\langle uvw \rangle$ fibres are clearly seen. However, the intensity levels are quite low as compared to the intensity levels for (200) pole figures of the β phase corresponding to the previous two conditions, namely 1173 K and 1293 K rolled materials. For the 80% rolled material at this temperature, the (200) pole figure shows an intense $\{113\}\langle uvw \rangle$ fibre.

Figs. 4.56 (a and b) and 4.57 (a and b) show the $\phi_2 = 0^\circ$ and 45° sections as well as $\phi_1 = 0^\circ$ and 90° sections of the ODF plots for 50% and 80% rolled materials. The $\{011\}\langle 100 \rangle$ orientations are found to be the strongest in the case of 50% rolled material, which further intensify in the 80% rolled material. The other strong orientations are $\{011\}\langle 011 \rangle$ which again become stronger in 80% rolled condition. The $\{013\}\langle 110 \rangle$ orientations are relatively weak in the case of 50% rolled material and become substantially strong in the case of 80% rolling deformation. Other orientations appearing in the ODF of 50% rolled material which are rather weak are $\{013\}\langle 031 \rangle$. In addition to these, a number of other strong orientations with high indices do appear in case of the 50% rolled material, such as $\{379\}\langle 5121 \rangle$, $\{420\}\langle 212 \rangle$, $\{3112\}\langle 130 \rangle$, $\{1211\}\langle 210 \rangle$, $\{233\}\langle 320 \rangle$, which do not appear in the

case of 80% rolled material. Similarly, a number of extra orientations also appear in the case of 80% rolled condition which are not inherited from the 50% rolled material. The strongest amongst them are $\{122\}\langle 245 \rangle$, $\{212\}\langle 425 \rangle$, $\{122\}\langle 210 \rangle$, $\{112\}\langle 111 \rangle$, $\{112\}\langle 110 \rangle$, $\{011\}\langle 110 \rangle$, $\{001\}\langle 230 \rangle$, $\{001\}\langle 320 \rangle$, $\{001\}\langle 320 \rangle$.

4.3.3.2 As-cast, rolled and furnace cooled

α_2 - phase

As stated in section 4.1, a piece of the 80% rolled material was furnace cooled from the rolling temperature, thereby transforming the β (B2) phase into α_2 . The (0002) pole figure for the specimen represents (Fig. 4.48 c) a completely non-basal texture with (0002) poles located almost 70° off from the centre towards TD.

The complete ODF for the furnace cooled material is displayed in Fig. 4.58 and the $\phi_2 = 0^\circ$ and 30° sections of the ODF for this material is presented in Fig. 4.50 (c). The most intense orientations which appear in this case are of $(hkl)[10\bar{1}0]$, $(hkl)[2\bar{1}\bar{1}0]$ and $(02\bar{2}1)[uvw]$ type with an exception $(\bar{1}2\bar{1}5)[5\bar{5}03]$.

4.3.4. Texture of material rolled at 1523 K

4.3.4.1 As-cast, rolled and water quenched

β - Phase

It has already been mentioned in section 4.1 that the material in this case consists of single phase β . The (200) pole figures for the 50% and 80% rolled

conditions are shown in Figs. 4.55 (c and d). The nature of these pole figures are almost similar to the ones for the case of 1373 K rolled material except for a little difference in the continuity of orientation contours. In the present case, the orientation contours become nearly continuous while in the former case (1373 K rolled material), isolated intensity maxima on the corresponding fibres are observed.

For a clearer understanding of the texture, ODF sections $\phi_2 = 0^\circ$ and 45° as well as $\phi_1 = 0^\circ$ and 90° are presented in Figs. 4.56 (c and d) and 4.57 (c and d) respectively. It can be seen from the ODFs of both the 50% and 80% rolled materials that all the components present in the case of 1373 K rolled material are present here, however, with improved sharpness.

4.3.4.2 As-cast, rolled and furnace cooled

α_2 -Phase

The material in the present case consists of transformed α_2 . The (0002) pole figure for this material rolled to 80% reduction and furnace cooled is shown in Fig. 4.48 (d). In contrast with the pole figure for the 1373 K rolled and furnace cooled material, the pole figure shows the presence of (0002) poles concentrated at the ND position. In addition, the pole figure also indicates the split TD character of the basal texture.

The basal character of texture is further confirmed by the corresponding ODF (Fig. 4.59). The examination of the $\phi_2 = 0^\circ$ and 30° sections of the ODF (Fig. 4.50 d)

reveals the presence of appreciably strong basal texture with orientation maxima at $(0001)[10\bar{1}0]$ and $(0001)[1\bar{1}00]$. Some other relatively weak orientations like $(\bar{2}4\bar{2}1)[10\bar{1}0]$, $(\bar{1}2\bar{1}2)[10\bar{1}0]$, $(01\bar{1}5)[2\bar{1}\bar{1}0]$ and $(01\bar{1}6)[0\bar{3}31]$ are also present.

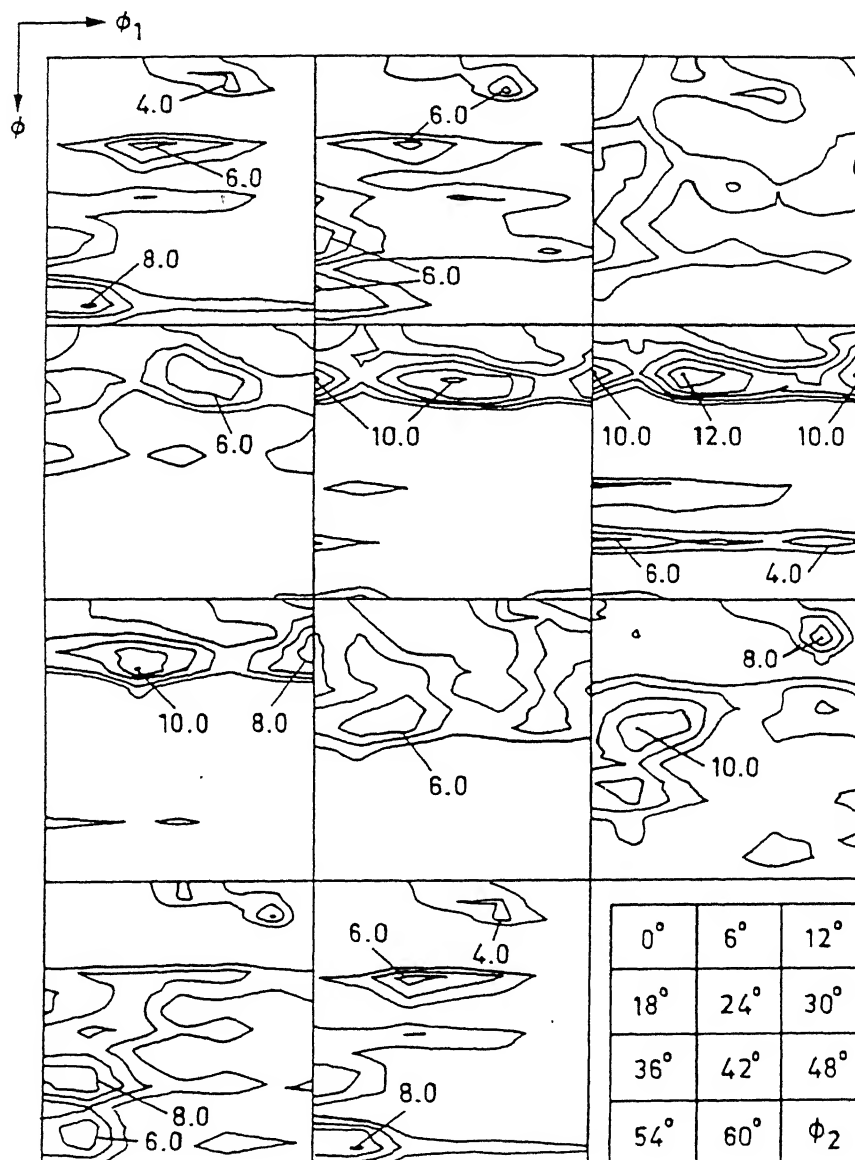


Fig. 4.54 Complete ODF of the material as-cast, rolled at 1293 K to 80% reduction and furnace cooled

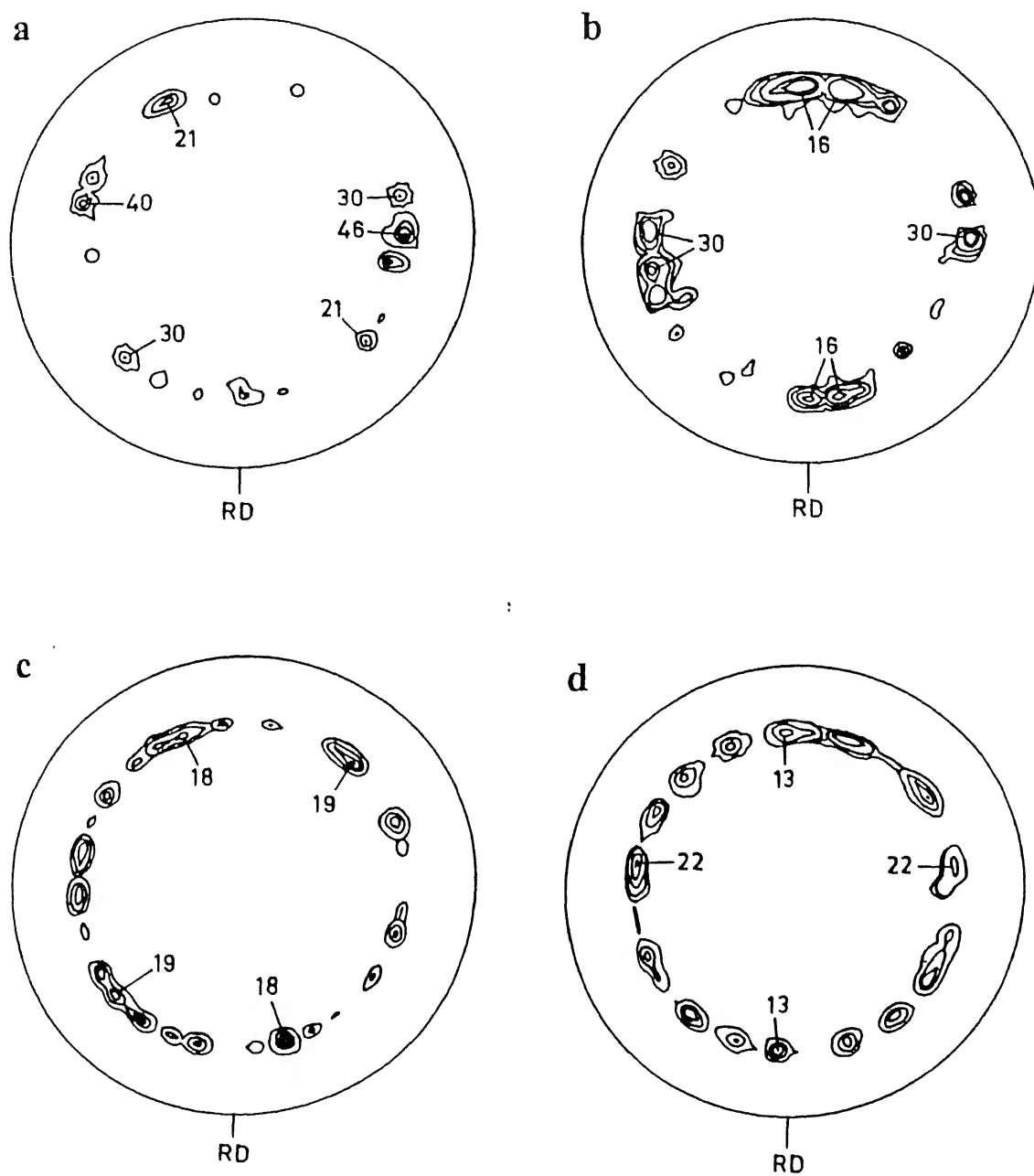


Fig. 4.55 $(200)_\beta$ pole figure of the as-cast material rolled to 50% and 80% reductions at (a, b) 1373 K and (c, d) 1523 K

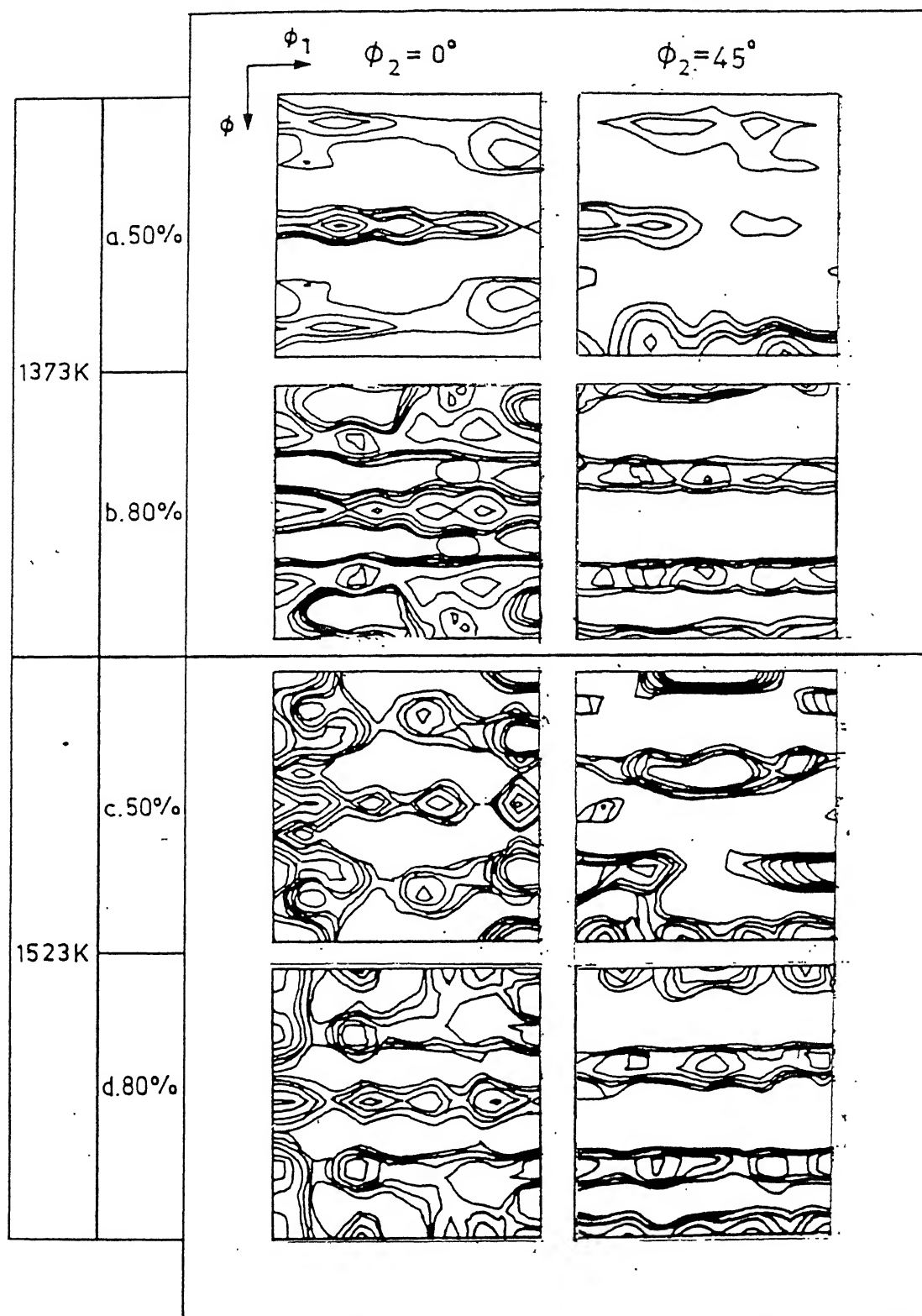


Fig. 4.56 $\phi_2 = 0^\circ$ and 45° sections of the ODFs of the as-cast material rolled to 50% and 80% reductions at (a, b) 1373 K and (c, d) 1523 K (all water quenched)

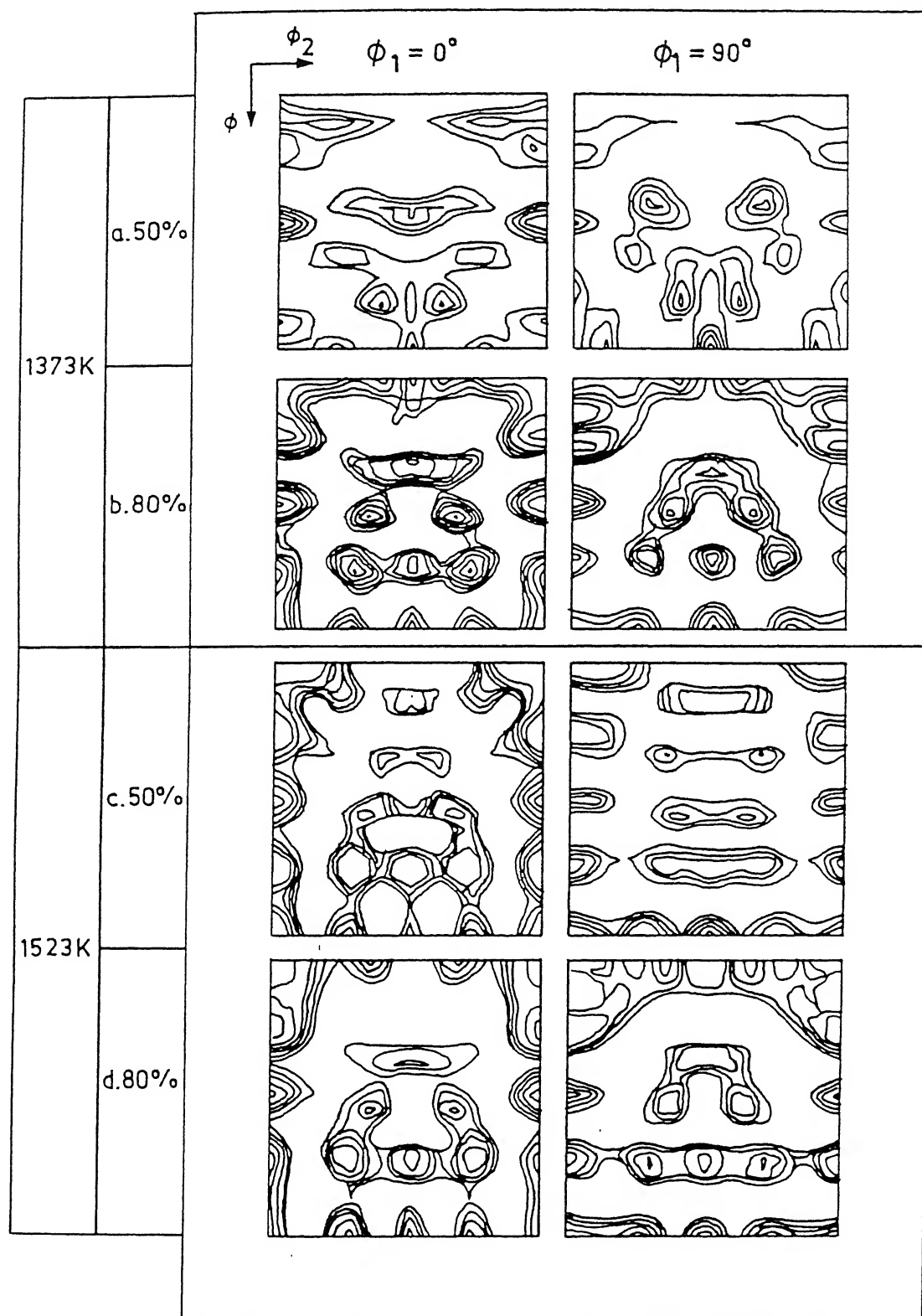


Fig. 4.57 $\phi_1 = 0^\circ$ and 90° sections of ODF of the material as-cast and rolled at (a, b) 1373 K and (c, d) 1523 K to reductions 50% and 80% each followed by water quenching

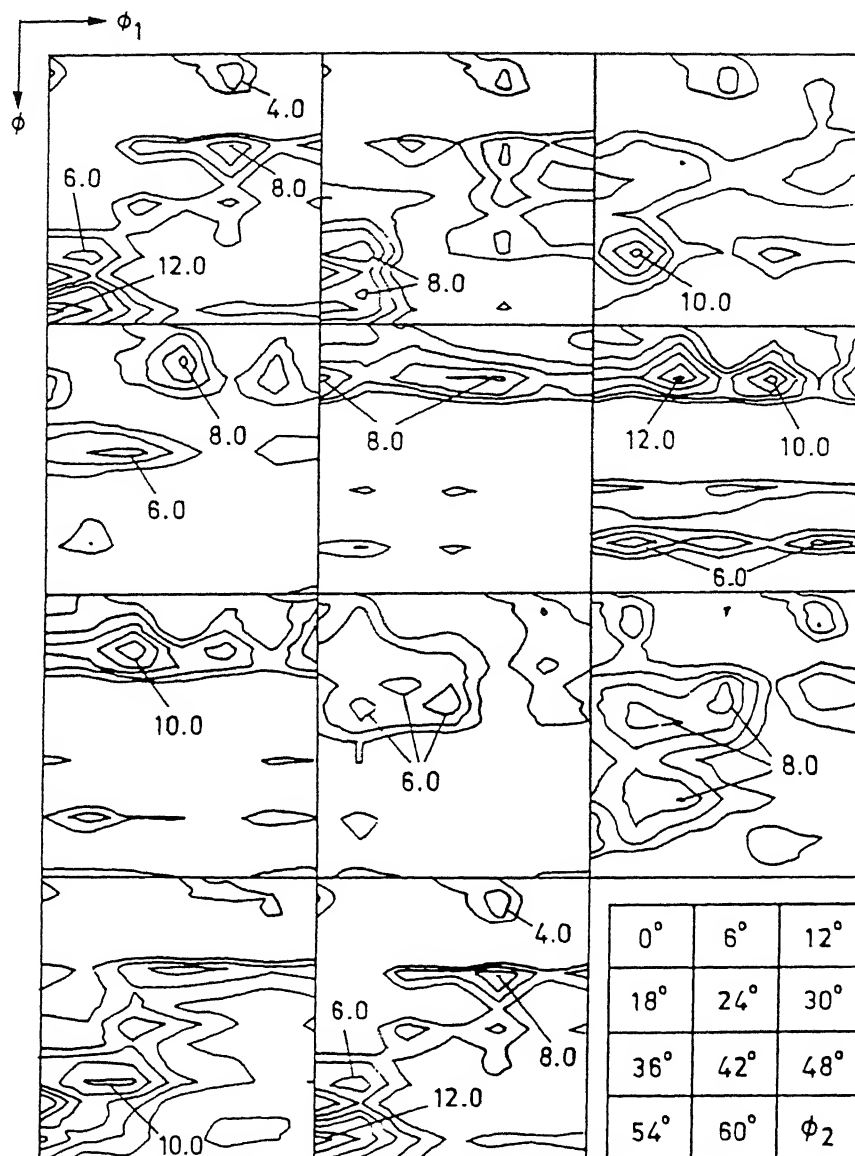


Fig. 4.58 Complete ODF of the material rolled at 1373 K to 80% reduction and furnace cooled

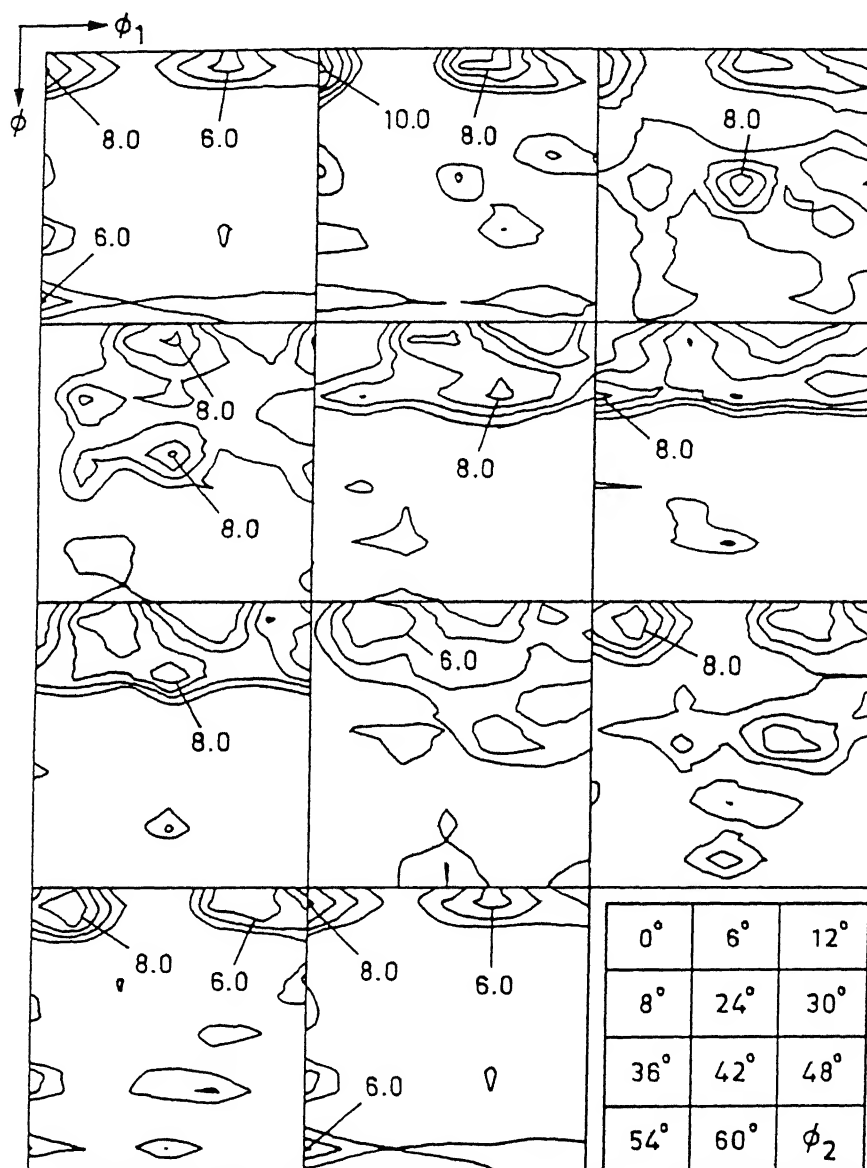


Fig. 4.59 Complete ODF of the material rolled at 1523 K to 80% reduction and furnace cooled

4.4 Discussion of the Results

As it has already been mentioned, the present investigation aims at examining the evolution of microstructures and crystallographic textures during thermomechanical processing of a Ti-24Al-11Nb alloy. The starting as-cast or heat treated materials possess Widmanstätten α_2 in prior β (B2) grains and significant microstructural and textural changes occur in the material during hot rolling. Since, the starting as-cast material is likely to have a slightly higher volume fraction of β (B2) because of the faster cooling rates during solidification from the melt in the water cooled copper crucible, it was decided therefore to examine the effect of hot rolling on a prior heat treated material also. This may lead to the maximisation of the α_2 (h.c.p.) content, as a result of which the platelets of α_2 are likely to undergo more or less unrestricted deformation upon being subjected to rolling at the temperatures where the volume fraction of the phases does not change significantly.

The deformation processing of the alloy was carried out (i) in the $(\alpha_2+\beta)$ phase field at two different temperatures, namely at 1173 K and 1293 K, (ii) at the β transus temperature, which is (1373 ± 10) K in the present case, and (iii) in the β phase field, at the temperature 1523 K. Thus, during rolling in the $(\alpha_2+\beta)$ phase field the material being deformed had different volume fractions of α_2 , had almost no α_2 during rolling at the β transus temperature and had literally no α_2 and coarse grains of β at the rolling temperature of 1523 K.

The thermomechanically treated materials were examined under two conditions; (a) hot rolled and water quenched after the last rolling pass, and (b) hot rolled and furnace cooled after the last rolling pass. While the objective of examining the material in the first condition was to study the microstructural features and textures obtained during high temperature deformation processing, that in the second condition was to study the changes occurring in the material during slow cooling after subjecting it to hot deformation.

All the above processing conditions led to different phase distributions in the finally formed material and therefore the present study is expected to give a comprehensive idea of the development of textures in the material with varying microstructures.

Another criterion behind the choice of these temperatures was the recrystallisation temperature for the α_2 and β phases. The recrystallisation temperature for the α_2 phase is expected to be around 1273 K [55] and that for β is higher than 1373 K [58] (these values, however must be modified by the amount and the rate of straining). Assuming that these temperatures could give some guidelines as to the expected microstructural conditions during processing, the rolling was performed in such a manner that there should be a complete idea about microstructural development as well as evolution of textures below and above the recrystallisation temperature for both these phases. All the above experimental conditions are expected to produce the following combination of phases after processing :

- (i) The as-cast hot rolled and quenched material will yield a microstructure consisting of mostly rolled primary α_2 , limited amount of secondary α_2 produced from rolled β and some retained rolled β (B2). The relative amounts of these phases will depend on the rolling temperature.
- (ii) The as-cast and prior heat treated (at 1173 K) material will contain the equilibrium amount of α_2 to start with $\sim 85\%$. Thus, the final microstructure after rolling and quenching here will consist mostly of rolled primary α_2 .
- (iii) The as-cast, hot rolled and furnace cooled material is expected to consist of rolled primary α_2 and transformed secondary α_2 with their amounts varying depending upon the rolling temperature.

The microstructural and textural evolution in the above three cases are discussed below.

4.4.1 Evolution of Microstructures

Thermomechanical processing has been found to have a profound effect on microstructural development. As shown in Fig.4.1, the as-cast alloy has a Widmanstatten structure of α_2 in a β (B2) matrix. The volume fraction ratio of α_2 to β (B2) is approximately 70 : 30. During hot rolling, the changes in the initial microstructure proceed via an elongation and flattening of the grains. As more and more deformation is imparted to the material, the microconstituents will be fragmented leading to a finer distribution of grains. As predicted by the equilibrium phase diagram

(Fig. 2.1), the volume fraction of β at 1173 K is around 15%. Therefore, during rolling at 1173 K, β (B2) will be gradually transformed into α_2 (henceforth termed as secondary α_2) in order that the volume fraction of β can attain the equilibrium value. Evidently, the equilibrium amount of β (B2) was not achieved in the 1173 K rolled material during rolling and intermediate annealing, as is evidenced by the presence of > 15% β (B2) by volume in the SEM microstructures of the quenched materials (Fig. 4.2). The amount of rolling reduction does not seem to alter the β (B2) volume fraction in any significant way although more of secondary α_2 is expected to be produced from β (B2) as the amount of deformation increases. Some of the β (B2) X-ray diffraction peaks, notably (200) and (211), show an increment in intensity with increasing rolling reduction (Fig. 4.29). This is also accompanied by increased intensities of some of the α_2 lines, such as (0002), (22 $\bar{4}$ 0) and (22 $\bar{4}$ 2). The relative intensities of the lines for the two phases do not at all agree with the data given in the relevant ASTM index cards. This is presumably due to the fact that both the phases are highly textured, as shown in Figs. 4.39 and 4.42. Although it is difficult to distinguish between the primary and the secondary α_2 in the room temperature microstructures and estimate their volume fractions, it is quite expected that higher rolling deformation will produce more of secondary α_2 from rolled β due to the longer reaction time and higher amount of deformation energy associated with heavier amounts of rolling.

The variation in the morphological feature, as examined in the present investigation, manifests in the morphology as well as quantitative distribution of α_2 and

β (B2) phases. The microstructures evolved during the present course of processing are : an equiaxed β (B2) with a more or less uniform distribution of submicron size lamellar α_2 , a Widmanstätten α_2 , a duplex microstructure with an uniform distribution of non-equiaxed α_2 in β (B2) matrix, an equiaxed α_2 and a very fine distribution of α_2 and β (B2). The evolution of microstructures has been discussed for each of the deformation temperatures in the following subsections.

4.4.1.1 Rolling in ($\alpha_2 + \beta$) Phase Field

As is evident from the Figs. 4.2 , at the rolling temperature of 1173 K, the deformation proceeds via an elongation and thinning of the initial Widmanstätten structure. The evolution of microstructure with fine distribution of α_2 and β (B2) is attributed to the heavy deformation imparted to the material. The ($\alpha_2 + \beta$) warm rolled structure is likely to possess high dislocation density in α_2 as well as β (B2). The α_2/β (B2) boundaries are not significantly distorted. The volume fraction of α_2 and β (B2) keep on changing during rolling, mainly by the movement of α_2/β boundaries. The volume fraction changes can also occur due to nucleation of secondary α_2 at high energy sites due to defect structures. During the course of successive rolling passes, these secondary α_2 also gets deformed along with the primary α_2 . As a result, a substantially higher dislocation density is achieved, which again promotes the nucleation of secondary α_2 laths. When the transformed α_2 is worked, the deformed structure again shows the breaking of α_2 laths. The process progresses in a cumulative manner leading to a higher volume fraction of α_2 as compared to the as-cast material.

Therefore, from the starting step onwards itself, the continuous break up of primary as well as secondary α_2 takes place.

Another noticeable feature in the microstructures of the as deformed material is that the material does not recrystallise dynamically or even statically (during intermediate soaking in between two successive passes), as indicated in the TEM microstructures. It is a well established fact that the hot deformation of metals and alloys in moderate to high strain rate processes such as rolling, forging, extrusion etc., occurs by dislocation motion which takes place at high enough temperature resulting in a continual formation of low flow stress substructures. The mechanism for this reduction in flow stress may occur either as a recovery process in which dislocation segments meet and annihilate through climb and glide mechanism, or as a recrystallisation process in which dislocations are absorbed at high angle grain boundaries. As shown in Fig. 4.60 ,constant strain rate tests carried out by Sagar *et al.* [58] show that the Ti-24Al-11Nb alloy undergoes dynamic recovery resulting in subgrain formation within the range of strain rates used during rolling in the present deformation schedule (Fig. 4.61). With the aid of this result, this mechanism stated above is able to explain successfully the microstructural refinement in the Ti-6Al-4V alloy [107]. The strongly deformed state leads to the initiation of recovery process as a result of intermediate annealing between the successive passes. In furnace cooled specimens, since the material is allowed to remain at temperatures close to 1173 K for sufficient time, some of these highly deformed regions lead to the formation of recrystallised grains. However, the time available during the cooling process being

insufficient for further recrystallisation of the material, regions of high dislocation density still persist.

Results of microstructural examination clearly indicate that the material undergoes perceptible dynamic changes as deformation proceeds at the temperature 1293 K. The changes are more noticeable in materials rolled 70% and above. Scanning electron microscopy of the α_2 phase (Figs. 4.12) at this stage shows a more equiaxed morphology. TEM microstructures (Figs. 4.14) also indicate that this phase is in an advanced stage of recovery as well as recrystallisation, specially after 80% rolling. These changes must have taken place dynamically during rolling and also during static annealing in between rolling passes. The furnace cooled samples showed even larger extent of recovery and recrystallisation (Fig. 4.18) indicating the prominent role played by static annealing and slow cooling.

The investigations carried out by Semiatin [56] and Sagar [58] on alloys having very similar compositions, predict the occurrence of dynamic recrystallisation at this temperature for the given range of strain rate (Figs. 2.5 and 2.8). Thus it is expected that both static and dynamic recovery and recrystallisation must be taking place in the α_2 phase in this alloy at this stage. The β phase in the hot rolled and quenched material does not show perceptible recovery effect although some recovery is evident in the β of the furnace cooled material (Fig. 4.12). This seems to indicate that slow cooling from the hot rolling temperature has been quite effective in causing relaxation effects in the β phase also.

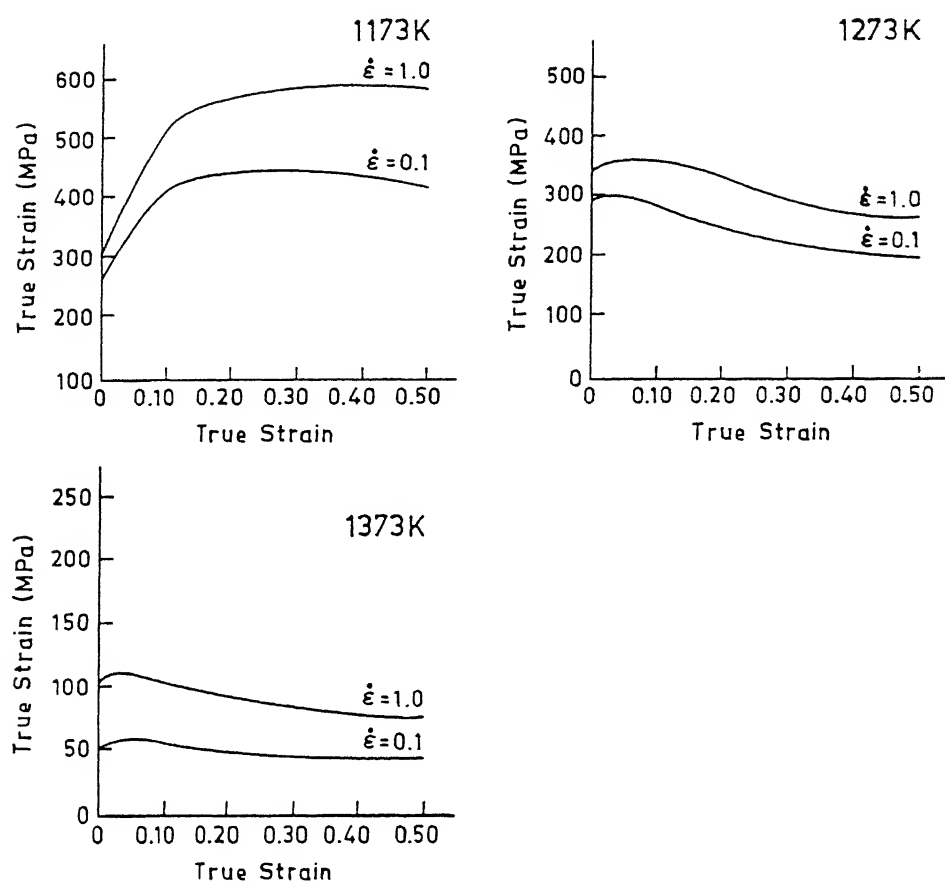


Fig. 4.60 Flow behaviour of as-cast Ti-24Al-11Nb alloy within the temperature range 1173 K-1373 K and strain rates 0.1 and 1.0 [58]

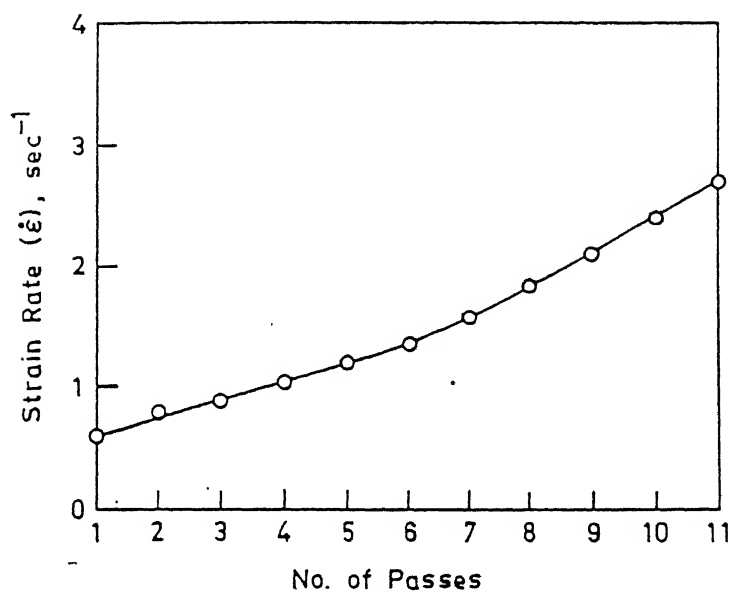


Fig. 4.61 Variation of strain rates during successive rolling passes

Physical Model for the Evolution of Microstructure during Rolling in ($\alpha_2 + \beta$) Phase Field

As the sheet rolling process is associated with nearly plane-strain deformation condition, it is expected that β grains would undergo pancaking in the thickness plane, and if no dynamic recrystallisation occurs at the rolling temperature and strain, they would remain elongated in the direction of rolling. Since the as-cast or the heat treated structure of the starting Ti-24Al-11Nb alloy comprises of α_2 plates in the Widmanstätten morphology within β grains, the plates of α_2 would also undergo deformation during rolling.

Depending on the rolling reduction imparted to the material, the *first stage* of deformation of α_2 plates which are within pancaking β grains would be either (i) their alignment in the rolling direction, (ii) buckling or (iii) kinking. Such features of deformation of α phase in ($\alpha + \beta$) titanium alloys have been widely reported in the literature [108]. However, in view of the physical model being proposed here, a comment will be made about possibilities of their occurrence. Since in a polycrystalline material plates of Widmanstätten α_2 are randomly oriented with respect to the rolling direction only those plates would tend to align themselves with the rolling direction which make an angle of $< 45^\circ$ with respect to it and have no closely spaced α_2 plates in their neighbourhood which otherwise would block any tendency for their rotation. Further, with all other conditions remaining same those plates of α_2 which have lower aspect ratios will tend to align themselves along the rolling direction. On

the other hand, all those plates of α_2 which either due to a higher angle of their orientation with respect to the rolling direction or due to the geometric constraint posed by other plates of α_2 in their neighbourhood can not easily orient themselves along the rolling direction would undergo either buckling or kinking.

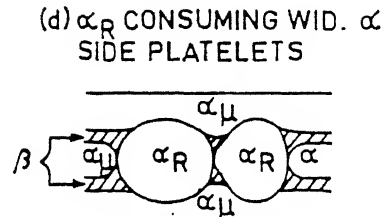
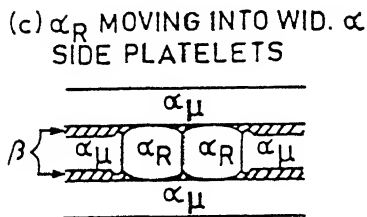
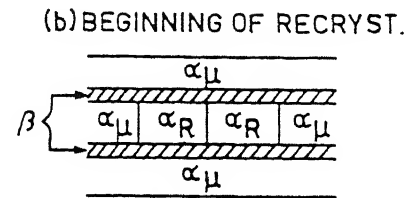
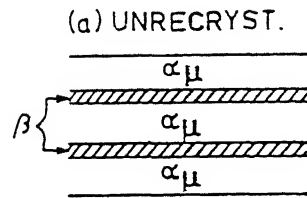
Once alignment, buckling or kinking of α_2 plates has been achieved, the *second stage* of their deformation involves the plastic deformation of aligned/buckled/kinked plates of α_2 . Thus, depending on the nature of the stress field locally imposed on individual plates of α_2 , they tend to elongate in the rolling direction. Though no involved calculations regarding local stress field distribution around α_2 plates in a plastically deforming matrix of β were done as part of the present study and have also not been reported by other researchers, several results regarding the variation of local stress and strain fields in composite materials consisting of a hard phase in softer matrix, as analysed by the finite element method (FEM), are available [109]. These results show that the nature of the stress around the hard plate-like phase in a deforming composite structure depends on (i) the orientation of plates with respect to the loading axis, (ii) aspect ratio of individual plates, (iii) volume fraction of the individual phases, (iv) relative strengths of the individual phases and (v) the ratio of their shear and Young's moduli. Assuming that similar results also follow during the deformation of Ti-24Al-11Nb alloy in the $(\alpha_2+\beta)$ phase field it may be concluded that due to different orientation of individual plates of α_2 with respect to the rolling direction the stress field around them will be different and therefore inhomogeneous. Different plates of α_2 therefore would undergo different degree of deformation.

Further, since (i) plates of α_2 in the starting Widmanstätten morphology are generally of non-uniform thickness and (ii) the orientation within a kinked or buckled plate of α_2 varies from location to location with respect to the rolling direction, it is expected that the individual plates of α_2 would undergo a non-uniform plastic deformation. Non-uniform deformation occurring in individual plates of α_2 thus sets in a non-uniform generation of adiabatic heat. Since titanium-base alloys, in general have poor thermal conductivity [110], a uniform generation of heat implies an inhomogeneous thermal field around deforming plates of α_2 .

It has already been mentioned that, depending on the temperature and strain rate of deformation, different softening mechanisms, namely dynamic recovery (DRV), dynamic recrystallisation (DRX) or flow softening (FS) may occur during hot working of Ti-24Al-11Nb alloy. It is assumed that as far as individual phases, i.e. β or α_2 , are concerned they undergo dynamic recovery or dynamic recrystallisation while flow softening occurs in the overall alloy [56, 58]. Thus, due to an inhomogeneous distribution of the (i) stress-field, (ii) strain rate field and (iii) temperature field within and around deforming α_2 plates different softening mechanisms may occur locally within them. Such differences occurring dynamically in α_2 plates are expected to have important implications on the sequence of microstructural evolution when the structure transforms from the Widmanstätten morphology of α_2 to an equiaxed morphology. These changes occurring in α_2 are considered here as the *third stage* of its deformation.

Depending on whether dynamic recovery or dynamic recrystallisation occurs either low-angle or high-angle grain boundaries leading to the formation of sub-grains or recrystallised grains within plastically deforming α_2 plates. As proposed by Margolin and Cohen [111] when sub-grains or new recrystallised grains of α_2 plates form the α_2/α_2 boundaries meet β (Fig. 4.62). In such a situation surface energy requirements, i.e. $\gamma_{\alpha_2\beta}$ and $\gamma_{\alpha_2\alpha_2}$, do not permit a dihedral angle of 180° . Thus, as proposed by Weiss *et al.* [112], in order to satisfy surface energy requirements in deforming two-phase systems the β phase has to move into the β/α_2 boundary leading to the grooving at the α_2/β boundary (Fig. 4.63) and a rotation of α_2/β boundaries toward one another. In effect, this grooving and rotation enlarge sub-grains or recrystallised grains of α_2 . This increase in size of α_2 sub-grain/recrystallised grain and the concomitant penetration of β into the α_2/α_2 boundary completes the fragmentation of α_2 plates and gives rise to an equiaxed/nearly-equiaxed morphology of α_2 .

(i)



(ii)

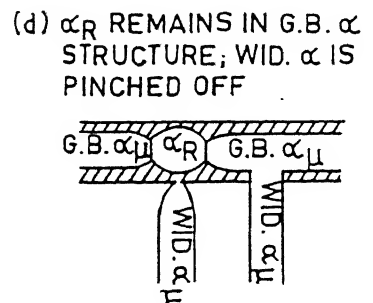
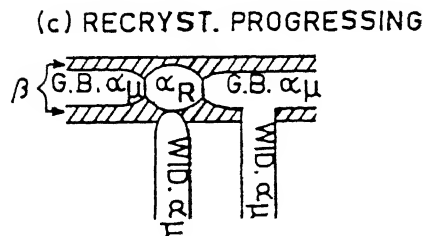
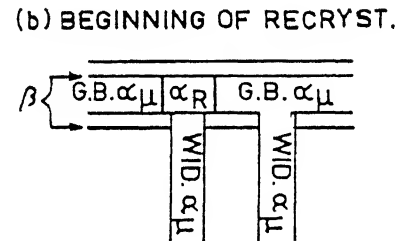
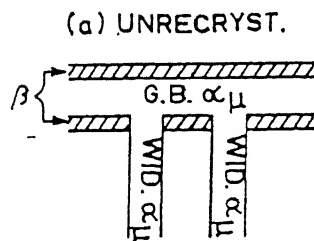


Fig. 4.62

Mechanism for conversion of Widmanstätten to equiaxed morphology;
(i) platelet α and (ii) grain boundary α [111]

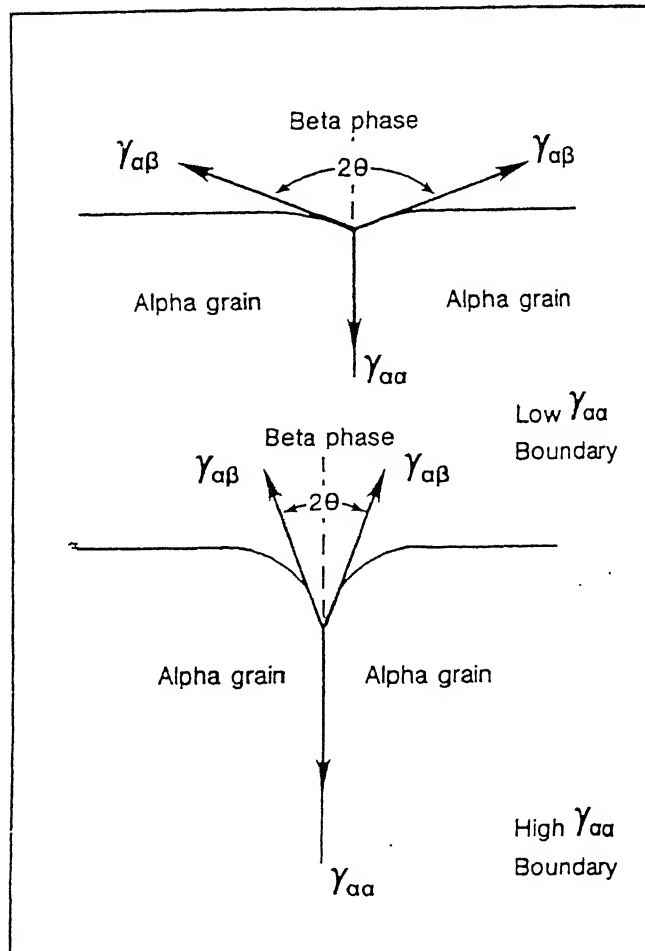


Fig. 4.63 Weiss Mechanism of β penetration for the formation of equiaxed α [112]

4.4.1.2 Rolling in the β Phase Field

The amount of α_2 in the 1373 K rolled and quenched material is quite small, while the 1523 K rolled and quenched material practically does not show the presence of any α_2 . Thus the optical microstructures of the above samples show retained β grains only. There is hardly any evidence of pancaking of the grains due to hot rolling excepting in the most heavily deformed materials; and even in those samples the effect of rolling on the grain shape is hardly discernible. It is therefore evident that the material effectively recrystallises to a great extent during hot rolling, the annealing between successive passes possibly contribute significantly towards this relaxation process.

The examination of the substructural features, using TEM, has revealed that in the material rolled at 1373 K (by 50% as well as 80%) there are clusters of small α_2 plates in isolated regions of β grains (Figs. 4.18). However the substructure of the material rolled at 1523 K and quenched, hardly contains any α_2 . In fact there are ample evidence of an advanced stage of recovery and that of recrystallisation of the β phase. At many places within β grains subgrains separated from one another by small angle boundaries as well as markings indicative of planar slip are visible (Fig. 4.19). At one or two isolated places localisation of deformation into slip bands can also be seen.

A comparison between the TEM microstructures obtained for the 1373 K and 1523 K rolled materials indicates clearly that the β phase in the latter are in amore advanced stage of recovery / recrystallisation than the β phase in the former case. In

addition, the temperature of 1373 K does not appear to be much above the β transus, as evidenced from the presence of α_2 platelets in their microstructures. The hardness values for the specimens processed at these temperatures also indicate the dynamic processes taking place inside the material (Table 4.2).

4.4.2 Evolution of Texture

The texture evolution during processing will be discussed by referring to development of texture in both the α_2 and the β phases separately.

4.4.2.1 Texture of the β (B2) Phase

Very little information is as yet available regarding the evolution of crystallographic texture in the β (B2) phase of $\text{Ti}_3\text{Al-Nb}$ alloys or even in other similar titanium $\alpha + \beta$ alloys. An attempt has been made in this investigation to characterise the hot rolling texture of the experimental alloy deformed at rolling temperatures ranging between 1173 K and 1523 K. At these temperatures, the material consists almost wholly of β and this can be retained at the room temperature by water quenching, in the ordered form B2. The phases α_2 and β are roughly 50% each at the rolling temperature of 1293 K, while at 1173 K the volume fraction of β is around 30%. Thus as the temperatures of rolling decreases the deformation of the β phase becomes more and more constrained due to the simultaneous presence of progressively higher amounts of the α_2 phase.

The texture of the β (B2) phase in the experimental alloy has been found to be much more complex than the texture obtained in the case of other b.c.c. materials like steels, on which most of the b.c.c. texture work done so far has been focused. In case of steels the hot rolling textures are rather weak. The high temperature phase in that case is f.c.c. austenite (γ). At relatively high temperatures of rolling (i.e. above the T_{nr} or no-recrystallisation temperature of γ), a weak recrystallisation texture with predominantly the cube component $\{001\}\langle 100 \rangle$ forms. This then transforms primarily into the rotated cube $\{001\}\langle 110 \rangle$ in the ferrite. If, however, the austenite is not able to recrystallise during, or after rolling, a sharp texture consisting of the components $\{110\}\langle 112 \rangle$, $\{112\}\langle 111 \rangle$, $\{123\}\langle 634 \rangle$ and a weaker $\{110\}\langle 001 \rangle$ develops in the austenite phase. On transformation to ferrite, a component $\{332\}\langle 113 \rangle$ forms primarily from the $\{110\}\langle 112 \rangle$ and another component $\{113\}\langle 110 \rangle$ forms predominantly from the $\{112\}\langle 111 \rangle$ component of the austenite. Thus the hot rolling textures in b.c.c. steels is basically a transformation texture unlike the deformation texture in case of the experimental alloy. When the hot rolled steels are cold rolled at room temperature, two fibres - an ND fibre with $\langle 111 \rangle \parallel$ ND and an RD fibre with $\langle 110 \rangle \parallel$ RD develop in the ferrite. Subsequent annealing leads to the sharpening of the ND fibre at the expense of the RD fibre. A number of theoretical models have been proposed to explain the formation of the cold rolling texture in steels on the basis of "pencil" glide, and these have been more or less successful in explaining the observed features. On the other hand the few models that have been proposed to explain the formation of annealing textures have not been that satisfactory.

One of the most distinguishing features of the $\beta(B2)$ phase textures in the present investigation is that the intensity levels of the contours in pole figures as well as in ODFs are rather high as compared to those of the α_2 phase. Similar observations have also been reported by Fu *et al.* [92] who found that the β texture was approximately four times more intense than the α_2 texture.

The textures of $\beta(B2)$ phase in the present case can be classified into two categories : (i) the texture of single phase $\beta(B2)$, and (ii) the texture of rolled $\beta(B2)$ phase in presence of significant amount of α_2 . The $\beta(B2)$ phase in the materials rolled at 1373 K and 1523 K belong to the first and those rolled at 1173 K and 1293 K belong to the second category.

(i) Texture of single phase $\beta(B2)$

The pole figures and ODFs of materials rolled 80% at 1373 K and 1523 K (Figs. 4.55 and 4.56) exhibit remarkable similarity in textures, in respect of the fibres and orientation maxima. In fact, the texture of $\beta(B2)$ phase in the material rolled to 50% at 1523 K is also not much different from the above two although somewhat weaker in intensity than the previous ones. The textures here are essentially β hot rolling texture and are found to consist mainly of $\{001\}\langle uvw \rangle$, $\{hkl\}\langle 001 \rangle$, $\{112\}\langle uvw \rangle$ and $\{332\}\langle uvw \rangle$ orientations.

Table 4.2, showing the hardness values of the β phase in samples rolled at 1373 K and 1523 K and finally quenched, indicate that the material is much softer in the

80% rolled (at 1373 K) and in the 50% and 80% rolled (at 1523 K) materials. The hardness in these three cases are significantly lower (by about 100 VHN points) than the hardness in the 50% and 70% rolled samples at 1373 K. The above observations point to a similar situation with respect to the former three samples, which have presumably undergone a static / dynamic recovery / recrystallisation during processing. If it were a dynamic recrystallisation process, the resulting texture would have been rather weak, nearly random. Presence of a strong texture, therefore, precludes any such dynamic phenomenon. On the other hand, it must be pointed out here that all the rolled samples were annealed at the rolling temperatures in between the successive passes. It is quite likely therefore that only static recovery/recrystallisation of the material possibly take place in these samples during the annealing process. It is to be noted that the studies aimed at determining the processing map for this alloy in β (B2) phase field also preclude the possibility of dynamic recrystallisation [58] in the temperature range and with the strain rates used. Experiments carried out [113] on an $\alpha + \beta$ alloy (Ti-6.5 Al-2.2 Mo-4.2 Zr-0.15 Si) which has a β -transus temperature of ~ 1283 K has been found not to undergo dynamic recrystallisation even at a temperature of 1573 K and for a reduction of nearly 80% in a single pass. On the other hand, the same material after rolling deformation of 60% at 1323 K followed by quenching and static annealing at 1293 K for 30 seconds only undergoes complete recrystallisation. It is therefore quite likely that the present alloy which has a β transus temperature of ~ 1373 K should be able to at least partially recrystallise when held in between successive passes in the course of multipass rolling at 1373 K and 1523 K.

An attempt has been made to compare the texture of β in the present case with the recrystallisation texture of a pure β titanium alloy (Ti-15V-3Cr-3Sn-3Al) which was cold rolled at room temperature by 90% and then annealed at 1073 K and 1223 K [114]. The recrystallisation texture at both these temperatures was found to consist mostly of $\{554\}\langle 225 \rangle$ orientation, close to $\{111\}\langle 112 \rangle$. A comparison of the recrystallisation texture of β obtained by Inoue *et al.* [114] and the β texture of the present alloy, hot rolled at 1373 K and 1523 K, clearly indicates the total dissimilarity between the two sets of results. The present results indicate the presence of strong orientations along certain fibres in the orientation space, such as the $\{001\}\langle uvw \rangle$, $\sim\{112\}\langle uvw \rangle$ and $\{221\}\langle uvw \rangle$ along with other orientations. Due to the absence of any report in the open literature on the hot rolling textures of alloys of compositions similar to the present one, no comparison is possible with other people's work also. All these indicate that it would possibly not be appropriate to compare the present results with those of Inoue *et al.* [114] since the processing of the material in the two cases was not at all comparable. The other important fact that the β of the present alloy, after quenching from the hot rolling temperature in the β phase, can exist in its ordered B2 form [4] while Inoue *et al.*'s alloy is expected to be in a disordered condition, can also have an important bearing on the significant texture differences that exist between the two cases.

(ii) Texture of rolled β phase in presence of significant amount of α_2

The textures of the β (B2) phase in the 1173 K and 1293 K rolled materials belong to this category. In both the cases significant amounts of the α_2 phase coexist with the β (B2) phase, the volume fraction of α_2 being more in the 1173 K rolled material than in the 1293 K rolled material.

An interesting point to note is that the general appearance of the ODF plots for the β (B2) phase in this category is significantly different from the ODF plots of β (B2) in the first category (Figs. 4.39 and 4.55 as well as Figs. 4.40 and 4.56). It has been more or less established now that the texture of the β (B2) phase belonging to the first category pertains to mostly the partially recrystallised state. On the other hand, hardly any recrystallisation of the β (B2) phase takes place in the 1173 K and 1293 K rolled materials, as revealed from microstructural examination. Thus the texture of the β (B2) phase in these materials can be construed as from the deformed (and sometimes partly recovered) state.

As shown in Figs. 4.40, although some visible differences in the overall texture do exist in the 50% rolled 1173 K and 1293 K materials, there is very little change in the locations of the intensity maxima in the ODF plots of the 80% rolled materials at the above two temperatures. The textures in the highly deformed state in both the materials show maxima at $\{001\}\langle 110 \rangle$, $\{112\}\langle 110 \rangle$, $\{112\}\langle 111 \rangle$ and $\{013\}\langle 331 \rangle$ locations.

Inoue *et al.* [114] investigated the cold rolling and recrystallisation textures of the metastable β phase (b.c.c.) in a Ti-15V-3Cr-3Sn-3Al alloy. The texture developed after cold rolling was found to be somewhat dependent on the initial solution treatment. However, the texture of the 90% cold rolled β was found to consist of a $\langle 110 \rangle \parallel$ RD partial fibre ranging between $\{001\}\langle 110 \rangle$ and $\{111\}\langle 110 \rangle$. These components are also observed in the texture of cold rolled steel sheets.

The texture of the β phase in the 1173 K and 1293 K hot rolled (80%) material, in the present case, does not show any $\langle 110 \rangle \parallel$ RD fibre as such, however, the $\{001\}\langle 110 \rangle$ component is quite strong, as observed by Inoue *et al.* [114] in their material. In addition, the texture of the present material rolled at 1173 K and 1293 K contain few other components which were not observed by Inoue *et al.* in their work. These differences could arise from the simple fact that whereas the material used by Inoue *et al.* was cold rolled after solution treatment, the present alloy was hot rolled at 1173 K and 1293 K, the temperatures at which the β phase does not have a reasonable chance to recrystallise. It should be mentioned here that whereas the material used by Inoue *et al.* [114] had a single β phase, the material in the present investigation contained both the β (b.c.c.) and α_2 (h.c.p.) phases - some of the XRD lines of both the phases are very close and it is quite difficult to isolate the their individual effect on the pole figures and the ODFs of these two phases. A further cause of difference in the textures in these two cases could arise from the fact that whereas the β phase in the alloy used by Inoue *et al.* [114] is expected to be in a disordered condition, the β of the present alloy, when retained by quenching can not be in a fully disordered state [4].

4.4.2.2 Texture of the α_2 Phase

As stated in Chapter 1, the aim of present investigation has primarily been to study evolution of texture in the h.c.p. α_2 phase as a result of thermomechanical processing. On the basis of microstructural features produced during processing, the texture of the α_2 phase can be classified under the following heads:

- (i) Texture of rolled primary α_2
- (ii) Texture of secondary α_2 .
- (iii) Texture of primary plus secondary α_2

(i) Texture of rolled primary α_2

Experimental Texture

The as-cast material rolled at 1173 K followed by quenching and the prior heat treated material similarly processed show nearly the same amount ($\sim 15\%$) of β at room temperature. Of course, it is understood that the β phase in the former case already existed when the material was raised to the temperature of rolling. On the other hand, most of the β in the latter material nucleate during rolling. As mentioned in Section 4.3.1, the differences in the textures of the α_2 phase in the two cases were not very significant in the sense that reasonably strong and perfect basal texture could be observed in the pole figures of the 80% rolled materials.

As seen in Figs.4.42 and 4.45, the basal pole distributions in the (0002) pole figures in both the materials show splitting along RD as well as TD at lower rolling reductions, however this tendency disappears after heavy amounts of rolling (80%). Although the pole figures of both the materials look quite similar, their ODFs (Figs. 4.43 and 4.46) show distinct differences in the sense that whereas in the heat treated alloy most of the orientations are clustered along the $[0001] \parallel \text{ND}$ direction, extra orientations appear along the $[10\bar{1}0] \parallel \text{RD}$, specially in case of the 80% rolled material in the as-cast specimens. It therefore appears that while the orientations near $[0001] \parallel \text{ND}$ must have arisen due to the rolling of the α_2 phase, the other orientations along the $[10\bar{1}0] \parallel \text{RD}$ could be possibly due to the texture produced in the β phase which was subsequently inherited by the secondary α_2 phase. A comparison of Fig. 4.44 with Fig. 4.50, depicting the ODF sections of the furnace cooled materials, will be quite interesting in this regard. In the furnace cooled materials, at room temperature, the phases present will be rolled primary α_2 and secondary α_2 produced from the rolled β . In fact, in the 1373 K rolled and then furnace cooled material (Fig. 4.50 c) the room temperature phase will consist of almost fully secondary α_2 . The texture here shows similar orientation distributions along the $[10\bar{1}0] \parallel \text{RD}$ as found in Fig. 4.44 (c). It is interesting to note that in the texture of the furnace cooled sample there are practically no orientations along $[0001] \parallel \text{ND}$ which must therefore be a characteristic of the rolled α_2 texture.

Very little work seems to have been carried out on the evolution of texture in Ti₃Al base alloys, in particular Ti-24Al-11Nb, during hot rolling. Whatever scanty information is available, it is in the form of mostly pole figures only [93,94]. The most comprehensive amongst these is due to Hon *et al.* [93], which aimed at examining the evolution of hot rolling textures in a Ti₆₅ Al₂₅ Nb₁₀ alloy. It has been reported that using a proper rolling process involving unidirectional multipass rolling at 1153 K, a basal texture could be developed. It was also inferred from their investigation that a lower temperature of rolling and a higher degree of rolling deformation could be favouring the evolution of basal (0002) α_2 texture with improved intensity. Rolling at higher temperature, where the content of β phase is more, could impose additional constraints on the rotation of α_2 grains, thereby lowering the intensity of (0002) α_2 . All evidences from the work by Hon *et al.* point to the fact that the sharp basal texture in the Ti₆₅Al₂₅Nb₁₀ alloy is caused by the deformation of the α_2 grains during the rolling process. These observations of Hon *et al.* [93] broadly tally with the results of the present investigation.

In spite of this agreement, a proper comparison of the present results with theirs was not possible as because they studied texture using pole figures only and those were not at all very detailed in nature. An attempt was therefore made to compare the present results with those observed in pure titanium and (α + β) alloys of titanium which do possess, the hexagonal α phase that is quite similar to the α_2 phase in the present alloy system under investigation. The rolling texture of titanium below

its allotropic transformation ($\alpha \rightarrow \beta$) temperature is likely to correspond to that of the rolled α_2 phase of the $\text{Ti}_3\text{Al-Nb}$ alloy in the present work.

Cold rolling of commercially pure titanium (hereafter referred as C.P. Ti) upto 40% reduction was found to produce a texture with major components as $\{0001\} \pm 40^\circ \text{TD} <10\bar{1}0>$ and $\{0001\} <11\bar{2}0>$ and some other minor components. After 80% rolling deformation the texture evolved mainly consisted of $\{0001\} \pm 40^\circ \text{TD} <10\bar{1}0> [118]$. Structural investigations by the same authors revealed the evidence of profuse twinning at lower degrees of deformation.

Here $\{0001\} \pm 40^\circ \text{TD} <10\bar{1}0>$ means that the hexagonal c-axes $<0001>$ are tilted $\pm 40^\circ$ from the sheet normal direction towards the transverse direction; $<10\bar{1}0>$ being parallel to the rolling direction.

Twinning, however, was not found to be present beyond 40% deformation and above. This led to the assumption that the final texture after heavy amount of deformation was due to glide only. This kind of behaviour has also been reported by Nauer-Gerhardt and Bunge [116] for texture evolution during cold rolling of C.P.Ti.

Investigations by Inoue and Inakazu [117] on a similar material, however, led to a completely different texture after heavy cold rolling. They observed a deformation texture consisting of a $(\bar{1}2\bar{1}0)[10\bar{1}0]$ orientation and a $(0001) [\text{uv}t0]$ orientation having a maxima at $(0001) [2\bar{1}\bar{1}0]$ at lower reductions and a $(\bar{1}2\bar{1}4)[10\bar{1}0]$ at higher levels of reduction. They further concluded that the $(1214) [1010]$ component

develops as a result of interaction between slip and twinning. This conclusion of theirs clearly implies that twinning is a dominant mode of deformation even during the later stages of deformation. This is in contrary to what Lee *et al.* [118] suggested and therefore the two viewpoints are difficult to rationalise. However, whereas the starting hot rolling texture reported by Lee *et al* [118] consisted of the components $\{0001\} \pm 40^\circ$ TD $\langle 10\bar{1}0 \rangle$ and $\{0001\} \pm 40^\circ$ TD $\langle 11\bar{2}0 \rangle$, the hot rolling texture of the starting material used by Inoue and Inakazu consisted of an orientation tube extending from $(02\bar{2}5) [2\bar{1}\bar{1}0]$ to $(\bar{1}2\bar{1}4) [10\bar{1}0]$ and the $(1\bar{2}10) [10\bar{1}0]$ orientation in which the $[0001]$ axis is parallel to the transverse direction. The resemblance of the major texture component during initial hot rolling and subsequent cold rolling in both the above mentioned cases suggest that cold rolling essentially leads to a sharpening of the starting texture. It is to be recalled here that, in the present case the texture of the starting as-cast as well as heat treated material is also a basal texture (Fig. 4.35), the strongest component being $(0001) [10\bar{1}0]$. Thus, it is quite likely that the basal texture will survive during the subsequent hot rolling in the α_2 phase field.

The question may be raised at this point on the advisability of comparing the hot rolling (or warm rolling) texture of $\text{Ti}_3\text{Al-Nb}$ with the cold rolling texture of C.P. Ti. In this connection it may be mentioned that for C.P. Ti both the cold and hot rolling textures can be described as $(0002) \pm \alpha^\circ [10\bar{1}0]$ which means that the (0002) poles are concentrated at $\pm \alpha^\circ$ from the sheet normal in the transverse direction and the $[10\bar{1}0]$ direction is parallel to the rolling direction [119]. This texture is supposed to

be affected by rolling temperature [120], rolling direction [121,122], reduction in thickness [123], heat treatment [124] and impurities.

The pole figures in the present investigation have invariably shown some significant deviation from the perfect basal texture, especially during lower degrees of deformation. The basal poles are sometimes found shifted from the centre towards the RD (Rolling direction) or towards the TD (transverse direction) or both. These textures have been termed as RD split or TD split respectively in the literature in which specific instances of formation of such textures have been reported both in case of C.P. Ti and Ti-6Al-4V alloy.

Nourbakhsh and O'Brien [125] investigated texture formation in C.P. Ti during cold rolling, the starting material having a random texture. They observed that at low strains Ti deforms mainly by twinning, whereas at strains above 40%, deformation takes place solely by slip. After cold rolling by about 20%, a split RD type texture forms in this material, and this changes into a split TD type during further deformation upto 40%. Twinning is believed to be responsible for the rapid development of texture as well as texture transition. However, the formation of the stable end texture is thought to be due to slip.

Tanabe *et al.* [119] reported that in a material with initial random orientation, the texture developed by rolling at temperatures below 973 K consisted of the (0002) poles concentrated at 20-30° from the sheet normal towards the rolling direction (split RD texture). At temperatures above 1023 K, additional peaks of (0002) poles

concentrated at $50\text{-}90^\circ$ from the sheet normal in the transverse direction (split TD texture). It was further reported that the split RD texture formed only at low reductions ($< 73.2\%$) and was changed to split TD texture at reductions above 80% or by annealing at 973 K. Their results indicated that the split RD texture is an intermediate component developed only at low reductions and is unstable during annealing. Split RD texture was also found to develop at low cold rolling reductions in a material with initial random orientation. This behaviour changed after cold rolling by an amount 34.4%, when both split RD and TD textures were obtained. On the other hand, for materials having initial textures showing the (0002) poles located 25° and 40° from the sheet normal towards the transverse direction (split TD texture), the cold rolling texture was found to be essentially similar to the starting texture, and no split RD texture was found to develop.

Theoretical investigations [126] based on twinning could explain the formation of new basal poles near the sheet normal and in the transverse direction at the early stage of cold rolling. However, as critical resolved shear stress for twinning is higher than that for slip at elevated temperatures [127], it appears difficult to account for the split RD/TD textures in hot rolled materials by the operation of twinning.

The possibility of the occurrence of twinning in the present material has been ruled out as it is an ordered material [4]. Careful experimentation using TEM has also not revealed any twinning during the rolling process. Thus twinning cannot be responsible for the formation of the RD split and TD split textures observed in the present investigation.

Inagaki [128] has further reported that the texture produced in C.P. Ti specimens hot rolled at temperatures below 1073 K (essentially in the α phase) is the same as the cold rolling texture, namely, $\{2115\} \langle 0110 \rangle$. In the present case, the stable end orientation of the α_2 rolling texture is a fibre texture within about 12° (in ϕ) from the basal $\{0001\} \parallel \text{ND}$ (Figs. 4.44 and 4.47), whether the starting material is as-cast or heat-treated. The final hot and cold rolling texture reported by Inagaki in the α phase, on the other hand, is $\{2115\} \langle 0110 \rangle$ which was presumably obtained from the component $\{0001\} \langle 0110 \rangle$ by rotation around $\langle 0110 \rangle$. Interestingly, the $\{0001\} \langle 0110 \rangle$ component, which is part of the $\{0001\} \parallel \text{ND}$ fibre, is the major component of texture obtained by Inagaki after about 50% deformations, in his material. Thus, whereas the texture of α_2 in the present investigation can be described by a partial fibre, obtained by rotation of about $10\text{-}12^\circ$ around the $\langle 0110 \rangle$ axis from the perfect basal texture, Inagaki's stable end texture in C.P. Ti is obtained by a rotation of about 33° around the same axis from the perfect basal. This difference could be characteristic of the materials themselves. The one important point of difference is that whereas Inagaki's starting material had a texture $\{1013\} \langle 1210 \rangle$, the initial texture of the $\text{Ti}_3\text{Al-Nb}$ in the present case was a near basal texture only.

On the basis of rigorous experimentation using the ODF method, Inagaki [129] suggested that the cold rolling texture develops in from hot rolled material with an initial texture of $\{1013\} \langle 1210 \rangle$.

- (i) at reductions below 30%, the $\{1013\}$ $\langle 1210 \rangle$ initial texture weakens remarkably by twinning and slip rotations;
- (ii) between 30 and 50% rolling, a $[0001]$ parallel to ND basal texture with its centre at the $\{0001\}$ $\langle 0110 \rangle$ orientation develops mainly through slip rotations; and
- (iii) at rolling reductions above 50% the $\{0001\}$ $\langle 0110 \rangle$ orientation rotates towards the $\{2115\}$ $\langle 0110 \rangle$ by rotation around the $\langle 0110 \rangle$ axes. The component $\{2115\}$ $\langle 0110 \rangle$ is therefore the stable end orientation in the cold rolling texture of C.P. Ti.

The evolution of texture in the primary α_2 phase in the experimental alloy will now be discussed with reference to the rolled α texture in a two phase ($\alpha + \beta$) Ti alloy such as the Ti-6Al-4V. In Ti-6Al-4V, the relative volume fractions of the α and β phases vary continuously with increasing temperature, and the hot rolled texture of this alloy will therefore be affected by rolling temperature as a function of the microstructural distribution of the constituting phases [130]. It has been further suggested [131] that texture development in ($\alpha + \beta$) alloys such as Ti-6Al-4V, is also affected by the geometrical arrangement of the constituting phases.

Tanabe *et al.* [119] investigated the development of hot rolling texture in Ti-6Al-4V sheets at different temperatures of rolling. They found that at temperatures below 1123 K, the texture consisted of both split RD and TD components. This kind of texture has also been found out by other workers [121, 122] for this alloy. In

contrast to the behaviour of C.P. Ti, the split RD component of the texture does not change to the split TD type by rolling at reductions over 90% or by annealing [119]. Thus this texture component is considered to be arising out of the effect of alloying additions only. The amount of β phase at this hot rolling temperature is about 15-30% [132] and therefore the texture at this stage is essentially that of rolled α with a little amount of transformed β texture. As stated earlier, the splitting of the basal texture in the present investigation could not be accounted for by taking twinning as a deformation mode. It therefore appears that this could be the effect of alloying additions only as in Ti-6Al-4V.

A somewhat more detailed investigation on the evolution of texture during thermomechanical processing of Ti-6Al-4V, using orientation distribution function (ODF) representation of texture, was carried out by Inagaki [133]. According to him, hot rolling of the material at temperatures below 1123 K results in the formation of a $[0\bar{1}10] \parallel \text{RD}$ partial fibre texture, whose centre is located at $(\bar{2}111)[0\bar{1}10]$. There is also a second component, namely, $[0002]$ 20° from ND fibre which consists of orientations having their $\langle 0002 \rangle$ axes inclined 20° from the normal direction. This latter component corresponds to the $(\bar{2}118)[8\bar{4}43]$ orientation [133]. These texture components basically refer to the α rolling texture in Ti-6Al-4V. The starting material used by Inagaki for hot rolling was only weakly textured. The (0002) pole figure at this stage showed basal poles of intensity $2 \times \text{Random}$, situated symmetrically along both RD and TD away from the ND.

Peters and Luetjering [134] investigated a two phase ($\alpha+\beta$) Ti-6Al-4V alloy with the primary objective of controlling the α grain size for equiaxed and bi-modal (equiaxed plus lamellar) microstructures with a view to obtaining grain sizes well below 10 μm . Side by side they also attempted to characterise and control the texture developed in this material due to heavy deformation. Two types of textures in deformed Ti-6Al-4V have been characterised by them: (i) the basal texture, where the basal planes (0002) lie parallel to the rolling plane and which has been achieved by cross-rolling at low temperatures [135]; (ii) the transverse texture, where the basal planes are perpendicular to the rolling plane and parallel to the rolling direction, which may be produced by deformation at high temperatures [136-138]. Sometimes, mixed textures containing both the basal and the transverse components have also been observed to form [138, 139]. Peters and Luetjering also observed that unidirectional rolling at 1073 K of a Ti-6Al-4V alloy, having nearly random initial texture, led to the development of a mixed texture containing both the Basal (B) and the Transverse (T) parts, the maximum intensities for both the types increased with increasing degree of deformation.

Evolution of experimental textures - comparison with existing simulations

The formation of the near basal texture in rolled primary α_2 will now be discussed in terms of the available modes of deformation in $\text{Ti}_3\text{Al-Nb}$ alloy. Although twinning does not seem to take part in the deformation process of this alloy, this mode of deformation plays a dominant role, along with slip, in the evolution of α rolling

textures in C.P. Ti as well as in $(\alpha+\beta)$ alloys, such as the Ti-6Al-4V. There has been some work on the simulation of α deformation texture in Ti and Ti alloys. These will now be enumerated and their relevance to the present case will be highlighted.

Several workers have tried to model the rolling textures of Ti and its alloys [140-142]. Titanium ($\frac{c}{a} < 1.633$) is known to possess three slip systems - the basal $\{0001\} \langle 11\bar{2}0 \rangle$, prismatic $\{1\bar{1}00\} \langle 11\bar{2}0 \rangle$ and pyramidal $\{10\bar{1}1\} \langle 11\bar{2}0 \rangle$ with an a-Burgers vector and $\{10\bar{1}1\} \langle 11\bar{2}\bar{3} \rangle$ with a c+a-Burgers vector. In addition it can undergo $\{10\bar{1}2\}$ twinning in tension, $\{11\bar{2}2\}$ twinning in compression and in some cases $\{11\bar{2}1\}$ twinning in tension [143-145]. At room temperature the CRSS for prismatic slip is lower than that for basal and pyramidal slip [146, 147].

Thornburg [148, 149] and Thornburg and Piehler [150] followed the course of rolling texture evolution in Ti and its alloys. They examined the active deformation mechanisms through TEM work and calculated the lattice rotations associated with various combinations of active glide systems. Thus they could account for the classical Ti texture with c poles tilted towards TD by assuming a combination of several glide systems along with $\{10\bar{1}2\}$ and $\{11\bar{2}2\}$ twinning systems. They also predicted that restricting the active deformation mechanisms to glide only would produce a texture with central c-poles. The latter type of texture is normally found in heavily rolled Ti-3% Al alloy, which does not show any twinning.

The rotation of the c-poles away from the central part of (0002) pole figures was predicted by Tenckhoff [151] on the basis of operation of several twinning systems. When the lattice is almost completely twinned, further twinning is blocked and therefore only glide can occur thereafter. Thus the splitting of the c-poles in the final stable texture, tilted 20°- 40° towards TD, could be accounted for by pyramidal glide with a (c+a) Burgers vector on the $\{11\bar{2}1\}$ or $\{10\bar{1}1\}$ planes.

Philippe *et al.* [152] tried to explain the typical split RD (R) and split TD (T) type rolling textures in Ti and its alloys. They have suggested that the combination of $\{10\bar{1}0\} < 11\bar{2}0 >$ and $\{10\bar{1}1\} < 11\bar{2}0 >$ glides and $\{10\bar{1}2\} < 10\bar{1}1 >$ tension twinning and $\{11\bar{2}2\} < 11\bar{2}\bar{3} >$ compression twinning leads to the formation of T type textures. On the other hand, the combination of $\{10\bar{1}0\} < 11\bar{2}0 >$ prismatic glide, $\{10\bar{1}1\} < 11\bar{2}0 >$ and $\{10\bar{1}1\} < 11\bar{2}\bar{3} >$ pyramidal glide and $\{10\bar{1}2\} < 10\bar{1}\bar{1} >$ twinning, the latter being strongly impaired, leads to the formation of R type textures. They further suggested that the addition of possible basal glide to the combination of deformation mechanisms would result in the c-axes coming closer to ND in a basal pole figure.

For the purpose of simulation of cold rolling textures, Philippe [153] considered three different materials based on Ti: (i) commercially pure Ti, T40, (ii) Ti-6Al alloy and (iii) Ti-6Al-4V alloy. The initial textures in these three materials along with their final experimental cold rolling textures and the corresponding simulations are shown for comparison, in the form of (0002) pole figures, in Fig. 4.64. As seen in this

figure the starting textures are rather different in the three alloys. For modelling the texture of T40, Philippe [153] considered the following deformation mechanisms: gliding on prismatic planes, cross slip with $\langle a \rangle$ direction and twinning. In the first stage of deformation $\{10\bar{1}2\}$ and $\{11\bar{2}2\}$ twinning are supposed to be activated upto about 50% deformation, after which deformation twinning is not considered as important and $\langle c+a \rangle$ pyramidal gliding is supposed to be activated instead. The simulated pole figure based on this model was found to have a good correspondence with the experimentally measured pole figure (Fig. 4.64). For the Ti-6Al and Ti-6Al-4V alloys, which had finer grain sizes as compared to T40, twinning was not considered very active and it was assumed that deformation essentially takes place by prismatic, basal and pyramidal $\langle c+a \rangle$ glides. In this case also good correspondence between the simulated and experimental textures was obtained. Philippe [153] also emphasised that for successful modelling work a good knowledge about both the evolution of microstructure and the deformation mechanisms involved is necessary.

A careful look at Fig. 4.64 shows that in case of the Ti-6Al alloy the initial starting texture is basal, as in the present investigation on $\text{Ti}_3\text{Al-Nb}$ alloy. The experimental rolling texture is of a split RD type which has been successfully simulated by assuming mainly basal, prismatic and pyramidal glide, but no twinning. Thus it is quite apparent that it is possible to derive the experimental texture which is sometimes found for the rolled α_2 in the present alloy, on the basis of glide only. Essentially, the starting texture in both the as-cast as well as heat treated material seem to be retained and somewhat strengthened by the subsequent rolling process.

As mentioned earlier, work done by Hon *et al.* [93] on a $\text{Ti}_{65}\text{Al}_{25}\text{Nb}_{10}$ alloy has shown that hot rolling of this alloy leads to the formation of basal texture of the type $(0002)[20\bar{2}0]$. They suggest that the compressive deformation during rolling tends to cause the (0002) slip planes to become parallel to the rolling plane. At the same time the tension in the rolling direction produces slip of the α_2 grains along $\langle a \rangle$ direction near the rolling direction. Further slip could cause rotation of the α_2 grains in a manner that makes the rolling direction (tensile axis) to move towards the ideal $[20\bar{2}0]$. This orientation is symmetrically disposed with respect to the $[11\bar{2}0]$ and $[2\bar{1}\bar{1}0]$ which are the $\langle a \rangle$ slip directions near the RD and is expected to be quite stable. All the above orientations have been indicated in a standard α_2 (0001) projection (Fig. 4.65), with $[10\bar{1}0]$ as the rolling direction.

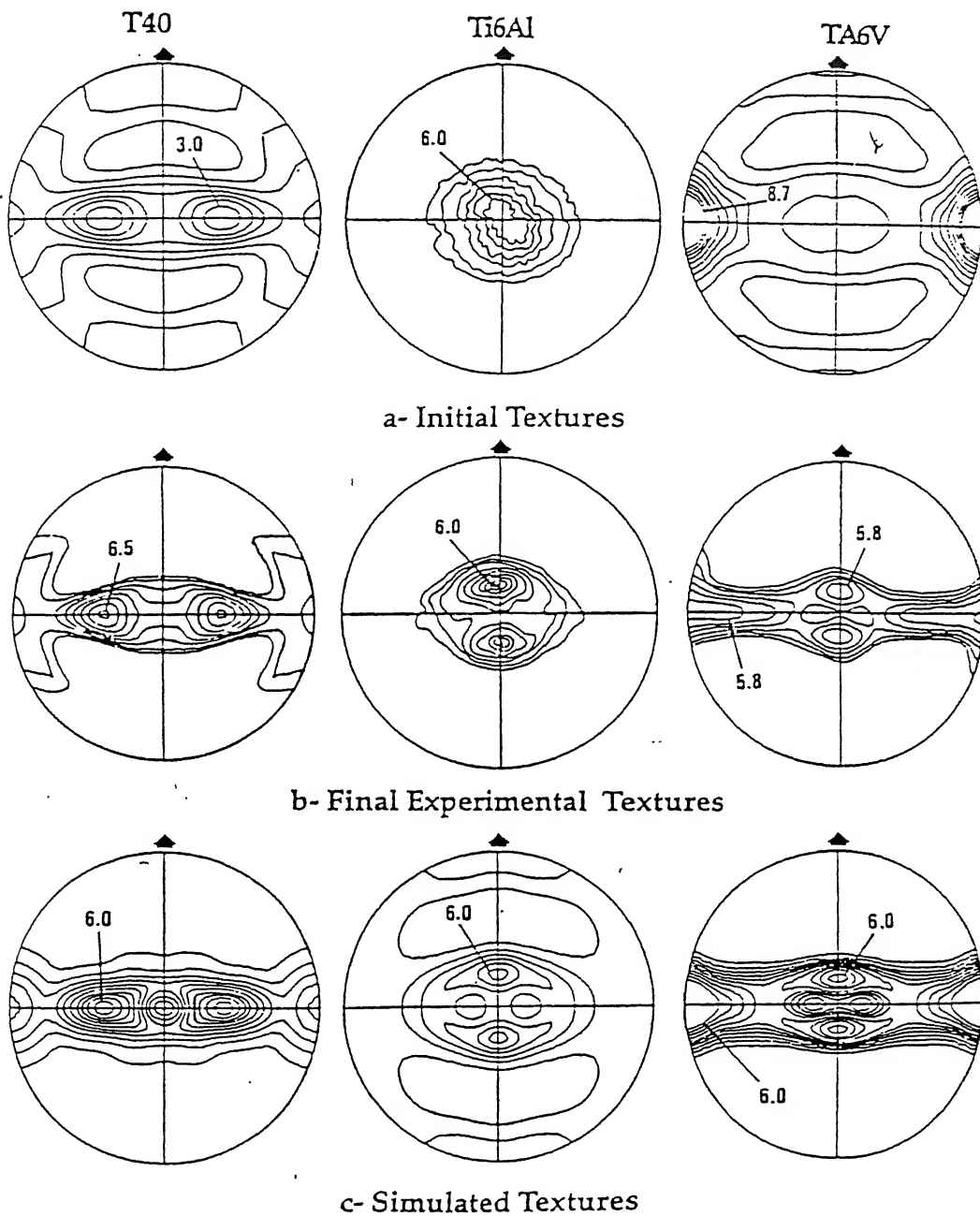


Fig. 4.64 Comparison of (0002) pole figures; (a) initial textures, (b) final experimental textures, and (c) simulated textures for unalloyed Ti and two Ti alloys

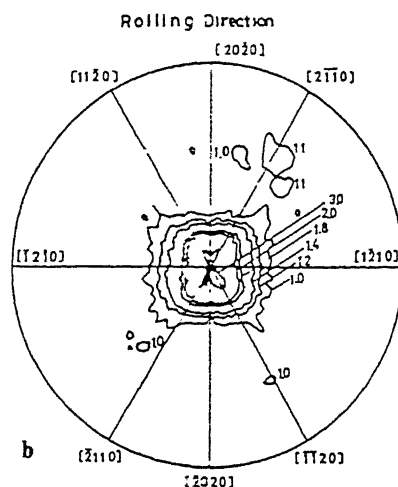


Fig. 4.65 $(0002)_{\alpha_2}$ pole figure for a 1153 K rolled material with a standard α_2 (0001) projection having $[10\bar{1}0]$ at the rolling direction superimposed on it [93]

Till now the experimental and simulated textures have been compared on the basis of pole figures only. Detailed simulation of rolling texture of α_2 phase in Ti_3Al , using three dimensional orientation distribution function (ODFs) has been carried out by Chen *et al.* [154]. An attempt will now be made to compare the present results with theirs.

The α_2 phase in Ti_3Al deforms on three distinct slip systems [38]: (i) basal $\{0001\} \langle 1\bar{1}20 \rangle$, (ii) prismatic $\{10\bar{1}0\} \langle 11\bar{2}0 \rangle$ (iii) pyramidal $\{11\bar{2}1\} \langle 11\bar{2}6 \rangle$. TEM analysis has shown that out of these the prism $\{10\bar{1}0\} \langle 11\bar{2}0 \rangle$ should be the dominant slip system [38, 34]. The CRSS for these slip systems in Ti_3Al as a function

of temperature, indicating the ($\alpha_2+\beta$) working temperatures used in the present investigation, is presented in Fig. 4.66 [4]. Although, the addition of Nb to Ti_3Al is considered to increase the tendency for basal slip and perhaps homogeneous prismatic slip, but does not seem to increase the propensity for 'c' component slip [4]. It has already been mentioned that twinning, which is a common deformation mode in hexagonal $\alpha\text{-Ti}$, can be excluded in Ti_3Al and $\text{Ti}_3\text{Al} - \text{Nb}$ due to the fact that they have ordered structures [4].

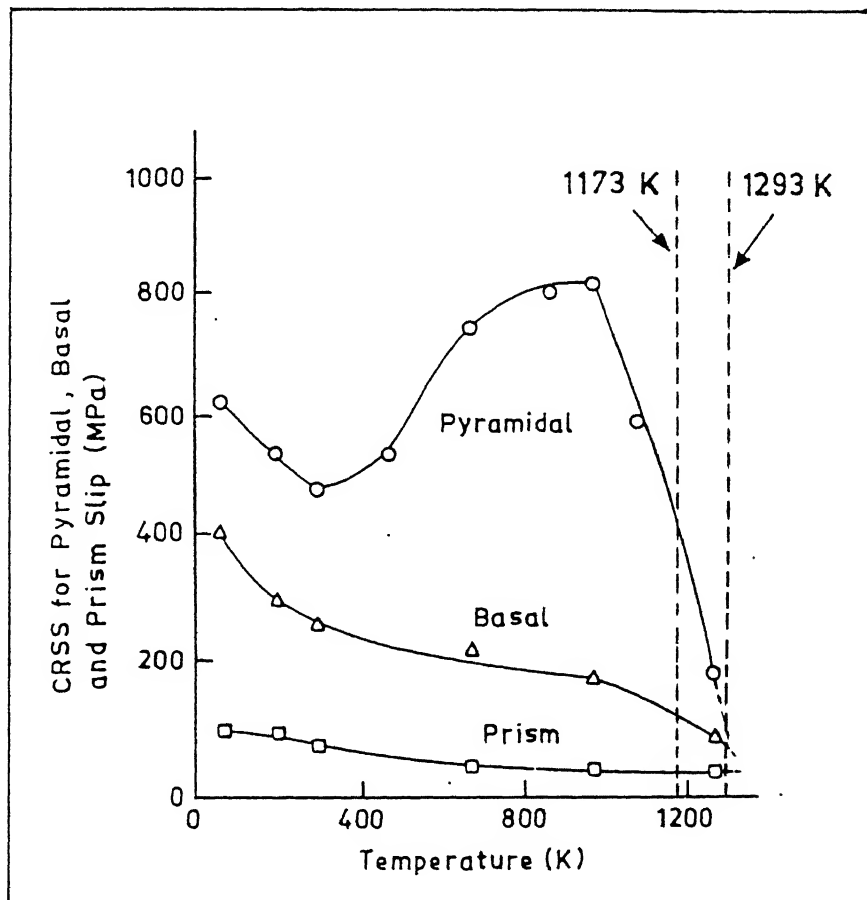


Fig. 4.66 Plot showing the variation of CRSSs for basal slip $(0001) \langle 11\bar{2}0 \rangle$, prismatic slip $\{10\bar{1}0\} \langle 11\bar{2}0 \rangle$ and pyramidal slip $\{11\bar{2}1\} \langle 11\bar{2}6 \rangle$ in Ti_3Al as a function of temperature [38]. Dashed vertical lines represent the rolling temperature used in the present investigation.

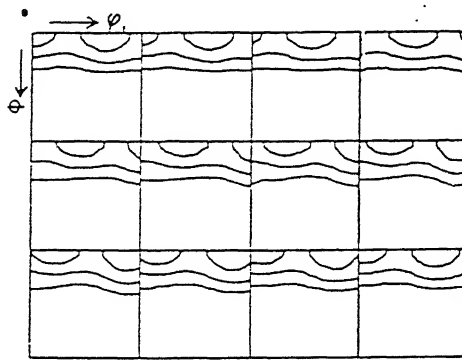
The room temperature rolling texture of Ti_3Al has been simulated by Chen *et al.* [154] using the Sach's deformation model. Fig. 4.67 (a) to (c) show the ODFs in cold rolled Ti_3Al alloy, as described in their paper [154], for the starting material and also after two different levels of deformation. The corresponding simulated textures are shown in Fig. 4.67 (d to f).

Some important orientations in the section $\phi_2 = 0^\circ$ are shown in Fig. 4.68 (a), while the locations of the stable orientations, obtained by the activation of basal, prism and pyramidal slip system respectively, according to the above model, have been shown in Fig. 4.68 (b), (c) and (d).

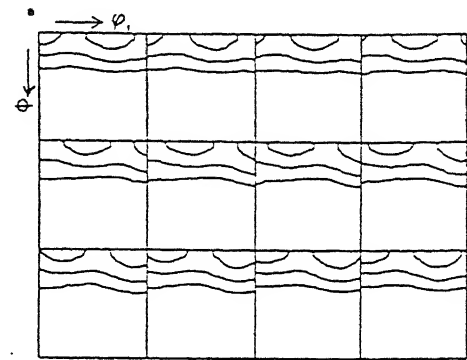
According to Minonishi *et al.* [38] the room temperature CRSS values for the α_2 phase in Ti_3Al are in the ratio 1:8:1.0:4.5 for the basal, prismatic and pyramidal slip systems respectively. These values indicate that prismatic slip should predominate during deformation in this alloy system. However, the cold rolling texture obtained by Chen *et al.* [154] clearly demonstrated that with deformation, grain orientations move perceptibly towards low ϕ angle position in the ODFs. This will be possible only when basal slip becomes the dominant deformation mode. Accordingly, Chen *et al.* [154] attempted to simulate the cold rolling texture using different CRSS ratios between the three slip systems. In fact, they found that there is a high degree of correspondence between the experimental and simulated textures when the modelling is carried out using the CRSS ratio 1:4.5:9 between basal, prismatic and pyramidal slips. The simulations clearly showed that during cold rolling upto a maximum of 35% reduction,

grain orientations accumulated towards low ϕ angle positions as well as around $(\bar{1}2\bar{1}0)[10\bar{1}0]$. Fig. 4.69 represents the path of orientation changes during simulation according to Chen *et al.* [154]. The arrows in this $\phi_2 = 0^\circ$ ODF section indicate the directions of orientation changes, and the lengths of the arrows show roughly the speed of this change. It is clear from this diagram that after deformation is complete, the grain distribution finally reaches two stable orientations, such as the boundary between areas E and D and area A.

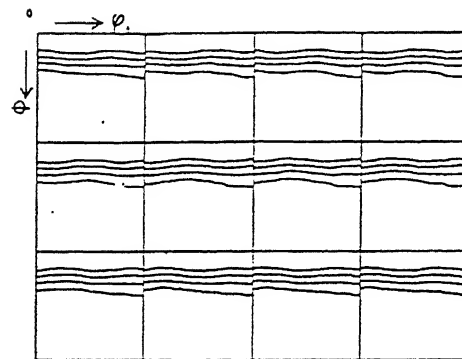
Clearly, the locations of the orientation distributions in the ODFs of the present alloy (Figs. 4.44 and 4.47) tally reasonably well with the locations of pole distribution maxima as found out in the above simulation. Thus, the simulation work by Chen *et al.* [154] seems to explain the evolution of α_2 rolling texture in the experimental alloy quite satisfactorily. However, it must be mentioned here that whereas Chen *et al.* [154] considered a maximum deformation level of 35% in their simulation, the deformation levels used in the present work vary between 50 and 80%.



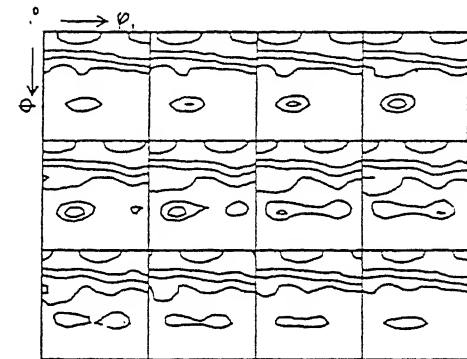
(a) 0% reduction(max.=3.7)



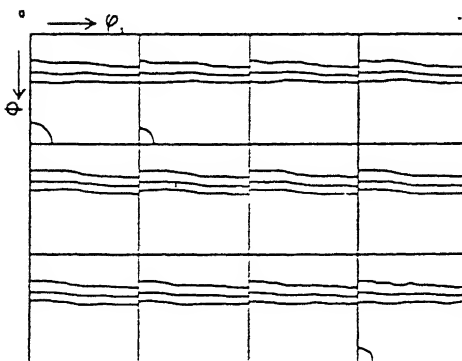
(d) 0% reduction(max.=3.7)



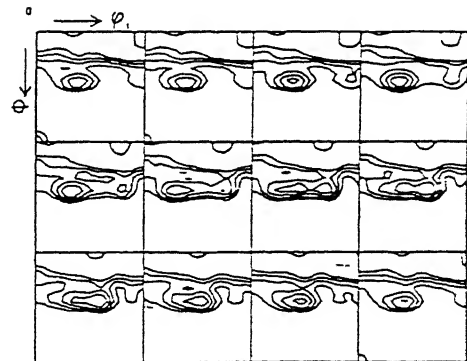
(b) 10% reduction(max.=5.6)



(e) 10% reduction(max.=4.7)

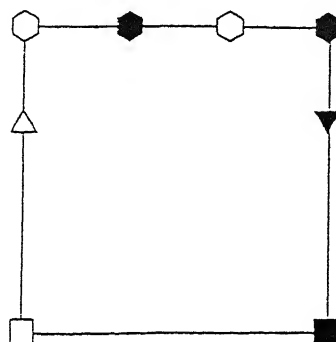


(c) 35% reduction(max.=3.7)



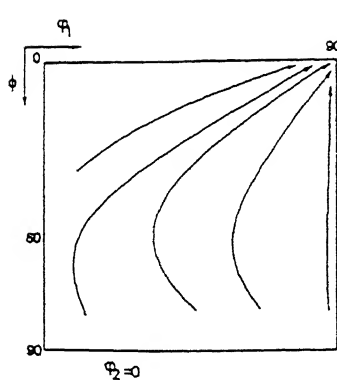
(f) 35% reduction(max.=7.6)

Fig. 4.67 Rolling textures of Ti_3Al ; Measured (a), (b),(c) and Simulated (d), (e), (f) [154]

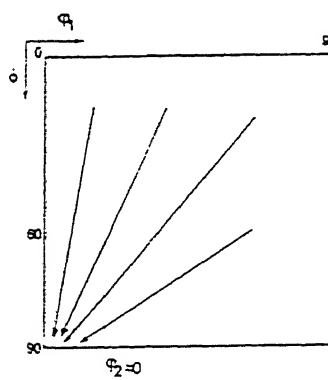


(a)

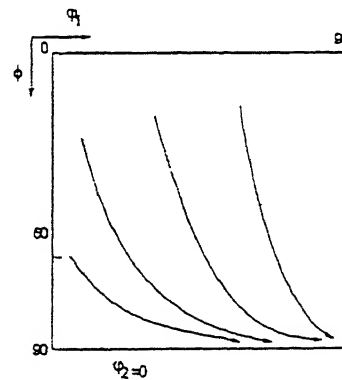
$\bigcirc\{0001\}\langle 10\bar{1}0\rangle$, $\triangle\{\bar{1}2\bar{1}3\}\langle 10\bar{1}0\rangle$,
 $\square\{\bar{1}2\bar{1}0\}\langle 10\bar{1}0\rangle$, $\bullet\{0001\}\langle 1\bar{2}10\rangle$,
 $\blacktriangledown\{\bar{1}2\bar{1}3\}\langle 2\bar{4}23\rangle$, $\blacksquare\{\bar{1}2\bar{1}0\}\langle 0001\rangle$



(b)



(c)



(d)

Fig. 4.68 (a) Some important orientations in the section $\phi_2=0^\circ$, (b), (c) and (d) the stable orientation predicted by the activation of basal, prism and pyramidal slip systems respectively [154]

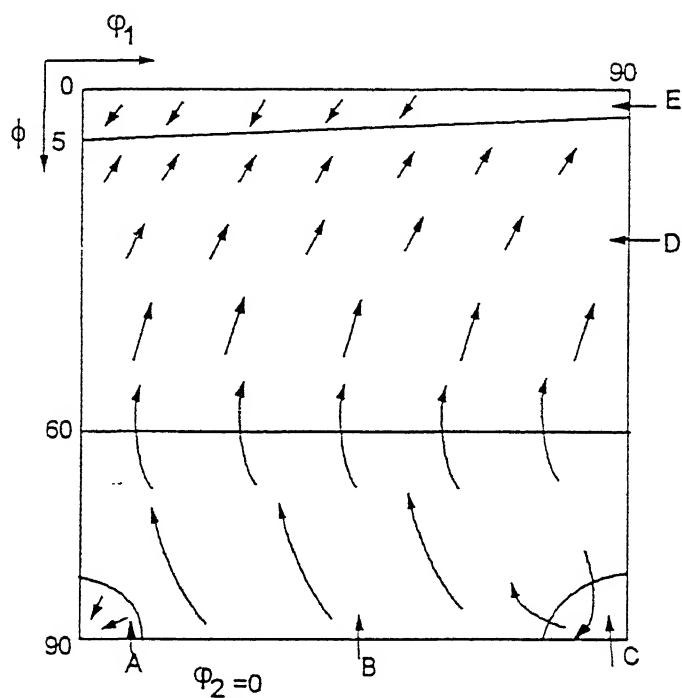


Fig. 4.69 Orientation changes during the simulating calculations in $\phi_2=0^\circ$ section [154]

(ii) Texture of secondary α_2

In the course of the present investigation there have been two cases where texture measurements were performed exclusively on the secondary α_2 phase. These are the materials rolled at 1373 K and 1523 K followed by furnace cooling. The optical microstructure of the 1373 K rolled (80%) and water quenched sample (Fig. 4.17) shows β grains with profuse strain markings inside. On the other hand, the 1523 K rolled (80%) and water quenched sample (Fig. 4.23) consists of larger β grains, which appear to be rather strain free (no strain marking inside the grains). Therefore in the former case, the secondary α_2 is expected to be derived from somewhat deformed β whereas in the latter case, the secondary α_2 phase results from more or less recrystallised β .

The textures of secondary α_2 in the above two specimens exhibit remarkable differences. The (0002) pole figure (Fig. 4.48) for the 1373 K rolled and furnace cooled material clearly shows a non basal type texture while the 1523 K material exhibits a $\{0002\} \langle uvw \rangle$ texture. The ODFs for both these conditions further reveal that the components like (0001)[10 $\bar{1}$ 0] and (0001)[1 $\bar{1}$ 00] which are very weak in 1373 K rolled condition get significantly sharpened in the case of 1523 K rolled and furnace cooled material. On the other hand, the component ($\bar{2}$ 4 $\bar{2}$ 1)[10 $\bar{1}$ 0] gets relatively weakened in the latter.

Texture development in the secondary α_2 phase occurs through three stages: (i) transformation during heating from α_2 (primary) $\rightarrow \beta$, attended by acquisition of a

texture by β from α_2 , (ii) development of rolling and/or recrystallisation texture in the β phase during hot rolling and (iii) transformation during cooling of $\beta \rightarrow \alpha_2$ (secondary), causing the formation of transformation texture.

In the $\text{Ti}_3\text{Al-Nb}$ system, continuous cooling from the β phase region results in precipitation of laths of α or α_2 in compositions of upto at least 11% Nb [4]. The crystallographic transformation between α_2 and β follows the Burger's relationship:

$$(0001)_{\alpha_2} \parallel (110)_{\beta} ,$$

$$[11\bar{2}0]_{\alpha_2} \parallel [\bar{1}\bar{1}1]_{\beta} .$$

The Burgers relationship between the α_2 and β phases is shown stereographically in a composite $(0001)_{\alpha_2}$ and $(110)_{\beta}$ stereogram (Fig. 4.70). This diagram illustrates the parallelism of slip vectors and planes in the two phases. The four possible $\langle 111 \rangle$ slip vectors in the β phase are enclosed in boxes. The β zones containing three of the four slip vectors which are also parallel to a possible α_2 slip vector, are indicated by dotted lines in this diagram. Such a diagram is very useful in determining the possible α_2 texture components from a parent β orientation.

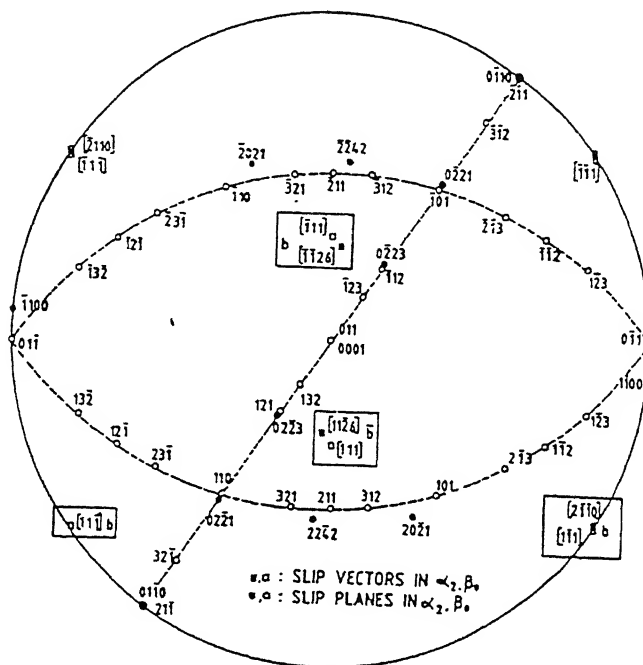


Fig. 4.70 Stereographic projections showing the Burger's relationship between α_2 and β phases and parallelism of slip vectors and planes. The four possible $\langle 111 \rangle$ slip vectors in β are enclosed in boxes. Dotted lines indicate β zones containing three of the four slip vectors which are parallel to a possible α_2 slip vector [35]

Table 4.3 The 12 orientation variants according to the Burger's relationship during $\alpha_2 \rightarrow \beta$ transformation [155]

Number of Variants	Correspondence planes	Correspondence directions
	β phase α phase	β phase α phase
V1	(011) \parallel (0001)	$[\bar{1}\bar{1}1] \parallel [2\bar{1}\bar{1}0]$
V2		$[1\bar{1}1] \parallel [2\bar{1}\bar{1}0]$
V3	$(\bar{1}01) \parallel (0001)$	$[1\bar{1}1] \parallel [2\bar{1}\bar{1}0]$
V4		$[111] \parallel [2\bar{1}\bar{1}0]$
V5	$(0\bar{1}1) \parallel (0001)$	$[111] \parallel [2\bar{1}\bar{1}0]$
V6		$[\bar{1}11] \parallel [2\bar{1}\bar{1}0]$
V7	$(101) \parallel (0001)$	$[\bar{1}11] \parallel [2\bar{1}\bar{1}0]$
V8		$[\bar{1}\bar{1}1] \parallel [2\bar{1}\bar{1}0]$
V9	$(\bar{1}10) \parallel (0001)$	$[\bar{1}\bar{1}1] \parallel [2\bar{1}\bar{1}0]$
V10		$[111] \parallel [2\bar{1}\bar{1}0]$
V11	$(110) \parallel (0001)$	$[1\bar{1}1] \parallel [2\bar{1}\bar{1}0]$
V12		$[\bar{1}11] \parallel [2\bar{1}\bar{1}0]$

The Burger's orientation relationship during $\beta \rightarrow \alpha_2$ transformation leads to a total of 12 orientation variants and these are shown in Table 4.3 [155]. According to these authors, the transformation texture components $(\bar{2}110)[0\bar{3}31]$, $(\bar{2}110)[0\bar{1}11]$ and $(\bar{2}110)[0\bar{1}13]$ could arise from the $\{001\} \langle 100 \rangle$ and $\{001\} \langle 110 \rangle$ orientations of the β according to the variants V3-V6 and V9-V12 in Table 4.3. Similarly, the components $(\bar{2}111)[2\bar{3}16]$, $(\bar{1}012)[5\bar{4}\bar{1}3]$, $(\bar{2}115)[5\bar{4}\bar{1}3]$ and $(\bar{2}110)[0\bar{1}11]$ could arise from the $\{112\} \langle 111 \rangle$ and $\{001\} \langle 100 \rangle$ orientations of the β according to the variants V1-V12 in Table 4.3.

The phenomenon of $\beta \rightarrow \alpha_2$ phase transformation in Ti was dealt with by Inagaki [128] in some details. Assuming that the main orientations of the hot rolling texture developed in unrecrystallised b.c.c. β phase in Ti consist of $\{100\} \langle 011 \rangle$, $\{311\} \langle 011 \rangle$, $\{211\} \langle 011 \rangle$, $\{111\} \langle 110 \rangle$ and $\{111\} \langle 112 \rangle$, orientations of the α_2 phase derived from the above orientations via Burger's relationship were calculated. Among the calculated product orientations, those having ϕ (Roe notation) in the range between 25° and 35° were plotted by Inagaki in the $\phi = 30^\circ$ (Roe notation) section. The same has been converted into Bunge notation and the resulting plot is shown in Fig. 4.71.

The superposition of the $\phi_2 = 0^\circ$ section of Fig. 4.71 on the $\phi_2 = 0^\circ$ sections of the ODFs of secondary α_2 produced from 1373 K and 1523K rolled (80%) β phase at once gives an idea of the origin of the different α_2 texture components in the parent β .

The texture in the former case shows only a weak maxima near $[0001] \parallel ND$ location, however there are significant pole densities in other parts of the relevant section. In fact all the pole densities here can be accounted for by assuming texture transformation from the components $\{100\} \langle 011 \rangle$, $\{311\} \langle 011 \rangle$, $\{211\} \langle 011 \rangle$, $\{111\} \langle 110 \rangle$ and $\{111\} \langle 112 \rangle$ orientations in the parent β .

The texture of the secondary α_2 formed from the 1523K rolled material is very much different from the one derived from the 1373 K rolled material (Fig. 4.48). It appears a little bit of a paradox since the secondary α_2 in both the cases are derived from high temperature β phase. However, as mentioned earlier, the β phase after hot rolling at 1373 K appears to have some strain left in it as shown by plenty of strain-markings within most of the grains (Fig. 4.17). It may be mentioned here that the temp. of 1373 K is near about the same as the β transus temperature in this material. On the other hand, the β of 1523 K rolled material is essentially recrystallised and strain free (Fig. 4.23). The difference in the secondary α_2 texture in the two cases can be understood in terms of the difference in the state of stress of β in the two cases.

Fredericks [156] proposed that if the β to α transformation takes place under constraints from the rolling deformation, only one of the six highly textured $\{110\}$ planes is favoured in transforming to the $\{0002\}$ planes of the product hexagonal phase. This could explain, why the $[0001] \parallel ND$ texture is almost absent in the texture of the secondary α_2 phase derived from the 1373 K rolled material.

It has also been argued [157] that if the textured β phase is allowed to recrystallise first, before transforming into the α -phase, all six $\{110\}$ planes will be equally favoured in transforming to the basal plane giving rise to a strong basal texture. Presumably, this is precisely what is happening during the $\beta \rightarrow \alpha_2$ transformation in the 1523 K rolled material. As can be seen in the optical micrograph, Figs. 4.23 , the β phase after rolling at 1523 K appears more or less fully recrystallised and in a strain-free condition. This is also corroborated by the series of TEM micrographs shown in Figs. 4.25. Thus the secondary α_2 produced from the 1523 K rolled material is expected to show basically a basal texture, which is clearly what is obtained in the present case.

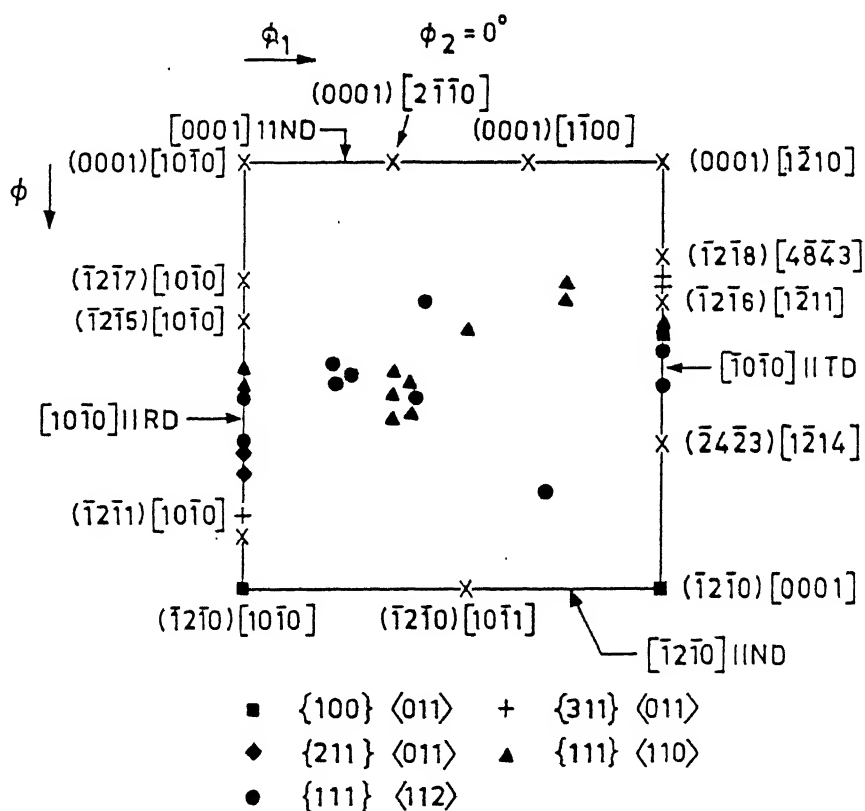


Fig. 4.71 The α/α_2 textures predicted from a few β orientations

(iii) Texture of primary plus secondary α_2

The samples which were rolled at 1293 K and either water quenched or furnace cooled belong to this category. In the former, the room temperature microstructure consists roughly of 50% primary α_2 (partially recrystallised) and 50% β . In the latter, the room temperature microstructure consists roughly of 50% primary and 40% secondary α_2 , plus some retained β .

The crystallographic texture of α_2 in the primary α_2/β sample differs very significantly from the texture of α_2 in the primary α_2 /secondary α_2 sample (Figs. 4.53 (b) and 4.50 (b)). The texture in the former case appears more intense than in the latter. The other major point of difference is the much stronger near basal components in the former as compared to the latter. This trend is also very clear in the corresponding (0002) pole figures (Figs. 4.51 (b) and 4.48 (b)). As has already been mentioned earlier, the few texture components along $[10\bar{1}0]\parallel RD$ found in the ODF of the primary α_2 /secondary α_2 sample (Fig. 4.50 b) are presumably due to the secondary α_2 derived from rolled β .

The ODF of the primary α_2/β sample shows, in addition to the near basal components, some other texture components lying on the $[10\bar{1}0]\parallel RD$ line with maxima nearer to $\{\bar{1}2\bar{1}0\} \langle 10\bar{1}0 \rangle$. As already mentioned earlier, at least some of the texture components lying along the above fibre could also be derived from the texture of rolled β by transformation. The formation of any secondary α_2 phase can be ruled out in this sample.

Chen *et al.* [154] from their texture simulation studies in Ti_3Al base alloys have shown that activation of the prismatic slip system will move material towards the $\{\bar{1}2\bar{1}0\} \langle 10\bar{1}0 \rangle$ location. Inagaki [133], who worked on the evolution of texture in a Ti-6Al-4V alloy during hot rolling, also suggested that the prismatic slip will enhance the formation of $\{\bar{1}2\bar{1}0\} \langle 10\bar{1}0 \rangle$ component of texture. At the hot rolling temperature of 1293 K the CRSS values for basal and prismatic slip in $\text{Ti}_3\text{Al-Nb}$ are not much different (Fig. 4.66). Thus rolling at this temperature is expected to involve profuse basal and prismatic slip resulting in a near basal texture plus some orientations along the $\{10\bar{1}0\} \parallel \text{RD}$ with maxima near to $\{\bar{1}2\bar{1}0\} \langle 01\bar{1}0 \rangle$. This is what has been observed in the texture of the primary α_2/β sample.

In the furnace cooled sample where both primary α_2 and secondary α_2 coexist, the near basal component appears rather weak (Fig. 4.48 b). The difference in the processing between this sample and the previous one was that while the former stayed after rolling in a high temperature region for a much longer period of time, the latter did not have that opportunity. In other words, the furnace cooled material underwent much more extensive recovery and partial recrystallisation as compared to the quenched material. These differences are also apparent in their TEM microstructures (Figs. 4.14 and 4.15). It, therefore, appears quite plausible that the tangible decrement of the near basal texture of primary α_2 in the furnace cooled sample has been caused by the annealing effect. The effect of annealing on the formation of basal texture will be dealt in much more detail in the next chapter.

Stability of Basal Texture on Annealing

In the previous chapter, the effects of various thermomechanical processing parameters on the evolution of texture and microstructure in the Ti-24Al-11Nb alloy were enumerated and discussed. It has already been suggested that in order to achieve good ductility and formability in this alloy, it is desirable to have a good basal $\{0001\} <uvw>$ texture [93]. In addition, it is also desirable to control the microstructure to optimise the properties in order to make the as-processed alloy suitable for various applications. The proper microstructural control is usually done by subsequent annealing treatments following the deformation processing. These treatments are most likely to affect the texture of the material also. It is therefore essential to have a comprehensive idea of the texture developed/modified as a result of post rolling heat treatment.

In order to examine the stability of the basal texture after heat treatment, the material with the processing sequence *as-cast* \rightarrow *heat treated* \rightarrow *hot rolled at 1173 K by 80% reduction in thickness* \rightarrow *water quenched*, was chosen. This starting material possesses the strongest basal texture as has already been found out. The heat treatments were planned in such a way that the effects of both α_2/β phase fraction as well as substructural/microstructural changes could be examined. Isochronal annealing was carried out for a period of 1 hour at four different temperatures within the range 1123 K-1293 K. At the highest temperature used (1293 K), the constituent phases (α_2

and β) assume equiproportional volume fractions as predicted by the phase diagram. Secondly, isothermal annealing was also performed at the temperature of 1173 K for various lengths of time. The temperature was chosen such that the volume fraction of the β phase will not vary significantly with time of annealing.

5.1 Isochronal Annealing

5.1.1 Microstructure

The Scanning electron micrographs of specimens annealed for 1 hour at temperatures 1123 K, 1173 K, 1233 K and 1293 K are given in Figs. 5.1 (a-d) respectively. It can be seen from the Fig. 5.1 (a) that there is some apparent change in the gross microstructural feature of 1123 K annealed material from the as rolled condition (Fig. 4.9 c). Definite signs of the rolling process is quite discernible in the SEM micrograph. However, the TEM micrograph (Fig. 5.2) shows definite signs of the onset of recovery. Thus the material at this stage is in a partially recovered condition. The microstructure of the 1173 K annealed material shows the presence of a few equiaxed grains (Fig. 5.1 b). The signs of deformation are not that apparent in this micrograph. The substructural features as seen in the TEM micrographs of this specimen (Figs. 5.3) indicate extensive recovery as well as the initiation of recrystallisation at many places.

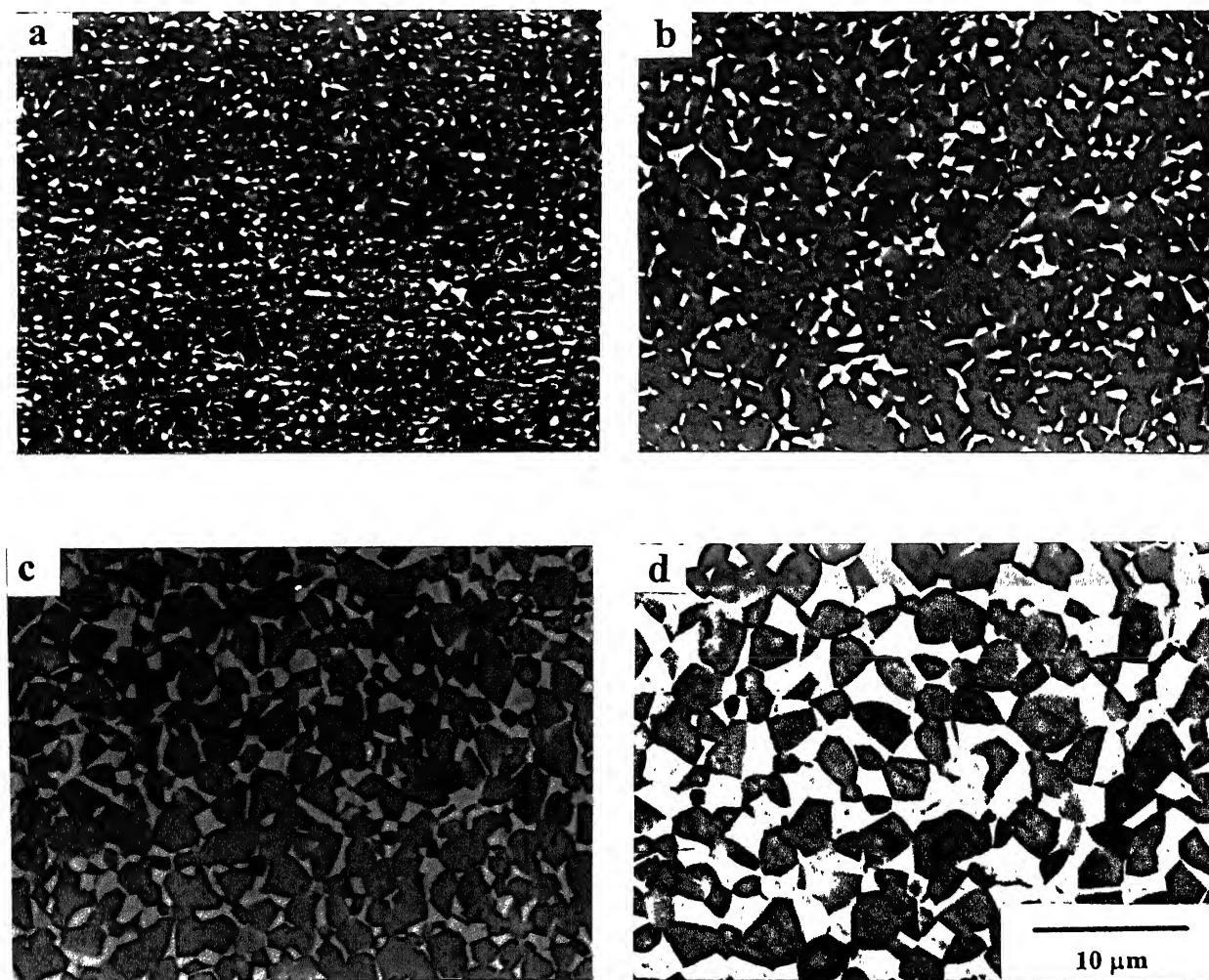


Fig. 5.1 SEM Micrographs of isochronally annealed (1 hr) specimens for the annealing temperatures (a) 1123 K, (b) 1173 K, (c) 1233 K and (d) 1293 K (all water quenched)

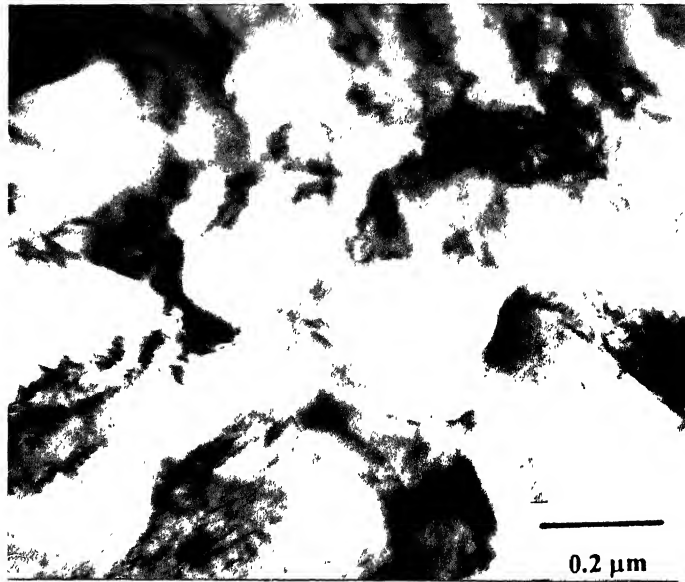


Fig. 5.2 TEM Micrograph of material annealed at 1123 K for 1 hr showing the onset of recovery process

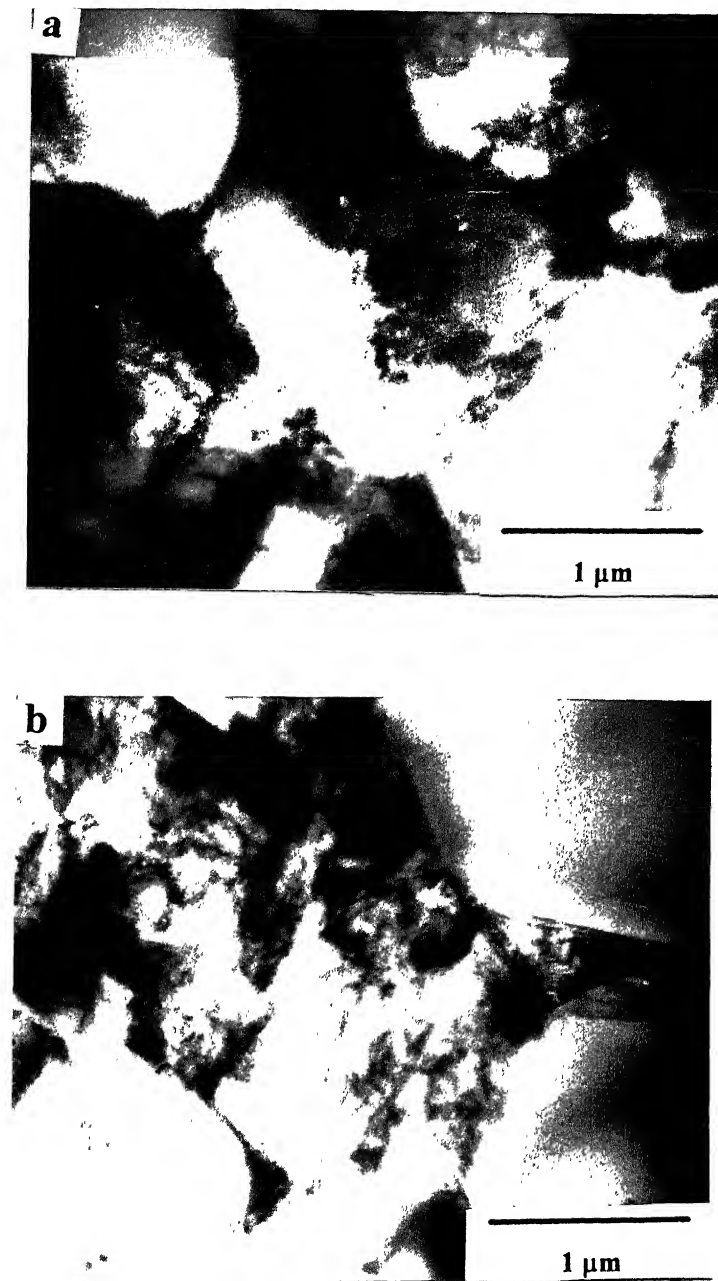


Fig. 5.3 TEM Micrograph of material annealed at 1173 K for 1 hr showing the features of (a) recovery process in α_2 and (b) recrystallised α_2 grains

The effect of annealing at the temperature 1233 K manifests itself in two different ways: (i) substructural changes accompanying recovery and recrystallisation and (ii) increase in the β content of the material. The SEM microstructure (Fig. 5.1 c) reveals a nearly uniform equiaxed grain structure for the α_2 phase with β occupying the triple point regions. TEM microstructures (Figs. 5.4) reveal almost fully recrystallised areas in many places in addition to some remnants of the highly recovered substructure.

After annealing at 1293 K for 1 hour the SEM micrograph shows a duplex structure with α_2 and β grains - both having nearly equiaxed morphology and of comparable sizes. Evidently, the volume fractions of α_2 and β here are 50:50. The TEM micrographs at this stage shows recrystallised grains (Fig. 5.5); it is difficult to distinguish the α_2 from the β grains by just looking at their features.

5.1.2 X-Ray Diffraction Profiles

The XRD profiles recorded for all the isochronally annealed samples are presented in Fig. 5.6. These profiles clearly indicate that there is slight decrement in the intensity of (0002) peak of the 1123 K annealed material compared to the starting as-rolled material. On the other hand the 1173 K and 1233 K annealed materials exhibit stronger (0002) peak reflection. The intensity of the basal reflection decreases drastically in the case of 1293 K annealed sample.

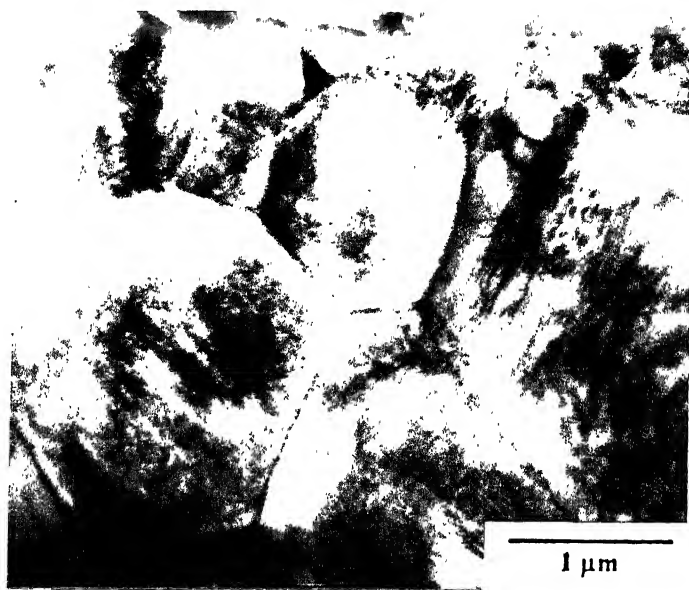


Fig. 5.4 TEM Micrograph of material annealed at 1233 K for 1 hr

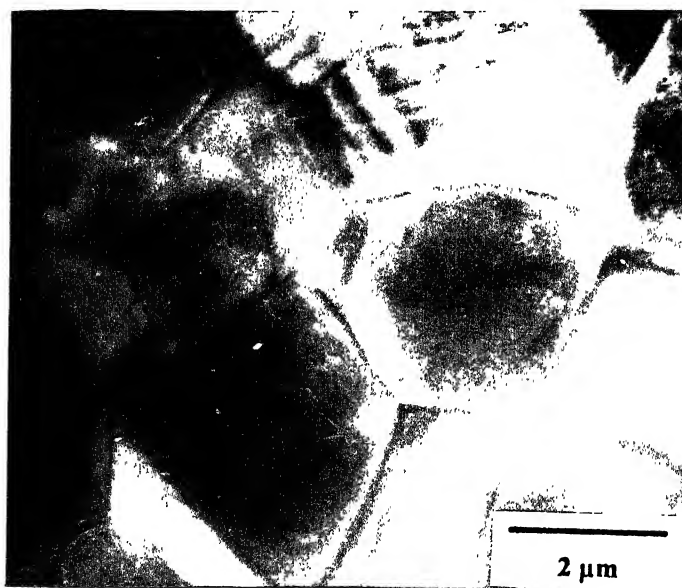


Fig. 5.5 TEM Micrograph of material annealed at 1293 K for 1 hr

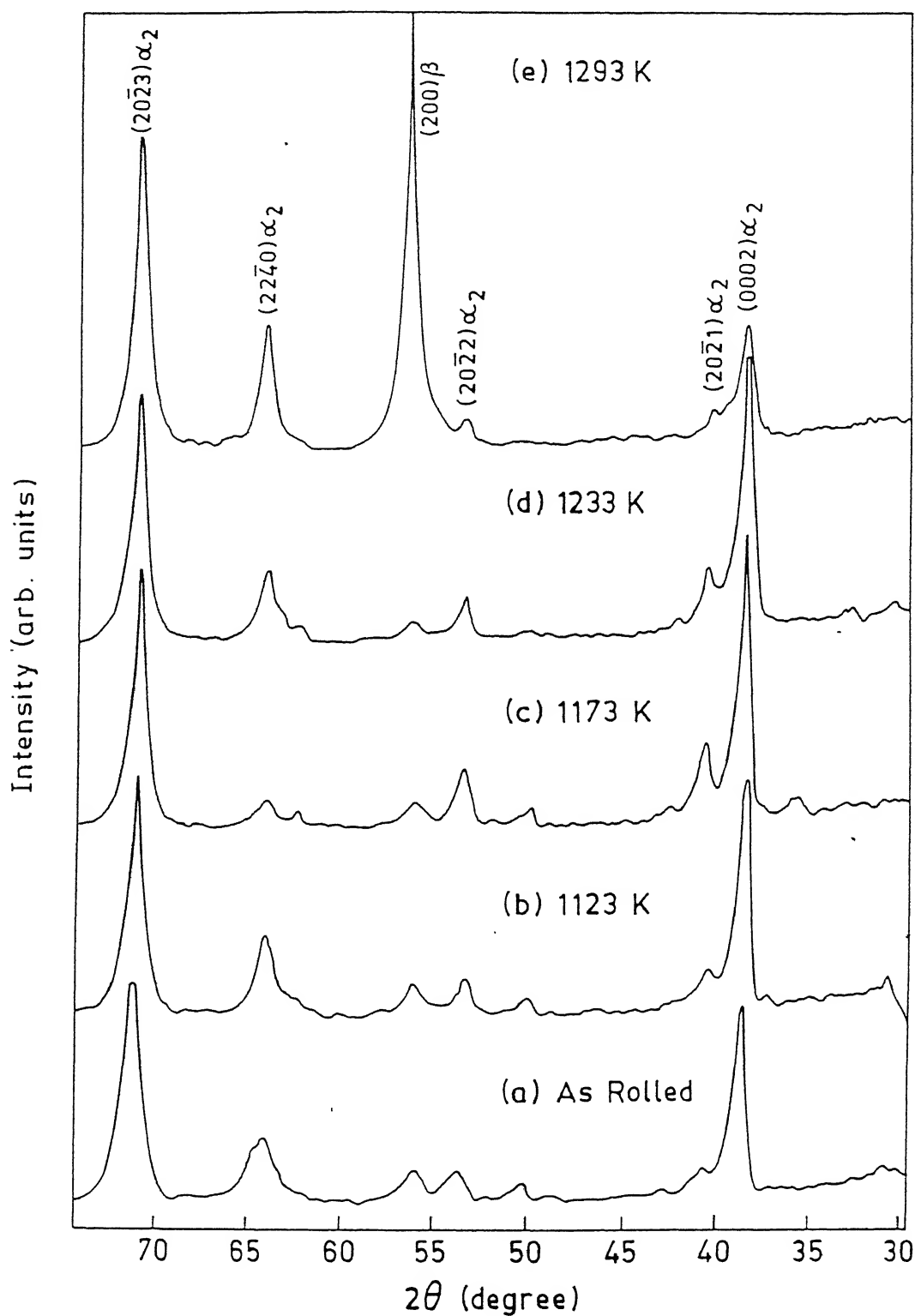


Fig. 5.6 X-ray diffraction patterns for the isochronally annealed specimens

5.1.3 Textural Changes

The textural investigations were confined to the α_2 (h.c.p.) phase only, as the main interest in the present case was to study the stability of basal texture of the starting material as a function of annealing.

The (0002) and (20 $\bar{2}$ 0) pole figures for the 1123 K, 1173K, 1233 K and 1293 K annealed samples are shown in Figs. 5.7 and 5.8 respectively. The rationale behind the use of the (20 $\bar{2}$ 0) pole figures in addition to the (0002) is as follows. It is commonly believed that in h.c.p. metals, after annealing, the recrystallisation texture appears quite similar to the rolling texture [158]. The relation between the two types of texture is usually described by a rotation about the hexagonal axis. As a result the disposition of the basal poles may remain approximately unaltered consequent upon recrystallisation. It is because of this, that (20 $\bar{2}$ 0) pole figures are considered to be more informative as compared to the (0002). The (0002) pole figures for all the four heat treated samples indicate the presence of a sharp basal texture in all of them. However, the corresponding (20 $\bar{2}$ 0) pole figures show that the maxima in the pole densities appear not exactly at the basal positions but slightly away from it. However, the maxima are arranged in the fashion of a near basal fibre texture. There are also subtle differences in the pole figures for the different samples. For example, the intensity of the near basal poles shows a drastic decrement (from 9.4R to 5.9R) in the 1123 K / 1 hr annealed sample as compared to the pole density in the starting material. The pole densities show an increase after heat treatment for 1 hr at temperatures 1173

K and 1233 K. The pole density again decreases after isochronal annealing at 1293 K for 1 hr. Another minor difference in the pole figures for the four samples is also clearly visible in the (0002) pole figures. For example, the basal poles in the 1173 K / 1 hr sample show a distinct RD split behaviour, whereas the basal poles in the 1293 K / 1 hr sample show a RD-TD split.

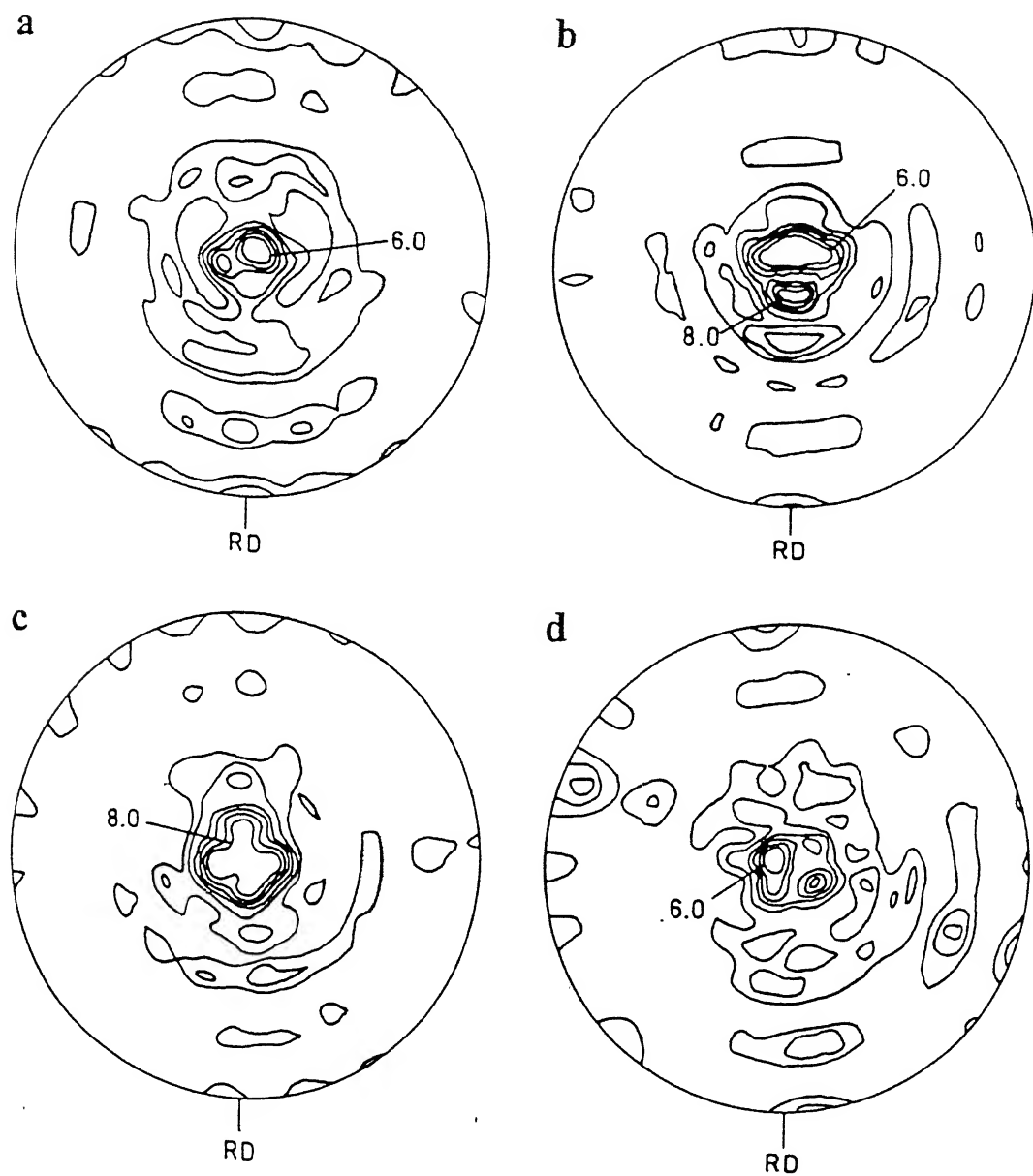


Fig. 5.7 (0002) pole figures for the isochronally annealed specimens; (a) 1123 K, (b) 1173 K, (c) 1233 K and (d) 1293 K

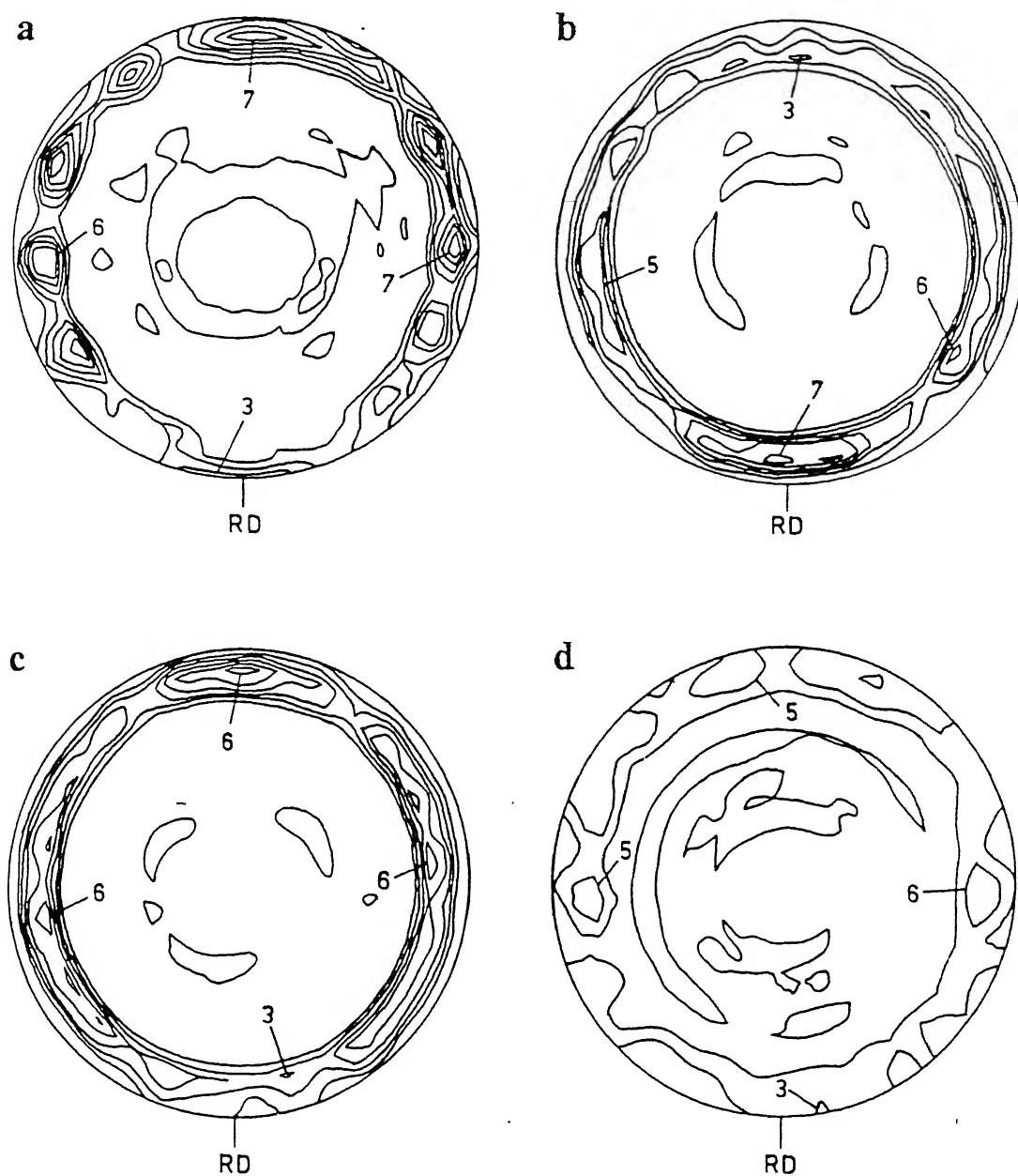


Fig. 5.8 $(20\bar{2}0)$ pole figures for the isochronally annealed specimens; (a) 1123 K, (b) 1173 K, (c) 1233 K and (d) 1293 K

The orientation distribution function (ODF) plots for all the isochronally annealed materials are shown in Figs. 5.9 to 5.12. In order to have a comparative study, the $\phi_2 = 0^\circ$ and $\phi_2 = 30^\circ$ sections of all the ODFs are separately given in Fig. 5.13 (a-d). The ODF plot of the 1123 K annealed material displays a number of orientations along $[0001]\parallel ND$, $[10\bar{1}0]\parallel RD$ and $[10\bar{1}0]\parallel TD$ fibres (Fig. 5.13 a). All the fibres are rather weak. The intensity of the near basal fibre is decidedly much weaker as compared to that in the starting material. The specimen annealed at 1173 K, on the other hand, shows the retention of the near basal texture, the fibre being located at 6° towards ϕ from the $(0001) \langle uvw \rangle$ (Fig. 5.13 b). In the $\phi_2 = 0$ section, the strongest maxima appears at near $(0001)[1\bar{1}00]$ location. The other strong maxima is located at near $(0001)[1\bar{2}10]$ position. From the $\phi_2 = 30^\circ$ section, it can be seen that the other texture maxima appear at near $(0001)[4\bar{3}\bar{1}0]/[5\bar{4}\bar{1}0]$, $(0001)[1\bar{2}10]$, $(0001)[2\bar{1}\bar{1}0]$ and $(01\bar{1}6)[2\bar{4}21]$. The last one is a non basal component.

The orientation distribution function plots for the 1233 K annealed material show a strong maxima at $\phi = 12^\circ$ from the ideal $(0001)[10\bar{1}0]$ (Fig. 5.13 c). The other strong orientation, rather the strongest orientation in this case is at $(0\bar{1}\bar{1}5)[3\bar{4}21]$. In addition to these two, there are other orientations like $(0001)[\bar{4}310]$, $(0001)[1\bar{2}11]$, $(0001)[0\bar{1}10]$ and $(0\bar{1}15)[2\bar{1}\bar{1}0]$, which are also reasonably strong.

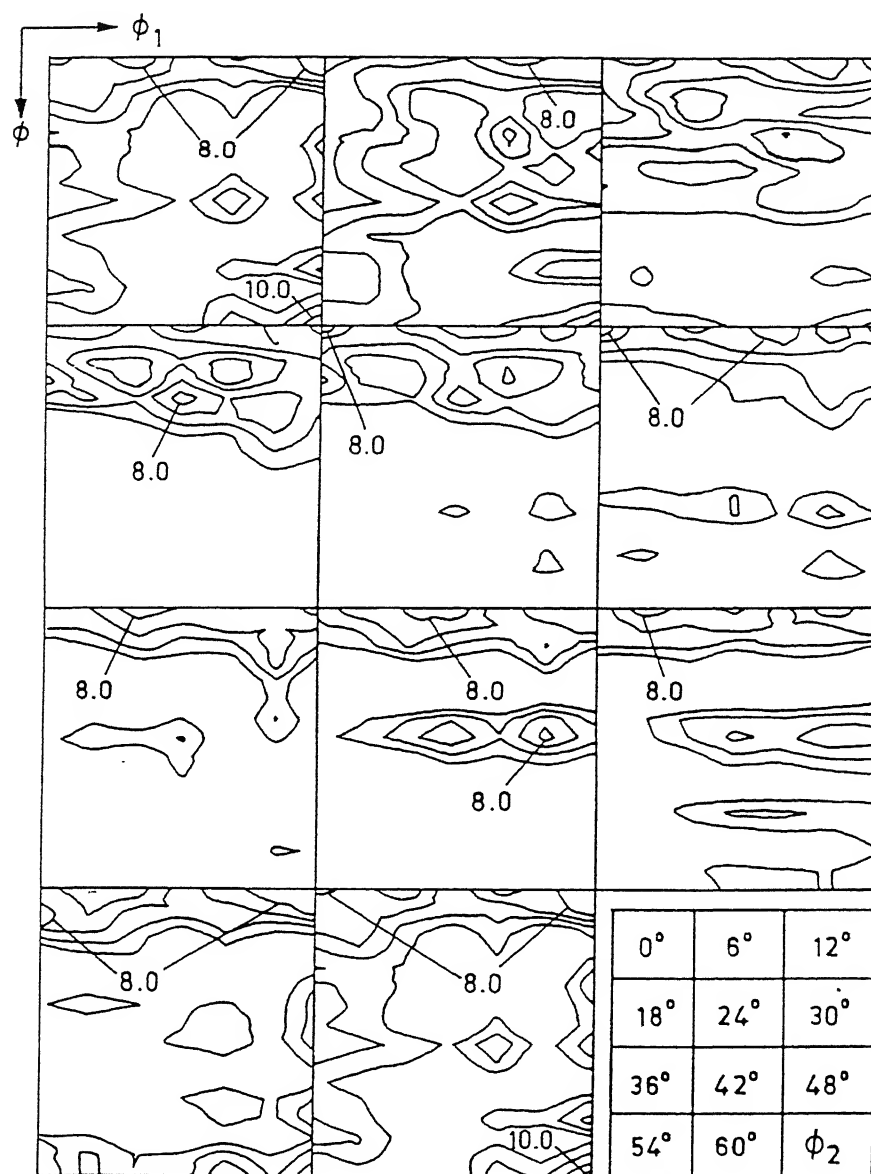


Fig. 5.9 Complete ODF of the material annealed at 1123 K for 1 hr

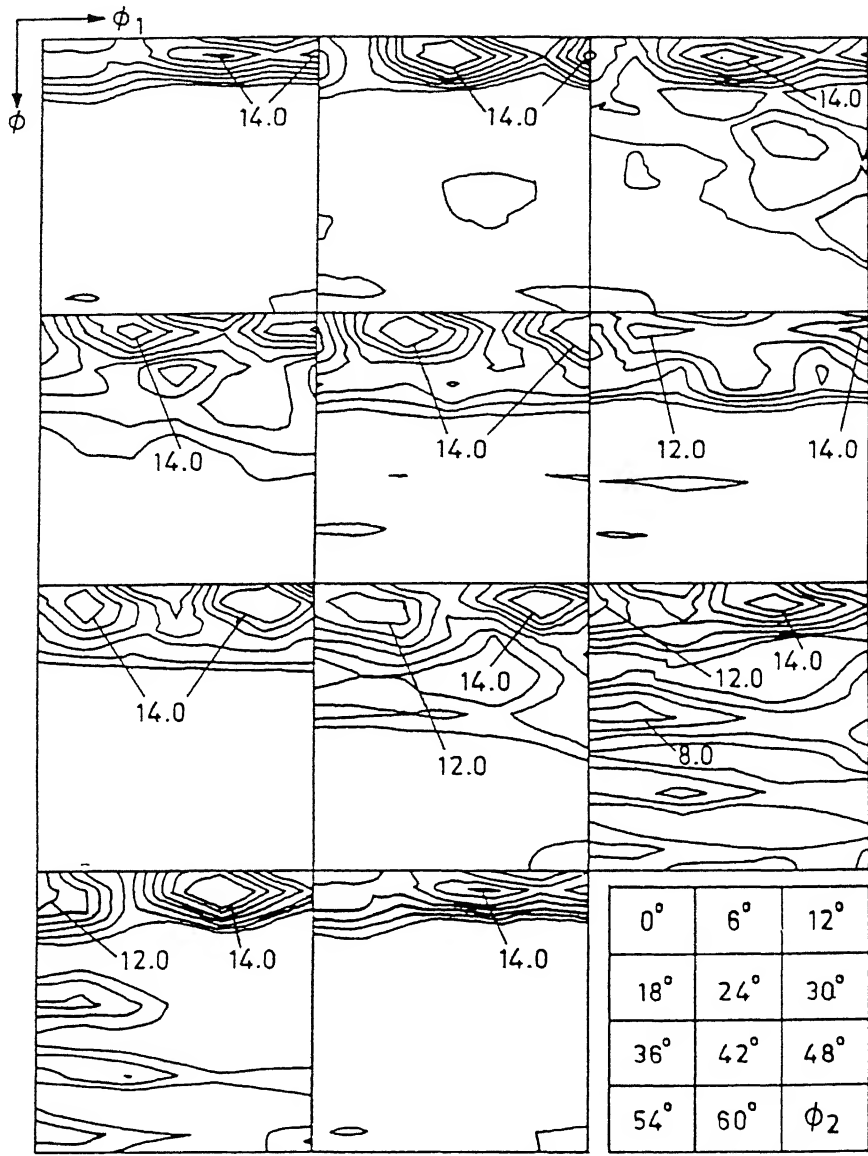


Fig. 5.10 Complete ODF of the material annealed at 1173 K for 1 hr

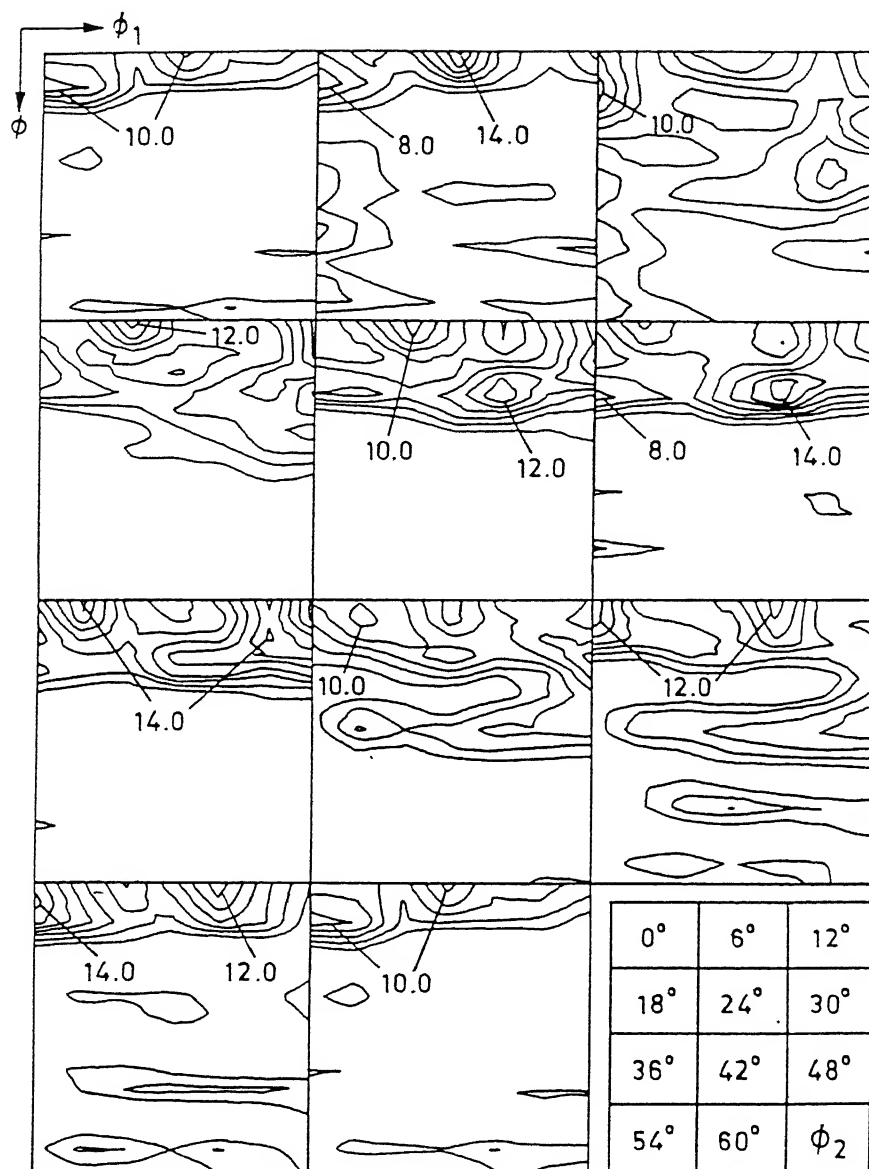


Fig. 5.11 Complete ODF of the material annealed at 1233 K for 1 hr

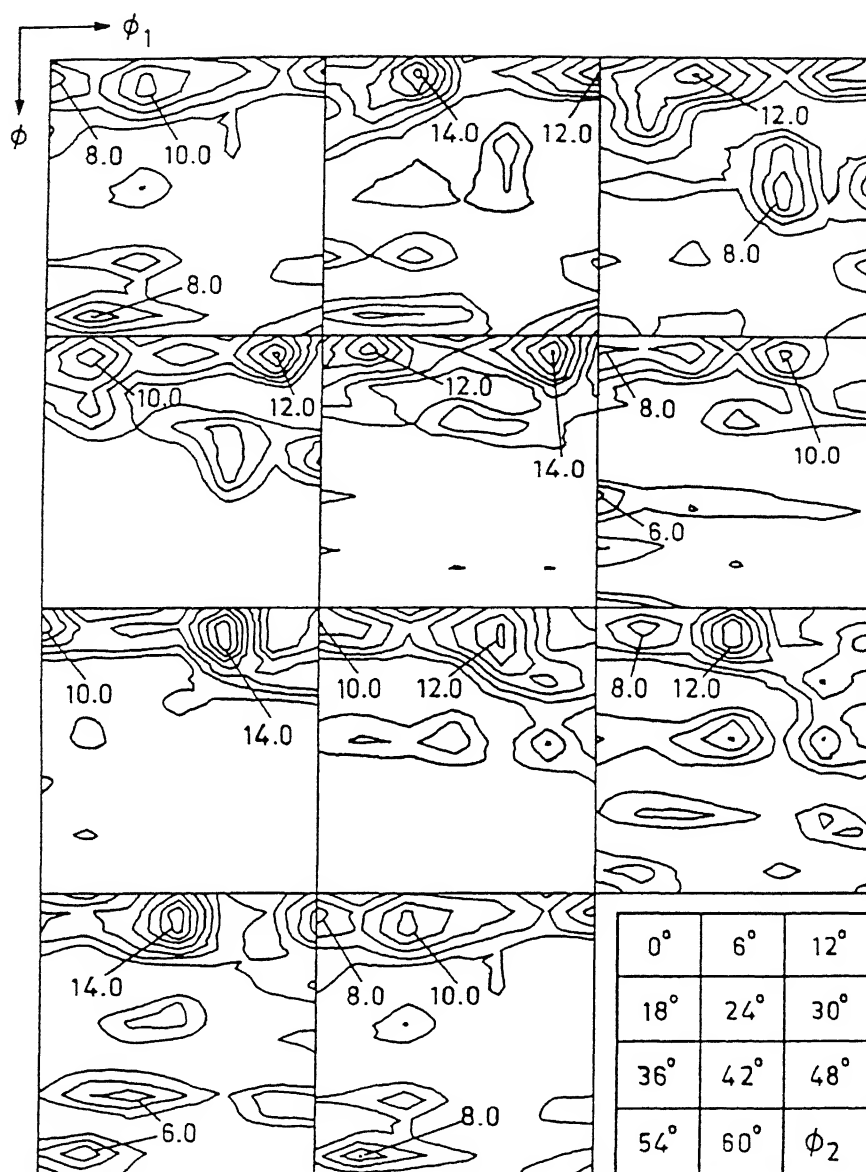


Fig. 5.12 Complete ODF of the material annealed at 1293 K for 1 hr

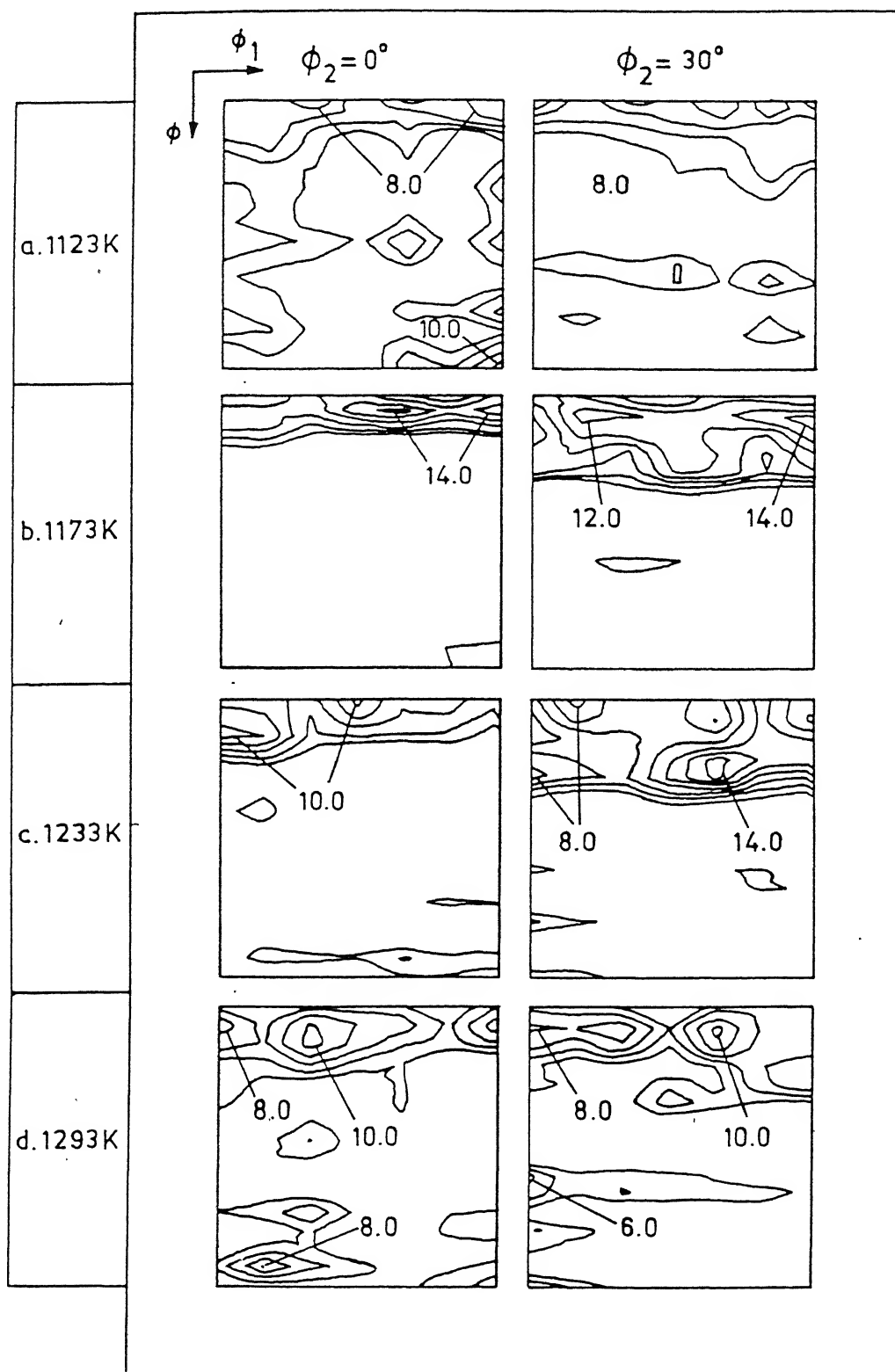


Fig. 5.13 $\phi_2 = 0^\circ$ and 30° sections of the ODF for the isochronally annealed materials; (a) 1123 K, (b) 1173 K, (c) 1233 K and (d) 1293 K

In the 1293 K annealed material, the main texture components as revealed in the ODFs are $(0001)[1\bar{2}10]$, $(0001)[10\bar{1}0]$, $(0001)[\bar{2}110]$, $(0001)[1\bar{1}00]$ (all at $\phi = 6^\circ$ from the ideal positions) and a few non basal orientations like the $(\bar{1}2\bar{1}0)[60\bar{6}1]$ (Fig. 5.13 d). In addition, a few relatively weak orientations like $(01\bar{1}6)[0\bar{3}31]$, $(0\bar{2}23)[2\bar{1}\bar{1}0]$, $(0\bar{2}21)[2\bar{1}\bar{1}0]$ and $(01\bar{1}0)[2\bar{1}\bar{1}0]$ do also appear in the ODF.

5.2 Isothermal Annealing

The textural changes on annealing were more thoroughly examined at 1173 K. The rationale behind the choice of this temperature was to study the stability of the near basal texture in this material as a function of annealing without the interference of any phase transformation of the type $\alpha_2 \rightarrow \beta$. When the as-cast \rightarrow heat treated material is hot rolled at 1173 K by 80%, it practically acquires the maximum α_2 volume fraction which persists at the room temperature after quenching. This α_2 also has a strong near basal texture. The purpose of annealing the starting material at this temperature for different lengths of time was to study the stability of the basal texture during recovery, recrystallisation and grain growth phenomena to which the material will be subjected. The accompanying developments in microstructures and changes in X-ray line profiles were also examined in this connection.

5.2.1 Microstructure

The scanning electron micrographs for the material annealed for 15 minutes, 30 minutes, 2 hrs and 12 hrs are shown in Figs. 5.14 (a-d). It is apparent from these microstructures and from the microstructure of the starting as rolled material (Fig. 4.9 c) that the material annealed for 15 min hardly shows any significant change from the microstructure of the starting material (Fig. 5.14 a). Annealing for 30 min produces a few equiaxed grains in the microstructure (Fig. 5.14 b). Further annealing upto 1 hr leads to an increase in the volume fraction of grains with equiaxed morphology (Fig. 5.1 b), while the material annealed for 2 hrs contains almost fully equiaxed grains (Fig. 5.14 c). The microstructure remains stable upto the annealing time of 8 hrs. On annealing for 12 hrs, the grains are seen to grow (Fig. 5.14 d).

The TEM study of the microstructures reveals that the material annealed at 1173 K for 30 min undergoes extensive recovery. The TEM microstructures displayed in Figs. 5.15 (a) and (b) show an overall view of the features, while the ones shown in Figs. 5.15 (c) and (d) indicate extensive recovery in the α_2 phase as well as the presence of a few recrystallised grains of α_2 . The β phase remains more or less in a strongly deformed state.

The TEM micrograph of the 1 hr annealed material shows a much more advanced stage of recovery and clear cut initiation of recrystallisation as shown earlier in Figs. 5.3 (a and b). The material annealed for 2 hrs shows signs of recrystallisation at many places, although isolated deformed areas are also seen. Figs. 5.16 (a-d) show

typical microstructures from deformed, highly recovered, partially recrystallised and fully recrystallised regions respectively. A typical feature showing fish-tail type feature is also seen at this stage (Fig. 5.16 e). The TEM micrographs from the samples annealed for 8 and 12 hrs mostly show large recrystallised grains only.

5.2.2 X-ray Diffraction Profiles

The XRD profiles recorded at slow scan for the isothermally annealed specimens are shown in Fig. 5.17. As it can be seen, the basal (0002) reflection keeps sharpening with the annealing time. The $(20\bar{2}1)$, $(20\bar{2}2)$, $(22\bar{4}0)$ and $(20\bar{2}3)$ peaks also sharpen indicating the stress relief occurring with annealing time.

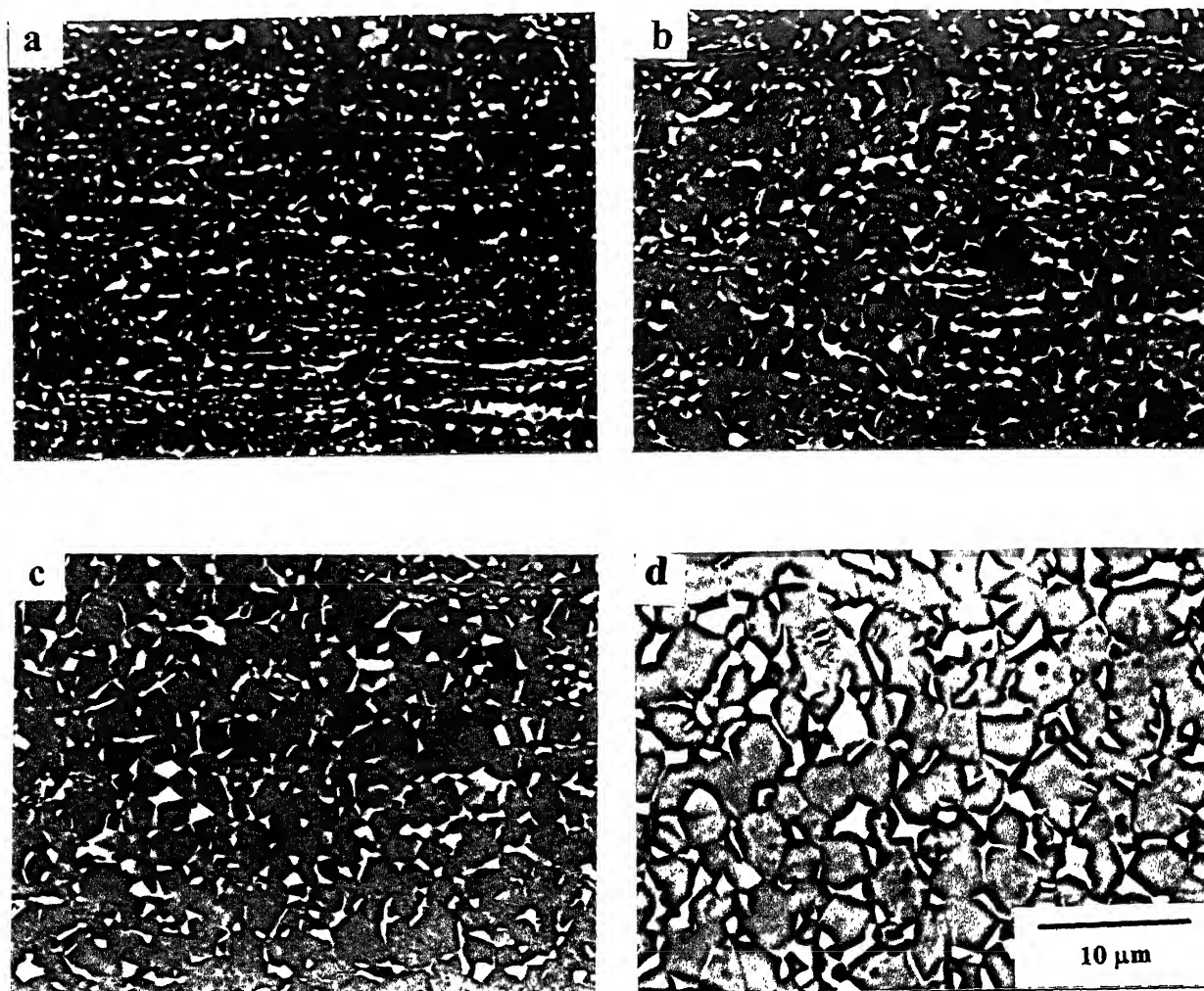
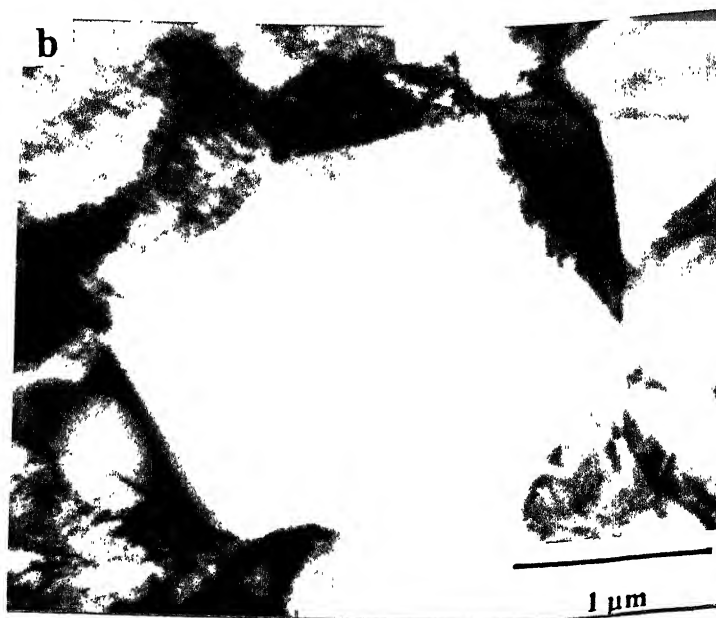
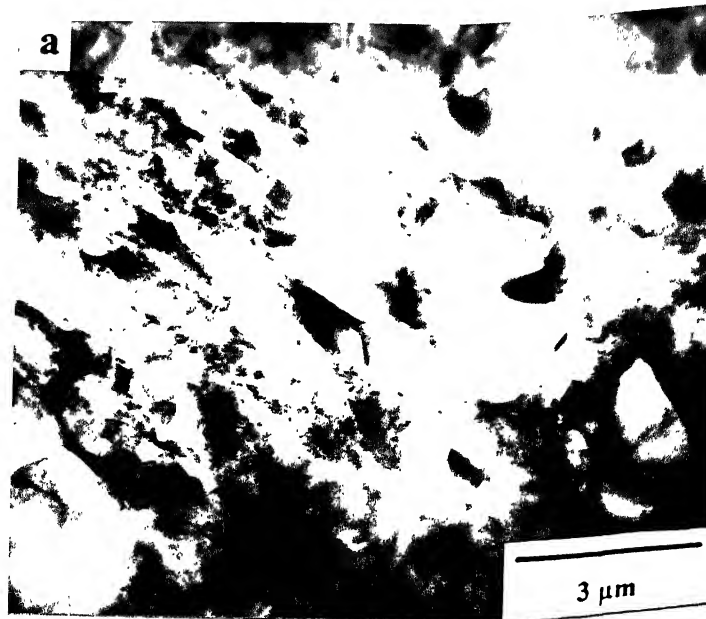


Fig. 5.14 SEM Micrograph of the material annealed at 1173 K for a period of (a) 15 min, (b) 30 min, (c) 2 hrs and (d) 12 hrs



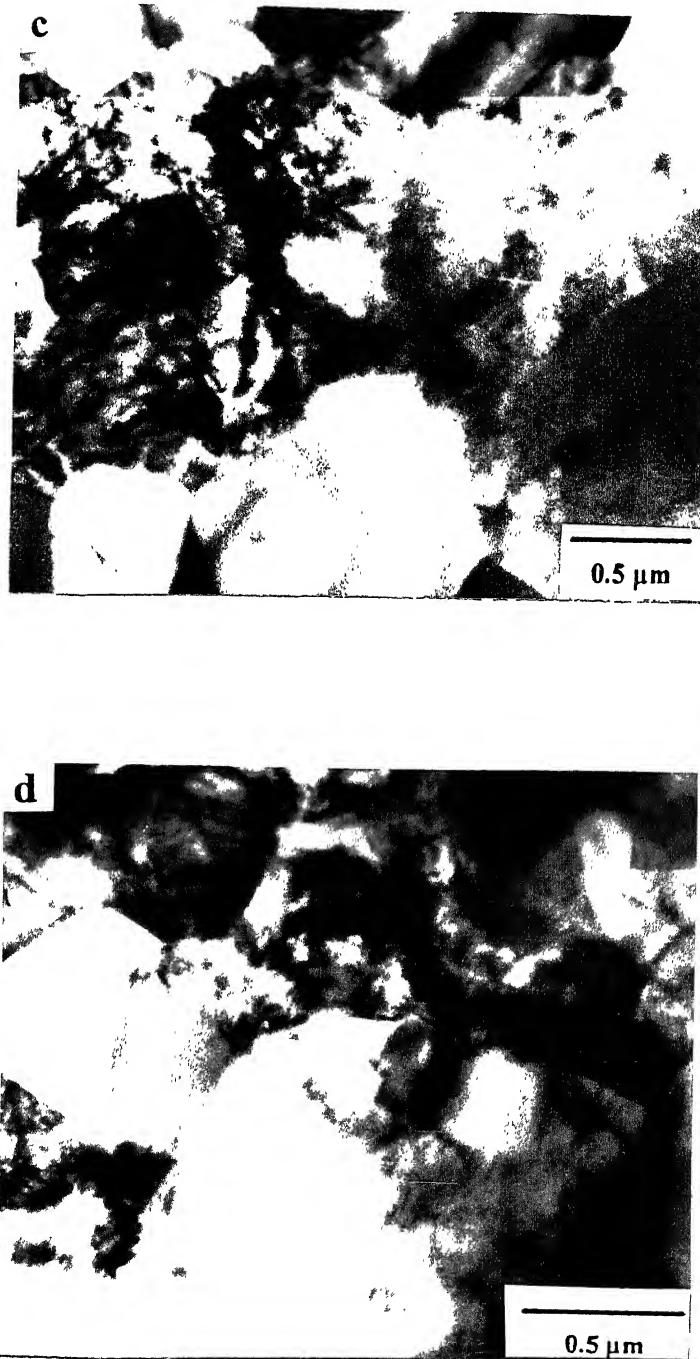
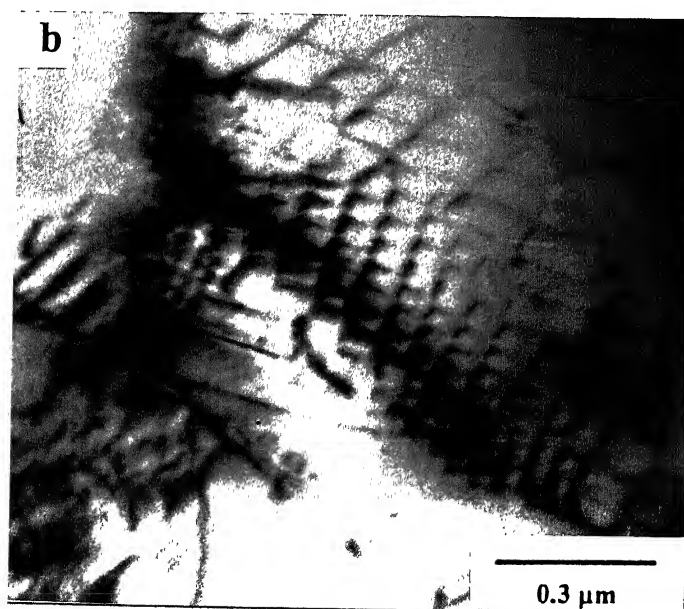
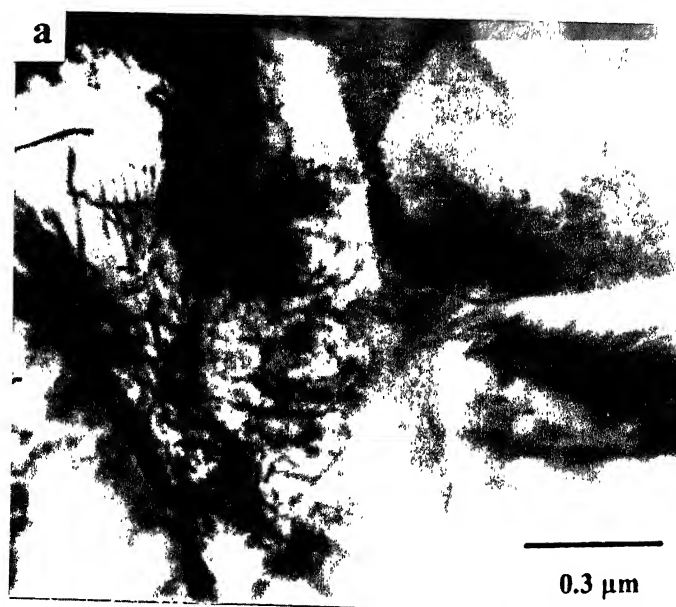


Fig. 5.15 (a,b)TEM Micrograph of the material annealed at 1173 K for a period 30 min showing an overall view of the microstructure (c,d) showing signs of recovery



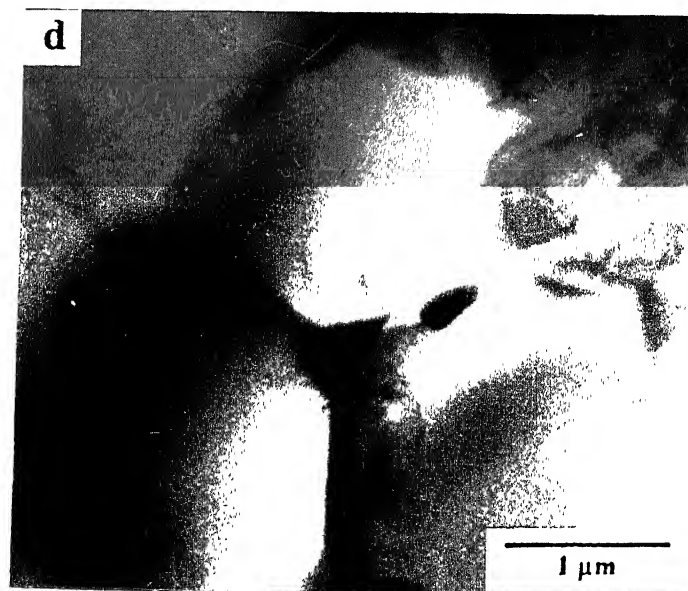
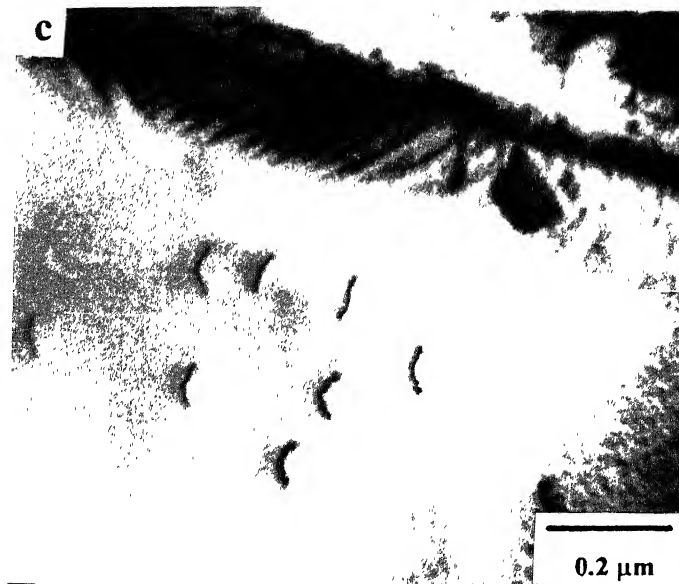


Fig. 5.16 TEM Micrographs of the specimens annealed at 1173 K for 2 hrs showing (a) partially recovered, (b) fully recovered, (c) partially recrystallised, (d) fully recrystallised and (e) a fish-tail type of structure at the grain boundary

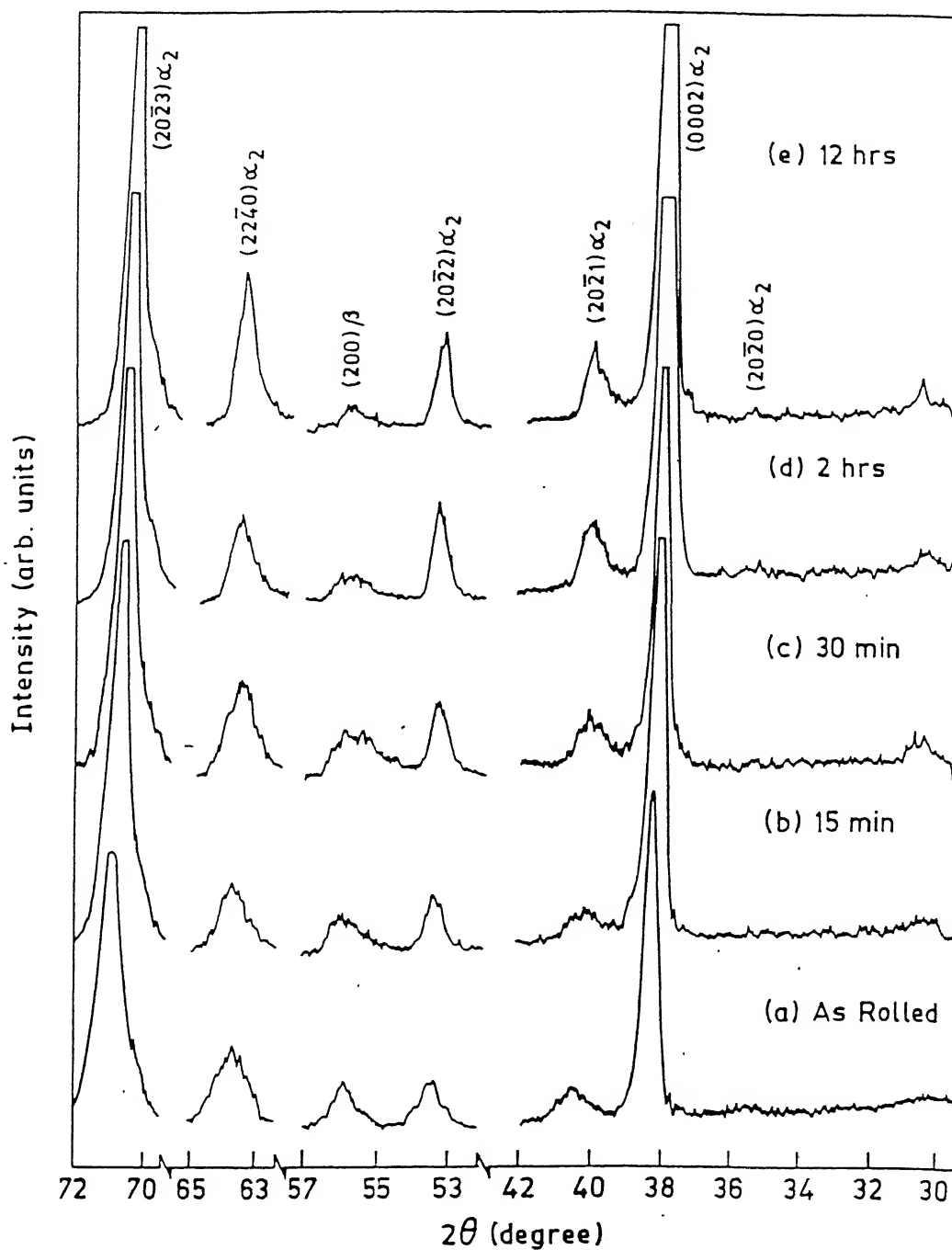


Fig. 5.17 X-ray diffraction profiles from the materials isothermally annealed at 1173 K

5.2.3 Textural Changes

The (0002) and (20 $\bar{2}$ 0) pole figures for the isothermally annealed specimens are shown in Figs. 5.18 and 5.19 respectively. As it can be seen from Fig. 5.18 (a), the specimen annealed for 15 min shows weakening of the basal texture as compared to the starting material (Fig. 4.45 c). There are some other weak orientations also in the pole figure. In addition, the basal texture shows a split TD tendency. For the specimen annealed for 30 min, the basal texture begins to get somewhat strengthened. However, the pole densities are seen to arrange all around the ND, thus causing a change in the splitting behaviour. The subsidiary orientations become somewhat weaker at this stage. Annealing treatment for 2 hrs brings about the tendency towards a split RD basal texture with pole density maxima remaining at the same intensity level as in the preceding sample. Annealing for a period of 12 hrs not only causes a weakening of the basal texture, but at the same time strengthens the non basal components.

The (20 $\bar{2}$ 0) pole figures also, as before, show the presence of a reasonably strong near basal fibre texture, the locations of the maxima along this fibre differ from sample to sample (Fig. 5.19). A remarkable weakening of the near basal texture, coupled with the strengthening of orientations other than the basal is also seen for longer periods of annealing (say, for 12 hrs).

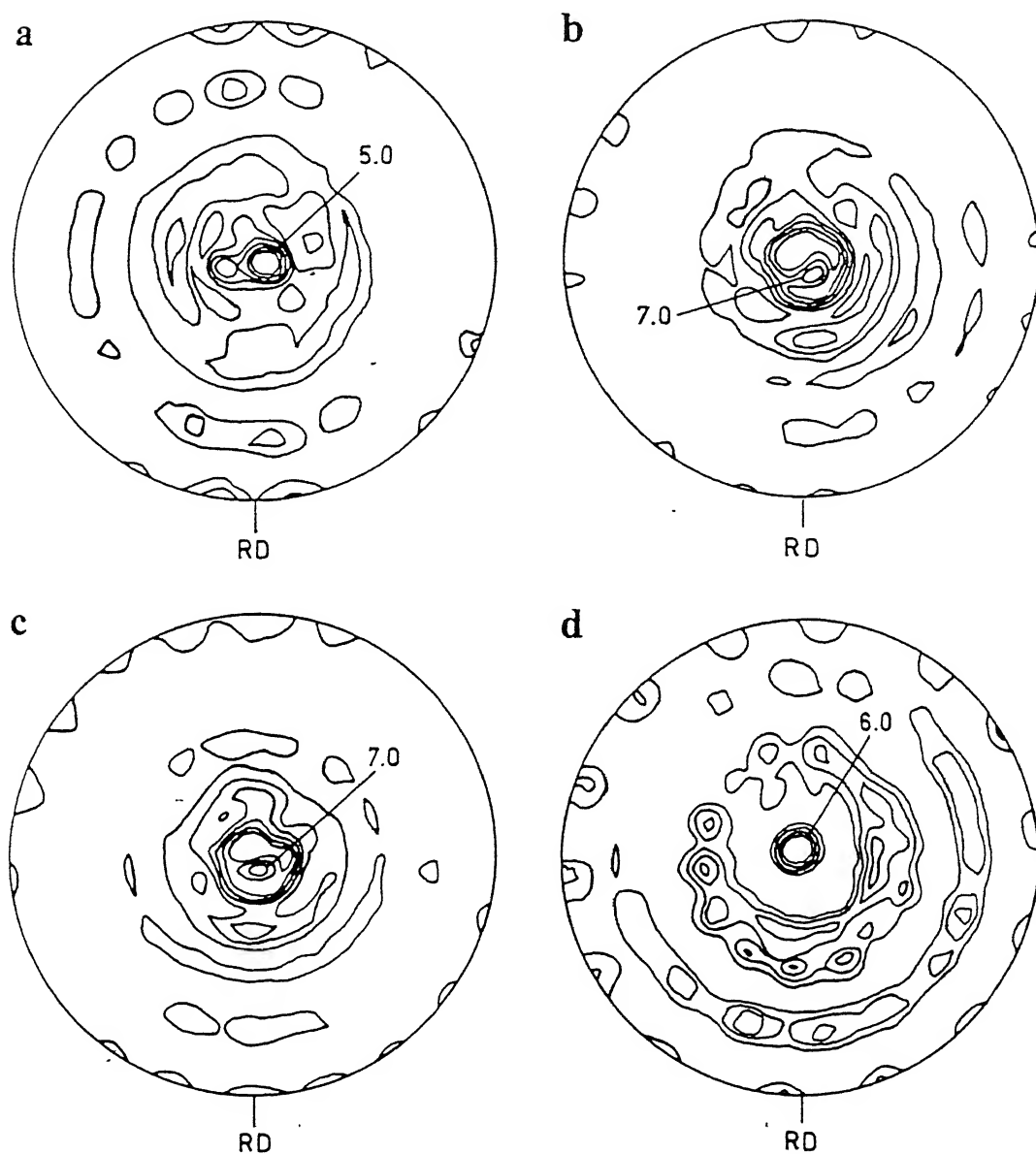


Fig. 5.18 $(0002)_{\alpha_2}$ pole figures for the isothermally annealed (1173 K) specimens for (a) 15 min, (b) 30 min, (c) 2 hrs and (d) 12 hrs

The orientation distribution function (ODF) plots for the materials annealed at 1173 K for 15 min, 30 min, 2 hrs and 12 hrs are shown in Figs. 5.20 to 5.23. For comparison purpose, the $\phi_2 = 0^\circ$ and 30° sections of the ODFs of the above samples are shown separately in Fig. 5.24. Fig. 5.24 (a), for the 15 min annealed material reveals the presence of a number of orientations including the basal, and the $[10\bar{1}0]\parallel RD$ and $[10\bar{1}0]\parallel TD$ non-uniform fibre spreads; the latter two are not found to be present in the ODF sections of the as-rolled starting material (Fig. 4.47 c). All these extra orientations other than the basal disappear in case of the material annealed for 30 min (Fig. 5.24 b). The ODF sections at this stage resemble those for the as-rolled material. The pole density maxima, for the 30 min annealed material, appear at $(0001)[2\bar{1}\bar{1}0]$, $(0001)[3\bar{4}10]$ and $(0\bar{1}16)[2\bar{1}\bar{1}0]$. The same trend continues for the 1 and 2 hrs annealed material with little shift in the positions of the maxima (Figs. 5.24 c and 5.24 d).

The ODF sections for the 12 hrs annealed sample show a drastic change in the texture developed. In addition to the near basal $\{0001\}\parallel ND$ texture, several fibres are also observed. These are (i) a fibre running from $(\bar{1}2\bar{1}3)[10\bar{1}0]$ to $(\bar{1}2\bar{1}3)[\bar{1}2\bar{1}2]$ in the $\phi_2 = 0^\circ$ section; (ii) a fibre running from $(\bar{1}2\bar{1}1)[10\bar{1}0]$ to $(\bar{1}2\bar{1}1)[\bar{1}2\bar{1}6]$ in the $\phi_2=0^\circ$ section; (iii) a fibre 6° away from $(02\bar{2}3)[2\bar{1}\bar{1}0]$ to $(02\bar{2}3)[0\bar{3}34]$ in the $\phi_2=30^\circ$ section; and (iv) a fibre running from $(02\bar{2}1)[2\bar{1}\bar{1}0]$ to $(02\bar{2}1)[0\bar{1}14]$ in the $\phi_2=30^\circ$ section. In addition, there is a reasonably strong peak component at $(01\bar{1}2)[2\bar{1}\bar{1}0]$.

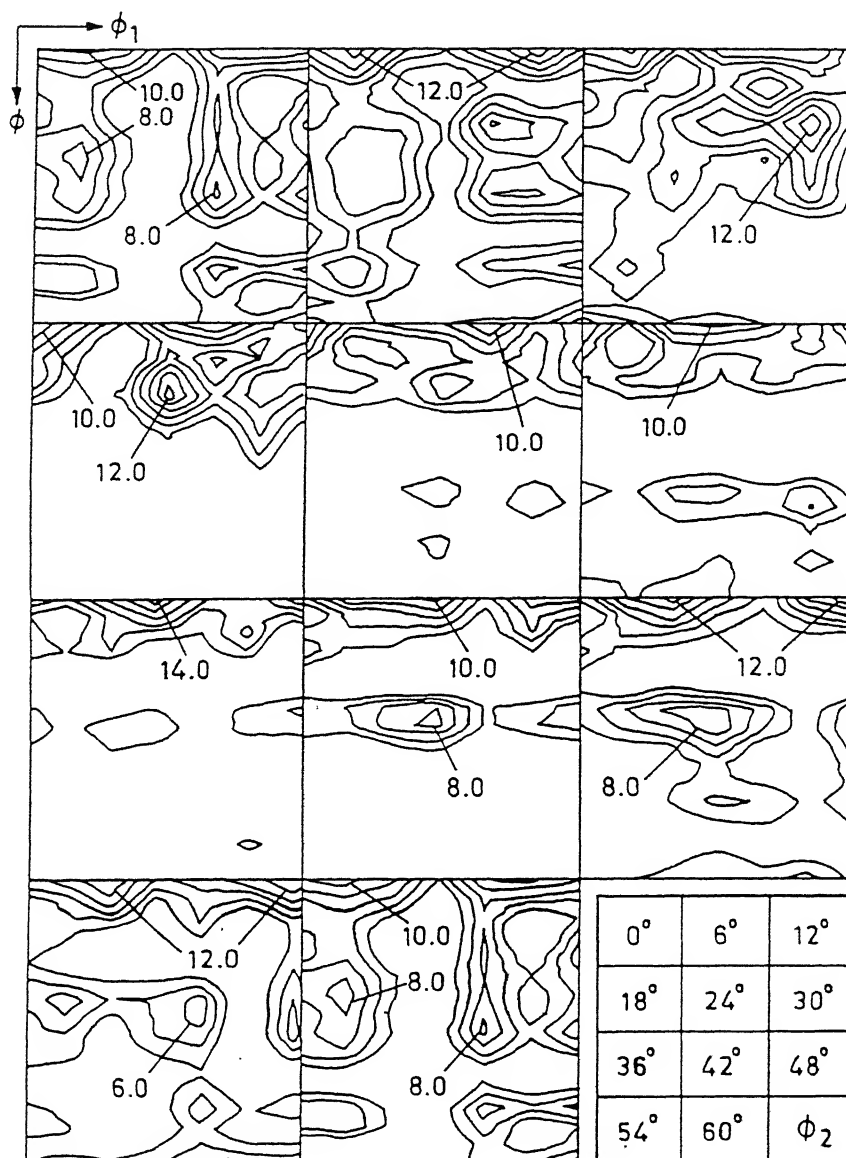


Fig. 5.20 Complete ODF of the material annealed 1173 K for 15 min

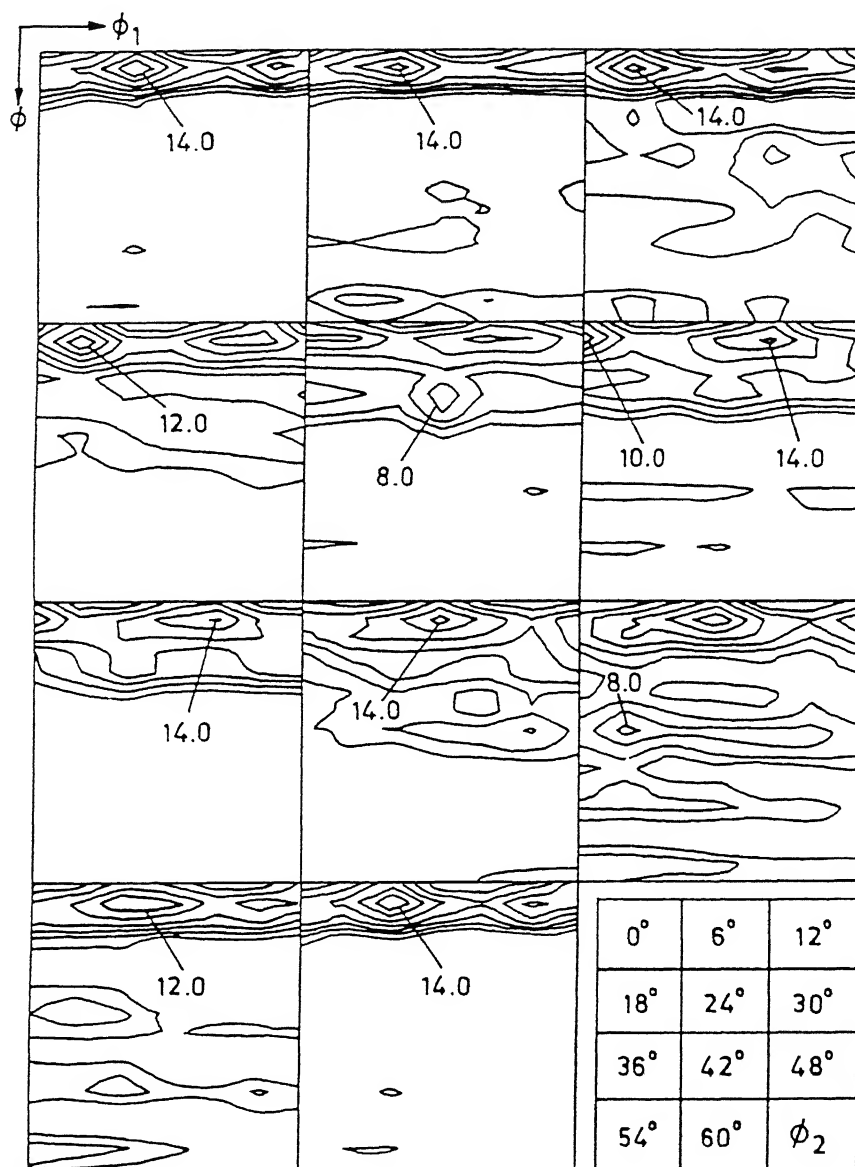


Fig. 5.21 Complete ODF of the material annealed 1173 K for 30 min

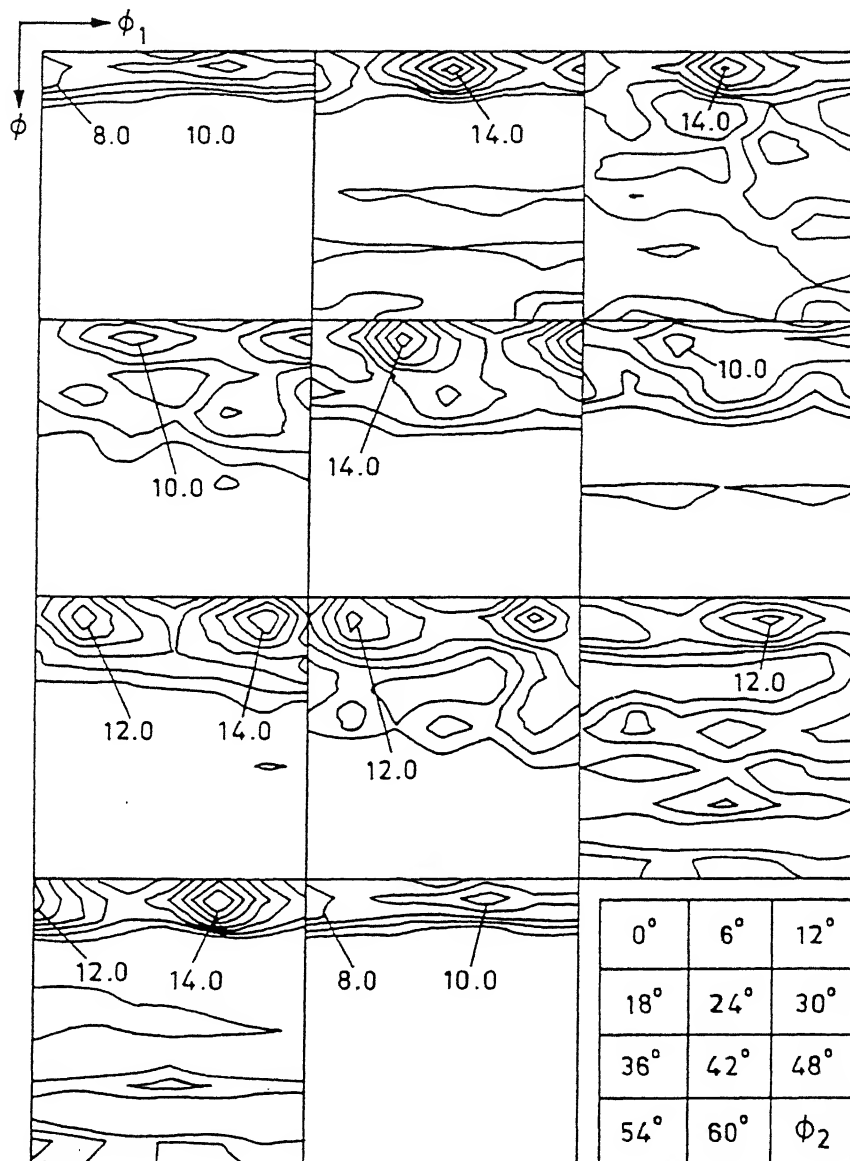


Fig. 5.22 Complete ODF of the material annealed 1173 K for 2 hrs

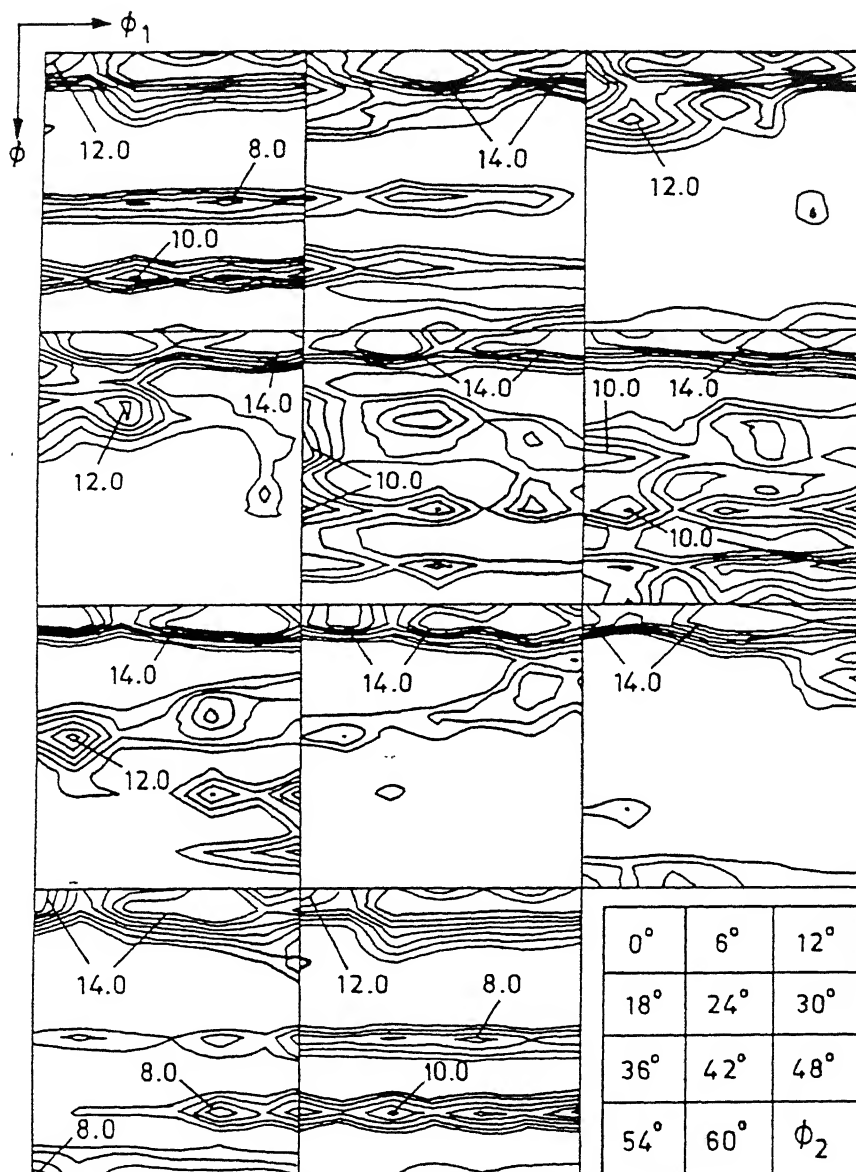


Fig. 5.23 Complete ODF of the material annealed 1173 K for 12 hrs

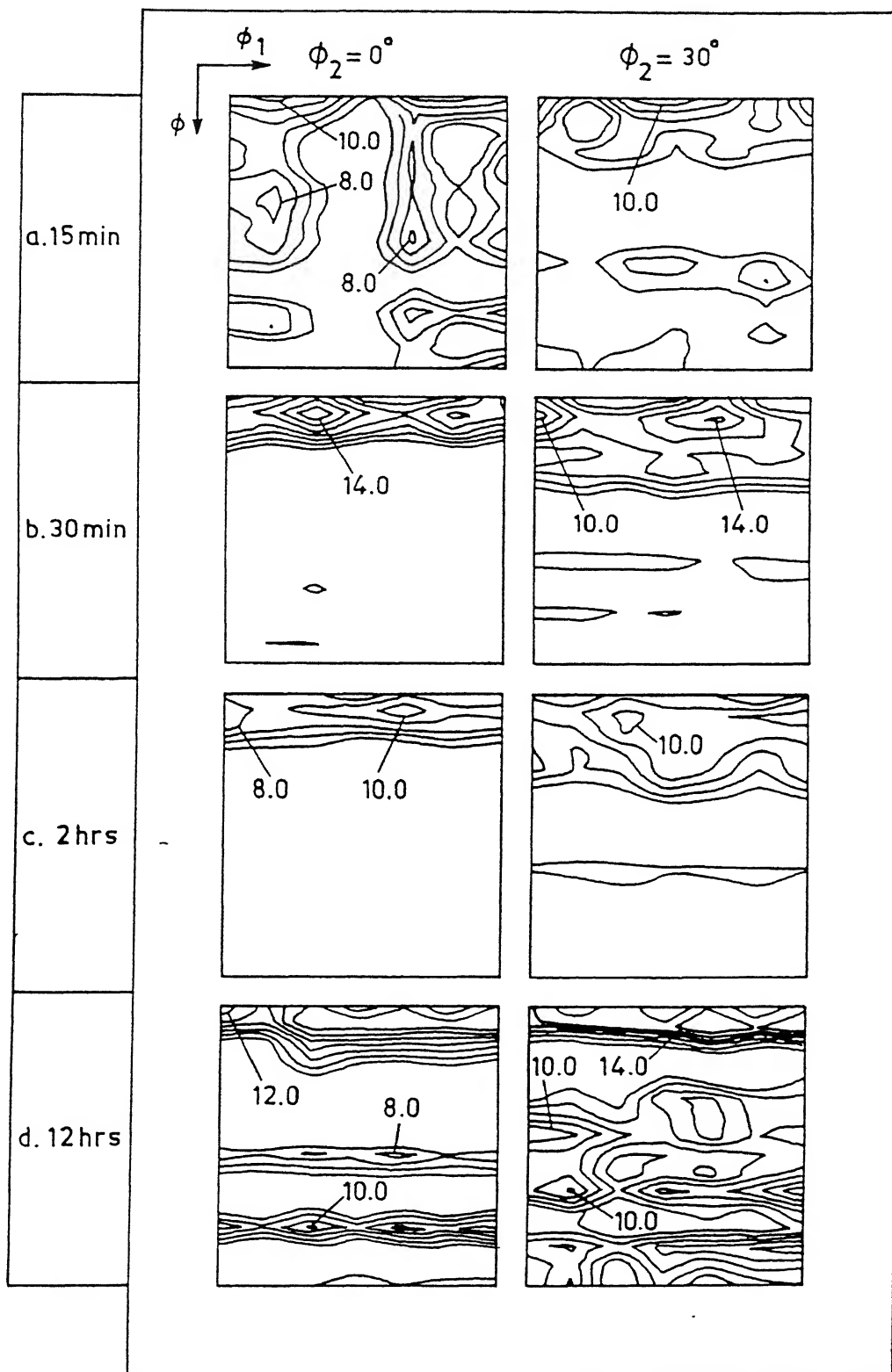


Fig. 5.24 $\phi_2=0^\circ$ and $\phi=30^\circ$ sections of the ODFs for the isothermally annealed (1173 K) specimens for (a) 15 min, (b) 30 min, (c) 2 hrs and (d) 12 hrs

5.3 Discussion of the Annealing Results

The work described in this chapter basically deals with the stability of the basal texture, formed during hot rolling, as a function of annealing. The physical processes which accompany annealing in this case are basically recovery, recrystallisation and limited grain growth of the α_2 phase. The temperature of annealing has been purposely kept low and quenching after heat treatment was practised so as to avoid the effect of phase transformation ($\alpha_2 \rightarrow \beta \rightarrow \alpha_2$) on the original basal texture.

The starting material, here, was the heat treated and then 80% rolled (at 1173 K) sample which was finally quenched in water. This led to the formation of a reasonably strong basal texture (Fig. 4.45 c). Detailed ODF indicated the presence of a near $[0001]\parallel ND$ fibre (Fig. 4.46 c).

Isochronal annealing of the material for 1 hr at 1123 K shows that the basal pole density decreases perceptibly (Fig. 5.7 a) as compared to the starting material. A look at the corresponding ODF (Fig. 5.13 a) shows that the near basal texture is perceptibly impaired and some new orientations, specially along the fibres $[0\bar{1}10]\parallel RD$ and $[0\bar{1}10]\parallel TD$ appear. Microstructural evidences indicate that lot of recovery of the original hot rolled structure goes on at this stage (Fig. 5.2). Thus any reorientation of the grains, which normally occur during recrystallisation (say), is not possible and therefore the textural change appears quite intriguing. Recent works [159, 160] on the effect of annealing on cold rolled ordered $Ni_3Al(B)$ and $Ni_3Al(B,Zr)$ has shown that these intermetallic materials undergo a change in order during cold rolling and the

state of order tries to revert back to the original state during annealing. As a result of this, the texture of the cold worked material decreases in intensity perceptibly during the recovery stage also when the changes in ordering are taking place, although no reorientation of grain due to recrystallisation etc. occurs. Since the α_2 phase in the present alloy is an ordered phase [4] and since hot rolling of the material at 1173 K can be considered as similar to cold rolling at least in this case, a situation similar to the cases of the Nickel aluminides can also be envisaged. The difficulty of monitoring the changes in the state of order in the α_2 phase lies in the fact that here the intensities of the superlattice lines are extremely low (Table 5.1)[161] and therefore very difficult to detect. Although no conscious effort was made during this investigation to study the changes in order during rolling and annealing of the experimental material, a comparison with the behaviour of similar intermetallic ordered phases may not be too far-fetched.

Table 5.1 Relative intensity values of all possible reflections for the Ti_3Al phase obtained from intensity calculation [161]

h	k	l	d	SL	theta	I/Imax(stoi)
2	0	0	2.488091		18.03699	24.64929
0	0	2	2.312		19.46395	26.30217
0	2	1	2.191039		20.58578	100
0	2	2	1.693665		27.05628	13.76157
2	2	0	1.4365		32.43188	15.50829
0	2	3	1.310286		36.01207	16.78311
0	4	0	1.244045		38.26226	2.335419
2	2	2	1.220161		39.15228	17.58967
0	4	1	1.201327		39.88751	12.58142
0	0	4	1.156		41.79192	2.498842
0	4	2	1.09552		44.68582	3.256072
0	2	4	1.048371		47.29409	2.959741
0	4	3	0.968064		52.73137	8.013978
2	4	0	0.94041		55.00544	2.653051
2	4	1	0.921545		56.71768	16.02244
2	2	4	0.900601		58.80591	10.90234
2	4	2	0.871106		62.17551	5.785402
0	2	5	0.866857		62.71242	8.785777
0	4	4	0.846833		65.46822	3.157322
0	6	0	0.829364		68.26289	6.971868
2	4	3	0.802786		73.66745	27.39454
0	6	2	0.780655		80.69805	31.81077
0	1	0	4.976182	SL	8.906095	2.403361
0	1	1	3.387331	SL	13.14598	5.333685
1	1	0	2.873	SL	15.55411	2.222396
0	1	2	2.096742	SL	21.55673	0.393903
1	2	0	1.88082	SL	24.17991	0.259239
1	1	2	1.801202	SL	25.32224	0.86852
1	2	1	1.742212	SL	26.24374	1.131288
0	3	0	1.658727	SL	27.6744	0.30543
0	1	3	1.472323	SL	31.55037	0.303806
1	2	2	1.459014	SL	31.87184	0.196163
1	3	0	1.380145	SL	33.93107	0.080549
0	3	2	1.347747	SL	34.86281	0.296096
1	3	1	1.322493	SL	35.62859	0.415285

1	2	3	1.192155	SL	40.25692	0.302084
1	3	2	1.185057	SL	40.54816	0.099265
2	3	0	1.141614	SL	42.44056	0.045629
0	1	4	1.126016	SL	43.17063	0.044356
2	3	1	1.108335	SL	44.03419	0.258155
1	4	0	1.085892	SL	45.19048	0.166079
1	1	4	1.072442	SL	45.91854	0.162885
1	3	3	1.02819	SL	48.527	0.232252
2	3	2	1.023626	SL	48.81688	0.07712
0	5	0	0.995236	SL	50.72146	0.018961
1	2	4	0.984851	SL	51.46617	0.07565
1	4	2	0.98288	SL	51.61062	0.302522
0	5	1	0.972955	SL	52.35442	0.11344
3	3	0	0.957667	SL	53.55667	0.075946
0	3	4	0.948402	SL	54.32154	0.152708
2	3	3	0.917385	SL	57.11557	0.237451
0	5	2	0.914138	SL	57.43164	0.039797
0	1	5	0.909232	SL	57.91898	0.120496
1	5	0	0.893749	SL	59.53919	0.041615
1	3	4	0.886204	SL	60.37904	0.085013
3	3	2	0.884768	SL	60.54305	0.170769
5	1	1	0.877508	SL	61.39363	0.262298
0	5	3	0.836089	SL	67.13469	0.16126
1	5	2	0.833629	SL	67.53898	0.109415
1	2	5	0.829903	SL	68.16968	0.33811
3	4	0	0.818079	SL	70.34002	0.06291
2	3	4	0.812282	SL	71.51871	0.134302
3	4	1	0.805569	SL	73.00501	0.440156
2	5	0	0.796827	SL	75.19977	0.33931
1	4	4	0.791466	SL	76.74778	0.761558
1	5	3	0.773169	SL	85.14036	1.588252
3	4	2	0.771223	SL	87.33689	0.968335

SL - superlattice reflection

With the advent of recrystallisation, the scenario starts changing. The materials which were isochronally annealed for 1 hr at 1173 K and at 1233 K again show mostly a basal texture of intensities comparable to that of the starting material (Figs. 5.7 and 5.8). The corresponding ODFs again indicate a near basal type of texture with components a few degrees off from the perfect $[0001]\parallel ND$. The SEM microstructures at these stages (Fig. 5.1 b and c) show a clear departure from what is seen in the microstructure of the 1123 K annealed material (Fig. 5.1 a). Whereas the latter shows clear indications of a rolled (deformed) structure, in the former the tendency to form a more equiaxed structure is clearly discernible. TEM microstructures also indicate that after isochronal annealing at 1173 K and 1233 K, the materials show distinct sign of recrystallisation of the α_2 phase. Thus, the textures of the materials at this stage can be considered as due mainly to recrystallisation and possibly some concurrent reordering process. It is commonly believed [158] that the rolling texture of h.c.p metals is retained upon recrystallisation. This very much appears to be the case in the present investigation. Isochronal annealing for 1 hr at 1293 K imparts a texture to the material which is distinctly different from the textures of materials annealed at 1173 K and 1233 K. The basal texture, here, is not perfect in the sense that the maxima in the pole density distribution are not uniformly arranged around ND; rather there is a split along the RD-TD direction (Fig. 5.7 d). The corresponding ODF shows a series of near basal components of somewhat lower intensity along with a couple of orientations near the $(\bar{2}110)[0\bar{1}10]$ location. Annealing at 1293 K gives rise to nearly equal volume fractions of the α_2 and β phases

(Fig. 5.1 d) - both the phases showing an equiaxed grain structure. Since the material was quenched from the heat treatment temperature, there was no scope of the formation of any secondary α_2 in this case. Thus the formation of texture components nearer $(\bar{2}110)[0\bar{1}10]$ in the α_2 must be due to the recrystallisation (and grain growth) in the α_2 phase. A look at the $\phi_2 = 0^\circ$ section of the ODF for the starting as-rolled material (Fig. 4.46 c) shows some intensity in a location not far from $(\bar{2}110)[0\bar{1}10]$. It is quite likely, therefore, that this component, which is pretty weak to start with, becomes significantly stronger, not so much during recrystallisation but especially during the grain growth stage of the α_2 phase.

The texture results of the 1173 K isothermally annealed materials seem to reinforce the above ideas. Thus, both the pole figures and ODFs of the sample annealed for 15 min at 1173 K (Figs. 5.18 a and 5.24 a) appear very similar to those of the sample annealed for 1 hr at 1133 K (Figs. 5.7 a and 5.13 a). Both the materials are in an advanced stage of recovery, as revealed from the relevant TEM micrographs also. Thus the texture of the sample annealed for 15 min at 1173 K is nothing but the texture in the recovery stage which, in all probability, is accompanied by a reordering process. The textures of materials annealed for 30 min and for 2 hrs at the same temperature (Figs. 5.18 or 5.24 b and c) appear rather similar to that of the starting as rolled material (Fig. 4.46 c). Since TEM microstructures indicate substantial amounts of recrystallisation at these stages, the corresponding textures can be assumed to be nothing but recrystallisation textures of the material. As mentioned earlier, the rolling textures seem to be retained in this material after recrystallisation. The relative

locations of the maxima along and close to the $[0001]\parallel ND$ direction are however found to be different between the texture patterns of the recrystallised samples on the one hand and that of the texture of the starting as rolled material on the other. It has been suggested [158] that in h.c.p. metals the recrystallisation textures seem to be usually related to the deformation textures by a rotation about the hexagonal axis, with the result that the disposition of basal plane poles will be remaining approximately unaltered, although there could be some minor displacements.

The sample which was annealed at 1173 K for a total period of 12 hrs shows a host of other orientations over and above the near basal (Fig. 5.24 d). As shown from the SEM microstructure (Fig. 5.14 d), the material is not only fully recrystallised at this stage, it shows evidence of grain growth also taking place. Thus the texture at this stage is a typical grain growth texture of the experimental alloy. The main texture components at this stage, other than the basal component, are the four fibres as mentioned in Section 5.2.3. Some of the end components of these fibres such as $(\bar{1}2\bar{1}3)[10\bar{1}0]$ and $(\bar{1}2\bar{1}1)[10\bar{1}0]$ are not very far from the $(\bar{1}2\bar{1}4)[10\bar{1}0]$ and $(\bar{1}2\bar{1}0)[10\bar{1}0]$ respectively, which have been reported to be present in the α recrystallisation texture of hot rolled C.P. Ti [117].

The $(\bar{1}2\bar{1}0)[10\bar{1}0]$ has also been found to be an important component in the deformation, recrystallisation and $\beta \rightarrow \alpha_2$ transformation texture of Ti-6Al-4V [133]. In a similar way, the component $(02\bar{2}3)[2\bar{1}\bar{1}0]$ found in the texture of the present alloy is not very far away from the $(02\bar{2}5)[2\bar{1}\bar{1}0]$ component of the α

recrystallisation texture of C.P.Ti [117]. The only difference between the present alloy on the one hand and the C.P. Ti and Ti-6Al-4V alloy on the other, appears to be that while in the former these components are observed only during the grain growth stage after recrystallisation, in the latter they essentially form as part of the recrystallisation texture, which practically does not show any basal component.

When the experimental material is annealed at 1293 K for 1 hr (i.e. within the $\alpha_2 + \beta$ phase field), it is expected that rapid grain growth of the α_2 after recrystallisation will occur simultaneously with the $\alpha_2 \rightarrow \beta$ transformation. The β grains will therefore eat into the α_2 and as a result some of the α_2 orientations can become extinct. It appears that the advancing β grains will first consume the α_2 grains having orientations other than the basal and then attack the ones with the basal texture. This is possibly why the texture of the 1293 K / 1 hr annealed material (Figs. 5.7 d and 5.13 d) does not show the fibres (other than the basal) present in the 1173 K / 12 hr annealed material. Even the basal component of the texture also appears a little bit less intense possibly due to the invasion of the β grains into the basal oriented α_2 .

It thus appears that the basal hot rolling texture remains rather stable during recrystallisation annealing at temperatures within the single phase α_2 phase. The growth of the grains, after recrystallisation is complete, produces orientations other than the basal. It also appears that annealing at temperatures in the $(\alpha_2 + \beta)$ phase field has the effect of decreasing the intensity of the basal texture to some extent. The

effect of $\alpha_2 \rightarrow \beta \rightarrow \alpha_2$ double transformation on the stability of the basal texture will be discussed in the next chapter.

Effect of $\alpha_2 \rightarrow \beta \rightarrow \alpha_2$ Transformation on the Stability of Basal Texture

In the preceding chapter, the effects of isochronal and isothermal annealing on the texture of the α_2 phase have been studied. The heat treatment schedule was designed to examine primarily the response of basal texture to annealing. The temperatures were chosen in such a manner that the α_2 phase does not undergo any structural transformation and therefore the textural changes associated with these heat treatments should purely be due to the thermal response of the substructure. In contrast, in the present chapter the effect of heat treatment involving $\alpha_2 \rightarrow \alpha_2 + \beta / \beta \rightarrow \alpha_2$ transformation on the basal texture has been studied. In order to make the study more general, the heat treatment was not restricted to materials with strong basal texture only; even those materials with a weak basal texture or a non-basal texture have also been subjected to heat treatment involving the $\alpha_2 \rightarrow \alpha_2 + \beta / \beta \rightarrow \alpha_2$ transformation.

The starting material was the as-cast alloy rolled to 80% reduction at 1173 K, 1293 K and 1373 K followed by furnace cooling after the finish rolling pass. Hence forward these samples will be referred to as R 1173, R 1293 and R 1373 respectively. Each of these materials was heat treated at 1173 K, 1293 K, and 1373 K and again furnace cooled to room temperature. The approximate volume fraction of α_2 at these three temperatures are ~85%, ~50% and negligible respectively. For convenience,

these heat-treated materials will be referred to by the following symbols listed in Table 6.1.

Table 6.1 Symbols being used in the present chapter for denoting different heat treated materials

Symbol	Rolling Temperature	Heat Treatment Temperature	Duration of Heat Treatment
R1173H1173	1173 K (FC)	1173 K (FC)	24 hrs.
R 1173H1293	1173 K (FC)	1293 K (FC)	8 hrs.
R 1173H1373	1173 K (FC)	1373 K (FC)	4 hrs.
R 1293H1173	1293 K (FC)	1173 K (FC)	24 hrs
R 1293H 1293	1293 K (FC)	1293 K (FC)	8 hrs.
R 1293H1373	1293 K (FC)	1373 K (FC)	4 hrs.
R 1373H1173	1373 K (FC)	1173 K (FC)	24 hrs.
R 1373H1293	1373 K (FC)	1293 K (FC)	8 hrs.
R 1373H1373	1373 K (FC)	1373 K (FC)	4 hrs.

The choice of the duration of heat treatment at a particular temperature was mainly based on the time response of the phase transformation at the three temperatures used [11].

6.1 Microstructure

6.1.1 Heat Treatment of 1173 K rolled and furnace cooled material

The SEM micrographs of the three heat treated materials along with the micrograph of the starting material are shown in Fig. 6.1 (a to d). The microstructure of the material heat treated at 1173 K for 24 hrs shows equiaxed primary α_2 grains with the β phase only at the triple junctions. The average size of the α_2 grains was estimated to be nearly 5 μm .

Heat treatment of the starting material at 1293 K for 8 hrs followed by furnace cooling results in a microstructure containing primary α_2 , substantial amount of secondary α_2 and β (B2). In this case, β forms as a continuous film around the equiaxed α_2 grains. The α_2 grains appear perceptibly larger than in the previous case. The secondary α_2 does not seem to form as separate entities, rather they are likely to grow on to the pre-formed primary α_2 grains.

When the starting material is heat treated at 1373 K for 4 hrs and then furnace cooled, the resulting microstructure shows a Widmanstatten pattern with varying sizes of α_2 platelets (Fig. 6.1 d). The α_2 here is obtained solely by transformation from the high temperature β phase and hence it will be called secondary α_2 . Some retained β is also seen at the α_2 plate boundaries.

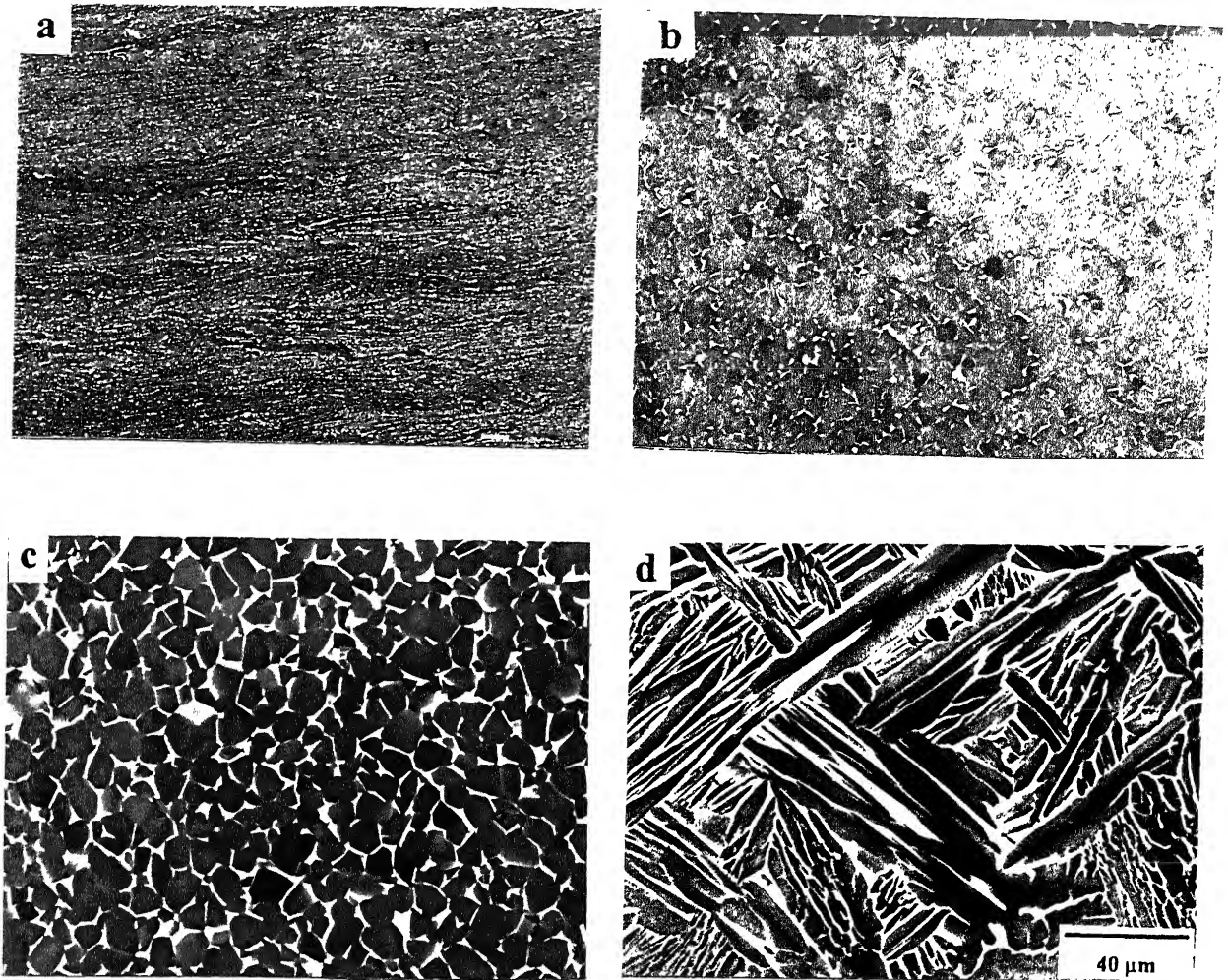


Fig. 6.1 SEM Micrographs of the 1173 K rolled (furnace cooled) material in the (a) as rolled condition, (b) heat treated at 1173 K, (c) heat treated at 1293 K and (d) heat treated at 1373 K (all furnace cooled).

Transmission electron microscopy (TEM) of a limited number of samples was carried out to have a better understanding of the microstructural changes. The TEM micrograph of the R 1173H1173 sample (Fig. 6.2) shows equiaxed primary α_2 grain with a discontinuous film of β at the grain boundaries. The low magnification TEM micrograph of R1173H1373, as given in Fig. 6.3 (a), shows a clear Widmanstatten microstructure. However, a high magnification micrograph from the same sample shows a few defects like dislocation etc. inside the α_2 grains (Fig. 6.3 b). Another high magnification micrograph (Fig. 6.3 c) shows that the film of retained β at the α_2 grain boundaries are rather thick and the difference in contrast across the boundaries suggests the likely presence of a different phase other than the β . Very often high dislocation activity can be seen on the two sides of the boundary (of β) between two transformed secondary α_2 grains (Fig. 6.3d).

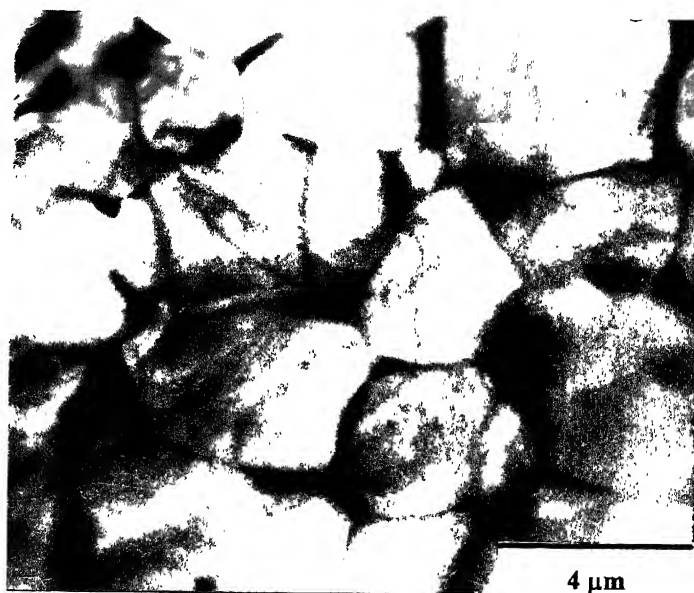
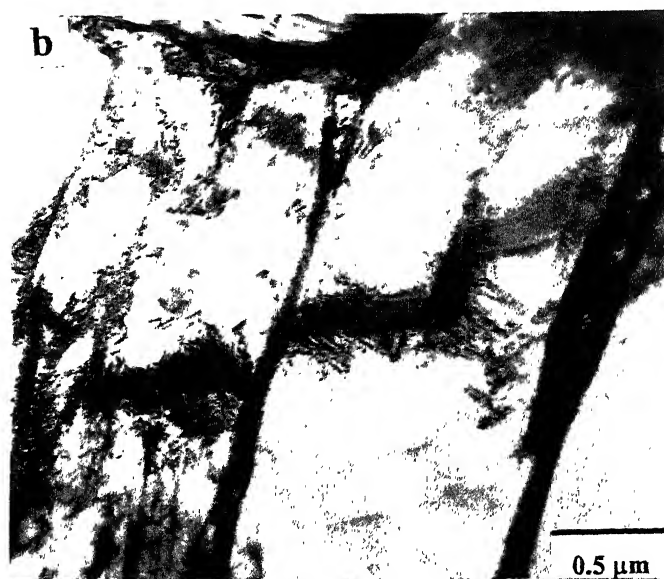


Fig. 6.2 TEM Micrograph of R1173H1173 specimen



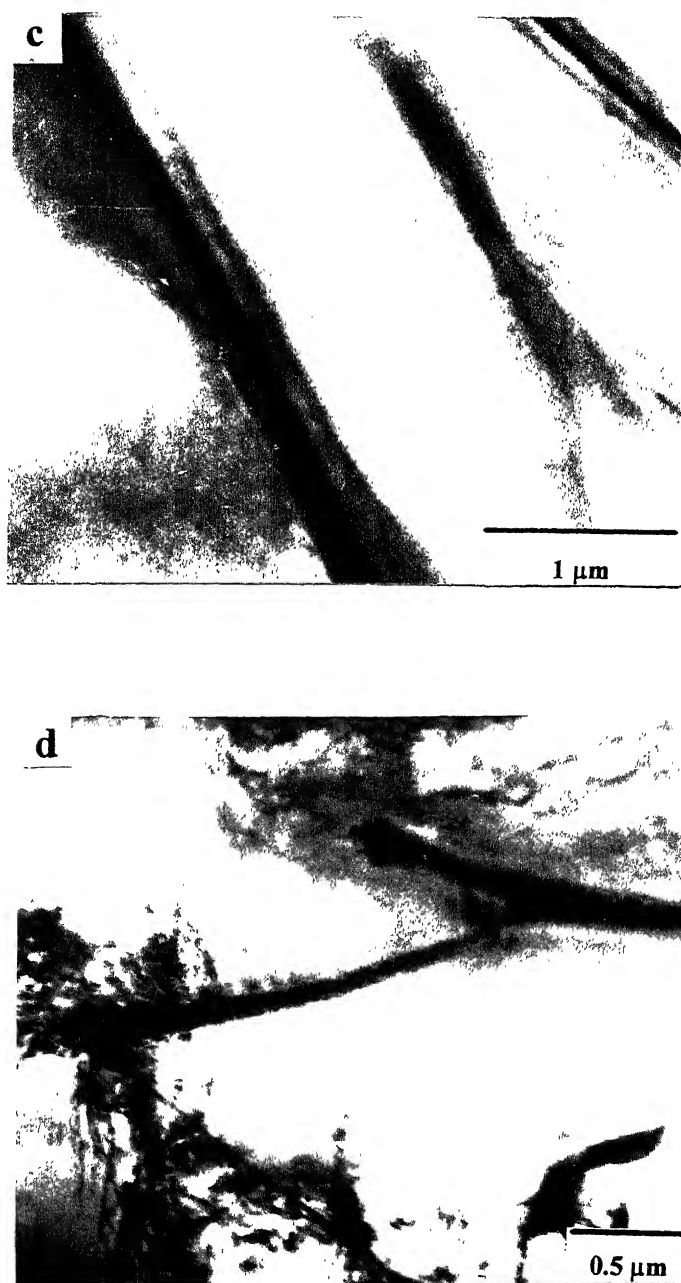


Fig. 6.3 TEM Micrographs of R1173H1373 specimen showing (a) general features, (b) presence of defect - like features inside α_2 grains (c) a film of retained β at the α_2 boundaries, and (d) high dislocation activity at the two sides of the boundary

6.1.2 Heat Treatment of 1293 K Rolled and Furnace Cooled Material

SEM microstructures of this material after heat treatment are shown in Fig. 6.4 (a to d). It can be seen from Fig. 6.4(b) that annealing at 1173 K for 24 hrs and furnace cooling leads to a clear tendency for the α_2 to become equiaxed. The β phase is found to be present at the grain boundaries.

Heat treatment at 1293 K for 8 hrs produces a similar tendency (Fig. 6.4 c). The α_2 grains become somewhat larger in size and the β forms a nearly continuous film around the α_2 grains. On the other hand, heat treatment at 1373 K for 4 hrs leads to a microstructure made up almost completely of secondary α_2 obtained by transformation of the rolled β during furnace cooling (Fig. 6.4 d). A thin continuous retained β film is formed around α_2 grain.

6.1.3 Heat Treatment of 1373 K rolled and Furnace Cooled Material

The microstructures of the starting as well as the heat treated materials are shown in Figs. 6.5 (a to d). It can be broadly concluded from Figs. 6.5 (a) and (b) that the microstructure of the material after heat treatment at 1173 K is similar to that of the starting material, both containing α_2 with Widmanstatten and equiaxed morphology. However, the relative amount of Widmanstatten α_2 in the heat treated material appears

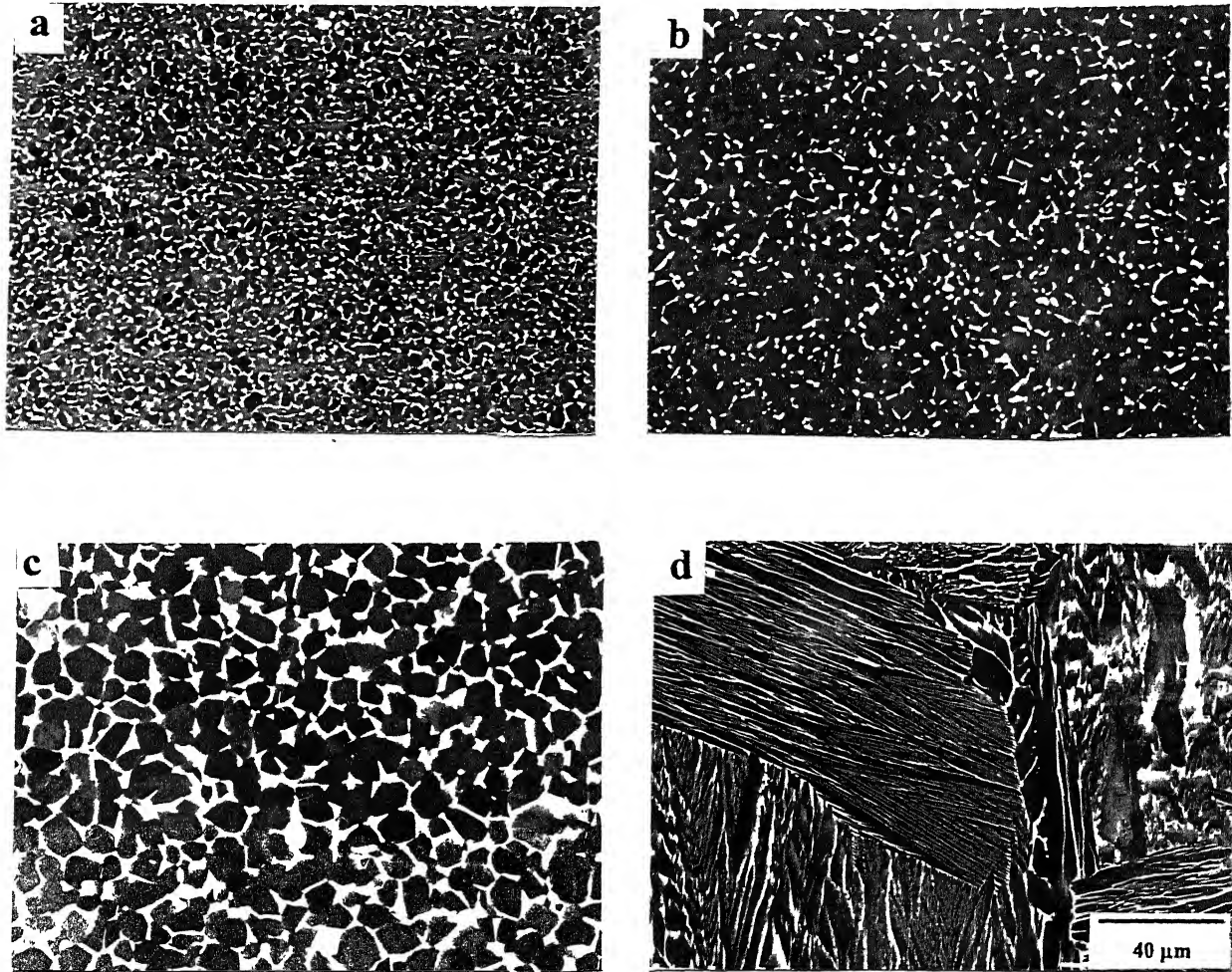


Fig. 6.4 SEM Micrographs of the 1293 K rolled (furnace cooled) material in the (a) as rolled condition, (b) heat treated at 1173 K, (c) heat treated at 1293 K and (d) heat treated at 1373 K (all furnace cooled)

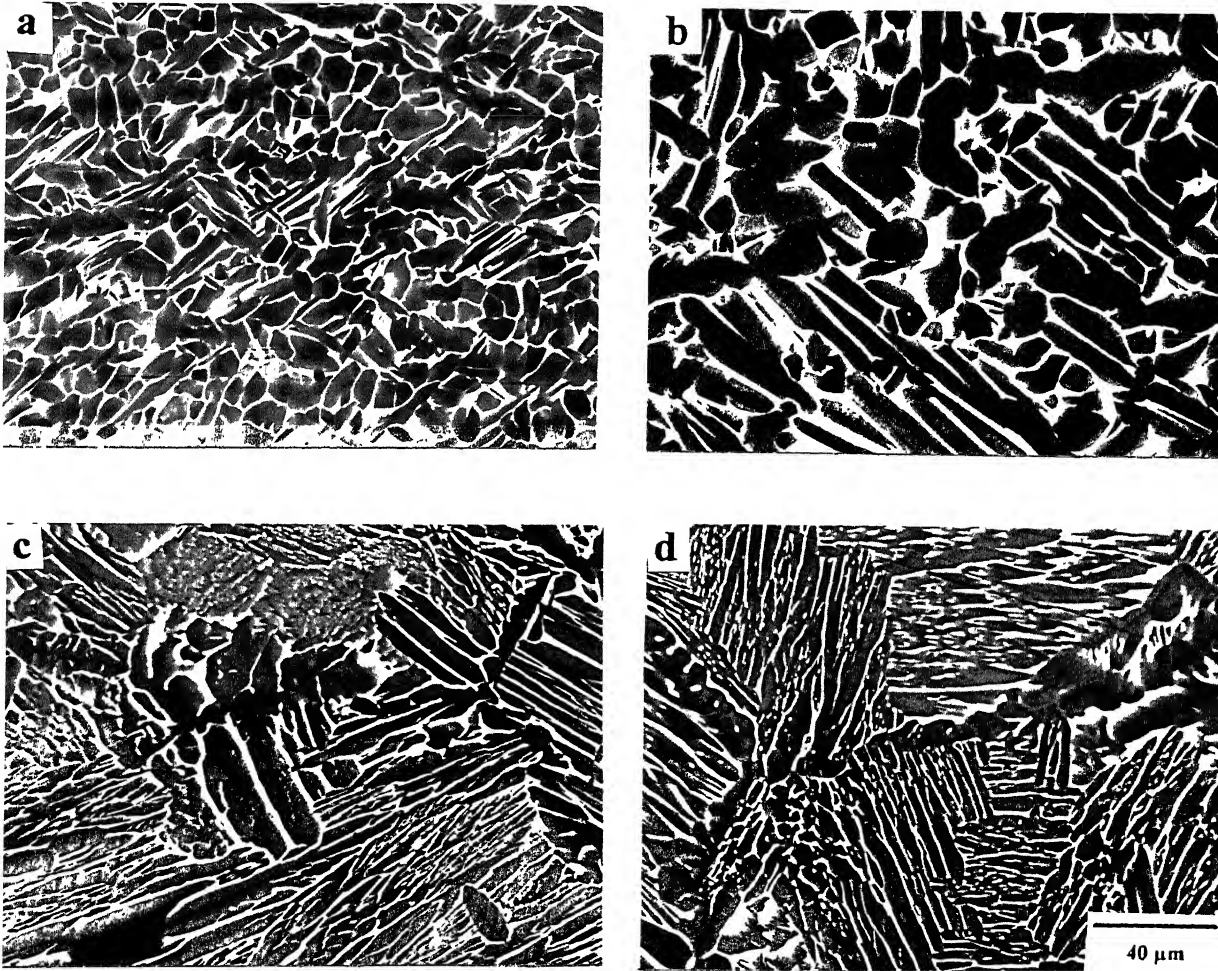


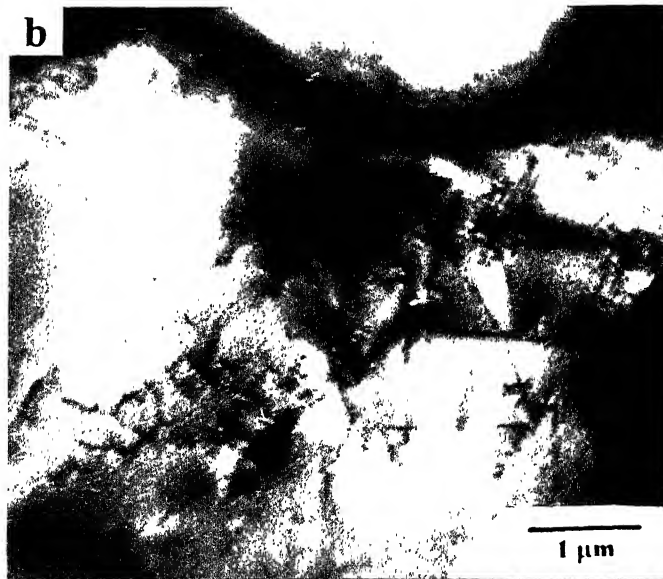
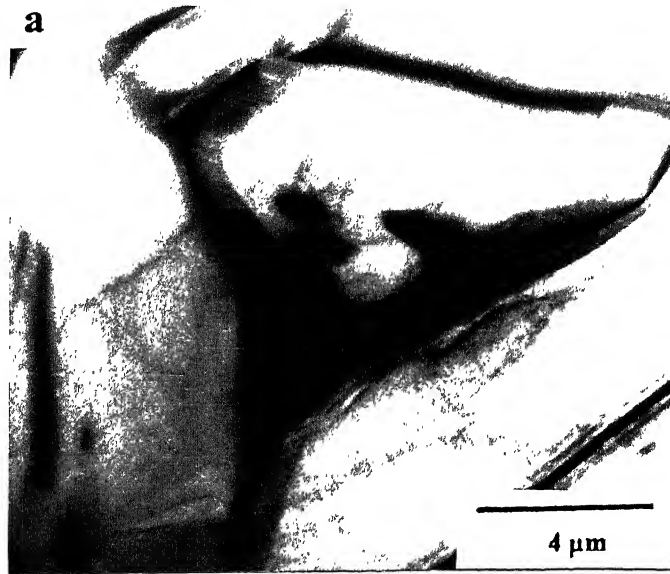
Fig. 6.5 SEM Micrographs of the 1373 K rolled (furnace cooled) material in the (a) as rolled condition, (b) heat treated at 1173 K, (c) heat treated at 1293 K and (d) heat treated at 1373 K (all furnace cooled)

substantially higher than that of equiaxed α_2 . The equilibrium amount of β is likely to be more here, as compared to the starting material and this is going to transform to secondary α_2 during subsequent furnace cooling. Retained β film around α_2 grains can also be seen in the microstructure.

In the case of 1293 K heat treated material, the secondary α_2 is found to be present in the Widmanstätten form (Fig. 6.5 c). During the course of this heat treatment, some primary α_2 is likely to transform into β and this gets re-transformed during cooling into secondary α_2 . Some equiaxed α_2 grains and some retained β phase at the grain boundaries of α_2 platelets are also seen in the microstructure.

Finally, in the 1373 K heat treated condition, almost fully Widmanstätten secondary α_2 is observed in the microstructure (Fig. 6.5 d). Presumably, primary α_2 gets transformed into β almost fully during heat treatment and this then re-transforms into secondary α_2 during furnace cooling. In this case also, some retained β can be seen at the boundaries of α_2 platelets.

Limited TEM study was carried out on thin foils made from the R1373H1173 and R1373H1373 samples in order to characterise the microstructure of the secondary α_2 in some detail. The microstructural characteristics of the annealed secondary α_2 can be seen in the TEM micrograph of the R 1373H1173 specimen (Figs. 6.6). A low magnification micrograph (Fig. 6.6 a) shows the general features of the substructural details such as the secondary α_2 platelets along with the β regions at the plate boundaries. Figs. 6.6 (b and c) represent the substructural features of the



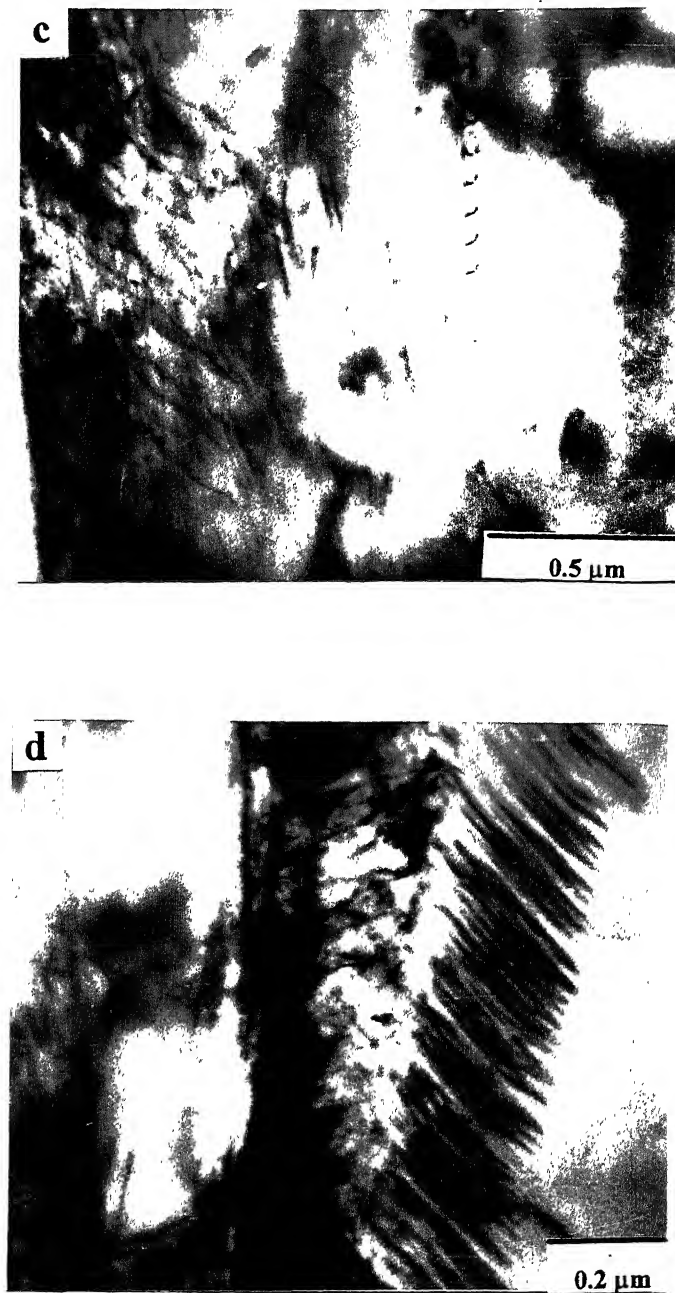
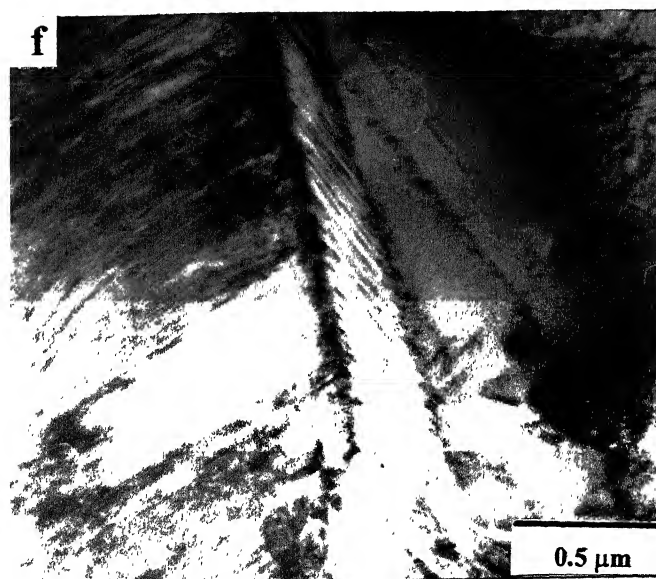
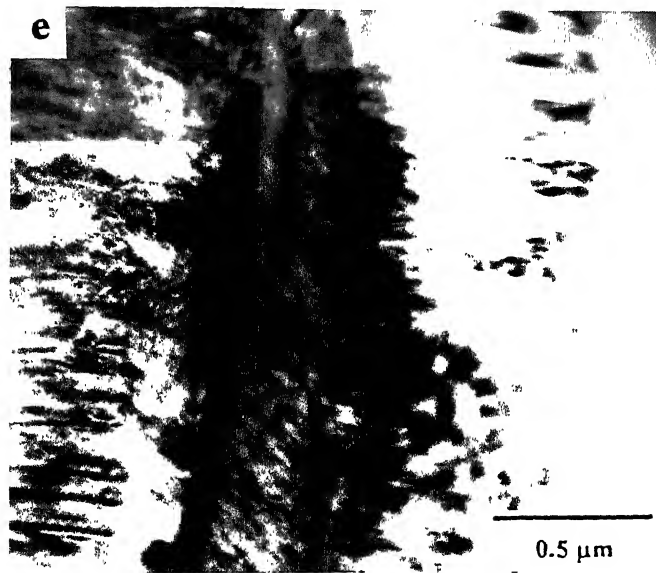


Fig. 6.6 TEM Micrograph of R1373H1173 specimen showing (a) general features, (b) dislocations and other defects present inside α_2 grain, (c) a clean α_2 grain surrounded by dislocations and other defects (d) the details of grain boundary feature of the micrograph (a)



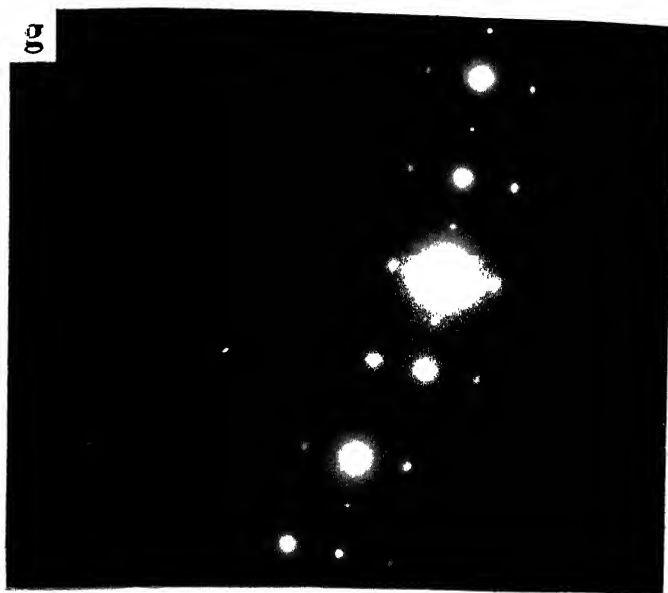


Fig. 6.6 (e) TEM Micrographs of the R1373H1173 specimen showing higher magnification views of the grain boundary region (f) the grain boundary region and (g) SAD pattern taken from the area 'X' shown in (e)

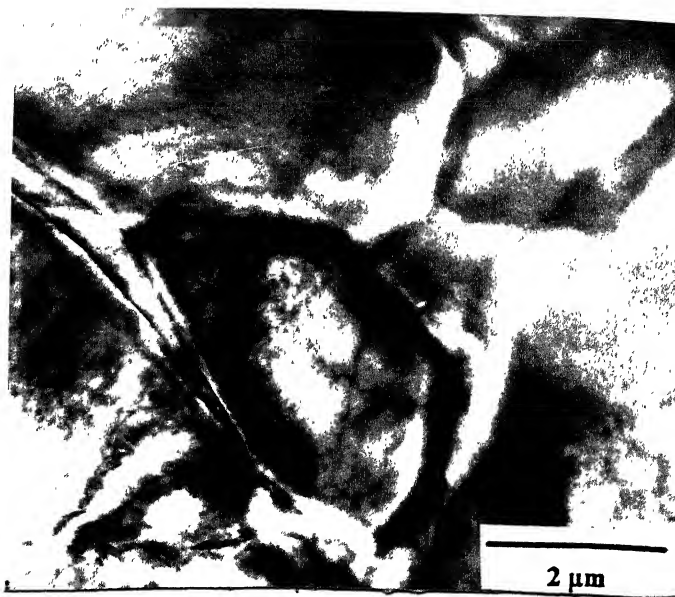


Fig. 6.7 TEM Micrographs of the R1373H1373 specimen showing general features

6.2 X-ray Line Profiles

The XRD profiles for the R1173 series of materials are shown in Fig. 6.8 along with the XRD profile of the starting material. The most significant results which can be obtained from these traces are that the main peak in all the heat treated materials is the basal, as in the starting material. There is significant weakening of the basal peak as the temperature of annealing increases.

The XRD profiles of the R1293 series of samples after heat treatment are presented in Fig. 6.9 along with the XRD profile of the starting material. The basal peak is once again the major peak in these patterns. However, significant weakening of this peak takes place as the heat treatment temperature increases. The integrated intensity ratio for $(20\bar{2}1)/(0002)$ shows a clear decrement with increase in the annealing temperature.

The XRD profiles of the 1373 series of sample after heat treatment are presented in Fig. 6.10 along with the pattern for the starting material. In all these patterns, the strongest peak is of $(20\bar{2}1)$. Incidentally, this is also the strongest line in the diffraction pattern of a random (powder) Ti_3Al sample as per the JC-PDS data file. The basal peak is weak in all the patterns and a general weakening of this peak takes place with increase in the temperature of heat treatment. The all along high intensity of the $(20\bar{2}1)$ peak in these patterns is indicative of the tendency towards texture randomisation.

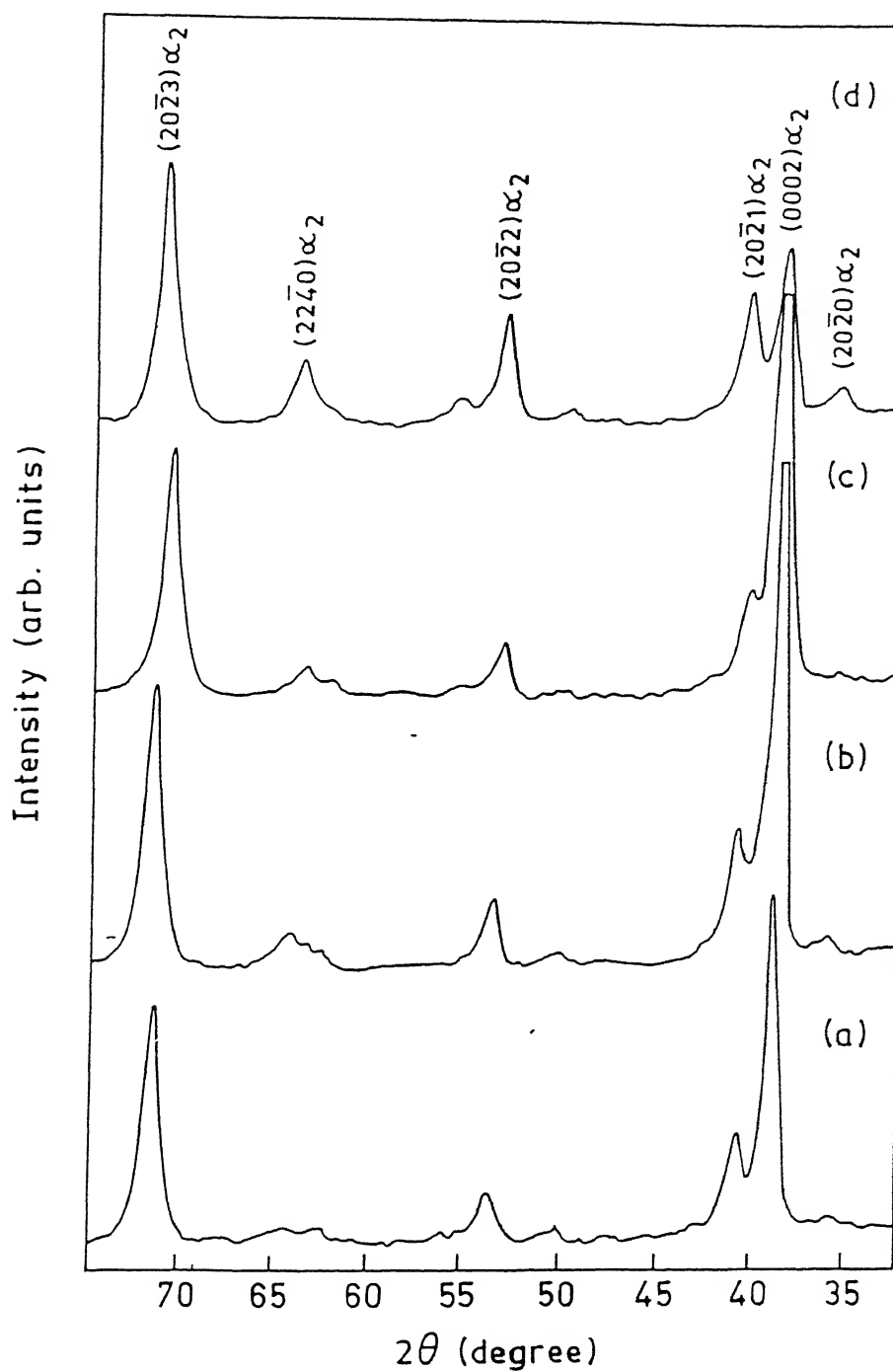


Fig. 6.8 XRD patterns for the 1173 K rolled (furnace cooled) material in the (a) as rolled condition, (b) heat treated at 1173 K, (c) heat treated at 1293 K and (d) heat treated at 1373 K (all furnace cooled)

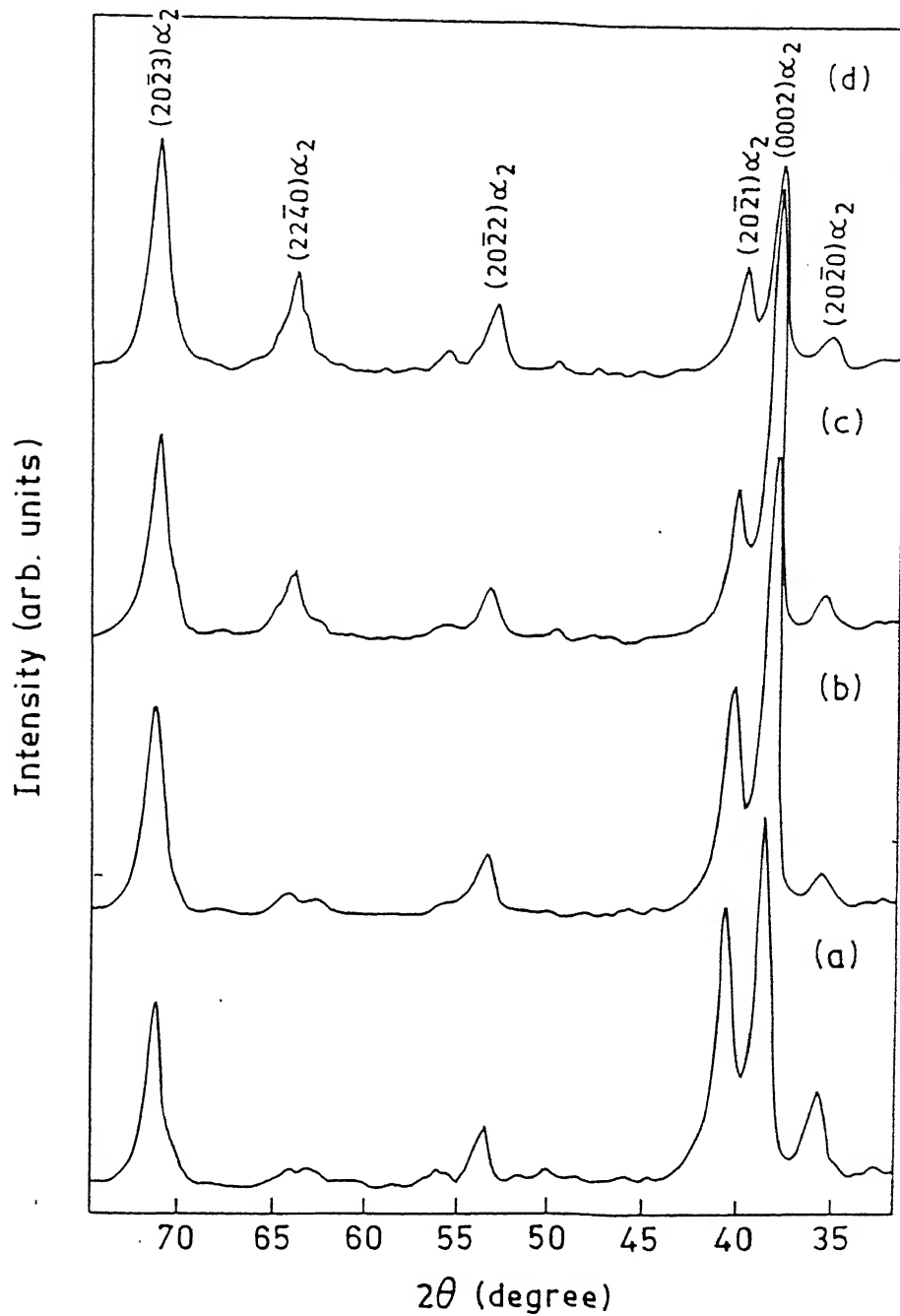


Fig. 6.9 XRD patterns for the 1293 K rolled (furnace cooled) material in the (a) as rolled condition, (b) heat treated at 1173 K, (c) heat treated at 1293 K and (d) heat treated at 1373 K (all furnace cooled)

6.3 Texture Results

The (0002) pole figures of the R 1173 series of samples along with the starting material are shown in Fig. 6.11 (a to d). Heat treatment appears to cause a degradation of the nearly perfect basal texture of the starting material. Heat treatment at 1173 K causes splitting along TD, while heat treatment at the higher temperature of 1293 K causes RD splitting. The 1373 K heat treatment of the material appears to remove most of the basal textured material, with the pole density maxima shifting by about $20/25^\circ$ from the perfect basal location. Still there is some perceptible intensity in the basal region.

The complete ODFs of the R 1173 series of samples are shown in Figs. 6.12 (a to c). For convenience, the $\phi_2 = 0^\circ$ and 30° sections of the ODFs of all the samples along with those of the starting material are presented in Figs. 6.13. The results clearly corroborate the general findings from the pole figures, in the sense that drastic deterioration of the $[0001]\parallel ND$ fibre takes place with increment of the heat treatment temperature. A study of the $\phi_2 = 0^\circ$ sections reveal that in all the heat treated materials some intensity appears along the $(\bar{1}2\bar{1}6)[uvw]$ line. In the case of the 1373 K heat treated material, a strong intensity maxima, in fact, appears at the $(\bar{1}2\bar{1}6)[4\bar{5}43]$ location. A study of the $\phi_2 = 30^\circ$ sections also shows that the intensity and perfection of the $[0001]\parallel ND$ fibre decreases continuously with increment in the heat treatment temperature.

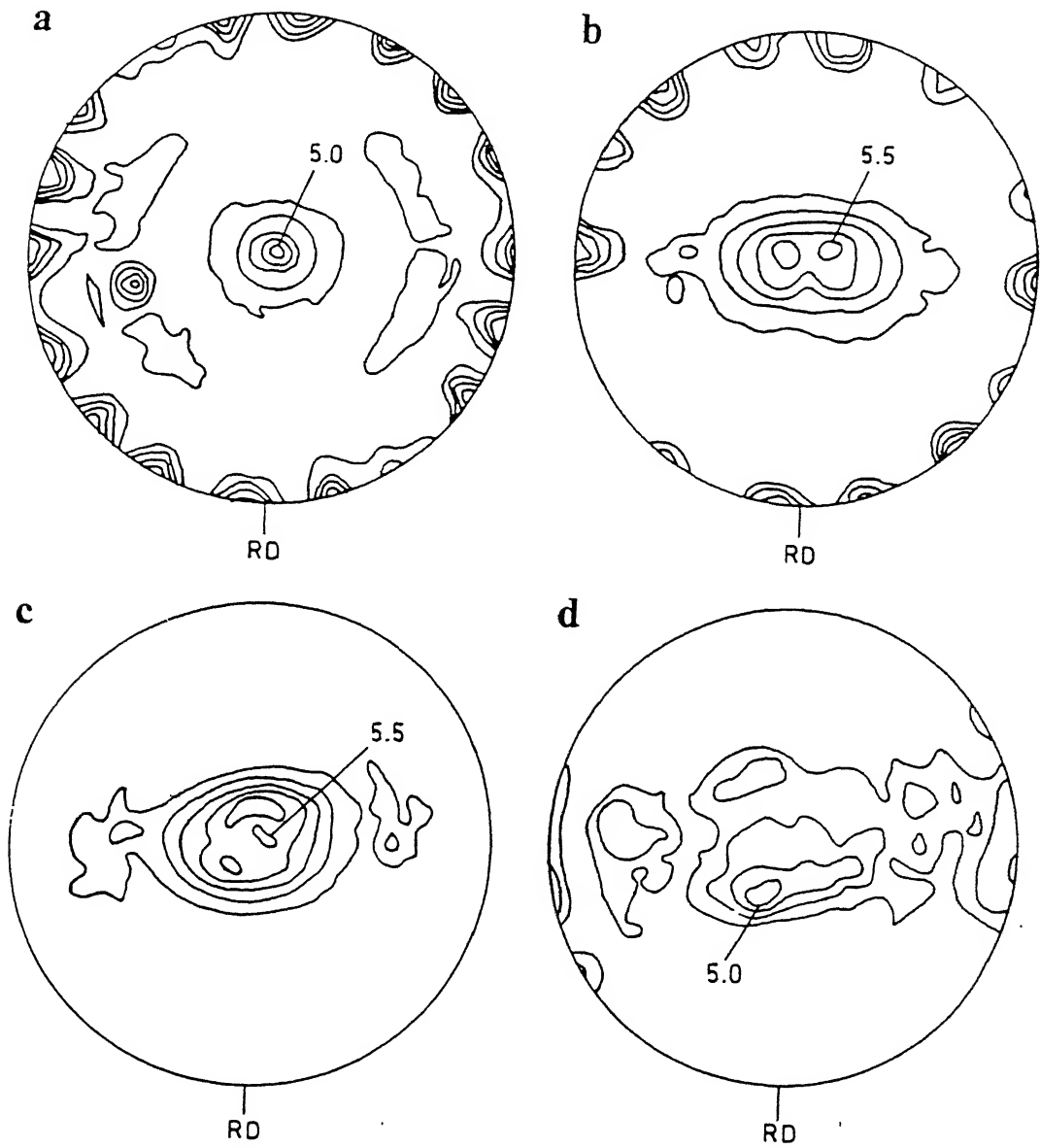


Fig. 6.11 (0002) pole figure of the 1173 K rolled (furnace cooled) material in the (a) as rolled condition, (b) heat treated at 1173 K, (c) heat treated at 1293 K and (d) heat treated at 1373 K (all furnace cooled)

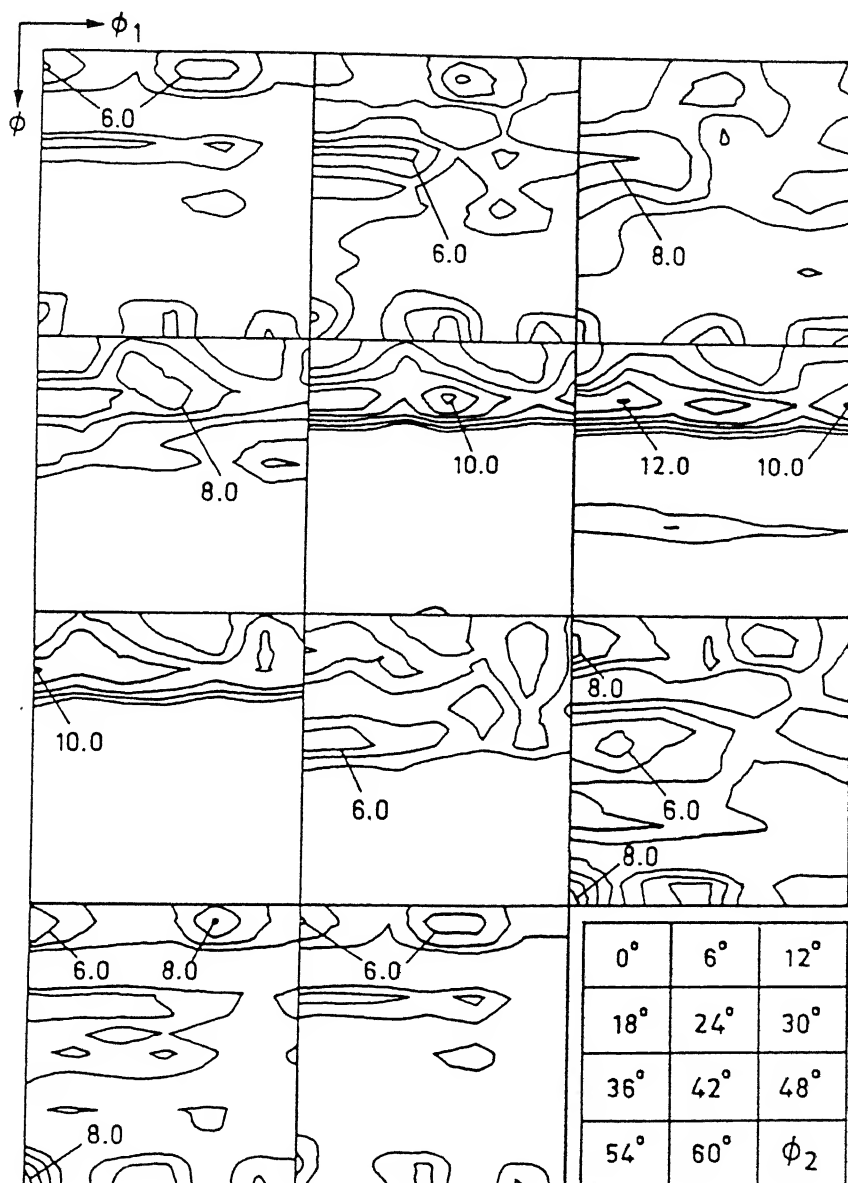


Fig. 6.12 a Complete ODF of the R1173H1173 material

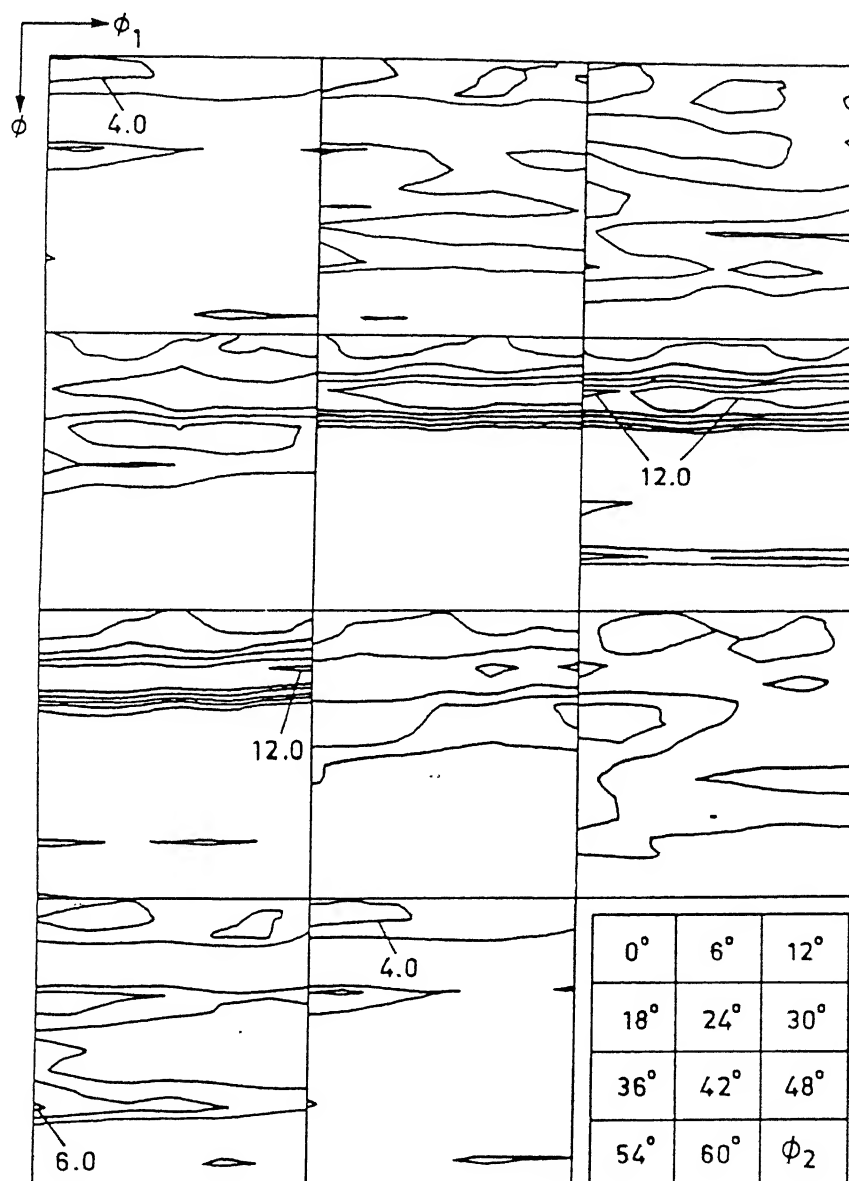


Fig. 6.12 b Complete ODF of the R1173H1293 material

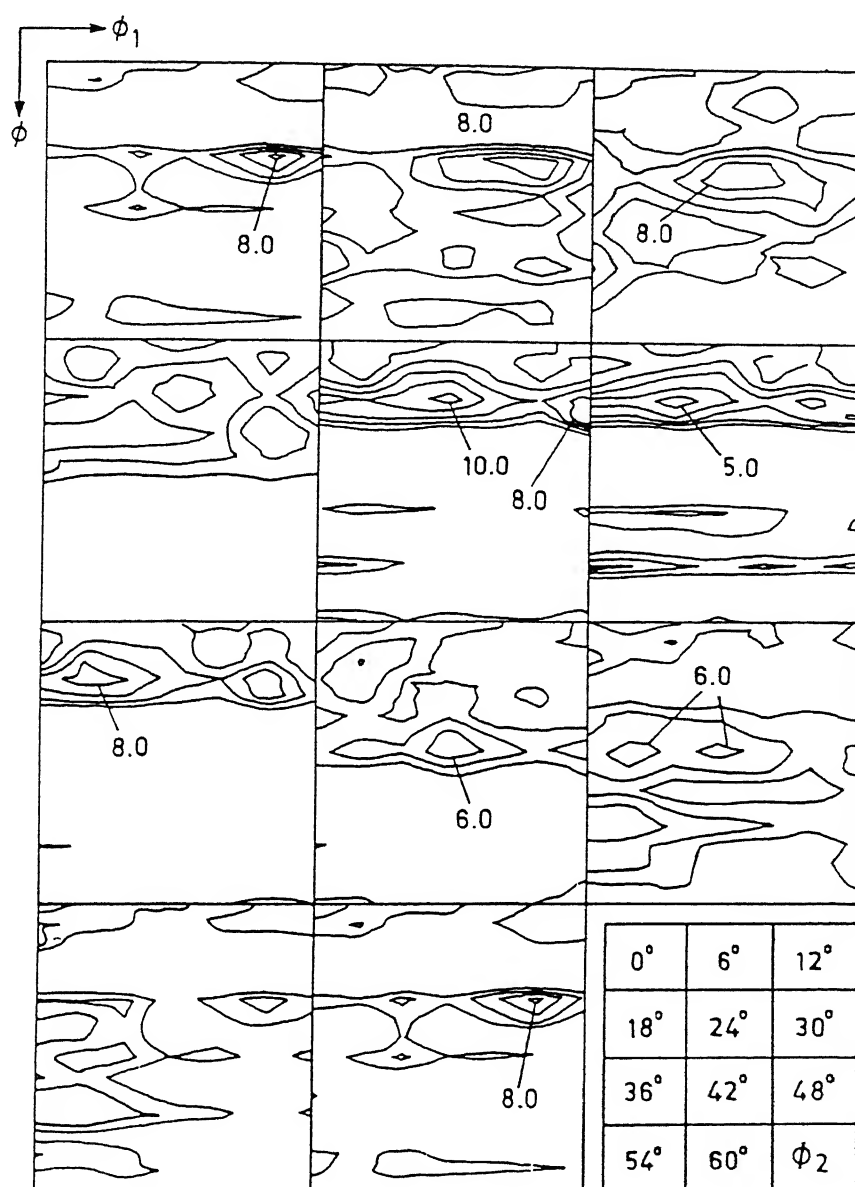


Fig. 6.12 c Complete ODF of the R1173H1373 material

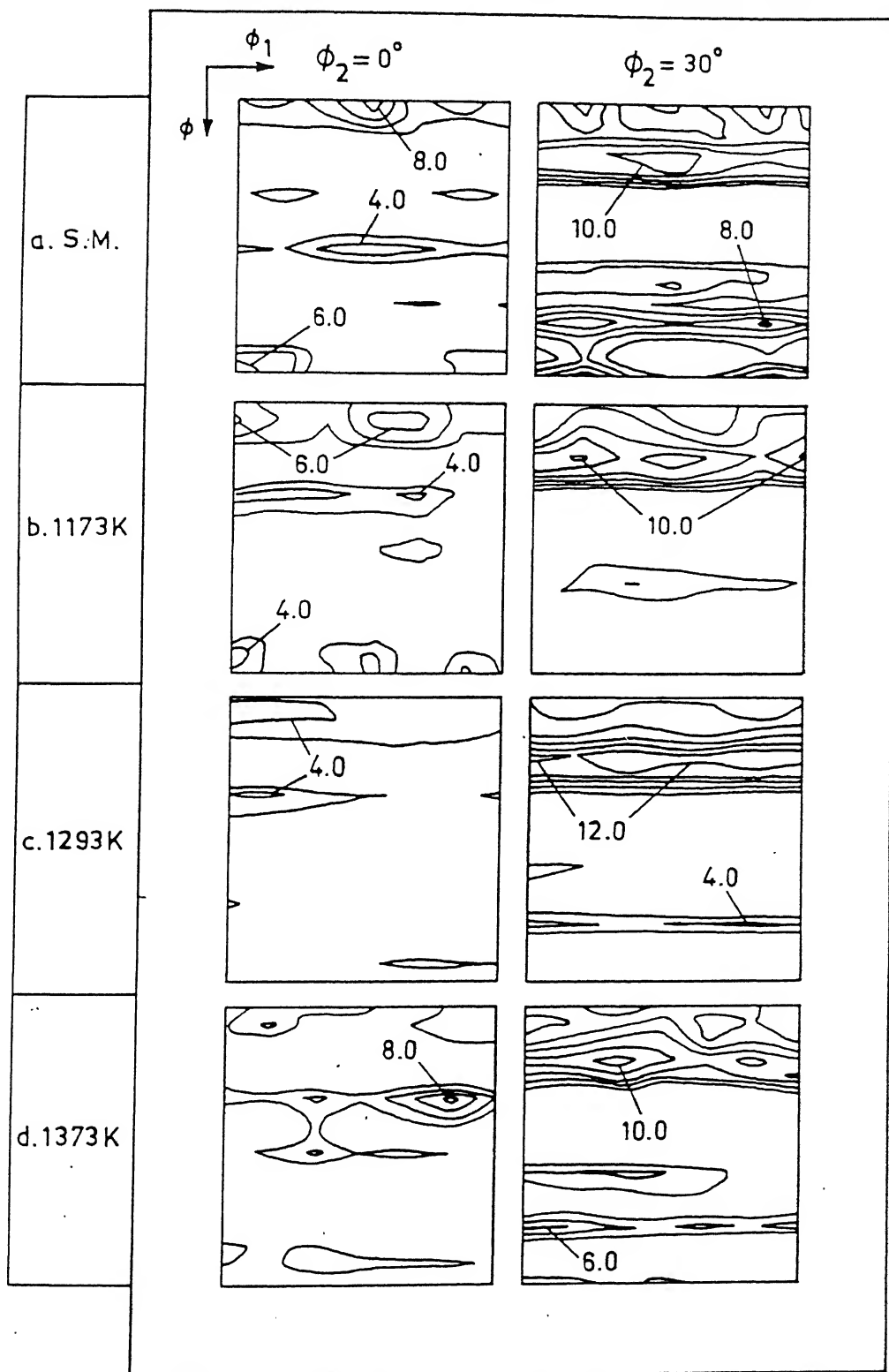


Fig. 6.13 $\phi_2 = 0^\circ$ and 30° sections of the ODFs of the 1173 K rolled (furnace cooled) material in the (a) as rolled condition, (b) heat treated at 1173 K, (c) heat treated at 1293 K and (d) heat treated at 1373 K (all furnace cooled)

In fact, the pole density maxima appear near the locations about 18° away (along ϕ) from the perfect basal fibre location. This component of texture can be written as $(01\bar{1}7)[uvw]$. In addition to the above, reasonably high pole densities are also seen at location 57° and 75° away (along ϕ) from the $[0001]\parallel ND$ fibre location, especially in the $\phi_2 = 30^\circ$ section of the 1373 K heat treated material. These texture components can be written as $(02\bar{2}3)[uvw]$ and $(02\bar{2}1)[uvw]$ respectively.

The (0002) pole figures of the R1293 series of samples along with the starting material are shown in Fig. 6.14 (a to d). As mentioned earlier, the starting material does not show a high pole density at the perfect basal location. In fact, the pole density maxima are situated on both the sides of the ND-TD line, quite far away from the basal location. After heat treatment at 1173 K, the high intensity poles appear to migrate near to the basal region and the highest pole density is obtained at around 18° - 22° away from the perfect basal location. Heat treatment at 1293 K again causes a deterioration of the basal texture. The pole density is found to be concentrated at a region 15° - 18° away from $[0001]\parallel ND$. There are a number of other orientations also present in the pole figure, especially situated along the periphery of the (0002) pole figure. These peripheral orientations seem to persist in the sample heat treated at 1373 K. Once again, there is a reasonably high pole density around the basal location. The complete ODFs of the above materials are shown in Figs. 6.15 (a-c).

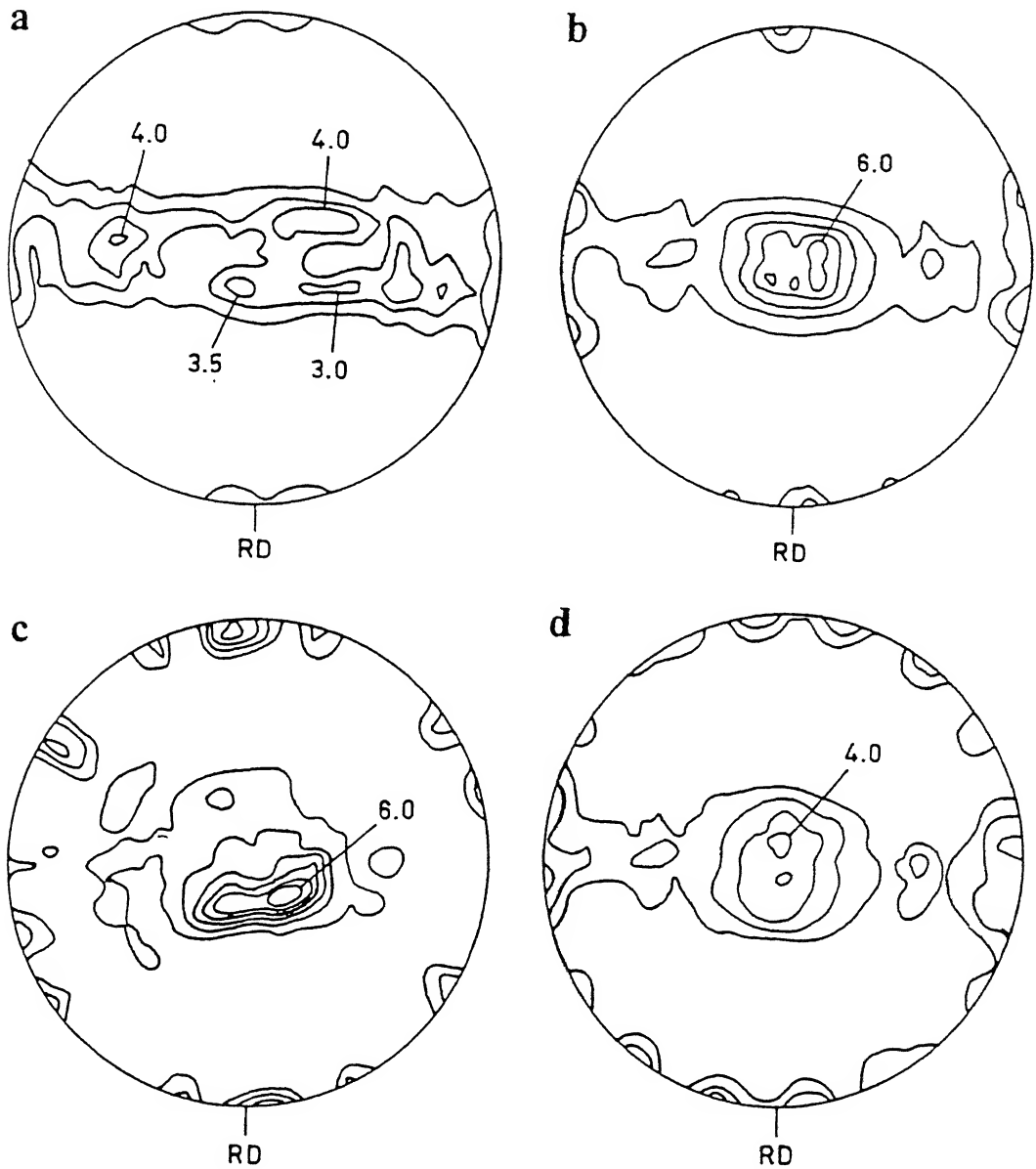


Fig. 6.14 (0002) pole figure of the 1293 K rolled (furnace cooled) material in the (a) as rolled condition, (b) heat treated at 1173 K, (c) heat treated at 1293 K and (d) heat treated at 1373 K (all furnace cooled)

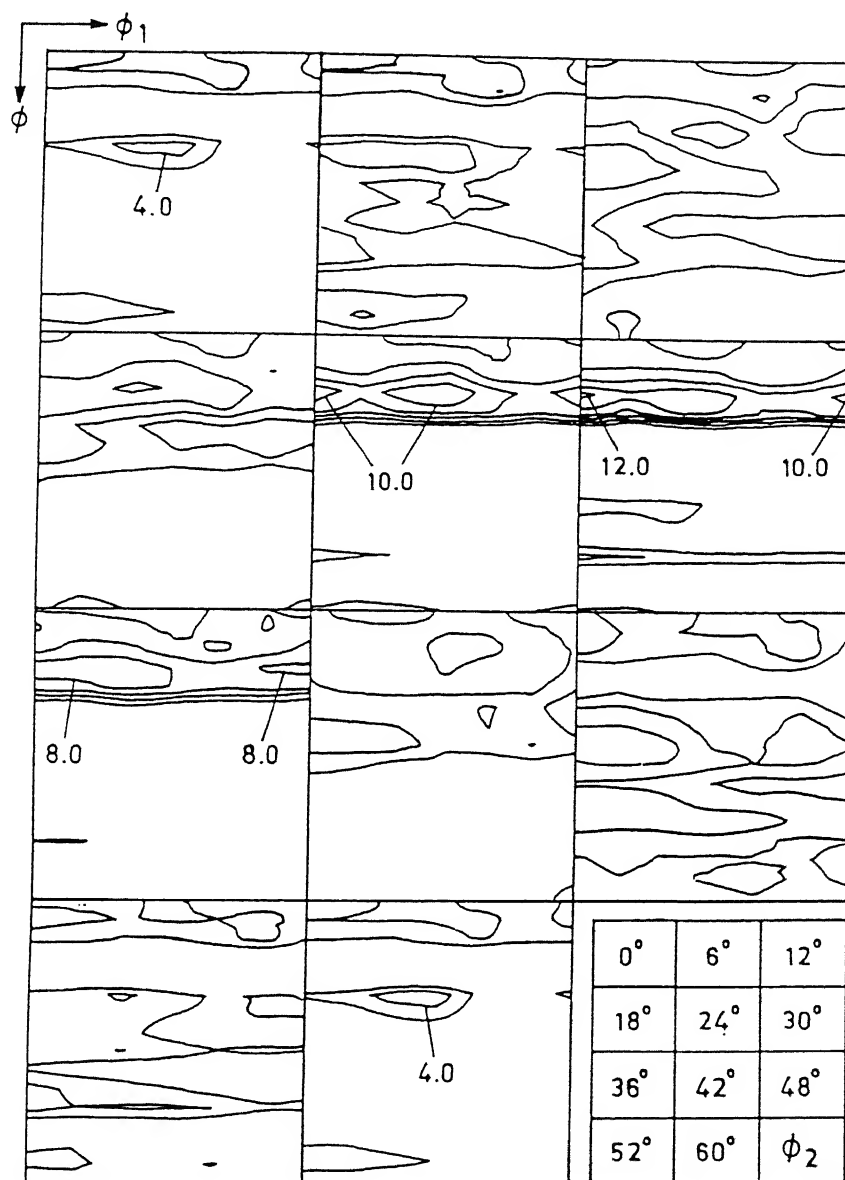


Fig. 6.15 a Complete ODF of the R1293H1173 material

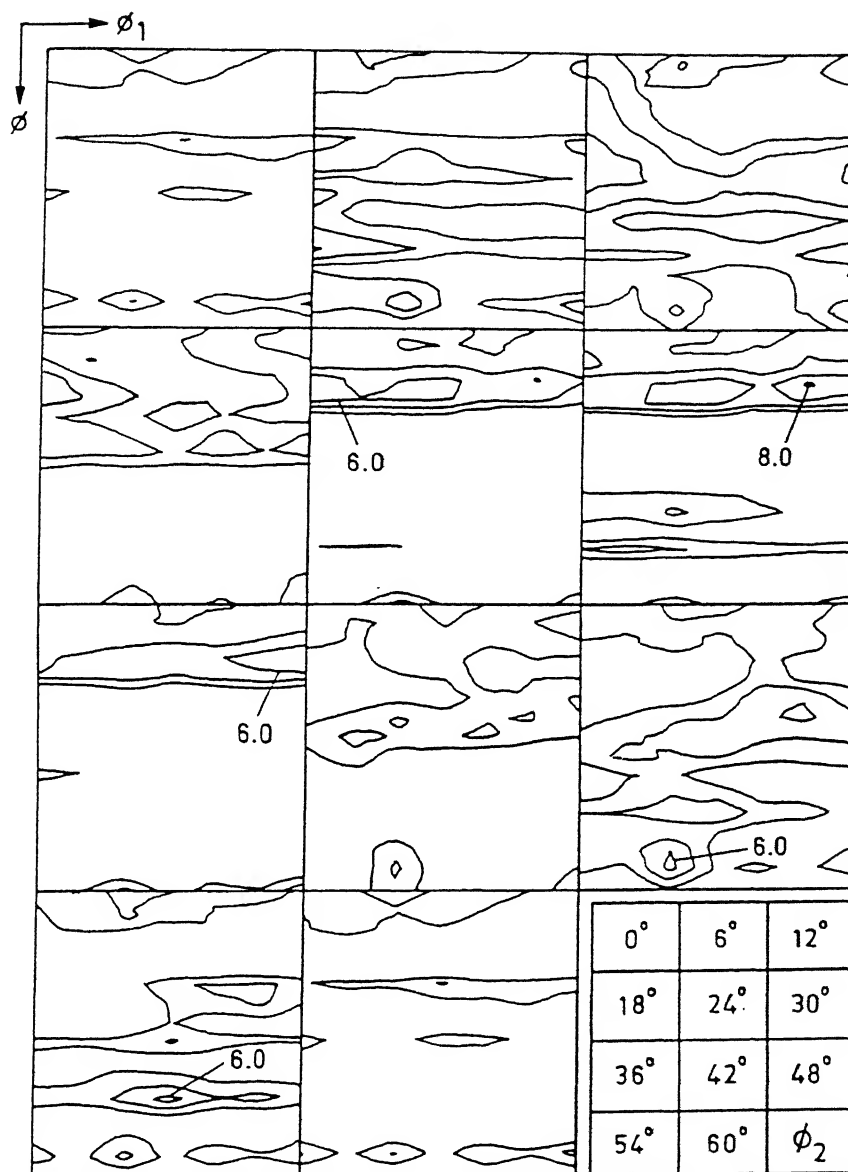


Fig. 6.15 b Complete ODF of the R1293H1293 material

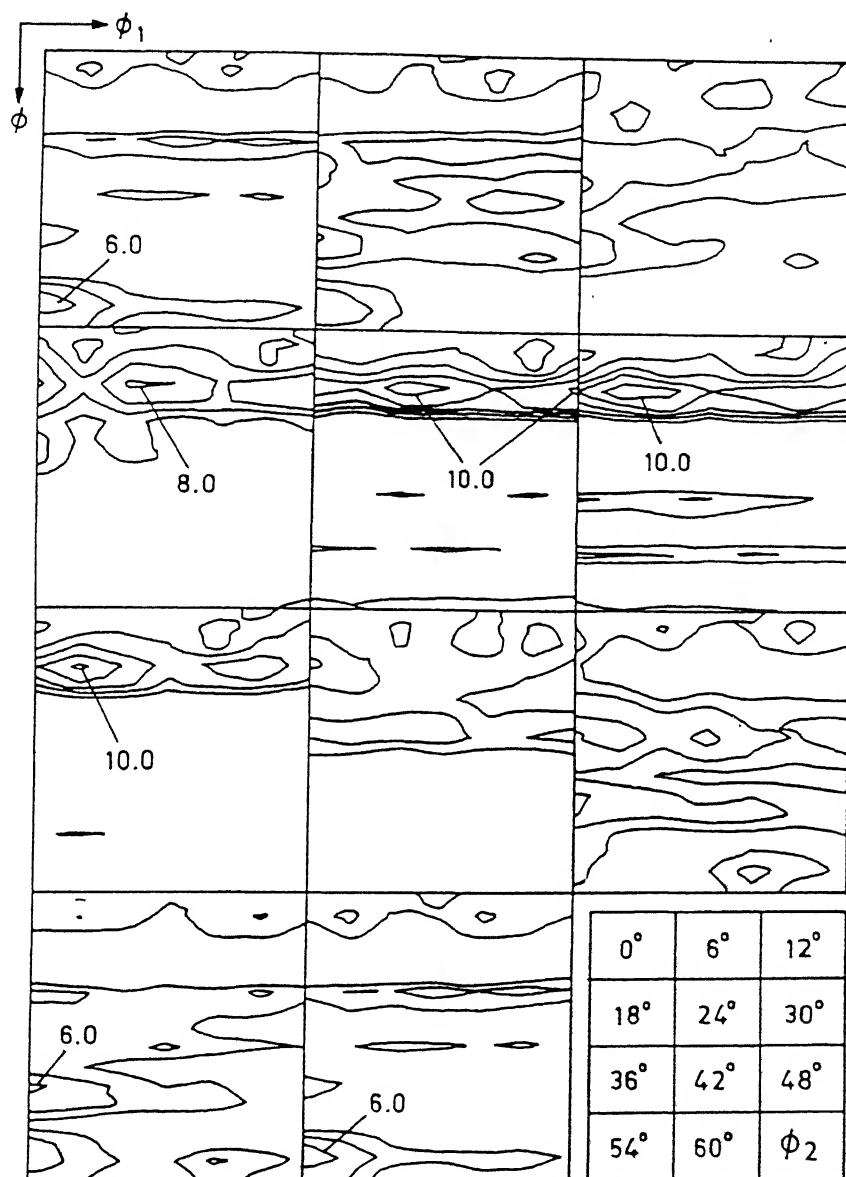


Fig. 6.15 c Complete ODF of the R1293H1373 material

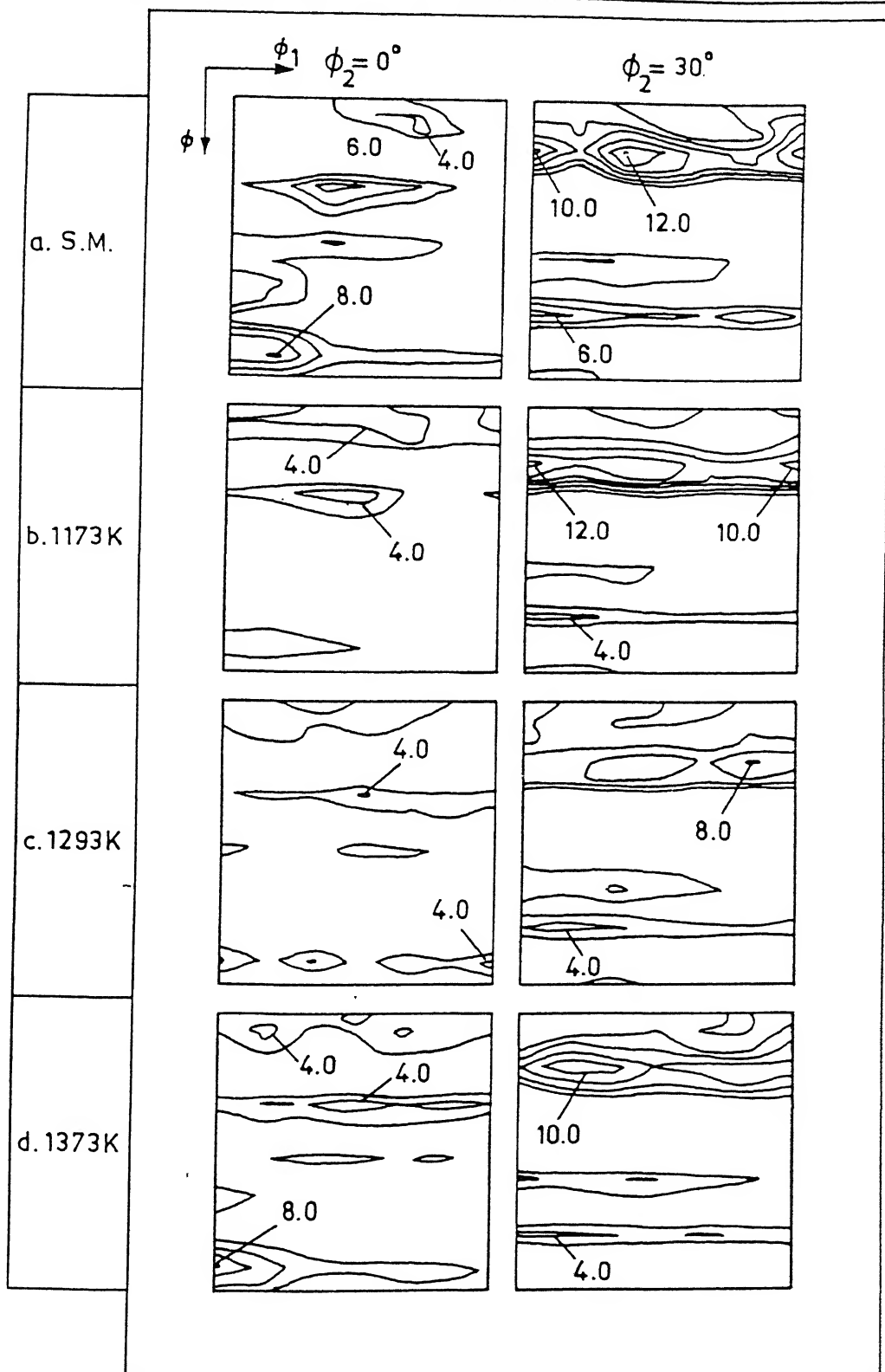


Fig. 6.16 $\phi_2 = 0^\circ$ and 30° sections of the ODFs of the 1293 K rolled (furnace cooled) material in the (a) as rolled condition, (b) heat treated at 1173 K, (c) heat treated at 1293 K and (d) heat treated at 1373 K (all furnace cooled)

Figs. 6.16 (a-d) show the $\phi_2 = 0^\circ$ and 30° sections of the ODFs of the starting as well as the heat treated materials of the R1293 series. Although the starting material hardly shows any orientation close to the basal, the $\phi_2 = 0^\circ$ sections of the R 1293H1173 and R1293H1373 samples show reasonably strong pole densities along the $0001\parallel ND$ fibre compared to which the R1293H1293 sample shows perceptibly lower pole density along this fibre. The $\phi_2 = 30^\circ$ sections of the ODFs indicate that in common with the starting material, a rather high pole density exists for all the heat treated samples along ϕ_1 at $\phi = 18^\circ$. This fibre can be written as $(01\bar{1}7)[uvw]$, as was also found in the previous case. Interestingly, the other orientations of significance which are observed in the ODFs of the different samples in this series, are common to all the samples, only their relative intensities are different for different samples. Thus, a component $(\bar{1}2\bar{1}6)[3\bar{2}\bar{1}1]$ appears in the $\phi_2 = 0^\circ$ section of the R1293H1173 sample; this gradually changes into a fibre of the type $(\bar{1}2\bar{1}6)[uvw]$ for the R1293H1293 and R1293H1373 samples. In a similar manner, in the same ODF section for the R1293H1173 sample, a component in between $(\bar{1}2\bar{1}0)[10\bar{1}0]$ and $(\bar{2}4\bar{2}1)[10\bar{1}0]$ can be observed. This gradually changes into an imperfect fibre in the R1293H1293 sample and then into a nearly perfect fibre in the R1293H1373 sample. As found out in case of the R1173 series of samples, reasonably high pole densities are also observed at location 57° and 75° away (along ϕ) from the $[0001]\parallel ND$ fibre location, in the $\phi_2 = 30^\circ$ section for all the heat treated samples of the R1293 series. These texture components can be written as $(02\bar{2}3)[uvw]$ and $(02\bar{2}1)[uvw]$ respectively.

The (0002) pole figures of the R1373 series of samples along with the starting material are shown in Figs. 6.17 (a to d). As mentioned earlier, the starting material shows absolute no basal texture component. The texture in all the heat treated samples appear not far from the random, although pole densities ranging between 2 to 4 are observed in many places within the pole figures. Isolated high pole density regions as observed in the starting as well as in the R1373H1173 and R1373H1293 samples can be identified as near $(11\bar{2}1)[1\bar{1}00]$ location. The complete ODF plots from these materials are shown in Figs. 6.18 (a-c).

Figs. 6.19 (a-d) show the $\phi_2 = 0^\circ$ and 30° sections of the ODFs of the starting material and the heat treated samples of the R1373 series. It is quite interesting to note that in both the ODF sections, the textures appear qualitatively similar in all the samples, including the starting material. Although the starting material does not show practically any orientation along the $[0001]\parallel ND$ ($\phi_2 = 0^\circ$ section), some intensity is observed at about $\phi = 6^\circ$ away from this fibre in both the R1373H1173 and R1373H1293 samples. On the other hand, the R1373H1373 sample shows some maxima at around $\phi = 12^\circ$ away from the above fibre. In the same ODF section, a reasonably strong inhomogeneous fibre at $\phi = 32^\circ$ from the perfect basal is found to be present for all the samples. This fibre can be identified as $(\bar{1}2\bar{1}6)[uvw]$ as was also observed in the previous cases. A strong component near the $(\bar{1}2\bar{1}0)[10\bar{1}0]$, as observed in the $\phi_2 = 0^\circ$ section of the starting material appears to weaken with increase in heat treatment temperature and ultimately disappears in the R1373H1373 sample.

As observed in the previous cases also, the $\phi_2 = 30^\circ$ sections of all the heat treated samples, here, along with the starting material, show a rather strong inhomogeneous fibre about $\phi = 18^\circ$ away from the $[0001]\parallel ND$, which can be identified as $(01\bar{1}7)[uvw]$.

Again rather strong orientations, arranged as somewhat imperfect fibres, are observed at locations 57° and 75° away (along ϕ) from the $[0001]\parallel ND$ location, in the $\phi_2 = 30^\circ$ sections for all the heat treated samples of the R1373 series, including the starting material. The pole densities along these fibres seem to increase perceptibly after heat treatment at 1173K and 1293 K; however, the pole densities along these fibres in the 1373 K heat treated samples is found to be comparable to that in the starting material. As mentioned earlier, these two fibres can be identified as $(02\bar{2}3)[uvw]$ and $(02\bar{2}1)[uvw]$ respectively.

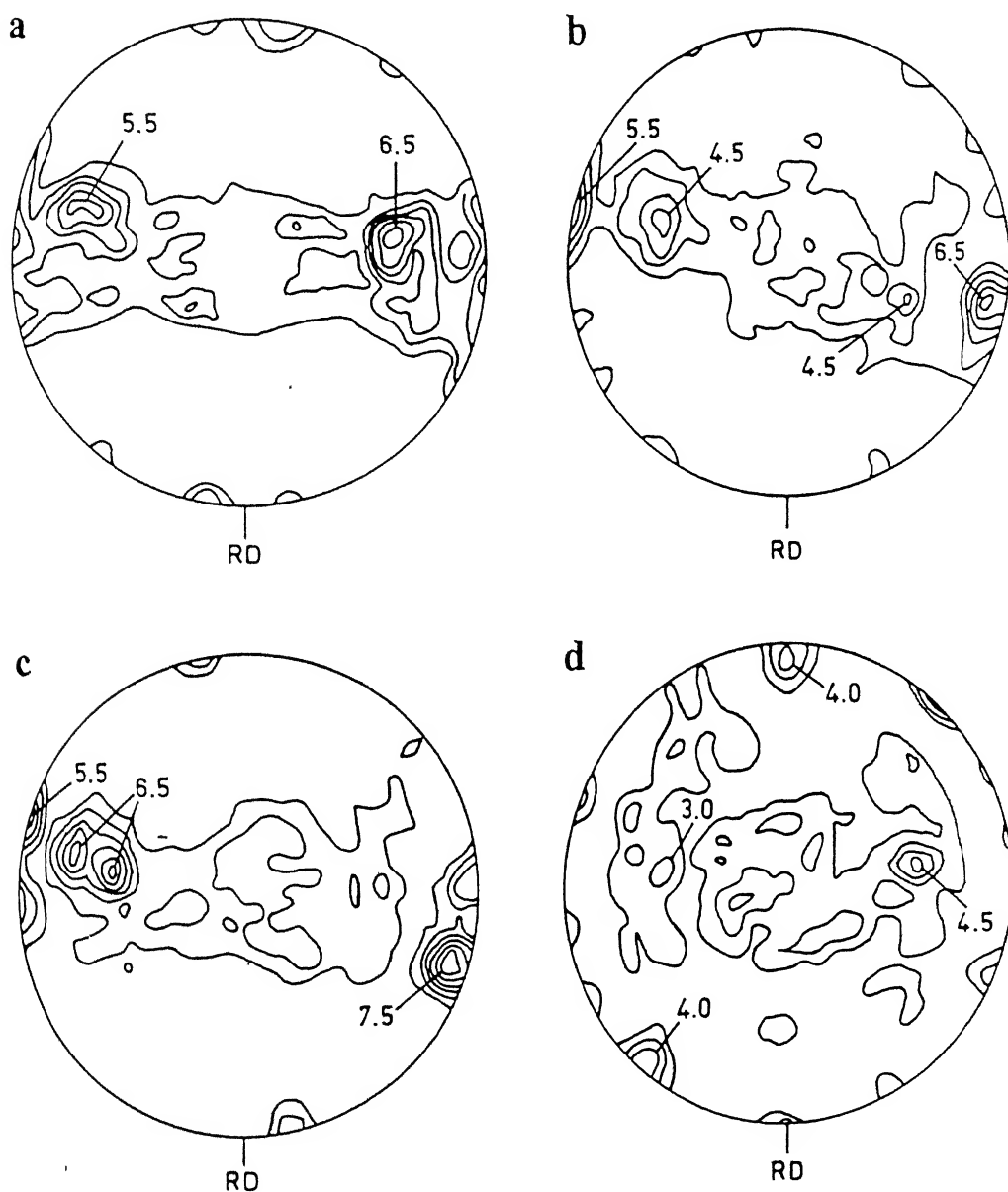


Fig. 6.17 (0002) pole figure of the 1373 K rolled (furnace cooled) material in the (a) as rolled condition, (b) heat treated at 1173 K, (c) heat treated at 1293 K and (d) heat treated at 1373 K (all furnace cooled)

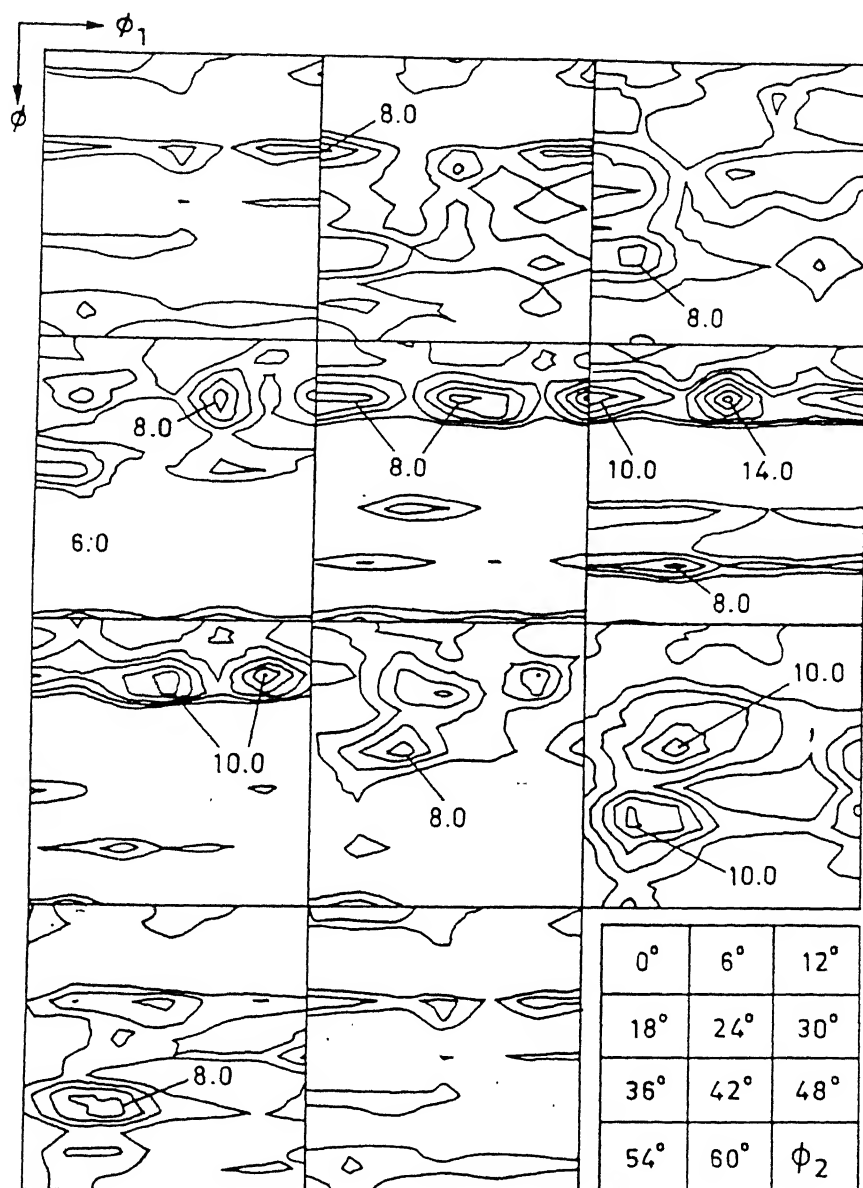


Fig. 6.18 a Complete ODF of the R1373H1173 material

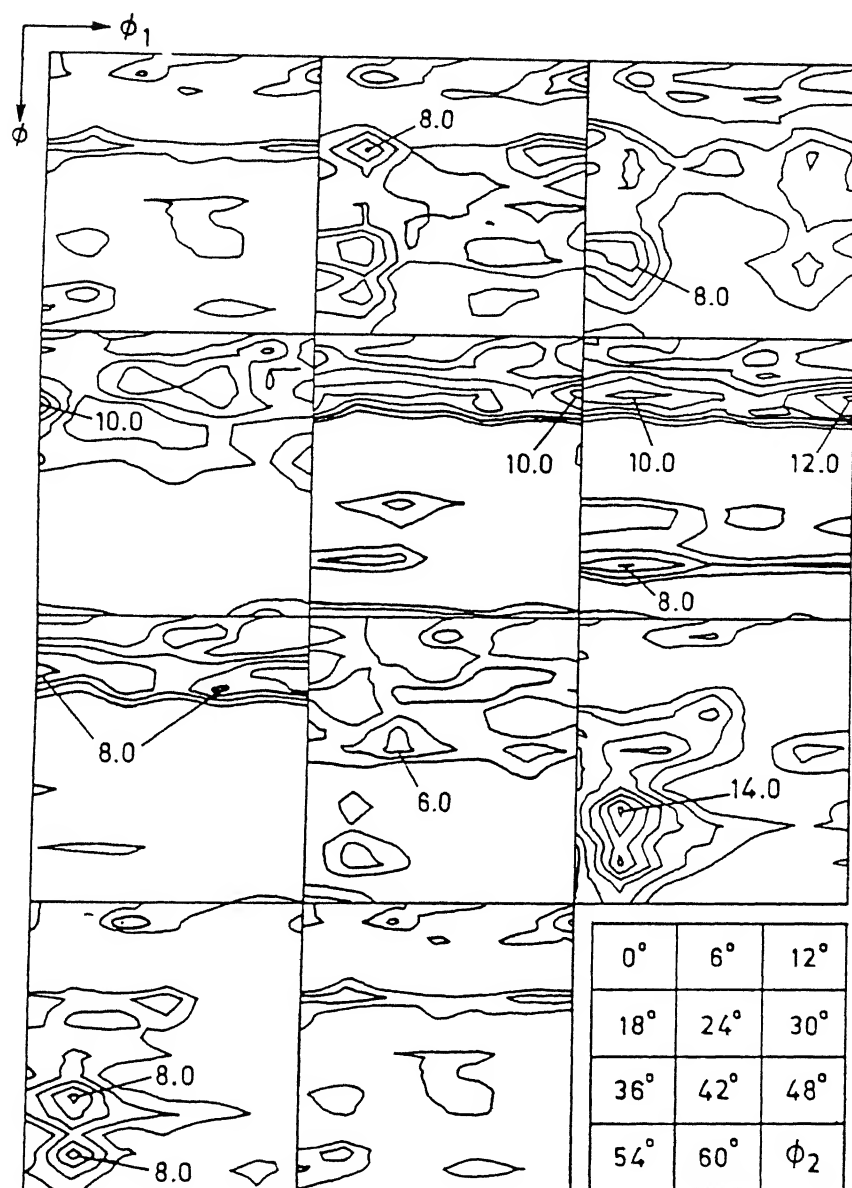


Fig. 6.18 b Complete ODF of the R1373H1293 material

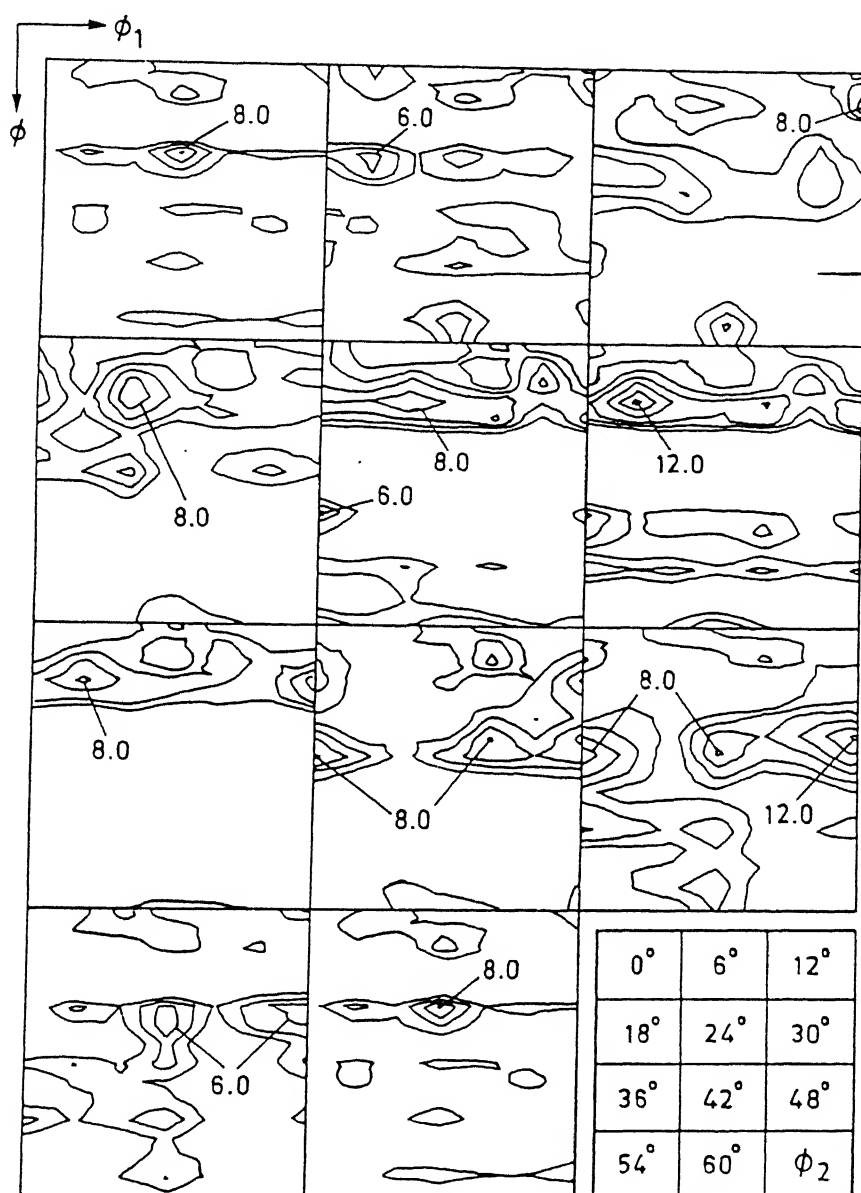


Fig. 6.18 c Complete ODF of the R1373H1373 material

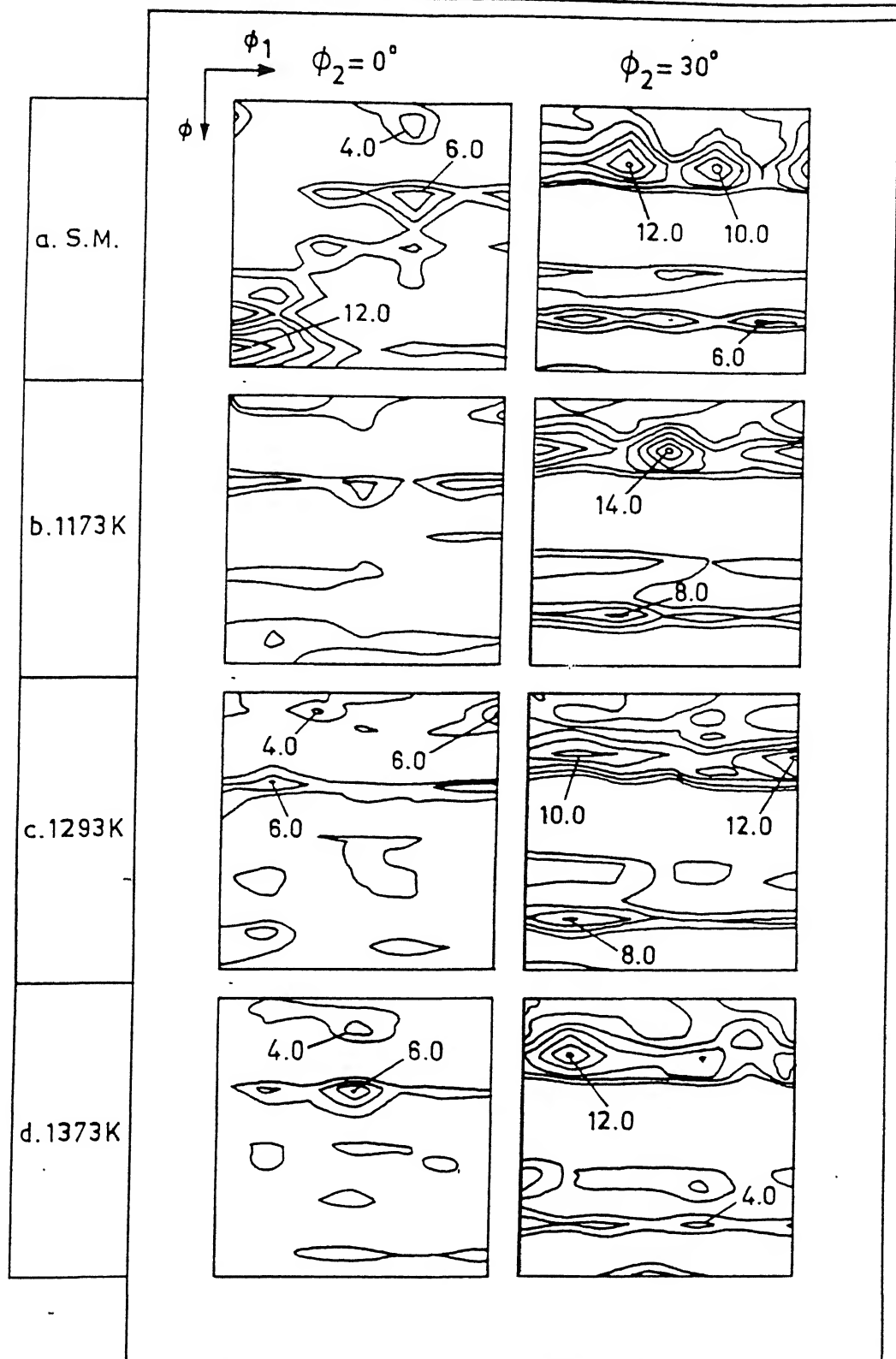


Fig. 6.19 $\phi_2 = 0^\circ$ and 30° sections of the ODFs of the 1373 K rolled (furnace cooled) material in the (a) as rolled condition, (b) heat treated at 1173 K, (c) heat treated at 1293 K and (d) heat treated at 1373 K (all furnace cooled)

6.4 Discussion of the Results

In this chapter an attempt has been made to study the effect of $\alpha_2 \rightarrow \beta \rightarrow \alpha_2$ transformation on the stability of the basal texture. For this purpose the starting materials chosen were R1173 FC, R1293 FC and R1373 FC. The starting texture in the first case is mainly basal (reasonably strong) plus some extra orientations. This texture pertains basically to the deformed primary α_2 phase, although some secondary α_2 is also expected to be present. In the second case, the texture consists of only a low pole density in the basal location along with some moderately strong non basal components. The phases present in this material are both primary α_2 (deformed and then recrystallised at 1293 K) and significant amount of secondary α_2 , obtained from the high temperature β by transformation during furnace cooling. In the third case the starting texture does not contain any trace of the basal component. The phase present is practically entirely secondary α_2 produced by transformation from β during furnace cooling.

It is quite apparent from Figs. 6.17 that when the starting texture does not contain any basal component, annealing at the three temperatures of 1173 K, 1293 K and 1373 K, followed by furnace cooling does not yield any perceptible basal texture. On the other hand, when the starting material has a reasonably strong basal texture (from deformed primary α_2) (Figs. 6.11), annealing at the successively higher temperatures of 1173 K, 1293 K and 1373 K appears to gradually degenerate the texture from the perfect basal. In contrast, when the starting material possesses only a

rather weak basal pole density (Fig. 6.14) subsequent annealing at 1173 K, 1293 K and 1373 K seem to improve the basal component perceptibly.

From what has been stated above, it is quite clear that when the starting material does not have any basal component (R1373 K material), partial or full transformation along the $\alpha_2 \rightarrow \beta \rightarrow \alpha_2$ cycle does not produce any basal component. In case of the R1173K material, where the primary α_2 is in a more or less deformed condition and which has a reasonably strong basal texture, subsequent treatment through the $\alpha_2 \rightarrow \beta \rightarrow \alpha_2$ cycle seems not to improve the basal texture at all. On the other hand the location of high pole density has been found to deviate from the perfect basal component as temperature of annealing increases. However, it is quite interesting to see that cycling the R1293 K material through the $\alpha_2 \rightarrow \beta \rightarrow \alpha_2$ transformation sequence helped in sharpening the original low density basal component by a remarkable extent.

An explanation of the above behaviour can be given in the following manner. The β phase that forms in the R1173 K material, as it is annealed at 1293 K or at 1373 K, comes about by transformation from deformed primary α_2 mainly (Figs. 4.8 and 4.21). On the other hand, the β phase in the R1293 K material, when annealed at 1293 K or at 1373 K, is obtained from somewhat strain-free primary as well as secondary α_2 grains (Fig. 4.15). In the former case the basal texture shows some perceptible deterioration, while in the latter significant improvement in the basal texture is noticed after the $\alpha_2 \rightarrow \beta \rightarrow \alpha_2$ transformation. As mentioned earlier (Section 4.4.2.2),

Fredericks [156] suggested that if the β to α_2 transformation occurs from deformed β , only 1/6th of the highly textured $\{110\}$ planes is favoured in transforming to the $\{0002\}$ planes of the product α_2 phase. It was further suggested [156] that during transformation from recrystallised β into α_2 , all the six $\{110\}$ planes should be equally favoured in transforming to the basal plane, producing thereby a strong basal texture.

In view of the above suggestions and the present observations, it appears that the transformation behaviour of β to α_2 (in terms of selection of variants) could be dependent on the nature of the original α_2 phase from which the β is derived during heat treatment. Thus when β forms from deformed primary α_2 (with a reasonably strong basal texture), it behaves as though it is deformed β and, therefore, retransforms into α_2 in a constrained manner, as suggested by Fredericks [156]. As a result, the product basal texture may be substantially impaired. This seems to be the case for the R1173 K material. On the other hand, β obtained from annealed and recrystallised α_2 (primary + secondary) behaves as though it is itself in a recrystallised condition, and therefore, retransforms into α_2 in a manner whereby all the variants leading to the basal component of the texture operate, thereby improving this particular component. This could be the case for the R1293 K material.

The present work, therefore, leads to two important conclusions: (i) If β is formed from α_2 having no basal texture component, further transformation from β to α_2 will not produce any basal texture; (ii) heat treating the material through the $\alpha_2 \rightarrow \beta \rightarrow \alpha_2$ cycle will produce the basal component in the final α_2 , provided this

component exists in the texture of the original α_2 . If the original α_2 is in a deformed condition, the basal component in the texture of the final α_2 phase will be impaired to some extent. By contrast, if the original α_2 is in a strain-free condition, the extent of basal texture in the final α_2 phase is expected to improve significantly.

Thus the textures obtained in all the heat treated samples which were subjected to the $\alpha_2 \rightarrow \beta \rightarrow \alpha_2$ cycle were from basically primary α_2 , mixture of primary and secondary α_2 or from pure secondary α_2 phase. The full discussion regarding the evolution of transformation textures in secondary α_2 formed from different microstructural states of the β phase has already been given in section 4.4.2.2. and will not be repeated here.

Conclusions

1. The initial as-cast material, which consists of nearly 70% α_2 and 30% β phase, possesses a strong solidification texture. The main orientations are centred around $[0001]\parallel ND$ (basal) with maxima at $(0001)[3\bar{1}\bar{2}0]$, $(0001)[1\bar{1}00]$ and $(0001)[1\bar{2}10]$. A few non basal components are also seen.
 2. Heat treatment of the as-cast alloy at 1173 K for 24 hrs, for the equilibration of phases, does not change the basal character of texture. However, in this case, a number of non basal components are also quite strong in intensity.
 3. The unrestricted rolling of primary α_2 at 1173 K leads to the formation of the sharpest $(0001)[uvw]$ basal texture.
 4. A rolling reduction of 70%-80% at 1173 K causes refinement of the microstructure due to fragmentation of α_2 platelets. The effect of temperature is not that apparent here since the substructural features correspond to the as-deformed state of the materials.
 5. Basal texture strengthens in intensity with amount of deformation at 1173K. However, beyond 70% rolling reduction the texture more or less stabilises.
-

6. Fast cooling (water quenching) from the rolling temperature helps in retaining the high temperature β phase, whereas slow cooling (furnace cooling) from the rolling temperature leads to the formation of secondary α_2 from the high temperature β . The difference in the cooling rates gets reflected in the microstructural and textural evolution.

7. When substantial amount of β phase is also present the deformation of primary α_2 becomes restricted and this gives rise to the formation of strong texture component along $[10\bar{1}0]||RD$ fibre. This is $(hkl)[10\bar{1}0]$ accompanied by a simultaneous decrease of the $(0010)[uvw]$ orientations.

8. The texture of transformed (secondary) α_2 is generally dictated by the texture of parent β -phase according to the Burger's Orientation Relationship. The resulting texture is mostly non basal when transformation takes place from deformed β . However, the texture of transformed (secondary) α_2 possess some basal components when transformation takes place from β phase in the annealed state.

9. The basic characteristics of the rolling texture does not change during isochronal or isothermal annealing. Although, the rolling (basal) texture somewhat weakens during recovery, it starts regaining its strength in the recrystallization stage. The texture starts deteriorating during grain growth.

10. For a material with a basal starting texture, heat treatment in the upper α_2 , $\alpha_2 + \beta$ or β phase fields does not change the basic character of the texture, although the sharpness and specially the width of the basal component increase to some extent with the increase in the heat treatment temperature.

11. Heat treatment of material with starting non-basal texture in the upper α_2 , $\alpha_2 + \beta$ or β phase fields does not produce any basal component irrespective of the heat treatment temperature.

12. When the starting material is reasonably strain-free and possesses a weak basal texture, heat treatment in the upper α_2 , $\alpha_2 + \beta$ or β phase fields helps in intensifying the basal component to certain extent.

13. When the as-rolled materials are subjected to supertransus processing (either $\beta \rightarrow \alpha_2 + \beta$ or $\alpha_2 + \beta \rightarrow \alpha_2$) very often a third phase (neither α_2 nor β) appears at the α_2 / β platelet boundaries. This is more prominent in the case of furnace cooled materials. This third phase could be the orthorhombic 'O' phase.

BIBLIOGRAPHY

1. W.J.G. Bunk, in *Advanced Aerospace Materials*, ed. Horst Buhl, MRE (Materials Research and Engineering), Springer - Verlag, New York, p. 1.
 2. R.E. Shafrik, *Metall. Trans. A*, 8A (1977), p. 1000.
 3. Y.W. Kim and F.H. Froes, in *High Temperature Aluminides and Intermetallics*, eds. S.H. Whang, C.T. Liu, D.P. Pope and J.O. Stiegler, The Minerals, Metals and Materials Society, 1990, p. 465.
 4. D. Banerjee, in *Intermetallic Compounds: Vol. 2, Practice*, eds. J.H. Westbrook and R.L. Fleischer, John Wiley & Sons Ltd., 1994, p. 91.
 5. H.A. Lipsitt, in *Advanced High Temperature Alloys: Processing and Properties*, eds. S.M. Allen, R.M. Pelloux and R. Widmer, Metals Park, Ohio (ASM) 1986, p. 157.
 6. H.A. Lipsitt, in *High Temperature Ordered Intermetallic Alloys*, eds. C.C. Koch, C.T. Liu and N.S. Stoleff, MRS Proc., 39, 1985, p. 351.
 7. J.P. McAndrew and C.R. Simloe, in *Development of Ti-Al-Cb Alloy for use at 1200F - 1800F*, ASD-TR-61-466, 1961, cited in Ref. 4.
 8. H. Winter, *U.S. Patent*, 1968, 3-411-901, cited in Ref. 4.
 9. M.J. Blackburn and M.P. Smith, in *Research to Conduct an Exploratory and Analytical Investigation of Alloys*, AFML-TR-78-18, 1978, cited in Ref. 4.
 10. D.A. De Luca, B.A. Cowles, F.K. Haake and K.P. Holland, in *Fatigue and Fracture of Titanium Aluminides*, WRDC-TR-89-4136, 1989, cited in Ref. 4.
 11. A.K. Gogia, *Ph.D. Thesis*, Banaras Hindu University, India and Defence Metallurgical Research Laboratory, India, 1991.
 12. M.J. Blackburn and M.P. Smith, in *Improved Toughness Alloys based on Aluminides*, WRDC-TR-89-4094, 1989 cited in Ref. 4.
 13. R.G. Rowe, *U.S. Patent*, 5-032-357, 1991, cited in Ref. 4.
 14. R.G. Rowe, in *Key Engineering Materials*, eds. F.H. Froes and T. Khan, Trans. Tech. Switzerland, 77-78, 1993, 61-70.
-

15. B. J. Marquardt, G.K. Scarr, J.C. Chesnutt, C.G. Rhodes and H.L. Fraser, in *Research and Development for Improved Toughness Aluminides*, WRDC-TR-89-4133, 1989.
16. M.J. Blackburn and M.P. Smith, in *Research and Development on Composition and Processing of Titanium Aluminide Alloys for Turbine Engines*, AFWAL-TR-82-4086, 1989, cited in Ref. 4.
17. S. Gama, in *Ternary Alloys*, eds. G. Retzow and G. Effenberg, MSI, VCH, FRG, 7, 1993, p. 382-398.
18. T.T. Nartova and G.G. Sopochkin in *Investigation of the Phase Structure of Ti3Al-Nb Alloys*, Russ. Metall, 2, 1970, 138.
19. T.T. Nartova and G.G. Sopochkin in *Phase Diagram of Alloys of the Ternary System Titanium – Aluminium – Niobium*, ed. I.I. Kornilov, Nauka, Moscow, 1970, p. 19, cited in Ref. 17.
20. T.T. Nartova and G.G. Sopochkin, *Russ. Metall.*, 2, 1970, 138.
21. D. Banerjee, A.K. Gogia, T.K. Nandy and V.A. Joshi, *Acta Metall.* 36, 1988, 871.
22. D.G. Konitzer, I.P. Jones and H.L. Frasar, *Scripta Metall.* 20, 1986, 265.
23. H. Bohm and K. Lohberg, *Z. Metallkde*, 41, 1958, 173.
24. R. Strychor and J.C. Williams, in *Solid-Solid Phase Transformations*, TMS, AMIE, New York, 1982, p. 249.
25. D. Banerjee, T.K. Nandy, A.K. Gogia, *Scripta Metall.*, 21, 1987, 597.
26. K. Muraleedharan, S.V.N. Naidu and D. Banerjee, *Scripta Metall.*, 24, 1990, 27.
27. K. Muraleedharan, A.K. Gogia, T.K. Nandy, D. Banerjee and S. Lele, *Metall. Trans. A*, 23A, 1992, 401-416.
28. R. Strychor, J.C. Williams and W.A. Soffa, *Metall. Trans.*, 19A, 1988, 225.
29. C.P. Chang, and M.H. Loretto, *Philos. Mag. A*, 63 (1991), 389-406.

Bibliography

30. H.T. Kester-Weykamp, D.R. Baker, D.M. Paxton and M.J. Kaufman, *Scripta Metall.* 24, 1990, 445.
31. L.A. Bendersky, W.J. Boettinger and A. Raytburd, *Acta Metall.*, 39, 1991, 1959-1969.
32. L.A. Bendersky, W.J. Boettinger and A. Roytburd, in *Proc. 6th Japan Institute of Metals Intermetallics Symposium*, ed. O. Izumi, Japan Institute of Metals, Sendai, 1991, p. 845.
33. L.M. Hsiung and H.N.G. Wadley, *Materials Science and Engineering, A* 192/193, 1995, 908-913.
34. S.A. Court, J.P.A. Lofvander, M.H. Loretto and H.L. Fraser, *Philos. Mag. A*, 61, 1990, 109-139.
35. D. Banerjee, A.K. Gogia and T.K. Nandy, *Metall. Trans. A*, 21A, 1990, 627-639.
36. D. Banerjee, R.G. Rowe and E.L. Hall in *High Temperature Ordered Intermetallic Alloys IV*, eds. L.A. Johnson, D.P. Pope and J.O. Stiegler, 1991, MRS Proc. 213, 285-290.
37. Y. Minonishi, *Philos. Mag. Lett.*, 62, 1990, 153-158.
38. Y. Minonishi, *Philos. Mag. A*, 63, 1991, 1085-1093.
39. T. Nakana, Y. Maeda and Y. Umakoshi, *ISIJ International*, 36 1996, 111.
40. P. Villars and L.D. Calvert, in *Pearson's Handbook of Crystallographic Data for Intermetallic Phases*. ASM International, Metals Park, Ohio, 1985.
41. J.C. Williams and M.J. Blackburn, in *Ordered Alloys: Structural Applications and Physical Metallurgy*, eds. B.H. Kear, T. Sims, N.S. Stoloff and J.H. Westbrook, Claitor's Pub., Baton Rouge, Los Angeles, 1970, p. 425.
42. S.M.L. Sastry and H.A. Lipsitt, in *Titanium '80, Science and trechnology*, eds. H. Kimura and O. Izumi, TMS-AIME, Warrendale, Pennsylvania, 1980, p. 1231.
43. S.A. Court, J.P.A. Löffvander, M.H. Loretto and H.L. Fraser, *Philos. Mag.* 61, 1990, 109.
44. A.K. Gogia, D. Banerjee and T.K. Nandy, *Metall. Trans. A*, 21, 1987, 609.



45. S.A. Court, M.H. Loretto and H.L. Fraser, *Scripta Metall.* 21, 1987, 997.
46. M. Thomas, A. Vassel and P. Veyssiere, *Scripta Metall.* 21, 1987, 501.
47. M. Thomas, A. Vassel and P. Veyssiere, *Philos. Mag. A.*, 59, (1989), 1013.
48. D.P. Pope and C.T. Liu, in *Superalloys, Supercomposites, and Superceramics*, eds J.K. Tien and T. Caulfield, Academic Press, San Diego, California, 1989, p. 583.
49. M. Thomas, A. Vassel and P. Veyssiere, *Philos. Mag.* 59, 1989, 1013.
50. J.P.A. Lofvander, S.A. Court, M.H. Loretto and H.L. Fraser, *Philos. Mag. Lett.* 1989, 60, 111.
51. M. Thomas, A. Vassel and P. Veyssiere, in *Proc. 6th World Conference on Titanium*, Vol. II, eds. P. Lacombe, R. Tricot and G. Beranger, J. de Physique, Les Ulis, France, 1988, p. 1085.
52. R.S. Mishra and D. Banerjee, *Materials Science and Engg. A*, 130, 1990, 151.
53. M. Yamaguchi and Y. Umakoshi, *Prog. Mater. Sci.*, 34, 1990, 17.
54. J. Marquandt, G.K. Scarr, J.C. Chesnut, C.G. Rhodes and H.L. Fraser, in *Proc. 6th World Conference on Titanium*, Vol. II, eds. P. Lacombe, R. Tricot and G. Beranger, J. de Physique, Les Ulis, France, 1988, p. 955.
55. J. Wittenauer, C. Bassi and B. Walser, *Scripta Metall.*, 23, 1381.
56. S.L. Semiatin, K.A. Lark, D.K. Barker, V. Seetharaman and B. Marquardt, *Metall. Trans.*, 23A, 1992, 295.
57. M. Long and H.J. Rack, *Materials Science and Engg., A* 170, 1993, 215.
58. P.K. Sagar, D. Banerjee and Y.V.R.K. Prasad, *Materials Science and Engg., A* 177, 1994, 185.
59. M. Long and H.J. Rack, *Materials Science and Engineering, A* 194, 1995, 99.
60. D.E. Albert and G.T. Gray III, *Acta Mater.*, 45, 1997, 343.

Bibliography

61. P.K. Sagar, D. Banerjee, K. Muraleedharan and Y.V.R.K. Prasad, *Metall. Trans. A*, 27 A, 1996, 1.
62. D. A.Koss, D. Banerjee, D. A. Lukasak and A. K. Gogia, in *High Temperature Aluminides and Intermetallics*, eds. S.H. Whang, C.T. Liu, D.P. Pope and J.O. Stiegler, TMS, Warrendale, PA, 1990, p. 175.
63. A.K. Gogia, T.K. Nandy, K. Muraleedharan, and D. Banerjee, *Mater. Sci. Engg. A* 159, 73.
64. D.M. Lukasak and D.A. Koss, *Metall. Trans.*, 21A, 1990, 135.
65. S. Kerry in *Titanium '92, Science and Technology*, eds. F. H. Froes and I.L. Caplan, TMS, Warrendale, PA, Vol. 2, 1993, p. 1227.
66. R.G. Rowe, M.F.X. Gigliotti and B.J. Marquardt, *Scripta Metall.*, 24, 1990, 1209.
67. C.H. Ward, J.C. Williams, A.W. Thompson, D.G. Rosenthal and F.H. Froes, in *Sixth World Conference on Titanium*, eds. P. Lacombe, R. Tricot, and G. Beranger, J. de Physique, Les Ulis, 1988, p. 1103.
68. J. Kumpfert, C.H. Ward, Y.T. Lee, and M. Peters, in *Proc. 7th World Conference on Titanium*, San Diego, 1992.
69. C.H. Ward, *Int. Mat. Rev.*, 38, 1993, 79.
70. J. Kumpfert, K.J. Grundhoff, H. Schrmann, Y.T. Lee, C.H. Ward and M. Peters, in *Proc. 2nd European Conference on Advanced Materials and Processes*, Vol. 2, eds. T.W. Clyne and P.J. Withers, Institute of Materials, London, 1991, p. 321.
71. G. Lutjering, G. Proske, J. Albrecht, D. Helm and D. Dauebler, in *Proc. 6th Japan Institute of Metals Intermetallics Symposium*, ed. O. Izumi, Japan Institute of Metals, Sendai, 1991, p. 537.
72. M.G. Mendiratta, and H.A. Lipsitt, *J. Mater Sci.*, 15, 1980, 2985.
73. W. Cho, A.W. Thompson and J.C. Williams, *Metall. Trans.*, 21A, 1990, 641.
74. R.W. Hayes, *Acta Metall.*, 39, 1991, 569.

75. D. E. Albert, and A.W. Thompson, in *Microstructure Property Relationships in Titanium Aluminides and Alloys*, eds. Y.W. Kim and R.R. Boyer, TMS, Warrendale, PA, 1991, p. 399.
76. W.O. Soboyejo, R.J. Lederich, and D.S. Schwartz, in *Microstructure/Property Relationships in Titanium Aluminides and Alloys*, eds. Y.W. Kim and R.R. Boyers, TMS, Warrendale, PA, 1991, p. 407.
77. R.S. Mishra and D. Banerjee, *Scripta Metall.*, 24, 1990, 1477.
78. T.K. Nandy, R.S. Mishra and D. Banerjee, *Scripta Metall.*, 28, 1993, 569.
79. R.G. Rowe and E.L. Hall, in *High Temperature Ordered Intermetallic Alloys IV*, eds. L.A. Johnson, D.P. Pope and J.O. Steigler, MRS Proc., 213, 1991, 449.
80. C.H. Ward, and S.J. Balsone, in *Microstructure/Property Relationships in Titanium Aluminides and Alloys*,. Eds. Y.W. Kim and R.K. Boyers, TMS, Warrendale, PA, 1991, p. 373.
81. R.G. Rowe, in *High Temperature Aluminides and Intermetallics*, eds. S.H. Wang, C.T. Liu, D.P. Pope, and J.O. Stiegler, TMS, Warrendale, PA, 1990, pp. 403-424, R.G. Rowe, *U.S. Pat.*, 1991, 5 032 357, R.G. Rowe in *Key Engineering Materials*, eds. F.H. Froes and T. Khan, Trans. Tech., Switzerland, vol. 77-78, 1993, 61.
82. K.S. Chan, *Metall. Trans.*, 21A, 1990, 2687.
83. K.S. Chan, *Metall. Trans.*, 23A, 1992, 183.
84. K.S. Chan, *Metall. Trans.*, A, 24A, 1993, 569.
85. D.A. Davidson in *Microstructure/Property Relationships in Titanium Aluminides and Alloys*, eds. Y.W. Kim and R.R. Boyer, TMS, Warrendale, PA, 1991, p. 447.
86. D.A. Davidson, J.B. Campbell and R.A. Page, *Metall. Trans.*, 22A, 377.
87. H.S. Yang, P. Jin, E. Dalder and A.K. Mukherjee, *Scripta Metall. Mater.*, 25, 1991, 1223.

Bibliography

88. A.K. Ghosh, C.H. Cheng, in *Superplasticity in Advanced Materials*, ed. S. Hori, M. Tokizane and Furushiro, The Japan Society for Research on Superplasticity, Osaka, Japan, 1991, p. 299.
89. N. Ridley, D.W. Livesey and M.T. Saleli, in *Proc. Int. Conf. on High Temperature Intermetallics*, London, 1991, p. 198.
90. S.C. Cheng, J. Wolfenstine and O.D. Sherby, *Metall. Trans.* 23A, 1992, 1509.
91. H.C. Fu, J.C. Huange, T.D. Wang and C.C. Bampton, *Acta Mater.*, 46, 1998, 465.
92. A. Dutta and D. Banerjee, *Scripta Metall.*, 24, 1990, 1319.
93. W.P. Hon, C.H. Koo, S.K. Wu and T.S. Chou, *Scripta Metall*, 25, 1991, 2171.
94. D.B. Knorr and N.S. Stoloff, *Mater. Sc. Engg., A* 123, 1991, 81.
95. W. Mao, Y. Yu and J. Xu, in *Proc. of International Conference on Texture of Materials (ICOTOM – II)*, eds. Z. Liang, L. Zuo and Y. Chu, Xian, China, 1996, p. 1004.
96. C.G. Rhodes, J.A. Graves, P.R. Smith and M.R. James, in *Structural Intermetallics*, eds. R. Darolia, J.J. Lewandowski, C.T. Liu, P.L. Martin, D.B. Miracle and M.V. Nathal, The Minerals, Metals and Materials, Society, 1993, p. 45.
97. A.D. Rollett, K. Muraleedharan, P.R. Smith and M.R. James, presented in TMS Fall Meeting, Cincinnati, October, 1996.
98. M. Hatherly and W.B. Hutchinson, *An Introduction of Textures in Metals*, The Institute of Metallurgists, London, 1979.
99. J. Hansen, J. Pospiech and K. Lüke, *Tables for Texture Analysis of Cubic Crystals*, Springer-Verlag, Berlin, 1978.
100. R.K. Ray, J.J. Jonas, M.P. Butron-Guillen and S. Savoie, *ISIJ International*, 34, 1994, 927.
101. H.J. Bunge, *Z. Metallkunde*, 56, 1965, 872.
102. R.J. Roe, *J. Appl. Phys.*, 36, 1965, 2024.

Bibliography

103. H.J. Bunge, *Mathematische Methodn der Texturanalyse*, Academic Verlag, Berlin, 1969.
104. H.J. Bunge, *Texture analysis in Materials Science*, Butterworths, London, 1982.
105. K. Lücke, H.J. Perlwitz and W. Pitsch, *Phys. Stat. Sol. (A)*, 7, 1964, 737.
106. K. Walther and K. Hennig, *Proc. ICOTON-7*, 1980, p. 1223.
107. P.E. Markovsky, *Mater. Sc. Engg. A* 203, 1995, L1-L4.
108. C. W. Collings, *The Physical Metallurgy of Titanium Alloys*. ASM International, Metals Park, OH 44073, 1984
109. H. J. McQueen and J. J. Jonas. *Metal Forming Interrelation Between Theory and Practice*, Ed. A.L. Hoffmanner, Plenum Press 1971, p. 393.
110. *Materials Properties Handbook: Titanium Alloys*, ASM International, 1996.
111. H. Margolin and P. Cohen, *Titanium '80, 4th International Conference on Titanium*, Kyoto, Japan, 1980, p. 925.
112. I. Weiss, F.H. Froes, D. Eylon and G.E. Welsch, *Metall. Trans. A.*, 17A, 1986, 1935.
113. K. Mallikarjun Baburao, *M. Tech. Dissertation*, 1998, IIT Kanpur.
114. H. Inoue, S. Fukwshima and N. Inakazu, *Materials Transactions*, JIM, 33, 1992, 129.
115. P.I. Welch, *Texture of Crystalline Solids*, 4, 1980, 99.
116. C.U. Nauer-Gerhardt and H.J. Bunge, *Proc. Eighth International Conference on Textures of Materials (ICOTOM 8)*, eds. J.S. Kellend and G. Gottstein, The Metallurgical Society, 1988, p. 505.
117. H. Inoue and N. Inakazu, *Proc. Eighth International Conference on Textures of Materials (ICOTOM 8)*, eds. J.S. Kellend and G. Gottstein, The Metallurgical Society, 1988, p. 997.
118. H.P. Lee, C. Esling and H.J. Bunge, *Textures and Microstructures*, 7, 1988, 317.

Bibliography

119. A. Tanabe, T. Nishimura and M. Fukuda, *Titanium '80; Science and Technology*, eds. H. Kimura and O. Izumi, 1980, p. 937.
120. C.J. McHargue and J.P. Hammond, *J. Met.*, Jan. 1953, 57.
121. D.L. Dull and M.F. Amateau, *Tech. Doc. News*, Feb. 1970, No. 1925-13.
122. F.A. Crossley, ASM Tech. Paper, *1970 Western Metal and Tool Conference and Exposition*, Mar. 1969, p. 10.
123. V.V. Muklayer, R.A. Adamsku and P.V. Geld; AN SSSR, *Izvestiya, Metally*. No. 6, 1968, p. 98. *cited in Ref. 12.*
124. J.H. Keeler and A.H. Geisler, *J. Met.*, Feb. 1956, 80.
125. S. Nourbakhsh and T.O' Brien, *Mater. Sc. Engg.*, 100, 1988, 109.
126. F.R. Larson, A. Zarkades and D.H. Avery; *Titanium Science and Technology*, Plenum Press, New York – London, 2, 1973, p. 1169.
127. H. Conrad, M. Doner and B. de Meester, *Titanium Science and Technology*, Plenum Press, New York – London, 2, 1973, p. 969.
128. H. Inagaki, *Z. Metallkde*, 81, 1990, 282.
129. H. Inagaki, *Z. Metallkde*, 82, 1991, 779.
130. K. Morii, H. Mecking and G. Lützerling, *Proc. of ICSMA 7*, Oxford, Pergamon Press, 1985, p. 251.
131. K. Morii, C. Hartig, H. Mecking, Y. Nakayama and G. Lützerling, in *Proc. Eighth International Conference on Texture of Materials (ICOTOM 8)*, eds. J.S. Kallend and G. Gottstein, The Metallurgical Society, 1988, p. 991.
132. S. Sasano, S. Komori and H. Kimura, *J. Japan Inst. Met.*, 38, 1974, 199.
133. H. Inagaki, *Z. Metallkde.*, 81, 1990, 434.
134. M. Peters and G. Luetjering, in *Titanium, Science and Technology, Proc. of the Fourth International Conference on Titanium*, Kyoto, Japan, ed. H. Kimura and O. Izumi, 1980, p. 925.

Bibliography

135. S.F. Frederick and G.A. Lenning, *Metall. Trans.*, 6B, 1975, 601.
136. F. Larson and A. Zarkades, MCIC-74-20, 1974, Battelle, Columbus, *cited in Ref. 133*.
137. A.W. Sommer and M. Creager, AFML-TR-76-222, 1977, *cited in Ref. 133*.
138. M.J. Blackburn, J.A. Feeney and T.R. Beck, *Advances in Corrosion Science and Technology*, 3, 1973, p. 67, Plenum Press, New York.
139. M.F. Amateau, D.L. Dull and L. Raymond, *Metall. Trans.*, 5 A, 1974, 561.
140. T.R. Thornburg and H.R. Piehler, *Metall. Trans.* 6A, 1975, 1511.
141. K. Wierzbanski, *Scripta Metall.*, 13, 1979, 759.
142. C.N. Tome, R.A. Lebensohn and U.F. Kocks, *Acta Met. et Mater.*, 39, 1991, 2667.
143. F.D. Rosi, F.C. Perkins and S.S. Seigle, *Trans. Met. Soc. AIME*, 206, 1956, 115.
144. H. Conrad, *Progress in Materials Sciences*, 26, 1981, 199.
145. G.Y. Chin, *Metall. Trans.*, 6A, 1975, 238.
146. P. Dervin, M. Pernot and R. Penelle, *Proc. 5th Int. Conf. on Textures of Materials*, Springer-Verlag, 1978, p. 505.
147. E.N. Kelly and W.F. Hosford, *Trans. Met. Soc. AIME*, 242, 1968, 654.
148. D.R. Thornburg, Ph.D. Thesis, 1971, Carnegie Mellon University, Pittsburgh, Pennsylvania, USA
149. D.R. Thornburg and H.R. Piehler, in *Titanium Science and Technology*, vol. 2, 1973, Plenum Press, p. 1187.
150. D.R. Thornburg and H.R. Piehler, *Metall. Trans.* 6A, 1975, 1511.
151. E. Tenckhoff, *Metall Trans.* 9A, 1978, 1401.
152. M.J. Philippe, C. Esling and B. Hochei *Textures and Microstructures*, 7, 1988, 265.

153. M.J. Philippe, *Materials Science Forum*, 157, 1994, 1337.
154. N. Chen, J. Xu, G. Ghu, W. Mao and Y. Yu, *Proc. of International Conference on Texture of Materials (ICOTOM – 11)*, ed. Z. Liang, L. Zuo and Y. Chu, Xi'an, China, 1996, p.971.
155. Z.S. Zhu, J.L. Gu and N.P. Chen, *Scripta. Mater.* 34, 1996, 1281.
156. S.F. Frederick, *AFML-TR-73-265*, 1973, *cited in* Ref. 134.
157. M. Peters, Ph.D. Thesis, 1980, Ruhr-University Bochum, *cited in* Ref. 134.
158. I. L. Dillamore and W.T. Roberts, *Metall. Rev.*, 1965, 65.
159. S. Ghosh Choudhury, Ph.D. Thesis, 1996, IIT Kanpur.
160. B. Bhattacharya, Ph.D. Thesis, 1997, IIT Kanpur.
161. Kanchan Kumari, M. Tech. Thesis, 1998, IIT Kanpur